Gas-phase PIV thermography based on phosphorescence for high-temperature applications

Von der Fakultät für Ingenieurwissenschaften, Abteilung Maschinenbau und Verfahrenstechnik der

Universität Duisburg-Essen

zur Erlangung des akademischen Grades

eines

Doktors der Ingenieurwissenschaften

Dr.-Ing.

genehmigte Dissertation

von

Andreas Kopf
aus
Herrenberg

Gutachter: Prof. Dr. rer. nat. Christof Schulz
Prof. Dr.-Ing. Frank Beyrau
Prof. Frédéric Grisch

Tag mündlichen Prüfung: 9.9.2022

Thermographie PIV en phase gazeuse basée sur la phosphorescence pour applications à hautes températures

Gas-phase PIV thermography based on phosphorescence for high-temperature applications

Thèse de doctorat de l'université Paris-Saclay et de l'université Duisbourg-Essen

École doctorale n° 579
Sciences Mécaniques et Energétiques, Matériaux et Géosciences (SMEMAG)
Spécialité de doctorat : Energétique

Unité de recherche : IFP Energies Nouvelles Mobilité et Systèmes (Rueil-Malmaison, FRANCE)

Thèse soutenue à l'université Duisbourg-Essen, le 9.9.2022, par

Andreas KOPF

Composition du Jury

Burak ATAKAN Prof. Dr. rer. nat., Université Duisbourg-Essen (IVG)	Président
Frédéric GRISCH Professeur, INSA-Rouen Normandie, UMR-CNRS 6614 - CORIA	Rapporteur & Examinateur
Frank BEYRAU Prof. Dr.-Ing., Otto-von-Guericke-Université Magdebourg	Rapporteur & Examinateur
Sébastien DUCRUIX Docteur, HDR, CentraleSupélec Laboratoire EM2C	Examinateur
Christof SCHULZ Prof. Dr. rer. nat., Université Duisbourg-Essen (IVG)	Co-Directeur de thèse
Gilles BRUNEAUX Docteur, HDR, IFP Energies Nouvelles	Co-Directeur de thèse

THÈSE DE DOCTORAT
NNT : 2022UPAST113

université PARIS-SACLAY

ÉCOLE DOCTORALE
Sciences mécaniques et énergétiques, matériaux et géosciences (SMEMAG)

Titre : Thermographie PIV en phase gazeuse basée sur la phosphorescence pour applications à hautes températures

Mots clés : Thermographie PIV (T-PIV), moteur optique, *in situ* thermométrie, diagnostique optique, capacité de survie, luminophores thermosensibles

Résumé : Dans ce manuscrit, le développement et l'application de la thermographie PIV à haute température sont présentés afin de mesurer simultanément la température et la vitesse des gaz de post-combustion dans la phase de détente d'un moteur à combustion interne (*internal combustion engine*, ICE) avec accessibilité optique. Le champ de température bidimensionnel est mesuré en utilisant une approche de ratio d'intensité à deux couleurs exploitant la dépendance en température des propriétés de luminescence de luminophores thermosensibles (*thermographic phosphors*, TP). La vitesse du gaz est, elle, mesurée via une approche PIV conventionnelle.

Alors que la PIV est une approche de diagnostic relativement bien établie pour mesurer la vitesse d'un gaz, 3 défis majeurs ont été identifiés pour la mesure de température dans les gaz de post-combustion utilisant les TP : (a) la capacité de survie des particules pendant la combustion pour garantir que les propriétés de luminescence ne sont pas détériorées, (b) la génération de données d'étalonnage des particules phosphorescentes en aerosol pour minimiser le biais venant de l'application d'une courbe d'étalonnage rapport-température d'un état d'agglomération différent (surface revêtue, poudre en tas) à des luminophores dispersés dans les gaz et (c) la suppression de la contribution du signal de la combustion dans le moteur, qui interfère spectralement et temporellement avec les propriétés optiques de luminescence des luminophores thermosensibles.

Deux luminophores thermosensibles SMP:Sn ($(Sr,Mg)_3(PO_4)_2:Sn^{2+}$) et YAG:Pr ($YAG:Pr^{3+}$) ont été choisis pour les mesures moteur parmi une large gamme de luminophores sur la base de différents paramètres comprenant la gamme de température, la sensibilité de signal avec un changement de température, les caractéristiques spectrales et la durée de vie d'émission de luminescence absolu. Ils ont ensuite été étudiés vis-à-vis des défis mentionnés ci-dessus.

Premièrement, pour étudier la capacité de survie des luminophores dans des conditions drastiques de combustion, les propriétés de luminescence des matériaux sont évaluées dans les gaz de post-combustion d'un brûleur prémélangé reproduisant les conditions rencontrées dans un ICE. Les particules sont recapturées au-dessus de la flamme et analysées *ex situ* par analyses microscopiques (MEB/EDX) et diffraction des rayons X (DRX) pour identifier les modifications chimiques ou structurelles. Alors que la luminescence induite par laser d'YAG:Pr peut être exploitée pour des mesures de température *in situ* dans les gaz d'échappement au-dessus de la flamme, aucune luminescence n'est détectée pour le SMP:Sn, quelles que soient les conditions de réaction dans les limites de stabilité de la flamme. L'analyse microscopique post-flamme du YAG:Pr n'a pas révélé d'altération alors que la morphologie et la composition chimique du SMP:Sn ont été fortement modifiées lors du passage dans la zone de réaction, ce qui explique la perte des propriétés de luminescence.

Deuxièmement, les propriétés de luminescences spectrales et temporelles des deux luminophores en aérosol sont caractérisées dans un jet chaud sur une gamme de température jusqu'à 825 K. Une courbe d'étalonnage rapport-température est établie en utilisant la méthode du ratio d'intensité à deux couleurs avec les mêmes filtres optiques que ceux utilisées par la suite dans le moteur. La durée de vie de l'émission des transitions photophysique d'intérêt, qui sont utilisées pour la méthode à deux-couleurs, est caractérisée sur l'ensemble de la gamme de température.

Enfin, des mesures de températures sont effectuées dans les gaz de post-combustion d'un moteur avec YAG:Pr, en proposant une nouvelle approche de correction en ligne pour réduire l'impact des interférences de signal dues à la combustion. Cette méthode combine une approche basée sur l'ajustement de la durée d'exposition

des caméras en fonction de la durée d'émission des luminophores thermosensibles, avec une correction en ligne de l'interférence due à la combustion. Pour ce faire, la durée d'exposition des deux caméras utilisées pour la méthode deux couleurs est ajustée individuellement, chacune avec un facteur valant le triple de la constante de durée de vie (3τ) d'émission de la transition correspondante dans le canal de détection. Cette approche permet de détecter 95% du signal de phosphorescence tout en minimisant l'impact des signaux parasites.

Pour l'approche de correction en ligne, deux images avec des paramètres d'acquisition similaires sont enregistrées avant et après l'émission du faisceau laser d'excitation. La première image, qui ne contient que le signal émanant de la combustion, est utilisée pour corriger la contribution de la combustion dans la deuxième image qui enregistre la luminescence induite par laser, en supposant que la combustion ne varie pas sur une courte durée d'exposition (< 175 µs) et la succession rapide des deux images (47,2 µs). Les effets potentiels de déplétion de l'intensificateur dus à la succession rapide de deux images sont analysés et pris en compte dans des mesures de calibration antérieures.

En utilisant cette nouvelle approche de correction, les températures sont mesurées avec succès dans les gaz de post-combustion du moteur à 540–580 angles vilebrequin (°VB). La température moyenne au point mort bas (540 °VB) est de 657 K avec une précision ($\pm 1\sigma$) de 74 K (11%) et décroît à 496 K (65 K, 13%) à 580 °VB.

Ce travail présente les premières mesures de températures dans les gaz brulés d'un moteur à combustion interne avec accès optiques pendant la phase de détente, en utilisant des luminophores thermosensibles. Cette thèse contribue au développement des diagnostics avancés par laser en étendant les conditions de mesures de températures vers le régime de post-combustion. Cela contribue non seulement à une amélioration de la compréhension fondamentale de la combustion dans les systèmes techniques, mais permet également de générer des don-nées expérimentales pour valider les simulations de mécanique des fluides numérique (*computational fluid dynamics*, CFD). Ces deux aspects ont vocation à contribuer au développement des futurs systèmes de combustion à haut rendement.

université PARIS-SACLAY

ÉCOLE DOCTORALE
Sciences mécaniques et énergétiques, matériaux et géosciences (SMEMAG)

Title: Gas-phase PIV thermography based on phosphorescence for high-temperature applications

Keywords: Thermographic PIV (T-PIV), optical engine, *in situ* phosphor thermometry, laser-based optical diagnostics, particle survivability, thermographic phosphor

Abstract: In this dissertation, the development and application of high-temperature thermographic phosphor particle image velocimetry (T-PIV) are presented to simultaneously measure the temperature and the velocity of the post-combustion gases in the expansion stroke of an optically accessible internal combustion engine (ICE). For this objective, micrometer-sized phosphor particles are dispersed in the air and fed into the engine. Two-dimensional temperature fields are measured using the ratiometric two-color approach by exploiting the temperature-dependent luminescent properties of thermographic phosphors (TP), and gas velocity maps are obtained based on particle-image velocimetry (PIV).

While PIV is a well-established approach, three major challenges have been identified for temperature measurement in post-combustion gases using thermographic phosphors: (a) particle survivability during combustion to ensure that the luminescence properties are not deteriorated once particles are exposed to flames, (b) the generation of calibration data for phosphor thermometry based on aerosolized phosphor particles, and (c) the suppression of signal contribution from combustion luminescence in the engine that can interfere spectrally and temporally with the phosphor luminescence.

SMP:Sn ($(Sr,Mg)_3(PO4)_2:Sn^{2+}$) and YAG:Pr ($YAG:Pr^{3+}$) were selected from a wide range of thermographic phosphors based on various parameters, including temperature sensitivity, spectral characteristics, and luminescence emission lifetime and examined according to the challenges mentioned above.

To investigate the particle survivability of thermographic phosphors in harsh combustion conditions, the phosphors' luminescence properties are investigated in the post-combustion gases of a lean premixed flame with combustion temperatures similar to those found in an ICE. The particles are recaptured above the flame and *ex situ* analyzed for chemical or structural changes using microscopic analysis (SEM/EDX) and x-ray diffraction (XRD). While laser-induced luminescence of YAG:Pr can be exploited for *in situ* temperature measurements after interaction with the flame, no luminescence remains for SMP:Sn for any reaction conditions within the stability limits of the flame. The microscopic analysis of post-flame YAG:Pr did not show any alteration, whereas the morphology and chemical composition of SMP:Sn changed upon passing the reaction zone, which is responsible for the loss of its luminescence properties.

Spectral and temporal luminescence properties of both aerosolized thermographic phosphors are characterized in a heated jet at temperatures up to 825 K. A calibration curve is established for ratiometric two-color thermometry. The luminescence lifetime of the transitions used for the two-color method is characterized over the entire temperature range.

Based on the previously gained knowledge, temperature measurements are carried out in the post-combustion gases of an ICE with YAG:Pr, using a novel online correction approach to reduce signal interference from combustion luminescence. This method combines a lifetime-based camera gating approach with online correction of combustion interference. For this purpose, the exposure duration of both cameras used for the two-color method is individually adjusted, each to a threefold of the emission lifetime constant (3τ) of the corresponding transition in the respective detection channel. This approach enables capturing 95% of the phosphorescence signal while minimizing interference. For online background correction, two subsequent images with similar acquisition parameters are recorded before and after the excitation laser pulse. The first image that only contains signal from combustion luminescence is used to correct the combustion contribution in the second image capturing the laser-induced luminescence, assuming that combustion luminescence does not change for the short exposure duration (<175 µs) and rapid succession

of both images (47.2 µs). Potential depletion effects of the intensifier due to the rapid succession of two images are analyzed and accounted for. Temperature fields are then successfully measured in the engine post-combustion gases at 540–580 crank angle degrees (°CA). The average temperature at the bottom dead center (540 °CA) is 657 K with a single-shot precision ($\pm 1\sigma$) of 74 K (11%) and decreases to 496 K (65 K, 13%) at 580 °CA.

In this work, temperature measurements in the expansion stroke in an optically accessible ICE using thermographic phosphors under fired conditions are presented for the first time. This dissertation contributes to the development of advanced laser-based diagnostics by extending the measurement conditions for temperature measurements towards the post-combustion regime. This cannot only advance a fundamental understanding of combustion processes but can provide experimental data to validate computational fluid dynamics simulations in the expansion stroke under fired engine conditions, which can both contribute to the development of future highly-efficient practical combustion and reaction systems.

université PARIS-SACLAY

ÉCOLE DOCTORALE
Sciences mécaniques et énergétiques, matériaux et géosciences (SMEMAG)

Titel: Thermographisches PIV basierend auf Aerosolphosphorlumineszenz für Hochtemperaturanwendungen

Schlüsselwörter: Thermographisches PIV (T-PIV), optischer Motor, In-situ-Phosphorthermometrie, Laserdiagnostik, thermographische Phosphore

Kurzfassung: In dieser Dissertation wird die Entwicklung und Anwendung eines bildgebenden optischen Messverfahrens zur simultanen zweidimensionalen Temperatur- und Geschwindigkeitsmessung von Verbrennungsgasen im Expansionshub eines optisch zugänglichen Verbrennungsmotors in gefeuertem Betrieb vorgestellt. Dazu werden mikrometergroße thermographische Phosphorpartikel in die Ansaugluft des Motors dispergiert und durch einen Laserlichtschnitt angeregt. Das Temperaturfeld der Gase wird durch die Intensitätsverhältnismethode unter Ausnutzung der temperaturabhängigen Lumineszenzeigenschaften thermografischer Phosphore (TP) gemessen. Das Geschwindigkeitsfeld wird durch die sich im Zylinder befindlichen Partikel zeitgleich über den herkömmlichen PIV-Ansatz (*particle-image velocimetry*) quantifiziert.

Während PIV eine vielfach angewendete Messtechnik zur abbildenden Messung von Strömungsgeschwindigkeiten ist, wurden für die Temperaturmessung von Gasen in technischen Verbrennungssystemen drei Heraus-forderungen identifiziert: (a) Die Lumineszenzeigenschaften der Phosphore können sich während der Interaktion mit der Flamme verändern und dadurch Messungen verfälschen, (b) Es muss eine Intensitätsverhältnis–Temperatur-Kalibrierkurve an in Luft dispergierten thermographischen Phosphoren im relevanten Temperaturbereich ermittelt werden, und (c) Interferierendes Verbrennungsleuchten (Chemilumineszenz, Schwarzkörperstrahlung), das dem gewünschten Signal spektral und zeitlich überlagert ist muss unterdrückt bzw. korrigiert werden.

Als thermografische Phosphore wurden SMP:Sn ($(Sr,Mg)_3(PO_4)_2:Sn^{2+}$) und YAG:Pr ($YAG:Pr^{3+}$) durch Evaluierung von Temperaturempfindlichkeit, spektralen Eigenschaften und Lumineszenzlebensdauer als geeignet für die Temperaturmessung in Verbrennungsumgebungen ausgewählt und im Hinblick auf die oben genannten Herausforderungen untersucht.

Die Lumineszenzeigenschaften der Phosphore wurden nach der Interaktion mit einer mageren Vormischflamme untersucht, um die Stabilität der Partikel unter Verbrennungsbedingungen zu erforschen. Die Partikel wurden oberhalb der Flamme aufgefangen und *ex situ* mikroskopisch (REM/EDX) und mit Röntgenbeugung (XRD) auf chemische und strukturelle Veränderungen untersucht. Während die laserinduzierte Lumineszenz von YAG:Pr für In-situ-Temperaturmessungen auch nach Interaktion mit der Flamme genutzt werden kann, gibt es bei SMP:Sn keine verbleibende Lumineszenz innerhalb der Stabilitätsgrenzen der Flamme. Die mikroskopische Analyse von YAG:Pr aus dem Flammenabgas zeigt keinerlei Veränderungen im Vergleich zu den Phosphorpartikeln vor der Verbrennung, während die Morphologie und die chemische Zusammensetzung von SMP:Sn beim Durchgang durch die Flamme verändert wurden, was zum vollständigen Verlust der Phosphor-Lumineszenz führt.

Die spektralen und zeitlichen Lumineszenzeigenschaften der beiden Phosphoraerosole wurden in einem beheizten Luftstrom für Temperaturen bis zu 825 K charakterisiert und mithilfe der Zweifarbenmethode eine Intensitätsverhältnis–Temperatur-Kalibrierkurve erstellt. Die Lumineszenzlebensdauerkonstanten der relevanten Übergänge wurden über den gesamten Temperaturbereich bestimmt.

Auf Basis der vorherigen Erkenntnisse wurden Temperaturverteilungen im optisch zugänglichen Motor durchgeführt. Dazu wurde ein neuartiger Messansatz entwickelt, durch den Störsignale aus der Verbrennung reduziert werden können. Dazu wird die Belichtungsdauer der Detektionskanäle der Phosphorlumineszenz jeweils auf das Dreifache der erwarteten Lebensdauer (3τ) der Emission eingestellt. Dadurch werden 95% des emittierten Signals eingefangen und gleichzeitig die Detektion an Störsignal minimiert.

Zusätzlich wird der Ansatz einer Fast-Echtzeit-Hintergrundkorrektur verfolgt, die die verbleibenden Interferenzbeiträge subtrahiert, die weder zeitlich noch spektral getrennt werden können. Dazu werden zwei Bilder derselben Aufnahmeparameter vor bzw. direkt nach dem Laserpuls aufgenommen. Das erste Bild enthält somit ausschließlich Verbrennungssignal, wohingegen das zweite Bild eine Überlagerung der Signale von Verbrennung und laserinduzierter Phosphoreszenz ist. Unter der Annahme, dass sich die Verbrennung während der Belichtungsdauer (<175 µs) und der schnellen Abfolge beider Bilder (47,2 µs) nicht ändert, können die verbrennungsbedingten Störeinflüsse aus dem zweiten Bild durch Subtraktion korrigiert werden. Mögliche Sättigungseffekte der Bildverstärker aufgrund der schnellen Abfolge beider Bilder werden identifiziert und korrigiert. Mithilfe dieser Methode wurden Temperaturfelder in einem optisch zugänglichen Motor zwischen 540 und 580 °KW (Kurbelwinkelposition) gemessen. Die Untersuchungen in dieser Arbeit ergeben, dass die durchschnittliche Gastemperatur im unteren Totpunkt (540 °KW) 657 K mit einer Einzelschusspräzision ($\pm 1\sigma$) von 74 K (11%) ist und bei 580 °KW auf 496 K (65 K, 13%) fällt.

In dieser Arbeit wird zum ersten Mal die innermotorische Temperaturmessung auch nach der Verbrennungsphase durch Phosphorthermometrie präsentiert. Diese Dissertation soll einen Beitrag zur Entwicklung fortgeschrittener laserbasierter Messtechnik leisten, indem sie die Messbedingungen für Temperaturmessungen auf den Bereich verbrannter Gase ausweitet. Dies führt nicht nur zu einer Verbesserung des fundamentalen Verständnisses technischer Verbrennungsprozesse, sondern erlaubt auch die Erzeugung experimenteller Daten zur Validierung von fluiddynamischen Simulationen im Expansionshub in gefeuertem Motorbetrieb. Beide Aspekte können zur Entwicklung von zukünftigen hocheffizienten technischen Verbrennungs- und Reaktionssystemen beitragen.

Acknowledgments

The present work results from a cooperation between the Institute of Combustion and Gas Dynamics–Reactive Fluids (IVG-RF, University Duisburg-Essen, Germany) and the IFP Energies Nouvelles (Rueil-Malmaison, France), where I was a research assistant and PhD student.

First of all, I would like to express my deepest gratitude to Prof. Christof Schulz for giving me the opportunity to do my PhD under his supervision. I am very grateful for your patience, the scientific freedom I enjoyed, and the trust you have shown in my work and me as a person at all times. I have learned a lot from your extraordinary scientific rigorousness and your incredible professionalism, which impresses me over and over again.

A special thanks to my co-supervisor Gilles Bruneaux for the continuous support and helpful conversations. Thank you for your advice and guidance through my scientific work. Your detached perspective has always helped me not to lose sight of the goal of the work, and to see the light at the end of the tunnel (hoping that it is not the front light of the upcoming train).

Furthermore, I thank Prof. Frédéric Grisch and Prof. Frank Beyrau for their interest in my work and for providing the reviews for this thesis.

Many thanks to my supervisors Michele Bardi and Torsten Endres for their daily support, scientific discussions, constructive feedback, continuous motivation and help, not at least in last-minute requests.

Sincere thankfulness to Christian Angelberger and Julian Kashdan for the unique opportunity to be part of your department. Thank you for your trust and for creating this pleasant and stimulating working atmosphere within R104. My special thanks to all the scientific and technical staff of the optical group at IFPEN, especially Jérôme Cherel and Vincent Ricordeau, for your help in any technical matters and tireless support in finding solutions to even the most complicated problems. I will always remember with great pleasure the legendary FTX ski weekends we spent together.

Many thanks to all IVG staff, especially Matthias Beuting, Sebastian Peukert, Ahmad Saylam, and Prof. Sebastian Kaiser, for your support and inspiration. You were a great help during my time in Duisburg! A special thanks go to the master's student Max Ciapka and the student assistants Mahmoud Elshahed and Amr Saeed. Without your help, it would not have been possible to fulfill this enormous workload during the short time in Duisburg at this quality. I would also like to thank the technical staff Erdal Akyildiz and Jörg “Aldi” Albrecht. You started to work your magic when we didn't know what else to do.

I would like to express my sincere gratitude to my fellow PhD students, especially Louise Ganeau, Edouard Suillaud, and Hassan Afailal, for your collegiality and friendship. Hassan, it was a great pleasure to share the office with you; thank you for the inspiring discussions on combustion problems, music, and geopolitics, and not at least for your patience with my deficiencies in French.

Many thanks to my friends from various orchestras and chamber music groups for the highly-rewarding time playing music together. An exceptional “Thank you!” go to my highly appreciated fellow scholars of the 16th Bronnbacher Stipendium of the “Kulturkreis der Deutschen Wirtschaft” for the stimulating discussions, new perspectives and, not at least for the balancing and fun weekends together.

But my greatest thanks go to my family: my wife Marlene and our daughter Amelie, who have been a great support and source of strength to me, at all times. Many thanks to my beloved sisters and my parents and for their immense love and unconditional support in everything I did.

Paris, July 2022 *Andreas Kopf*

Da steh‘ ich nun, ich armer Tor,
und bin so klug als wie zuvor!

Johann Wolfgang von Goethe

Table of contents

Nomenclature

Small Greek symbols		Unit
α	Crank angle degree	°
α, β	Crystal phases	–
γ	Normalized cross-correlation coefficient	–
ε	Geometric compression ratio	–
θ	Incident angle	°
κ	Isentropic exponent	–
μ	Mean value Viscosity	– N s/m^2
λ	Wavelength	nm
ν	Frequency	1/s
ϱ	Density	kg/m^3
σ	Standard deviation	–
τ	Emission lifetime Response time	s s
ϕ	Collection efficiency Fuel/air equivalence ratio Phase shift	– – s
ψ	Temperature sensitivity Time-independent wave function	%/K –
ω	Vibrational frequency Rotation rate	1/s 1/s

Capital Greek letters		Unit
Ω	Angular frequency	1/s

Small Latin letters		Unit
a, b, c	Constants	–
c	Speed of light	m/s
c_0, c_1, c_2	Fitting parameters (Brübach algorithm)	–
d	Diameter	m

Small Latin letters (continuation)		Unit
e^-	Elementary charge	C
f	Focal length	mm
g	Degeneracy	–
h	Planck constant	m^2 kg/s
$\hbar$	Reduced Planck constant	m^2 kg/s
i, j	Pixel position	–
k	Frame number Restoring force constant	– kg/s^2
k_B	Boltzmann constant	J/K
l	Length	m
m	Mass	kg
$\dot{m}$	Mass flow rate	kg/s
n	Principal quantum number Quantity of substance	– mol
p	Pressure	N/m^2
t	Time	s
u	Velocity	m/s
v	Velocity Vibrational quantum number	m/s –
x, y, z	Spatial coordinates	–

Capital Latin letters		Unit
A	Area	m^2
E	Energy	J
I	Current Intensity	A a.u.
N	Electron population	–
R	Configurational coordinate Ratio Resistance Rydberg constant Universal gas constant	nm – Ω 1/m J/(K mol)
Re	Reynolds number	–
S	Signal intensity Sutherland constant	a.u. K

St	Stokes number	–
T	Temperature	K
U	Voltage	V
V	Potential energy Volume	J m^3
W	Transition probability	1/s

Acronym	Meaning
AOI	Angle of incidence
BBR	Blackbody radiation
BGFR	Burnt-gas flow reactor
BG	Background
BS	Beamsplitter
BSE	Backscattered electrons
CA	Crank angle
CARS	Coherent anti-Stokes-Raman spectroscopy
CFD	Computational fluid dynamics
CMOS	Complementary metal-oxide semiconductor
CR	Compression ratio
CTS	Charge-transfer state
cw	Continuous wave
DCBS	Dichroic beamsplitter
DNS	Direct numerical simulation
DOHC	Double overhead camshaft
EDX	Energy-dispersive x-ray spectroscopy
ETD	Everhart-Thornley detector
FF	Flatfield
FFT	Fast Fourier transformation
FRS	Filtered Rayleigh spectroscopy
FWHM	Full width at half maximum
HAB	Height above burner

ICCD	Intensified charge-coupled device
ICE	Internal combustion engine
IMEP	Indicated mean effective pressure
IPCC	Intergovernmental Panel on Climate Change
IR	Infrared
IRO	Intensified relay optics
LDV	Laser Doppler velocimetry
LES	Large eddy simulation
LIF	Laser-induced fluorescence
LII	Laser-induced incandescence
LP	Longpass
MCP	Multi-channel plate
MFC	Mass flow controller
MTF	Modulated transfer function
NC	Normally-closed
ND	Neutral density
Nd:YAG	Neodymium-doped yttrium aluminum garnet
OD	Optical density
PB	Pellin-Broca prism
PE	Primary electrons
PAH	Polycyclic aromatic hydrocarbons
PIV	Particle image velocimetry
PMT	Photomultiplier tube
QMSCC	Quantum mechanical single configurational coordinate
R	Reflection
RANS	Reynolds-averaged Navier-Stokes
ROI	Region of interest
S	Singlet state
SAD	Selected-area diffraction
SE	Secondary electron
SEM	Scanning electron microscope

SLM	Standard liter per minute
SNR	Signal-to-noise ratio
SP	Short pass
SRAPT	Scattering referenced aerosol phosphor thermometry
ss	Solid solution
T	Transmission Triplet state
TBC	Thermal barrier coatings
TC	Thermocouple
TDC	Top dead center
TEM	Transmission electron microscope
TLC	Thermochromic liquid crystals
TP	Thermographic phosphor
T-PIV	Thermographic particle image velocimetry
TSP	Temperature sensitive paints
TTL	Transistor-transistor logic
UV	Ultraviolet
XRD	X-ray diffraction

1 Introduction

Since the pre-industrial era, the anthropogenic emission of carbon dioxide (CO_2) has increased continuously, reaching its tenfold in 2014 in annual CO_2-equivalent emissions, relatively to 1850. According to the Intergovernmental Panel on Climate Change (IPCC), it is extremely likely that the increased emission of greenhouse gases, including CO_2, is accountable for global warming [1]. In 2015, the Framework Convention on Climate Change of the United Nations agreed on a resolution ("Paris Agreement") to limit global warming to an average of "well below" 2 °C relative to the pre-industrial levels and to undertake efforts to reduce it to 1.5 °C [2]. In 2015, 18% of the global greenhouse gas emissions (GHG[1]) were directly related to road transportation only [3,4]. In order to fulfill climate targets and to meet more restrictive legislation on engine emissions related to road transportation, where the large majority of passenger and commercial vehicles are still based on internal combustion engines (ICE) and conventional fuel [5], significant efficiency improvements are necessary. In addition to optimization of the overall powertrain, where the interplay of the single components can still be improved, further improvement of internal combustion engines is important. Numerical methods like computational fluid dynamics (CFD) are playing an increasingly important role in engine development as well as research engineers. Direct numerical simulation (DNS) is the most accurate method, where the smallest eddies of turbulent processes are numerically resolved through very fine meshing. Due to high computational costs, this will be limited to simplified test cases for the foreseeable future. To make numerical simulations more accessible and applicable, other numerical methods like large eddy simulation (LES) or Reynolds-averaged Navier-Stokes simulation (RANS) rely on modeling that requires experimental validation. Validation from realistic combustion environments is essential for accurate modeling, showing the need for reliable experimental data capturing the physics in this environment.

Temperature and fluid velocity are the most important physical parameter to understand in-cylinder processes. Mixing is particularly important [6] and in engines certainly governed by in-cylinder flows, which in return determine fuel conversion, pollutant formation, and the overall combustion efficiency [7]. Nearly all chemical processes during combustion are a function of temperature, which itself has a direct influence on the flow properties through gas density and viscosity. Temperature and velocity also influence heat transfer from combustion gases to the surrounding combustion chamber, which deteriorates the thermal efficiency of an engine. The brake thermal efficiency (ratio of mechanical energy to the fuel energy supplied to the engine) of current production engines for passenger cars is up to 30–36% and 40–47% for spark-ignition and Diesel engines, respectively [8]. Neglecting friction, the remaining losses split approximately equally to heat losses via exhaust gas and cylinder wall. For the latter, up to 90% of the cumulative heat transfer occurs during combustion in less than 40 crank angle degrees (°CA) after top dead center (TCD) from turbulent convective heat transfer [9], so the temperature of post-combustion gases provides a measure to quantify heat losses in the engine. This penalty is currently addressed by engine manufacturers and researchers likewise, e.g., by the application of thermal barrier coatings (TBC) to the combustion chamber to reduce thermal losses [10]. To evaluate the impact of a

[1] Road transportation GHG emission include CO_2, CH_4, N_2O.

TBC, an accurate measurement of the in-cylinder temperature and velocity fields is desired throughout a wide range of engine conditions, especially in the exhaust gases, where current measurement techniques fail. Despite the strong need for a robust and easily applicable technique to simultaneously measure two-dimensional temperature and velocity under harsh conditions, including the post-combustion gases in the exhaust stroke of an internal combustion engine, a suitable technique is yet to be found. A temperature and velocity *in situ* measurement technique for simultaneous application to reactive and turbulent conditions has very high requirements on the spatial and temporal resolution, robustness to cyclic variations, intrusiveness, as well as low sensitivity to competing processes like chemiluminescence or black-body radiation.

Velocity measurements in reacting flow conditions have been used for decades to understand flow physics using particle image velocimetry (PIV). PIV is an inexpensive approach and facile to apply to technical systems and provides instantaneous information about two- or three-dimensional areas. The flow of interest is seeded with micrometer-sized particles and illuminated by two consecutive laser pulses, separated by the delay time Δt. The particle (Mie-) scattered light of both laser pulses is recorded by a camera. A cross-correlation method is applied to correlate the variation in position from a particle or a particle pattern in the two images. Assuming that velocity does not change between the two pulses, the velocity can be calculated from the in-plane particle displacement between the images. Even if this approach is technically straightforward, some challenges remain in the application to a sensitive measurement environment like an optical engine. Manufacturers of optical measurement systems provide solutions, including automatized post-processing. Therefore, this technique is widely applied, including for in-cylinder flows of internal combustion engines [11,12] or to resolve transient phenomena in combustion [13,14]. Microchannel-PIV with a 1-µm spatial resolution [15] belongs to the current state-of-the-art to the same extent as PIV around a full-scale heavy-duty truck in a wind tunnel, or tomographic PIV using multiple cameras for 3D velocity measurements in biomedical applications [16] or in combustion research [17,18].

Measuring temperature in turbulent reacting flows is challenging, considering the required spatial and temporal resolution as well as potential cross-dependences to surrounding gases in environments of practical interest. Laser-based diagnostics have become popular in the last decades, using various temperature-dependent spectroscopic effects for remotely probing local temperature. Laser-induced fluorescence (LIF) using organic tracers [19] or small molecules [20] is a common approach for temperature measurements. This is, however, restricted to conditions prior to combustion or to regions where these molecules naturally occur during combustion. Optical tracers applicable for temperature measurements in the post-combustion regime have high requirements for thermal and chemical stability. Thermographic phosphors (TP) can be used for remote temperature sensing, and they have recently received a lot of attention for remote temperature sensing due to their advantageous physical properties: TPs are ceramic materials doped with optically active ions. They have high melting points [21], are insensitive to the composition of surrounding gas [22], and are mostly chemically inert [23], which thus enables measurements in more versatile conditions, including oxygen-rich reactive flow conditions. Upon laser excitation, they show temperature-dependent luminescence properties in the temporal or spectral domain. Both dependencies can be exploited for temperature measurements using the lifetime or intensity-ratio approach, respectively, with a previously acquired calibration which is necessary to translate phosphor luminescence to temperature information. It is of interest to combine temperature and velocity measurements using thermographic phosphors to simplify experimental complexity and to share measurement equipment. The phosphor material can be grinded to µm-sized particles and simultaneously used for velocity measurements to track the motion of the particles following the conventional double-

pulse PIV approach. The combination of both approaches is commonly referred to as thermographic particle image velocimetry (T-PIV).

While this approach has been previously validated in literature and preceding work under inert conditions of an internal combustion engine [24,25], some challenges need to be addressed if this technique is being pursued in post-combustion flow conditions. Three main challenges have been identified and will be investigated throughout this work. The first challenge relates to particle survivability. Thermographic tracer particles (and their luminescent properties) are susceptible to particle deterioration when exposed to combustion. That requires selecting such phosphor material that can withstand harsh conditions while the luminescent properties remain unchanged. The second challenge involves generating representative calibration data to translate phosphor luminescence into temperature information over a wide range of temperatures. Recent literature suggests that a systematic error can be introduced if the agglomeration state of the phosphor material changes between measurements in the calibration environment and those in the system of interest. The third challenge is the suppression of signal contribution from combustion luminescence. This interference occurs both spectrally and temporally, making it difficult to isolate the luminescence of the phosphors, especially when phosphor luminescence signal levels are low at elevated temperatures.

This dissertation will address these challenges mentioned above, and simultaneous, two-dimensional imaging data of temperature and flow velocity in the post-combustion regime of an optically accessible internal combustion engine are presented for the first time. After the introductory thoughts in this chapter, the basic principles of phosphor thermometry are explained in Chapter 2, followed by a presentation of the methodology of data reduction (Chapter 3). All experimental environments used throughout this work are detailed in Chapter 4, according to the three challenges identified. The following sections present the results from the phosphor survivability study (Chapter 5) and the signal-ratio–temperature characterization measurements of a phosphor aerosol (Chapter 6). Temperature measurements in a burnt-gas flow reactor are presented in Chapter 7 as a proof of concept in a system of practical interest. Chapter 8 combines the learnings from all previous chapters and presents simultaneous temperature and velocity measurements in an optical engine under motored and fired operation, where strong emphasis is put on the more challenging temperature measurements. This dissertation closes with a conclusion and outlook in Chapter 9, where potential future research fields are proposed.

This work shall contribute to the development of a gas-phase PIV-thermography technique based on thermographic phosphors for post-combustion gases. This will not only help to understand fundamental phenomena such as convective heat transfer in internal combustion engines but also to provide experimental data for CFD code validation and thus benefit the development of future, highly fuel-efficiency internal combustion engines.

2 Theoretical background to phosphor thermometry

The following section will explain the physical principles of phosphor thermometry, which are necessary to understand the temperature-dependent luminescent properties of thermographic phosphors. The interaction of matter and light is described for isolated atoms with the help of the atomic model introduced by Bohr and then extended to molecules and crystalline solid-state structures like thermographic phosphors. Extending Bohr's model, quantum mechanics provide insight into the structure and different energy states of matter. This is important to understand competing transitions between energy states of thermographic phosphors, which form the fundamentals of temperature-dependent spectroscopic properties.

2.1 Photoluminescence of thermographic phosphors

2.1.1 Light-matter interaction

According to the atomic model presented in 1913 by Niels Bohr, electrons can move around an atomic core on distinct orbits without emitting radiation. The orbits have discrete energies, and an electron can change orbits by absorbing or emitting electromagnetic radiation [26]. If an electron is on a higher orbit than the lowest unoccupied one, the electron is in an excited state and can relax into the ground state by emitting a photon of the energy

$$\Delta E = h\nu \tag{1}$$

with the frequency ν and h being the Planck constant. Figure 1 (left) shows the structure of a hydrogen atom with the spontaneous emission of radiation when an electron de-excites to a lower shell. The energy of the electrons is given with $E_\mathrm{n} = -\frac{Rhc}{n^2}$, where R is the Rydberg constant, c the speed of light, and n is the principal quantum number, which denotes the orbit of the electron concerned. Consequently, the energy of an electron is discretized and inversely proportional to the square of the principal quantum number. However, with upcoming quantum mechanics it became clear that electrons or atoms cannot be considered as classical particles but as delocalized particles in the atomic shell [27]. In the quantum mechanical view, any particle can be described using the complex wave function $\psi(x)$, which can be derived by solving the Schrödinger equation for this particle (electron, photon, atom, molecule). The time-independent Schrödinger equation for the motion of an electron with the mass m_e relatively to the atomic core is [27]

$$-\frac{\hbar^2}{2m_\mathrm{e}}\nabla^2\psi + V\psi = E\psi \tag{2}$$

with the reduced Planck constant $\hbar = h/2\pi$, the differentiation ∇^2 with respect to the electron position x, the potential energy V, and the total energy E. The solution of the Schrödinger equation in spherical coordinates for an electron in the potential of the hydrogen atom then forms the atomic orbitals. For

molecules consisting of two or more atoms, the electrons can take additional energy levels, which can be derived from their additional vibrational and rotational degrees of freedom.

In a diatomic molecule, the atoms can also vibrate relatively to each other. In the analogy of harmonic oscillation of two masses in classical mechanics, the pair of two nuclei form a quantum mechanical oscillator, which can also be described with a wave function. If the potential V in Equation 2 has the form of a harmonic potential $V(x) = \frac{1}{2}m\omega^2x^2$, with $\omega = \sqrt{k/m}$ being the eigenfrequency and k the restoring force constant in the classical case, the solution of the Schrödinger equation is mathematically the solution of a harmonic oscillator. A solution to this equation is a Hermitian polynomial of v-th order[2]. Possible vibrational energy levels are quantized and given with $E_{\mathrm{vib}} = (v + \frac{1}{2})\,\hbar\omega_0$ with $v = 0, 1, 2, \ldots$. Vibrational energy levels are thus equidistant, and the energy is non-zero in the ground state. The residence probability density function of an atom in a diatomic molecule is given with the absolute square of the wavefunction $|\psi^2|$. For $v = 0$, the maximum of the residence probability is in the center. For $v = 1$ there are two maxima with a minimum in the center of the potential, and for $v = 2$ there are three maxima. For very high quantum numbers, the maxima are closely spaced and transition towards the continuous distribution of classical systems. This is referred to as Bohr's correspondence principle and is very important for the consistency between the classical and quantum mechanical view.

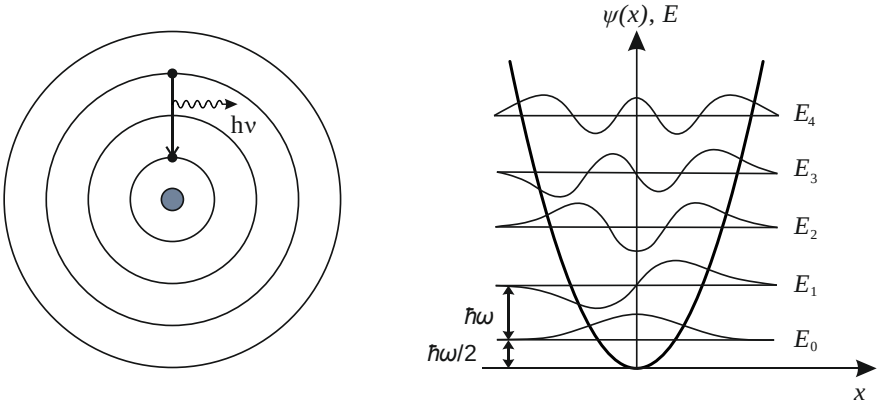

Figure 1: Left: Atomic model of a hydrogen atom after Bohr with the spontaneous emission of a photon. Right: Wavefunction of a quantum mechanical oscillator with its energy levels in a harmonic potential. Vibrational energy levels are not to be confused with the electronic states.

If a particle is exposed to electromagnetic radiation with the energy according to the energy gap between two energetic states, energy can be transferred to the particle, which is called induced absorption. The respective wavelength of the exciting photon can be calculated with $\lambda = c/\nu$ according to the energy gap between the two states from Equation 1. The frequency of the photon is ν, with the wavelength λ, the speed of light c and Planck's constant h. If the particle is in an excited state, it can also return to the ground state via a non-radiative de-excitation path. These processes compete with each other and form the basics of luminescence processes, which will be detailed in the next section.

2.1.2 Fundamentals of luminescence

Photoluminescence is the excitation and subsequent radiative relaxation of luminescent material. A particle in an excited state always returns to the ground state, but not always by emitting radiation. Figure 2 illustrates the absorption of radiation to an excited state (annotated as 1), which can then relax back to the ground state (0) in a radiative or non-radiative process: $W_{1\to0} = W_{\mathrm{r}} + W_{\mathrm{nr}}$.

[2] The Latin letter v annotates the vibrational quantum number and is not to be confused with the Greek letter ν that is the frequency of a photon.

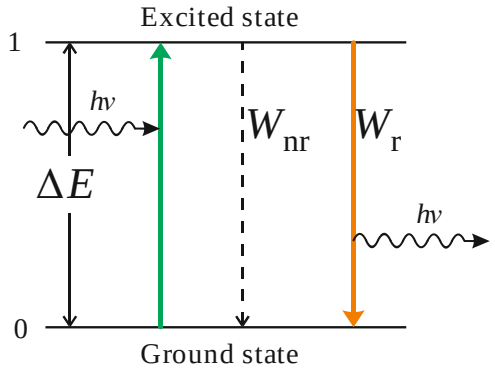

Figure 2: Schematic description of a simplified two-level system with absorption and resulting luminescence.

Both transitions occur at different rates, according to their radiative (r) and non-radiative (nr) transition probability. W_r and W_{nr}. The depletion of the excited electronic state can be written as

$$\frac{dN_1}{dt} = -(W_r + W_{nr})N_1, \tag{3}$$

where N_1 is the electron population in the excited state. From the solution of this differential equation, an exponential decay function for depopulation of the excited state,

$$N_1(t) = N_1^{t=0} e^{-(W_r+W_{nr})t} \tag{4}$$

can be rewritten as the time decay of the radiative emission intensity $I(t)$ from the excited state since the intensity is directly proportional to the depopulation rate of the excited state.

$$I(t) = N_1^{t=0} W_r e^{\frac{-t}{\tau}} \tag{5}$$

The lifetime of the emission τ, or decay time constant, is defined as a function of the radiative and the total non-radiative transition probability:

$$\tau = \frac{1}{W_r + W_{nr}}. \tag{6}$$

The radiative transition rate W_r is also known as the Einstein coefficient for spontaneous emission. Figure 2 shows a strongly simplified picture, where the radiative transition from a single atom only considers two electronic states. Molecules of two or more atoms also have vibrational and rotational degrees of freedom, and the electronic states are subdivided into vibrational and rotation energy levels, resulting in possible additional transitions. Luminescent materials of practical interest are often large molecules, for example $(Sr,Mg)_3(PO_4)_2:Sn^{2+}$, and the transition between different states is governed by events occurring at different timescales.

The Jablonski energy diagram can help to better understand the physical process of luminescence. The diagram in Figure 3 shows different luminescent processes that can occur at different timescales. Energy potentials and vibrational energy levels are shown with horizontal lines, where the electronic states (thick lines) are subdivided into vibrational states (thin lines). Radiative excitation and emission between electronic states are represented with vertical, colored arrows, and non-radiative transitions are shown in black.

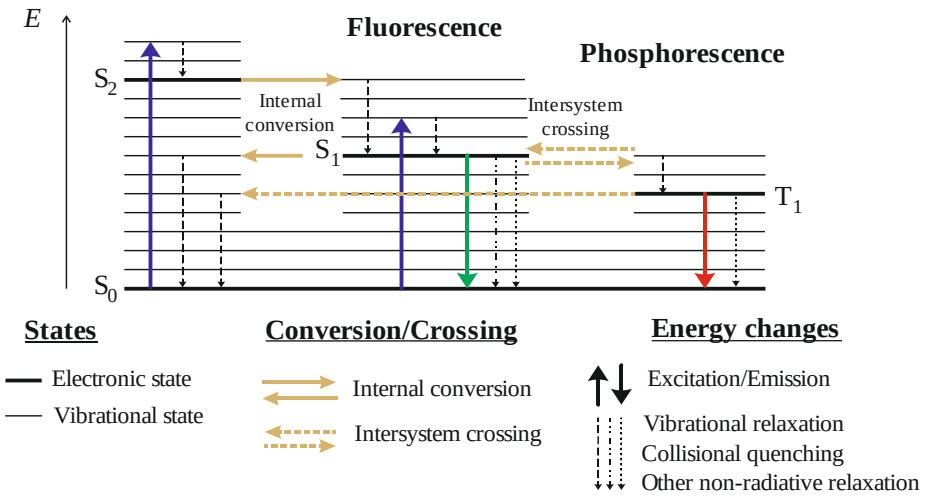

Figure 3: Jablonski energy level diagram showing different transitions for typical luminescent materials. Schematically adapted from Ref. [28].

Upon excitation, which is quasi-instantaneous (~10^{-15} s), the molecule relaxes into the most stable ground state, S_0, but not always via radiative pathways. The excitation is shown with a dark blue arrow. Vibrational relaxation occurs if an excited molecule returns to the lowest vibrational state from a vibrationally excited energy level within an excited electronic state (e.g., $v' = 2$ in S_2). This energy is dissipated as heat in the crystal lattice or transferred as thermal energy to surrounding molecules (e.g., $v' = 0$ in S_2). This process occurs at ~10^{-12} s but can be slower if larger energy gaps need to be bridged by vibrational relaxation. If two electronic states are sufficiently close, an electron can undergo internal conversion (S_2 to S_1) via a higher vibrational state of a lower electronic state (here: $v' = 4$ in S_1), however, this process is slower (10^{-5}–10^{-9} s). Internal conversion is an intra-system process that does not change the system's energy. It is usually accompanied by vibrational relaxation, and thus the energy is again dissipated in vibrations of the crystal lattice [29].

The molecule can de-excite from the excited state S_1 by emitting a photon. If deactivation occurs from an excited singlet state S_1, this is referred to as *fluorescence*, which is typically faster than 10^{-8} s [28]. The emission wavelength λ is determined by the Planck law and the associated energy gap of the transition (see Equations 1 and 2). Due to previous non-radiative transitions like vibrational relaxation, the emitted photon has a lower energy than the exciting radiation. The emission is thus shifted towards longer wavelengths, and this energy difference is called Stoke shift. Several other non-radiative processes from S_1 compete with fluorescence, like relaxation or collisional quenching, where the energy is transferred to neighboring molecules, for example, molecular oxygen. These emissions strongly depend on the temperature, type, and concentration of the quenching molecule. These quenching mechanisms shall not be treated here, and the reader is referred to the respective literature [19,30,31].

Electrons can be organized in different orbits or spin orientations in electronic states. If the spin orientation of the electrons is antiparallel, this is referred to as the singlet states (S_0, S_1, S_2), whereas a triplet state (e.g., T_1) is characterized by parallel spin orientation. The transition between these two states requires a change in the spin orientation of the electron, which is forbidden by the laws of quantum mechanics. Resonant effects and magnetic interactions like spin-orbit coupling, where neighboring atoms share the electrons allow these transitions, however, at very low probabilities [27,32]. This leads to low rate constants and thus to a significantly longer timescale for this transition. Radiative emission from the triplet state ($T_1 \rightarrow S_0$) is called *phosphorescence* and has a typical timescale from 10^{-8} up to 100 s [28]. The energy of S_1 is higher than T_1, which is why the emitted wavelength of phosphorescence is usually longer than that of fluorescence, with the exception of up-conversion phosphors [33]. In practice, this facilitates spectral separation between excitation and detection for phosphorescence relatively to

fluorescence. According to Turro [34], the transition probability for this forbidden process increases with the size of the atoms in the molecule. This also explains why inorganic phosphorescent materials of practical interest usually consist of heavy metal ions doped with lanthanoids or transition metals. Similar to fluorescence, competing non-radiative processes are strongly temperature dependent (see Equation 4). For example, if the molecule is thermally activated in the triplet state T_1, it can also return to an excited singlet state S_1, where all the processes mentioned above become possible again. If the molecule then relaxes via radiative emission, this is called *delayed fluorescence*, which has the emission spectrum of fluorescence but the timescale of phosphorescence [29].

While the Jablonski diagram (Figure 3) is useful for understanding the luminescence processes in general, it is insufficient to explain luminescence in thermographic phosphors. As mentioned above, a thermographic phosphor consists of a ceramic host material doped with rare-earth (lanthanide) or transition metal activator ions, which function as the luminescence center. The luminescence ions are not static but vibrate within the lattice, so the ions and the surrounding ligands form an oscillating system. This can lead to dopant–dopant or dopant–host interactions since the bond strength varies with the interatomic distance. If the dopant concentration is in the order of a few percent, the luminescence center can be treated as a free ion, the interaction between two dopant ions can be neglected [35], and only the interaction of the luminescence center with the host lattice needs to be considered. The probability of an electronic transition varies with the distance between the ion and ligand, called the configuration coordinate. In the following section, a simplified configurational coordinate diagram is introduced to illustrate absorption and emission, as well as non-radiative transitions in a vibrating environment.

2.1.3 Configurational coordinate diagram

Similarly to a pair of nuclei, the ion and ligands in a phosphorescent crystal form a quantum mechanical oscillator. In this case, a vibrational mode can be understood again with the analogy of a harmonic oscillator with the central ion being stalled and the surrounding ligands moving back and forth in phase. The vibrational energy characterizes its state and can be described with the vibrational wave function in analogy to a diatomic molecule introduced in Section 2.1.1. In a configurational coordinate diagram, the metal–ligand distance, denoted as R, is the structural parameter that varies during a vibration. Figure 4 shows the potential energy curve of the atomic core of a luminescence center as a function of the configurational coordinate R. The configurational coordinate can be interpreted as the deviation of the atomic core from the ion equilibrium distance. The symmetrical parabolic energy curve stems from the simplified assumption of a one-dimensional oscillation.

The electron is promoted to an excited state by absorbing a photon according to the respective energy gap (A → B). According to the Frank-Condon principle [27], the transition occurs to that state, where the wave functions of the initial and final state have the maximum spatial (vertical) overlap. The vibronic (vibrational-electronic) transition is vertical in the configurational coordinate diagram (R = const.) due to the assumption that an electron displaces instantaneously relative to the large inertia of the atomic core. In Figure 4, this transition is visualized $v'' = 0$ to $v' = 3$. Neighboring energy levels with lower transition probability, both in ground and excited state, result in a broadened absorption and emission band, respectively. This is represented with dashed lines and an arbitrary absorption spectrum, which has its maximum at the energy of the most probable transition (here: $v' = 3$). Therefore, the larger the equilibrium distance ΔR between ground and excited state, the broader is the absorption spectra, which in practice, facilitates the excitation of the phosphors. After excitation, vibrational relaxation occurs at the ground vibrational level ($v' = 0$) of the excited state, and energy is dissipated as phonons in the lattice (B → C). From the lowest vibrational level, the electron relaxes into an elevated vibrational level of the electric ground state by emitting a photon (C → D) at the wavelength according to ΔE_r. After emission, the system returns to the ion equilibrium distance through vibrational relaxation (D → A).

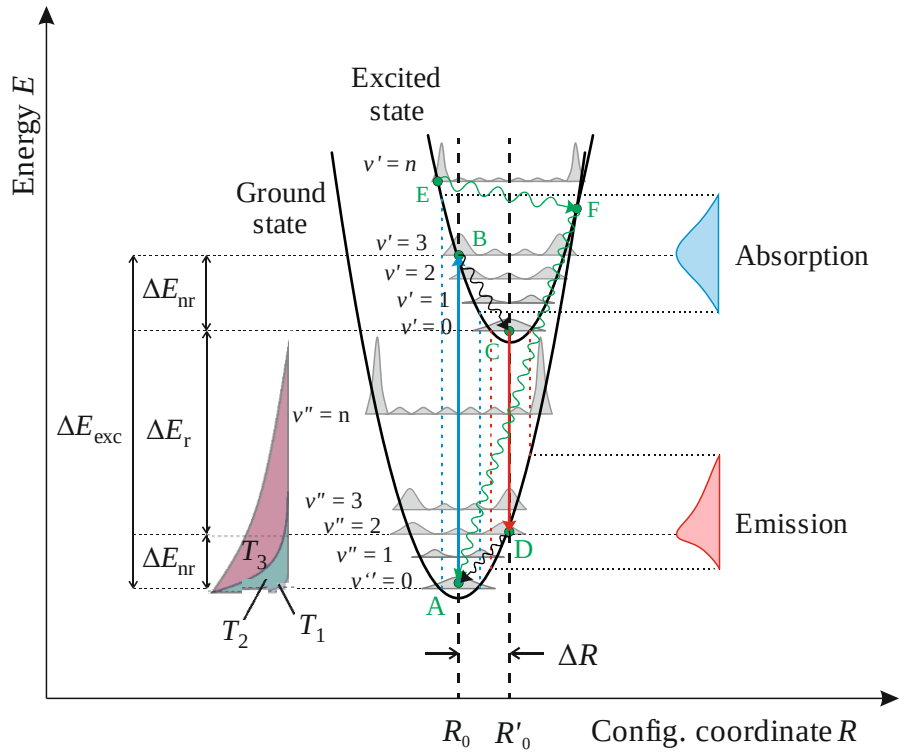

Figure 4: Configurational coordinate diagram including different electronic transitions in a vibrating environment. The broadened absorption and emission spectra are shown on the right. The electron population from the Boltzmann distribution for three different temperatures $T_3 > T_2 > T_1$ are qualitatively shown on the left. The electron population is normalized towards the population of the lowest vibrational level ($N_v/N_{v=0}$).

Temperature has a significant effect on the transitions in a vibrating crystalline environment. For example, the population of vibrational states changes with temperature or the thermal dilatation of the host lattice, which strongly influences the crystal field strength and impacts, in return, the vibrational modes of the lattice. The following sections outline the physical background of varying transitions with varying temperatures and link the influence of temperature to the respective measurement approach.

2.1.4 The influence of temperature on electronic transitions

For any temperature $T > 0$ K, the electrons follow a population distribution over different energy states according to the Boltzmann distribution [27]:

$$N_i = N \frac{g_i \mathrm{e}^{-\frac{E_i}{k_\mathrm{B} T}}}{\sum_j g_j \mathrm{e}^{-\frac{E_j}{k_\mathrm{B} T}}}, \tag{7}$$

where N is the total electron population, and N_i *is* the population in the given state i with its degeneracy[3] g_i, the respective energy E_i, temperature T and the Boltzmann constant k_B. At increasing temperatures, higher vibrational levels ($v'' > 0$) become more populated. In Figure 4, the electron population for three different temperatures ($T_1 - T_3$) is given, where the population is normalized towards the population of the lowest vibrational level ($N_v/N_{v=0}$) as the total number of electrons is constant. In the case of a gas, this can be interpreted as vibrational energy in the molecules. In a solid material like a phosphor, the equivalent is vibrations of the atoms in the crystal lattice, referred to as phonons. If the system is in thermal equilibrium, the population distribution only depends on temperature (Equation 5). According

[3] A state is degenerated if there is more than one state that corresponds to the same energy level. The degree of degeneracy denotes the number of states, which share the same energy and is given in non-negative natural numbers ($g \in \mathbb{N}_0$).

to the Boltzmann distribution, higher vibrational energy levels are more densely populated at increasing temperatures, both in the electronic ground state as well as in the excited state. This increases the probability of additional transitions during absorption and emission, resulting in broadened absorption and emission spectra.

2.1.4.1 Influence on non-radiative emissions

At increasing temperatures, vibrational levels in the electronic ground state (v'') and higher vibrational levels in the electronic excited state (v') become more densely populated after excitation. The probability of non-radiative relaxation to the ground state increases exponentially with temperature and can also be described with the Boltzmann distribution (Equation 6)

$$W_{\mathrm{nr}} = N_i \mathrm{e}^{-\frac{E_i}{k_{\mathrm{B}} T}}, \tag{8}$$

with the Boltzmann constant k_{B}, the energy gap E_i for the non-radiative transition from the respective energy level i and the temperature T [36,37]. By substituting Equation (8) in (6), it becomes clear that the emission lifetime is solely dependent on T and decreases with increasing temperature since the lifetime is the inverse sum of radiative and non-radiative emissions.

$$\tau = \frac{1}{W_{\mathrm{r}} + N_i \mathrm{e}^{-\frac{E_i}{k_{\mathrm{B}} T}}} \tag{9}$$

Different mechanisms can be responsible for de-excitation via non-radiative pathways, which depend on the material's lattice properties and, thus, the energy levels. If $\Delta R \neq 0$, the potential energy curves of both electronic states will necessarily have an intersection point (annotated as F in Figure 4), which is referred to as strong coupling between both states. If vibrational levels above the intersection point are populated, e.g., from radiative excitation to point E or thermal activation from lower vibrational levels, vibrational relaxation directly to the electronic ground state can occur via the intersection point (F) from phonons released into the crystal lattice (E → F → A, shown in green in Figure 4). This process is also called cross-over relaxation. The probability of this non-radiative relaxation increases with temperature and with a higher coupling of the electronic states (increasing ΔR).

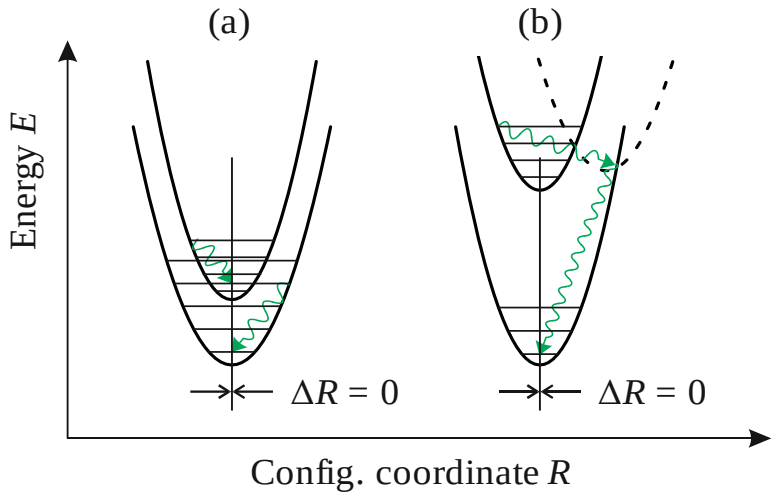

Figure 5: Non-radiative transmissions are shown in green: (a) vibration band overlap and (b) interaction with charge-transfer state (CTS).

If the vibrational energy levels of the electronically excited and ground state overlap (Figure 5a), deactivation can occur via non-radiative vibrational relaxation. The energy of the excited state is transferred to an optically inactive ion and dissipated in the lattice as phonons. This is particularly likely for low

energy gaps between the two electronic states and if $\Delta R = 0$ as shown in Figure 5a. The probability of this non-radiative de-excitation path increases at elevated temperatures [35,38]. At comparably low temperatures, non-radiative transitions are governed by spontaneous phonon emission. However, as higher vibrational modes are populated at increasing temperatures, the probability of multi-phonon emission[4] increases due to the stimulated emission of phonons [39]. The probability for multi-phonon emission of equal energy is given by

$$W_{\mathrm{nr}}^{n} = W_{\mathrm{nr},0}\left[1 - \mathrm{e}^{-\frac{\Delta E}{k_{\mathrm{B}}T}}\right]^{-n}, \tag{10}$$

and increases from the constant non-radiative emission rate $W_{\mathrm{nr},0}$ at low temperatures to T^n dependence as temperature increases [40]. In Equation 9, *n* is the order of the multi-phonon process to overcome the energy gap ΔE. The rate of multi-phonon emission decreases with the energy gap, so high-order ($n > 6$) multi-phonon emission is unlikely to bridge large energy gaps [40,41]. Note that this only holds for the case of low and intermediate coupling between the activator and host, but provides a simplified explanation of why the emission lifetime is approximately constant over initially low temperatures and only decreases above a threshold temperature.

A charge-transfer state can also connect the energy levels of both electronic states (Figure 5b). This can be understood as an intersystem energy band that allows direct interaction between the host material and the activator. This behavior was first introduced by Struck and Fonger [42] to explain different spectral properties of the same luminescence center, e.g., Eu^{3+} in different host lattices, e.g., Y_2O_2S and La_2O_2S [41] or YF_3 and Y_2O_3 [35]. The probability of non-radiative transitions occurring via CTS highly depends on the host material and increases with temperature.

The increase in non-radiative emissions leads to a varying emission lifetime at increasing temperatures, as shown in Equation 8. This characteristic can be exploited for temperature measurements with a suitable calibration, where the emission lifetime constant is calibrated against known temperatures. This approach is usually referred to as the lifetime approach, and its suitability for temperature imaging measurements will be discussed in Section 2.3.1. It was also shown that the probability of non-radiative electronic transitions increases at rising temperatures, which is referred to as thermal quenching. Luminescence signals stemming from radiative transitions quantified or related to a temperature-independent signal, e.g., particle Mie scattering, can also be used for temperature imaging [43]. This approach will be introduced in Section 2.3.4. However, increasing temperature also influences the spectral and temporal properties of a phosphor. The underlying mechanisms will be detailed in the following sections.

2.1.4.2 Influence on the spectral properties

A thermographic phosphor consists of a crystal lattice, where the host material and the dopant each exhibit distinct energy levels. The energy levels vary with the distance between adjacent atoms or the chemical bonds, which are again both strongly impacted by temperature. The resulting shift and broadening of the emission lines will be briefly explained here. Figure 6 shows some crystal-field-induced line-broadening mechanisms.

Line broadening

- The thermal displacement of the crystal components relative to the incident exciting electromagnetic wave can lead to a spectral shift, similar to the movement of molecules in the gas phase. The

[4] Emission of *n* phonons.

averaging of multiple shifts leads to a spectral broadening of the emission (Doppler broadening) [32].

- Vibrations in the crystal lattice increase with temperature, which leads to a changing crystal field at the position of the rare-earth ion. This, in turn, causes line broadening of the respective optical transition [44].
- Deviation from a non-perfect crystal field can also result in the broadening of the emission lines. Firstly, anisotropic thermal expansion of the crystal lattice induces spatially distributed changes in the energy levels, resulting in spectral line broadening. Secondly, spatial inhomogeneities in the lattice (defects or impurity atoms) can lead to various shifts of the respective energy levels, causing inhomogeneous line broadening [32].

Line shift

- Thermal expansion of the host lattice leads to a reduced crystal field strength and, thus, reduced Stark-component separation. This results in a frequency shift of the spectral emission lines, which increases with temperature [44].
- The population of higher energy levels at increasing temperatures facilitates thermal activation. Therefore, thermographic phosphors usually exhibit increased blue emissions at rising temperatures, compared to their red emissions, as larger energy gaps are more likely to be fed by thermal activation at higher temperatures ("blue shift") [38].

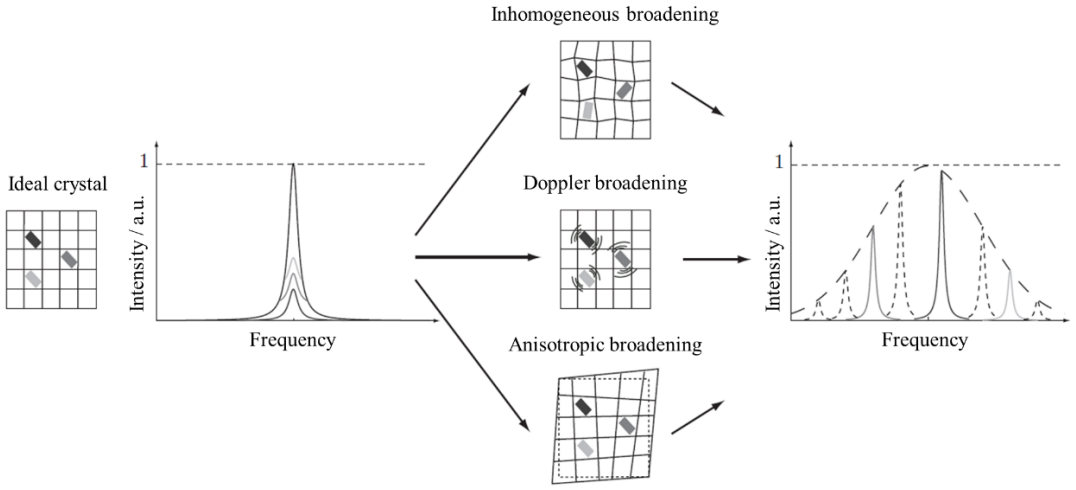

Figure 6: Line broadening mechanisms induced by thermal dilatation of the crystal. Adapted from Ref. [32].

2.1.5 The influence of the crystal structure on phosphor luminescence

Thermographic phosphors usually consist of a crystalline host lattice doped with rare-earth ions or transition-metal ions (activator). The host lattice can take a versatile role in the luminescence phenomena. In the absence of an activator, it can function as a luminescent center itself (e.g., in the $CaWO_4$ phosphor used in commercial scintillators to convert x-rays to visible luminescence) or absorb the excitation energy and transfer it to the activator. Even if the optical activator mainly determines the luminescence, the spectral properties of an activator ion can change if it is doped into different host lattices (e.g., $Y_2O_2S:Eu^{2+}$ and $La_2O_2S:Eu^{2+}$). The crystal field strength determines the spectral position and the emission intensity, which strongly depends on the host material [35].

If an activator or impurity ion is present, the inter-atomic distances and, thus, the strength of the crystal field can change. This fact offers a wide variability in combining different hosts/activators or mixing the composition of the host lattice, but this can also be a limiting factor in its luminescence.

In strontium orthophosphate $Sr_3(PO_4)_2$, Sr can be partially replaced by Mg to adapt the material's luminescence properties. This leads to a mixed Sr–Mg orthophosphate, where the luminescence properties vary as a function of the amount of Mg in the Sr-phosphate lattice since the doping concentration has an impact on the crystal phase. Figure 7 shows different crystal phases (right) and luminescence regions (left) over temperature for the SMP:Sn phosphor ($(Sr,Mg)_3(PO_4)_2:Sn^{2+}$) for various Mg-phosphate ($Mg_3(PO_4)_2$) mole fractions, varying from 0% (pure $Sr_3(PO_4)_2$) to 100% (pure $Mg_3(PO_4)_2$) according to Sarver et al. [45]. Depending on the mole fraction of $Mg_3(PO_4)_2$, the material can form a mixture of both crystalline solids that co-exist in a new crystal phase, referred to as a solid solution ("ss"). The crystal phase of the mixed orthophosphate $(Sr,Mg)_3(PO_4)_2$, which has, e.g., a mole fraction of 10–35% $Mg_3(PO_4)_2$, is referred to as β-$Sr_3(PO_4)_2$ in literature, even if it refers to the β-phase of the mixed $(Sr,Mg)_3(PO_4)_2:Sn^{2+}$. For consistency, the nomenclature throughout this work is aligned with the one from the respective references. At increasing mole fractions of the Mg-phosphate, the phosphor can also form different co-existing crystal phases (e.g., β-$Sr_3(PO_4)_2$ "ss" and the $SrMg_2(PO_4)_2$ at mole-fractions between ~35–65%).

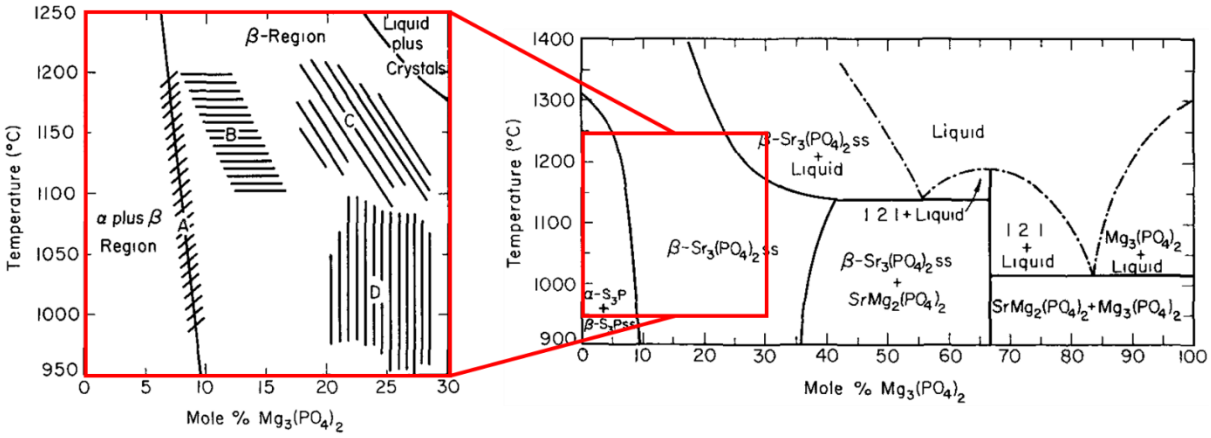

Figure 7: Right: Phase diagram of the mixed orthophosphate $Sr_3(PO_4)_2$–$Mg_3(PO_4)_2$. Left: The respective luminescence regions for different lattice compositions at $Mg_3(PO_4)_2$ mole-fractions from 10–30%. A: Transition region between the mixed phases α-/β-$Sr_3(PO_4)_2$ and the β-$Sr_3(PO_4)_2$ phase. B: Region of the maximum luminescence. C: Region of maximum phosphor sintering. D: Region of "diffuse x-ray lines" indicating amorphous crystal structure. Reproduced and adapted from Ref. [45] with permission of IOP Publishing. © The Electrochemical Society.

The luminescence region A is the transition regime between mixed α-/β-$Sr_3(PO_4)_2$ and pure β-$Sr_3(PO_4)_2$. The luminescence regions B–D all fall within the same crystal structure of β-$Sr_3(PO_4)_2$ but at varying mole fractions of the Mg-phosphate. The luminescence region B is the region of the maximum brightness, whereas the α-$Sr_3(PO_4)_2$ is non-luminescent [45]. Region C is irrelevant for luminescence, and D refers to an amorph structure that does not have luminescent properties. This shows that a small change within a few mole-% of the lattice composition can induce a modification of the crystal structure or formation of new phases, which can vary the luminescence up to a total loss of the material's luminescence properties.

Various examples show that the luminescence properties of thermographic phosphors have many influencing factors besides temperature. Even though there is currently a strong approach to model the transition probabilities and thus predict phosphor luminescence properties with the aid of a quantum mechanical single configurational coordinate model (QMSCC) [46,47], these processes are highly materials-dependent and still not fully understood for phosphors of practical interest. Therefore, calibration of the luminescence properties against temperature at known conditions is always required for thermometry approaches using phosphors, unlike for other spectroscopic diagnostics approaches such as coherent

anti-Stokes Raman spectroscopy (CARS), where theoretical spectra are calculated and used to interpret experimental data [32,48].

2.2 Temperature and thermometry

Temperature is an intensive thermodynamic state variable and is strongly connotated with thermal equilibrium. Unlike extensive state variables that vary with the size of a system (e.g., volume *V* or the amount of substance *n*), temperature does not change with system size and is thus scale invariant. Scale invariance holds for all practical systems; however, the laws of thermodynamics are limited to macroscopic systems and do not apply to the atomic scale. The reason for this can be seen in the molecular kinetics approach to temperature, which describes the macroscopic observables of thermodynamics as average values of statistically fluctuating state variables [49].

Statistical thermodynamics bridges molecular (quantum-mechanical) properties of matter to macroscopic state description [27]. In the easiest case of a mono-atomic gas, the temperature T is defined with the kinetic energy resulting from the translational mode of motion in all three dimensions:

$$\langle E_{\mathrm{kin}} \rangle = \langle \frac{1}{2} m v^2 \rangle = \frac{1}{2} m \langle v^2 \rangle = \frac{3}{2} k_{\mathrm{B}} T \tag{11}$$

$\langle E_{\mathrm{kin}} \rangle$ is the mean kinetic energy, $\langle v^2 \rangle$ the mean square of the velocity vector in each dimension, m the atomic mass and k_{B}=1.381×10^{-23} J/K the Boltzmann constant. With k_{B} being a constant, it is obvious that the absolute temperature T is an absolute measure of the inner energy of multiple atoms or molecules in thermal equilibrium. For molecules consisting of two or more atoms, energy can also be stored in the motion of additional degrees of freedom (rotation, vibration). According to the equipartition theorem in statistical physics, the inner energy is equally distributed across all degrees of freedom in thermal equilibrium. On a macroscopic level, this results in a higher heat capacity for molecules compared to the sum of all its atoms due to the additionally gained degrees of freedom. Atoms exchange energy by colliding with each other, so thermal equilibrium can only be reached with a sufficiently large ensemble, which is referred to as canonical ensemble in statistical thermodynamics. Therefore, temperature cannot be allocated to a single atom or molecule.

Thermometry is the *art* of measuring temperature of a practical system, based on physical properties that vary with temperature (e.g., density, length, electric resistance, electrical voltage, color, magnetism, dielectric coefficient, thermal radiation). As most of these correlations are theoretically reasonably complex, the approach of calibration is mostly used to infer temperature. If two extensive state variables, which vary in a similar manner (e.g., mass m and volume V), are put in a ratiometric relationship, the resulting variable is invariant to scales and thus an intensive state variable (for this example, the density ϱ) [50].

Other than based on the physical property, temperature measurement techniques can also be classified according to their impact of the measurement on the system. This is of interest for turbulent technical systems, where the measurement should have the least possible impact. Table 1 categorizes different temperature measurement techniques according to their intrusiveness. Invasive techniques use a probe that penetrates the medium and influences the system. Even though most of the devices used in daily life fall into this category, such as clinical thermometers or thermocouples, the suitability of this approach is very limited for practical systems. Semi-invasive methods use temperature-sensitive matter that can be deposited on a surface or dispersed into a liquid, for example, thermographic phosphors (TP). The contactless detection of the luminescence properties of the material can then be used to infer temperature from the system of interest. This enables measurements in environments that are not accessible with probes, however, the measurement approach relies on the assumption that the temperature-sensitive

material is in thermal equilibrium with the measurement object. Non-invasive techniques use the optical properties of the object itself to measure temperature. This prevents the unwanted interference of the measurement on the measuring object or can be used for very distant measurements.

Temperature measurements using thermographic phosphors are semi-invasive. Even if temperature-sensitive matter is added to the system of interest, back coupling effects can be mitigated for practical turbulent systems, for example, by reducing the particle diameter to the micrometer scale. This will be analyzed in detail in Sections 2.4 and 2.5, where possible systematic errors are identified.

Table 1: Various thermometry methods according to [51].

Invasive	**Semi-invasive**	**Non-invasive**
Thermal expansion	Thermochromic liquid crystals (TLC)	Infrared thermography
Thermoelectrical effect	Thermographic phosphors (TP)	Refractive index methods
Electric resistance	Temperature-sensitive paints (TSP)	Absorption and emission spectroscopy
Capacitive thermometer	Heat-sensitive paints (HSP)	Line reversal
Noise thermometer	Fiber optic probes	Spontaneous Rayleigh and Raman scattering
Quartz thermometer		Coherent anti-Stokes Raman scattering (CARS)
Paramagnetic and nuclear magnetic resonance thermometry		Degenerative four-wave mixing
		Laser-induced fluorescence (LIF)
		Speckle methods
		Acoustic thermography

2.3 Measurement approaches using thermographic phosphors

Previously, the physical phenomena leading to the temperature dependence of the luminescence properties of thermographic phosphors were explained. In the following sections, measurement techniques are introduced that exploit different facets of the temperature dependence of phosphor luminescence, together with their applicability for measurements in reacting, turbulent conditions with particle image velocimetry (PIV). The techniques can be divided into time-resolving (2.3.1 and 2.3.2) and time-integrating techniques (2.3.3 and 2.3.4) and will be described accordingly.

2.3.1 Lifetime method

Figure 8 shows schematically the temporal luminescence intensity decay of a thermographic phosphor following pulsed laser excitation for three different temperatures. The time-resolved luminescence decay is recorded with a photomultiplier tube, and an exponential function is fitted to the data. The emission lifetime τ can be extracted from the fitting parameters and can be interpreted as the time until the emission intensity decays to 1/e (~36.78%) of the initial intensity I_0.

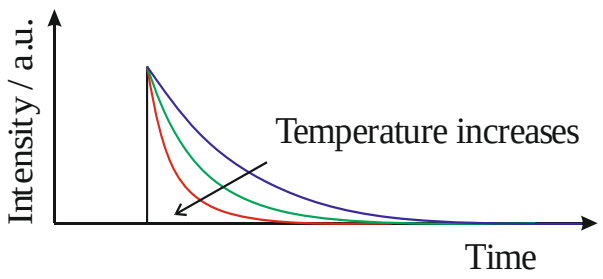

Figure 8: Emission intensity decay (schematically) of thermographic phosphor for various temperatures.

A temperature-lifetime calibration curve can be used to determine temperature. Figure 9 shows such calibration curves for multiple YAG-based phosphors, where the dependence of temperature on emission lifetime can vary over several orders of magnitude. However, it can also be seen that most of the

phosphors have a threshold temperature, e.g., 1100 °C for YAG:Dy, below which the lifetime is nearly constant over a large range of temperatures. This is due to multi-phonon relaxation that becomes only significant as the energy gap, which itself decreases at increasing temperatures, is small enough to be bridged by multi-phonon relaxation (see Section 2.1.4.1). This should be considered in selecting a thermographic phosphor for the appropriate temperature range for high-sensitivity measurements.

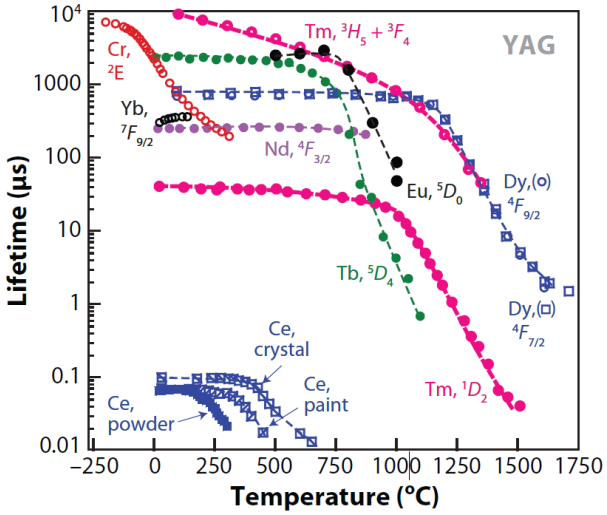

Figure 9: Phosphor emission lifetime over temperature for several phosphors. Reproduced from Ref. [52].

This technique has been applied for point measurements over a range of temperatures, from 200 K [53] up to 1600 K [54], with a precision as good as 1 K [55] and on the surface of an optical engine [56]. While the lifetime method for point measurements is fairly straightforward, two-dimensional (2D) imaging measurements using the lifetime method feature several restrictions to the phosphor and the measurement equipment. It requires the use of a high-speed camera with a frame rate fast enough to resolve the phosphor luminescence decay. The lifetime of the phosphor should be long enough to be captured by the high-speed camera and short enough for the timescale of the temperature changes in the flow, but also of the flow velocities. Someya et al. applied the lifetime method for combined 2D temperature and velocity measurements in an optical engine under motored conditions using $Mg_4FGeO_6:Mn^{4+}$ and a high-speed camera at 40 000 frames per second [57]. The flow velocity in an IC engine cylinder at the top dead center is in the range of ~0.5 m/s at a gas temperature of around 850 K. The luminescence lifetime is approx. 50 µs according to the characterization provided by Brübach et al. [58]. The intensity decay is captured with four images over a total measurement duration of 105 µs. During this time, the average flow displacement for the mentioned flow speeds would be 53 µm. However, for realistic flow speeds around 8 m/s encountered in engines, the particle displacement would be 0.84 mm, equivalent to 17 pixels with the optical system used in this work (47 µm/pixel). Despite potential optimization by choosing other phosphors or higher acquisition frequencies, this technique bears an inherent uncertainty in accurate temperature calculation as the lifetime fitting needs to be performed over the intensity from different pixels. Furthermore, the intensity of a pixel is the superposition of multiple particles traveling through the observed region that is imaged on this respective pixel.

Other measurement approaches use the lifetime of thermographic phosphors. Similarly to the measurement of the intensity decay time of a thermographic phosphor, the rise time is also temperature-dependent and can be calibrated against temperature. The phosphor emission intensity can be described according to [59]:

$$I_{\mathrm{em}}(t) = \left[c_1 + c_2\left(1 - \mathrm{e}^{\frac{-t}{\tau_{\mathrm{rise}}}}\right)\right]\mathrm{e}^{\frac{-t}{\tau_{\mathrm{decay}}}} \tag{12}$$

The two scaling constants c_1 and c_2 as well as the rise and decay time constants τ_{rise} and τ_{decay} are extracted from the fit parameters. This was applied for measurements of thermal barrier coatings between 300 and 1000 K using the phosphor mentioned above (Y_2O_2:Eu^{3+})[5], and the authors found higher temperature sensitivity for the rise time constant for temperatures below 800 K.

2.3.2 Amplitude-modulated lifetime approach

If a phosphor is not excited by a pulsed light source but by a sinusoidally modulated light source at the angular frequency Ω, the luminescence response of the phosphor follows the same modulation, separated by a phase shift ϕ. The governing equations for excitation and emission are given in Equations 13 and 14 using a modulated excitation source [61]:

$$I_{\mathrm{ex}}(t) = I_0(1 + a\sin(\Omega t)) \tag{13}$$

$$I_{\mathrm{em}}(t) = bI_0\left(1 + \frac{a}{\sqrt{1+\Omega^2\tau^2}}\sin(\Omega t + \phi)\right) \tag{14}$$

The approach of frequency-modulated phosphor thermometry is schematically shown in Figure 10. The amplitude of the luminescence emission is also decreased by $(1+\Omega^2\tau^2)^{-1/2}$, relative to the excitation intensity. The lifetime can be calculated from the loss in amplitude or from the phase shift of the emission according to:

$$\tau = \frac{\tan(\phi)}{\Omega}\,. \tag{15}$$

Excitation is usually achieved using a laser diode [61], a light-emitting diode [62], or a continuous wave (cw) laser with a Pockels cell for intensity modulation [63]. Signal detection is usually performed with a photomultiplier for point measurements. Imaging measurements would theoretically be possible by delaying every consecutive frame of a high-speed camera relative to the modulation and sinusoidal interpolation of the intensity in every pixel [61].

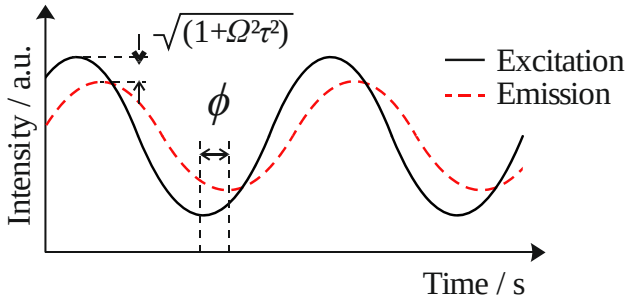

Figure 10: Schematics for intensity-modulated excitation and phase-shifted emission from a thermographic phosphor.

The advantage of this approach is that the modulation frequency can be adjusted to the sensitivity of the respective temperature range [32]. However, 2D measurements underlie the same restriction regarding

[5] The temperature dependence of the rise time of this phosphor is likely due to transition from the $^5D_1$ to the $^5D_0$ state from the two symmetry sites C_2 and C_{3i} [60].

phosphor selection and the applicability in turbulent flows, as mentioned in the previous section for lifetime imaging.

2.3.3 Two-color method

In Section 2.1.4, the influence of temperature on the spectral emission properties of a thermographic phosphor was detailed. The intensity ratio or two-color method exploits this fact for temperature measurements. The temperature-dependent variation in emission spectra is recorded based on the intensity ratio from two spectrally separated wavelength ranges defined by optical filters.

$$S = \int_t \int_\lambda I(t, \lambda)\, \mathrm{d}\lambda\, \mathrm{d}t \tag{16}$$

The signal S is determined by the spectral transmission properties of the optical filters as well as the exposure time of the detector. Assuming that the optical filters transmit the entire spectral emission from an emission line, the ratio of both emissions can be calculated from Equation 16 by integrating Equation 5 over time, assuming that the measurement time is significantly larger than the lifetime ($t \gg \tau$).

$$R = \frac{S_1}{S_2} = \frac{N_{1,\mathrm{i}} W_{\mathrm{r},1} \tau_1}{N_{2,\mathrm{i}} W_{\mathrm{r},2} \tau_2} \tag{17}$$

If the radiative transition stems from two different electronic states in thermal equilibrium ($\tau_1 = \tau_2$), the ratio of the population from both excited states ($N_{1,i}/N_{2,i}$) can be expressed using the Boltzmann distribution (Equation 5):

$$R(T) = \frac{g_1 W_{\mathrm{r},1}}{g_2 W_{\mathrm{r},2}} \mathrm{e}^{-\frac{\Delta E_{21}}{k_\mathrm{B} T}} \tag{18}$$

The degeneracy of both states is g, and the probability for radiative transition is W_r, ΔE_{21} is the energy gap between both states, and T is the temperature of the phosphor. The measured ratio can be translated to temperature using a calibration curve at known temperatures. This technique is straightforward and mostly insensitive to experimentally varying parameters like seeding density or laser fluence.

Two-dimensional measurements can be simply achieved using a 2D detector. This method is widely applied for surface measurements [64], temperature measurements in sprays [65], in a burning droplet [66], in liquids [67], or in aerosol phase [25,68]. The 2D two-color thermometry approach has been combined with PIV in multiple references [57,69–71]. The applicable flow conditions are given by the luminescence properties of the phosphor. For example, a relatively long-lived phosphor can be used in flows of short time scales if the emission is strong enough to enable short detector exposure. The restrictions of this approach and the choice of appropriate phosphors will be discussed in Section 2.4.3.

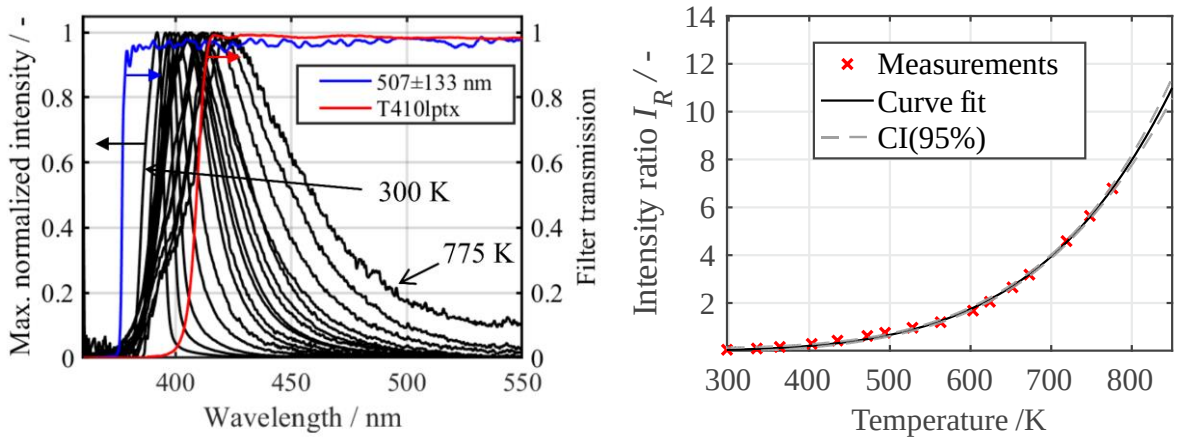

Figure 11: Left: Temperature-dependent phosphor emission spectra (black) with the filter transmission characteristics (colored lines) for aerosolized ZnO:Zn. Right: Ratio-temperature calibration curve for the same filter combination (right). The confidence interval of the fit is shown with a dashed line. Both figures are reproduced from Ref. [25] with permission from SAGE Publishing.

2.3.4 Intensity-based temperature imaging

As mentioned in Section 2.1.4, the temperature dependence of the phosphor luminescence intensity (e.g., resulting from thermal quenching) can also be used for temperature measurements. However, since the measured intensity depends on many other parameters (such as laser intensity, detection efficiency, etc.), a ratiometric method was developed that compares the phosphor luminescence to an independent signal that has no (or a different) temperature dependence, hence yielding a temperature-dependent intensity ratio. This technique is named scattering-referenced aerosol phosphor thermometry (SRAPT) [43]. In this approach, the ratio between the temperature-insensitive elastic Mie-scattering and the thermally quenched phosphor luminescence is calculated and related to temperature. This method has the advantage that the entire phosphor emission spectrum can be used for the ratio calculation, whereas in the two-color ratio-based imaging approaches, different proportions of the emission spectrum are split over two detectors, inherently decreasing the signal level per detector and thus, increasing shot noise. Apart from the Mie scattering detector, the seeding concentration is monitored by extinction measurements with an additional cw laser, increasing the experimental complexity. While this approach allows 2D measurements at high precision of up to 1.7%/K at 780 K for YAG:Ce^{3+}, this technique suffers from uncertainties, as the elastic Mie scattering signal is also dependent on the particle shape and diameter, the scattering angle as well as the laser fluence [43]. As a result, the SRAPT ratio varies with the laser fluence as well as particle diameter and seeding density, also imposing additional inherent limitations: firstly, this technique cannot be applied to reacting conditions, with a net balance of particle matter being non-zero during the process, e.g., soot formation in internal combustion engines. Secondly, this technique is limited to reaction conditions, where no entrainment of unseeded air can occur. The authors provided proof-of-concept temperature measurements in a heated jet (no co-flow), however, mixing with surrounding, unseeded air influences the distribution of elastically (Mie-) scattered light and thus biases the SRAPT ratio in the outside region of the jet.

2.4 Combined temperature and velocity measurements for post-combustion measurements

2.4.1 Particle image velocimetry (PIV)

Particle image velocimetry is frequently used to measure the velocity field of a fluid using tracer particles. The particles are dispersed into the flow and illuminated by two consecutive laser pulses, separated by a known time interval, and a camera records the elastically scattered light. The displacement of the particles between two pulses is inferred using a cross-correlation algorithm to calculate the velocity with

the time interval between both laser pulses. This technique is an indirect measurement approach since the velocity of the tracer particles is probed instead of the fluid velocity. Consequently, it needs to be ensured that the difference between both velocities remains negligible (no-slip condition). After a step change in velocity, the slip between particle and fluid velocity decreases exponentially. The response time of a particle τ_p of the density ϱ_p in the fluid with the viscosity μ is given with:

$$\tau_\mathrm{p} = d_\mathrm{p}^2 \frac{\varrho_\mathrm{p}}{18\mu}. \tag{19}$$

The dimensionless Stokes number *St* is defined as the ratio between the particle response time and the characteristic time scale of the flow

$$St = \frac{\tau_\mathrm{p}}{\tau_\mathrm{f}}, \tag{20}$$

where τ_f describes the flow characteristic, for example, as the ratio of a characteristic length scale and velocity [72]. A Stokes number below 0.1 is usually sufficient for accurate flow tracing [73,74].

PIV is an imaging technique, thus, the design of the optical system as well as the postprocessing parameters for data evaluation is equally important. For further reading on theoretical basics, the reader is referred to the respective literature [72], and only a few key statements will be enumerated in the context of this work. Keane and Adrian have identified dimensionless parameters to optimize conventional dual-pulse PIV systems [75].

- The number of particles in an interrogation area should be higher than 15 (seeding density).
- The particle displacement in the measurement plane during the two pulses should not exceed 0.25 times the area used for cross-correlation analysis.
- The particle displacement through the measurement plane should be limited to 0.25 times the light-sheet thickness.
- The velocity within an interrogation area should vary less than 5%.

As PIV is well-established, this work will focus on the thermometry part of T-PIV, where the added particles are used for measuring the gas-phase velocity and temperature simultaneously. The materials requirements for measurements in turbulent, reactive flow conditions will be discussed in the next section.

2.4.2 Particle tracer fidelity check

For PIV, the added particles must follow the flow with an acceptable velocity response, which is related to their inertia and cross-section (Equation 17). Particles used for PIV are usually Al_2O_3 or TiO_2 with densities of 3.94 and 4.23 g/cm^3, respectively. For 2-µm particles, they have a velocity-response time of around 60 µs [76,77]. Thermographic phosphor particles used in this work, like YAG:Pr (4.55 g/cm^3) or SMP:Sn (3.9 g/cm^3), have very similar densities [78,79] and the particle size (d_{50}) is reduced to 1.8 and 1.6 µm, respectively, as measured by Coulter counter analysis.

For an estimation of the Stokes number for relevant IC engine conditions, different timescales of the engine flow are identified by Cosadia et al. [80]. For demonstration purposes of this technique, only large-scale flow motions are considered. For the case investigated in this thesis, relevant flows are related to the tumble motion during the compression stroke[6]. The time scale of the tumble (rotation around

[6] The flow timescale in the expansion stroke governed by the down-movement of the piston is significantly higher than that of the tumble motion. Therefore, only the tumble motion is considered to estimate the Stokes number.

the axis perpendicular to the axis of the engine cylinder) is inverse to the rotation rate ω_t of the tumble in analogy to [80].

$$\tau_f = \tau_{tumble} = \frac{1}{\omega_t} \tag{21}$$

The fastest flow speed of the tumble motion is ~10 m/s at the radial periphery of the cylinder ($l_{max} = d_{bore}/2$) at engine conditions similar to Ref. [25]. With the rotation rate being $\omega_t = u_t/l_{max}$, the time-scale of the tumble is $\tau_{tumble} = 3.9 \times 10^{-3}$ s. For an estimation of the particle response time τ_p at the respective engine conditions, the viscosity at elevated temperatures can be estimated from the viscosity at ambient conditions (index 0) through the Sutherland correlation:

$$\mu = \mu_0 \left(\frac{T_0 + S}{T + S}\right)\left(\frac{T}{T_0}\right)^{\frac{3}{2}} \tag{22}$$

S is the Sutherland constant in Kelvin, which is 111 K for a temperature range between 170–1900 K with an error of 2% [81]. The response time for a YAG:Pr tracer particle at 600 K is $\tau_p = 2.75 \times 10^{-5}$ s (Equations 19 and 22). The Stokes number (Equation 20) for this condition is $St = 0.0072$, and more than a magnitude below the acceptable value for accurate flow tracing.

2.4.3 Suitable phosphor materials for T-PIV for post-combustion measurements

If PIV is extended to T-PIV in the post-combustion regime, additional materials prerequisites are mostly related to the thermometry approach:

- **Resistance to combustion:** The phosphor will have been exposed to a combustion environment at temperatures above 2000 K. The luminescence properties of the phosphors should not be affected by exposition to combustion. This includes resistance to oxidation as the global stochiometric ratio in the engine is lean and the resistance to structural modification at the respective temperatures, given the sensitivity of the luminescence to structural alteration of the crystal lattice (Section 2.1.5).
- **Strong luminescence:** During measurements in reactive conditions, the phosphorescence signal is subject to thermal quenching. Therefore, the global phosphor luminescence should be strong to extend the measurement range to high temperatures (>700 K) and to enable good measurement precision. It should also be strong enough to be discriminated against competing signals like chem-iluminescence or black-body radiation.
- **High sensitivity:** The sensitivity of the phosphor's luminescence properties to temperature changes should be high for high-precision temperature measurements. Using the intensity-ratio method, the filter combination strongly influences the temperature sensitivity. The sensitivity increases the fur-ther both filter transition bands are away from each other, however, at the expense of the total signal captured. Therefore, high sensitivity is equally important as strong luminescence.
- **Luminescence lifetime:** The temporal requirement for the phosphor lifetime has an upper and lower limit.
    - The timescale of the phosphor should be short relative to the one of the flow to ensure that the particle displacement during detection is negligible. It should also be fast enough to reduce the contribution from long-living signals, e.g., blackbody radiation or chemiluminescence.
    - It should be long enough to allow the exclusion of short-lived signals (e.g., elastic scattering of laser light, PAH fluorescence, LII) through delayed gating without significant signal loss[7].

[7] In terms of luminescence yield. The delay of the exposure by 1/10 of the decay time constant τ already leads to the loss of 9.5% of the total luminescence signal.

- **Excitation wavelength:** To reduce the experimental complexity, the absorption spectra of the phosphor should be broad and accessible with laser light sources, which are available to laboratories, e.g., through frequency multiplication from Nd:YAG lasers. It should also not interfere with optical components or fuel components (e.g., deep-UV or near-infrared).
- **Emission wavelength:** The phosphor's emission should be in the visible range. This simplifies the use of intensified scientific cameras, where the quantum efficiency is usually high in the visible spectrum of light.
- **Cross-sensitivity:** The phosphor should have low sensitivity to the seeding density or laser fluence, both parameters which are subject to cyclic variations in a highly transient system like an internal combustion engine.
- **Handling/agglomeration properties:** For aerosol measurements, the phosphor should be easily dispersible into the air. Phosphor particles are subject to electrostatic attraction or agglomeration from, e.g., the shape of the particles, which can significantly vary from phosphor to phosphor. Flow properties can be improved by adding nanometer-sized particles. Increasing the quantity of this additive accelerates engine wear, which should therefore be reduced to a minimum.

2.5 Error analysis

A comprehensive error analysis is indispensable in a complex environment like reactive flow conditions for accurate and precise temperature measurements using phosphor thermometry. According to their nature, errors can be categorized into systematic and statistical errors. Statistical errors decrease with an increasing number of repetition measurements, so the *exact* temperature value would precisely be determined after an infinite number of measurements under similar conditions in a perfect measurement system. However, this value may not represent the *true* temperature if external influences systematically bias the measurement. The quantitative description is named measurement accuracy and is defined as the "closeness of agreement between a measured quantity value and a true quantity value of a measurand" by the Joint Committee for Guides on Metrology [82].

2.5.1 Statistical errors: Precision

The precision of a measurement increases with the number of repetitions. The standard deviation is a measure to quantify precision. A slight deviation signifies high precision. It should be distinguished between temporal and spatial precision for imaging measurements in a real measurement environment.

Temporal precision from a data set of *k* subsequent measurements, also called shot-to-shot variation, is the arithmetic mean from the standard deviations calculated for each pixel *i* from *k* single shots:

$$\sigma = \frac{1}{N_i}\sum_{i\,=\,1}^{N_\mathrm{i}}\sqrt{\frac{1}{N_k-1}\sum_{k\,=\,1}^{N_k}\left(T_{i,k}-T_{i,\bar{k}}\right)^2}\ , \tag{23}$$

where $T_{i,\bar{k}}$ is the mean temperature of the *i*-th pixel over all individual experiments:

$$T_{i,\bar{k}} = \frac{1}{N_k}\sum_{k\,=\,1}^{N_k} T_{i,k}\,. \tag{24}$$

The standard deviation is given with $\pm 1\sigma$ if not annotated otherwise. Sometimes it is useful to provide relative precision, where the standard deviation is referenced to its mean temperature from all pixels:

$$\sigma_{\mathrm{rel}} = \frac{\sigma}{T_{\bar{i},\bar{k}}} = \frac{\sigma}{\frac{1}{N_k}\frac{1}{N_i}\sum_{i=1}^{N_i}\sum_{k=1}^{N_k} T_{i,k}} \tag{25}$$

The spatial precision is calculated similarly to Equation 23, where the standard deviation is first calculated from all pixels *i* of a single shot and afterwards averaged over all individual experiments *k*. It only makes sense to use this measure for a region where the temperature gradient is low. The relative spatial precision is calculated analogously to Equation 25.

2.5.2 Systematic errors: Accuracy

In an idealized measurement system, it is firstly assumed that the phosphor particles are in thermal equilibrium with the measurement object and that the semi-intrusiveness nature of this diagnostics does not influence the system of interest. Secondly, it is assumed that there is no signal interference and that the luminescence properties of the phosphor are solely governed by temperature. Lastly, the measured signal can be unambiguously reduced to a scalar quantity (lifetime or intensity ratio), which itself can be converted to temperature with a continuous (or infinitely closely spaced) calibration. In Ref. [83], sources of systematic errors are proposed and classified into six categories. Based on this categorization, potential systematic errors are identified and discussed for the application of aerosol phosphor thermometry in post-combustion conditions in this work:

1) Thermal interaction

a. Thermal equilibrium between the thermographic phosphor and measurement object is not reached. This is especially relevant in turbulent reacting flows, where fast changes are expected. Theoretical heat transfer considerations on the response time t_{95} until a particle reaches 95% of the steady-state temperature following a step temperature change of the surrounding gas temperature is below 30 µs [84]. The considerations were made for a 2-µm phosphor particle (YAG) for a step change from 300 to 2000 K, which is representative of combustion conditions [68].

b. Feedback of the phosphor on the thermal properties of the measurement object. The thermal capacity of the measurement system is modified by adding thermal inertia from the tracer particles. This can change the temperature of the measurement object relative to the unseeded flow conditions, e.g., gas cooldown in the compression stroke or heating in the expansion stroke. Laser-induced heating from particle excitation can lead to thermal interaction with the measurement object. With the existence of a particle counting system, the added thermal inertia can be estimated with knowledge of the heat capacity of the phosphor, but it is expected to be low. The latter is insignificant at low excitation fluences applied in gas-phase thermometry [85].

2) Photophysical properties of the phosphor

a. Transfer function of the phosphor:
   i. The finite nature of the phosphor decay time is equivalent to a temporal low-pass filter. Therefore, the timescales of the phosphor emission should be shorter than the timescales of temperature changes.
   ii. If the two emission bands used for the intensity-ratio approach have different decay times, it is essential that the full decay of both bands is detected ($t_{\mathrm{detection}} > \tau$). If they differ by orders of magnitude and this limits the measurement through the insufficient signal-to-noise ratio of one emission band, the exposure duration of each detector must cover the respective emission by the same extent (e.g., $t_{\mathrm{detection}} = 3\tau$). This forms the principle for the post-combustion gas temperature measurements in Section 8.2 and will be discussed with the luminescence lifetime characterization in Section 6.1.

b. Parameters influencing the transfer function:

i. Particle disintegration from heat treatment: High temperatures before or during the measurement can lead to diffusion of the optically active ion or structural modification of the crystal host, both deteriorating the phosphors' capabilities to sense temperature. This is relevant if the temperature history of the phosphor in the calibration differs from that of the measurements. These processes are difficult to quantify and should be avoided if possible. Since this cannot be avoided in certain applications, such as measurements in the post-combustion regime, these effects will be further investigated within the scope of this thesis and presented in Section 5.3.

ii. Chemical and physical environment: Thermographic phosphors are widely considered to be chemically inert and insensitive to the pressure and composition of the surrounding gas [23]. This is a significant advantage over organic tracers used for tracer LIF [86] in reacting flow conditions with temporal and spatial fluctuations in gas composition. However, Brübach et al. found strong sensitivity of the oxygen concentration to the luminescence properties of Y_2O_3:Eu^{2+} [87], which continues to be a potential source of errors. No influence of magnetic fields on the properties of Y_2O_2S:Eu was found for magnetic flux densities of up to 0.8 T [88].

iii. Agglomeration state: Several previous studies revealed that the luminescence properties of thermographic phosphors vary according to their agglomeration state (bulk powder, surface coating, liquid dispersion, or aerosol [89–92]). Therefore, in this work, all measurements with the aim of establishing the ratio-temperature calibration are carried out with the phosphor being in a similar agglomeration state as in the system of interest (Section 6).

iv. Phosphor excitation: Potential systematic errors stemming from the excitation wavelength and pulse duration have been investigated [22]. In general, this can be avoided by using similar Q-switched laser light sources in all measurements for calibration and the system of interest. In contrast, the laser fluence depends on several parameters such as beam path, optical components, fluctuations in the excitation source, and possible absorption effects in the measurement environment. This can mostly be avoided using ratiometric techniques, unless the phosphor shows non-linear spectral dependence on the laser fluence, as reported for BAM:Eu^{2+} [91]. This error source can be minimized by using the same laser fluence throughout both measurements, characterization measurements of a phosphor aerosol as well as the measurements in the system of interest (optical engine, burner). Both ends of the laser sheet are blocked to reduce the inherent inhomogeneities in the laser fluence due to the Gaussian beam profile.

3) Detection system and signal interference

a. Transfer function of the detection system:

i. The signal captured by the detector is a convolution of the phosphor luminescence with the spatial, spectral, and temporal signal response of the entire detection system. The first is already a superposition from the phosphorescence signal from the total measurement volume, which can contain cold or hot regions, so there can be a bias from high-temperature gradients throughout the measurement volume. The second provides possible sources of error for spectral measurements if the spectral response of the detection system varies between the calibration and measurement in the system of interest. Ratiometric measurements avoid this if the ratio is referred to as a measurement from known conditions, e.g., at homogeneous temperatures. This will be discussed in Section 3.3.3. Alternatively, the transfer function of each detection system can be inferred and corrected by calibrating it against a homogeneous light source with known spectral characteristics, e.g., an Ulbricht sphere. While the spatial resolution for intensity ratio measurements is mainly limited by its optical components, the temporal response for decay time measurements is limited by the electronic components of the detection system (temporal lowpass filter). This is particularly critical for short decay times, requiring a fast frequency response. This will be discussed with the setup for lifetime imaging in Section 4.3.1.

ii. Systematic errors can arise if the intensity response of the detector is non-linear with incident light. Scientific detectors like PMT and CMOS usually avoid this, or intensified cameras if operated in their specified dynamic range. However, intensified high-speed cameras used in this work can suffer from depletion effects at high frame rates [93]. This is investigated and discussed in Section 3.6.

b. Movement of the measurement object: For aerosol measurements in turbulent flows, the spatial displacement of the object during detection must be smaller than the spatial resolution of the detection system. This is equally important for the lifetime approach as for the intensity-ratio approach. However, the detection time of the latter approach can be arbitrarily shortened and is only limited by shot noise if the phosphor luminescence is not strong enough.

c. Optical and electrical interference:

i. The signal acquired by the detector contains a contribution from phosphorescence, background from ambient light, and interference from black-body radiation or chemiluminescence. These contributions can be accounted for if they are invariant in time and contribute equally to both imaging channels in the intensity ratio approach. This can elsewise lead to systematic errors in the intensity ratio approach if the interference varies significantly, either in the spectral or temporal contribution on both detectors.

4) **Algorithm for data processing:** The procedure for the intensity ratio calculation is relatively straightforward. Potential errors can arise if the data, like the luminescence emission decay, cannot be unambiguously reduced to a scalar value. This is relevant mainly for the lifetime method if the decay time constant τ varies over several orders of magnitude. In a perfect exponential decay curve, the decay time constant can be extracted from the fitting parameters as introduced above (Section 2.3.1). From the limitation of real data, only the data points from a given section of the decay curve are used to extract the lifetime constant. If the intensity decay varies over several orders of magnitude or includes a multi-exponential decay characteristic, the placement of the fitting window influences the decay time constant τ and is thus a potential source of errors. Brübach et al. proposed an algorithm for lifetime fitting, where the fitting window is iteratively chosen based on the least-square fitted lifetime [38]. This algorithm was adapted and implemented in a master thesis [94] supervised within this work. This algorithm is used for lifetime calculation for all mono-exponential luminescence emission decay functions throughout this work and will be briefly introduced in Section 3.1.

5) **Calibration error:** The interpolation between data points of the signal-ratio–temperature calibration curve can lead to a systematic error. This depends on the spacing between calibration measurements and the type of interpolation. In regions of strong gradients, increasing the density of measurement points is recommended. To improve monotony, it can be of interest to fit the data to a higher-order polynomial or to a power function. The uncertainty of the fit can be a measure of the accuracy of this measurement approach.

6) **Calibration thermometer:** A systematic error can emerge from the inaccuracy of the thermometer measuring the reference temperature in the calibration environment. The uncertainty of the calibration thermometer thus limits the maximum accuracy.

3 Data processing methodology

In this chapter, all methods are explained that were applied across various experiments, such as the post-processing procedure to determine the luminescence lifetime or calculate the temperature from two-color luminescence imaging data. This includes a discussion of different approaches to the flat-field (white-field) correction or the development of a mapping algorithm that is applied to transfer two or more images onto the same coordinate system from multiple imaging cameras.

3.1 Characterization of the luminescence decay

3.1.1 Determination of the phosphor luminescence lifetime constant

The temporal decay behavior of the luminescence signal of thermographic phosphors after pulsed laser excitation is, in most cases, not mono-exponential. Therefore, unambiguously determining a specific luminescence lifetime can be difficult and a source of systematic errors (see Section 2.5). The luminescence lifetime τ can be determined from fitting an exponential function to the measured signal trace, but the results depend on the region where the fit is applied. The same fitting window must be used for all measurements for reproducible lifetime determination. This is, however, not practical for cases where the lifetime changes by orders of magnitude, or where the signal intensity drops significantly with increasing temperature. Therefore, Brübach et al. [58] proposed an algorithm where the fitting window is iteratively calculated based on the Levenberg-Marquard curve fitting algorithm based on the least-squares method [95,96]. All evaluation of mono-exponential lifetimes in this work is based on iterative window fitting. This was implemented in a master thesis supervised within this work [94] and will therefore only be briefly described here.

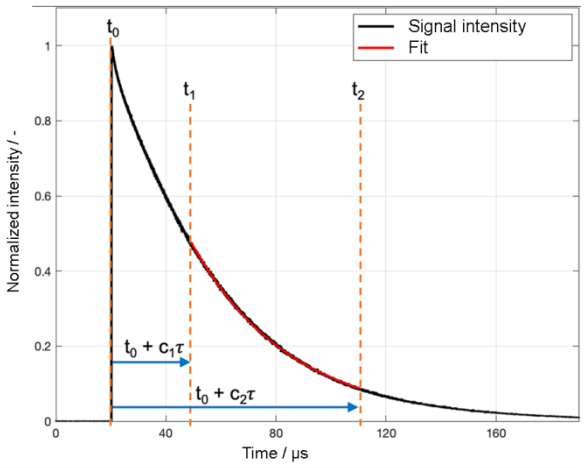

Figure 12: Luminescence decay for SMP:Sn at ambient temperatures with the coefficients c_1 and c_2 for an iterative definition of the fitting window. Adapted from Ref. [94].

In certain regions of the signal, the intensity decay can be approximated with a mono-exponential function

$$I(t) = I_0 \mathrm{e}^{\frac{-t}{\tau}} + I_{\mathrm{offset}}. \tag{22}$$

The intensity offset I_{offset} can be calculated from the signal before the laser pulse at t_0. An initial guess for the lifetime is $\tau_0 = c_0\,\Delta t$, where Δt is the entire detection range and $c_0 = 1/20$ chosen for the mono-exponentially decaying luminescence. The sensitivity of this input parameter was investigated within the implementation of the algorithm [94], and it was shown that a variation only resulted in the number of iterations necessary and a maximum deviation of $10^{-4}\tau$ in some cases. The starting (t_1) and end point (t_2) can now be calculated according to:

$$t_1 = t_0 + c_1\tau \tag{23}$$

$$t_2 = t_0 + c_2\tau \tag{24}$$

The lifetime τ of the next iteration is calculated from the fit, given by the fitting window t_1 and t_2. The stopping criteria is defined with:

$$\max(\tau_\mathrm{i}, \tau_\mathrm{i} - 1, \tau_\mathrm{i} - 2) - \min(\tau_\mathrm{i}, \tau_\mathrm{i} - 1, \tau_\mathrm{i} - 2) < 10^{-3}\left[\frac{1}{3}(\tau_\mathrm{i} + \tau_\mathrm{i} - 1 + \tau_\mathrm{i} - 2)\right] \tag{25}$$

The flow diagram of this algorithm is shown in Figure 13. The parameters c_1 and c_2 chosen for the fitting window are 1 and 3.5, respectively. The selection of these parameters is generally a tradeoff between a low statistical and low systematic error, as the signal-to-noise ratio is high at the beginning, but the decay properties in this region are also most influenced by interfering parameters other than temperature, e.g., scattered light or other short-lived species [83]. Even this is not expected to be a significant source of errors as a gated PMT is used (100 ns gate delay), and the spectral resolution is in the lower nm-range due to the selectivity of the spectrometer.

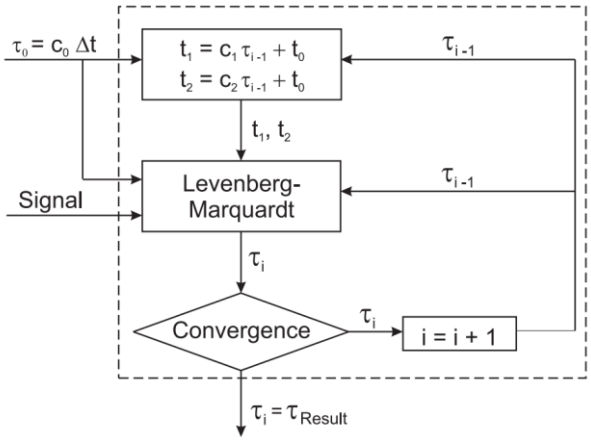

Figure 13: Flow diagram to determine the luminescence lifetime from the intensity decay curve according to Brübach. Reproduced from [58].

3.1.2 Multi-exponential luminescence decay

For phosphors showing multi-exponential luminescence decay, the emission follows a number of superimposed mono-exponential decays. One of the phosphors used, YAG:Pr, shows two distinct emission bands (emission centered at 490 and 610 nm) that are used for thermometry. The red emission can best be fitted as a bi-exponential decay. In this case, the intensity decay can be described with two exponential functions containing the decay time constants τ_1 and τ_2 with its respective weight constants a_1 and a_2, according to [97]:

$$I(t) = a_1 e^{\frac{-t}{\tau_1}} + a_2 e^{\frac{-t}{\tau_2}} + I_{\text{offset}} \tag{26}$$

The offset is calculated and subtracted as introduced in the previous section. In Figure 14, the multi-exponential decay of the red YAG:Pr emission (610 nm) is shown on a logarithmic scale. It can be seen that the emission decay can also be represented by two mono-exponential functions, which appear each as a straight line on the logarithmic scale. The absolute value of the slope of the fit is equivalent to the reciprocal value of the evaluated lifetimes. The lifetimes can again be calculated from the fitting parameters of the bi-exponential fit. In this case, the two lifetimes τ_1 and τ_2 are evaluated to be 27 and 135 µs.

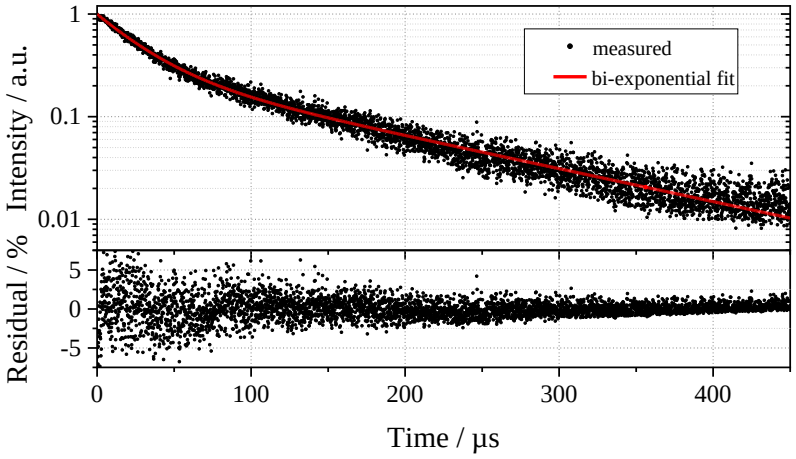

Figure 14: Normalized intensity decay of YAG:Pr (610 nm emission) at 510 K shown on a logarithmic scale with a bi-exponential fit. The two lines show that a mono-exponential fit would not represent the data well. The calculated residual is shown in the bottom diagram. Every second data point is only shown to improve visibility.

The bi-exponential decay consists of two single-exponential decays. If the decay is already sufficiently advanced (e.g., $t > 5\tau_1$), the lifetime τ_2 can be calculated with very good accuracy from the second term from Equation 26 only. Therefore, it is easier to determine the long lifetime constant. In the literature, this is often applied for YAG:Pr [98] because the beginning of the decay is superimposed by interfering signals from other species or scattered laser light. Since a gated PMT was used for these measurements (Δt = 100 ns), interference from scattering can be excluded here, and therefore, a multi-exponential decay can be determined.

3.2 Characterization of the spectral properties from luminescence decay

By combining a monochromator and a PMT, phosphor luminescence decay curves can be detected at given wavelengths. If the total emission intensity is temporally integrated at each wavelength and measurements are carried out over the spectral range of interest, phosphor emission spectra can be obtained. A LabView routine was developed under the supervision of a student research assistant to automatize incremental grating positioning of the monochromator, data acquisition, and read-out from the oscilloscope. Figure 15 shows the schematics used to calculate the phosphor emission spectra from nm-based intensity decay measurements. Emission spectra are compiled from at least five laser pulses at each wavelength position to reduce statistical uncertainties. Different compilation methods were attempted, for example, recording five consecutive laser pulses at each wavelength position with subsequent time-averaging or detecting one laser pulse per wavelength position and averaging from five individual spectra.

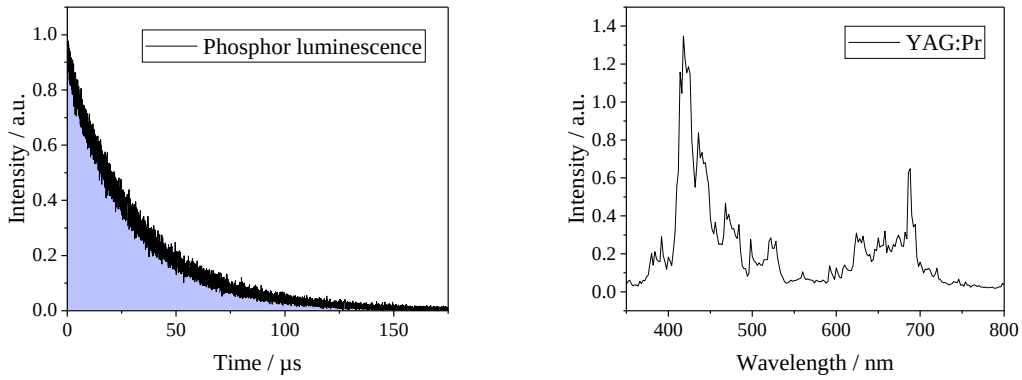

Figure 15: Schematics for spectra determination of nm-based luminescence decay curves from YAG:Pr measurements under 266 nm laser excitation. The surface under the luminescence emission decay curve (left) represents the signal intensity at the respective wavelength (right). The resulting emission spectra are not corrected for the spectral sensitivity of the PMT.

With the given signal decay in the range of 500 µs (only 175 µs are shown in Figure 15), the repetition rate of the measurements is limited by the repetition rate of the laser used (10 Hz), leading to a measurement duration of 45 seconds to acquire a spectrum between 350 and 800 nm with one-nanometer increments. The acquisition of an emission spectrum, where each wavelength position is compiled from five laser shots (in either of the compiling order), the total duration is nearly 4 minutes (225 seconds). The long measurement duration increases the impact of shot-to-shot fluctuations in one spectrum from slowly changing measurement conditions like particle dispersion, for example, when phosphor deposits from the inner side of the tube detach or phosphor agglomerates form. This significantly increases signal intensities at one wavelength, leading to very noisy spectra. A correction method was implemented in the master thesis [94], which uses an intensity-based criterion (>170% intensity variation within two subsequent wavelength shots). This correction method neglects any data point where the intensity is higher than 170% of the mean of the two neighboring data points to detect excessive seeding (and thus signal) at this wavelength position when compiling the spectrum. The value of 170% was arbitrarily chosen and showed good performance in removing laser shots from occasional excessive seeding. While this successfully reduces low-frequency noise from short-term fluctuations in particle load, this procedure does not consider longer-term variations, for example, if the nozzle of the particle seeder clogs over time and continuously reduces particle load.

The shot-to-shot fluctuations in laser intensity also increase the noise contribution of the spectra. They are corrected using the single-shot laser fluence measured with an additional photodiode (not shown in Figure 38) equipped with a bandpass filter for the laser excitation wavelength (266 nm), assuming a linear relationship between excitation and emission intensity. However, additional lowpass filtering in the frequency domain was necessary to remove high-frequency noise from incomplete correction of fluctuating particle load that was not accounted for with the intensity-based criterion and to smooth the spectra. The impact of the correction methods on the ratio calibration was evaluated, and the highest variation from the uncorrected spectra is below 1.9% at 1000 K for aerosolized SMP:Sn [94].

While this correction approach is generally successful for broad-band emitting phosphors like SMP:Sn, no useful measurements could be obtained for line emitters such as YAG:Pr. Despite the correction of the spectral sensitivity of the PMT with an integrating sphere, some inconsistencies between the manufacturer specifications and measurements of the spectral sensitivity of the PMT (Hamamatsu H11526-20-NF) were also encountered [94]. Therefore, the phosphor emission spectra from PMT measurements are not used to calculate a ratio-temperature calibration curve, and thus, the results are not shown. For measurements in the engine and the BGFR environment throughout this work, the two-color-based

calibration curve will be used to determine temperature, and therefore the focus will be placed on two-color characterization (Section 6.2).

3.3 Temperature image processing via the intensity-ratio method

Figure 16 shows the post-processing steps to derive temperature fields from 2D phosphor luminescence measurements using the two-color intensity-ratio measurements with two input images I_A and I_B. A series of operations is necessary to correct for the contribution of interfering signals (background), the spatially-dependent sensitivity of the camera (white-field correction), or to reduce statistical uncertainty (via spatial averaging). In the last step, both channels are divided by each other to obtain an intensity ratio image that can be translated to temperature with the knowledge of the temperature response of the thermographic phosphor (normalized ratio–temperature calibration). This section describes the post-processing procedure according to the flow diagram shown in Figure 16. If some steps require more consideration, it is mentioned in the text and explained in the following subsections (3.3.1–3.3.3).

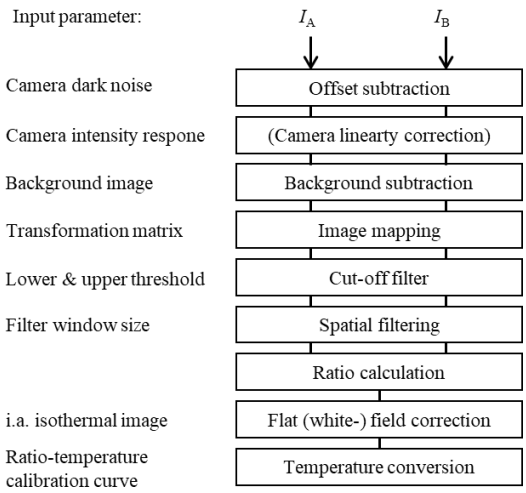

Figure 16: Flow diagram for image postprocessing to derive temperature from the two-color intensity ratio method. Scheme according to Ref. [23].

Camera linearity

For signal quantification, the signal response of the camera must be linear with the incident signal. While scientific cameras have a linear intensity response, it can be of interest to vary the signal gain to decrease the relative noise contribution from constant noise sources like read-out noise. If it is necessary to adapt the camera gain within one measurement series, e.g., due to strongly varying signal levels, the resulting variation in camera sensitivity needs to be calibrated and considered in data analysis. The method to obtain a gain calibration curve is explained in Section 3.3.1.

Background subtraction

Signal background is considered any unwanted signal in the camera, which does not stem from the phosphor luminescence, for example, ambient light, signal from elastically scattered laser light, laser-induced fluorescence from chemical species, chemiluminescence, or natural soot luminosity. In most cases, the background is spatially and temporally stable, thus, a background image can be subtracted as an average image with the laser in the absence of phosphor particles. The camera dark image (or dark charge) that originates from thermally-induced charge does not need to be separately subtracted as it is constant in the luminescence and background image and thus cancels out during background subtraction if the exposure duration is identical and the temperature of the sensor for both images. If the cameras

operate in different intensifier gains, the background image must be acquired at similar gains. In turbulent reactive flows, the background cannot be accounted for based on averaged images because it is subject to strong spatial and temporal fluctuations (e.g., from soot luminosity) and is also related to the presence of particles (blackbody radiation from hot phosphor particles). Therefore, a novel approach is presented in this thesis to correct for background from combustion interference and will be explained in detail in Section 3.6.

Image mapping

In ratiometric measurements, both individual imaging channels need to be accurately mapped onto each other by aligning the images to a common calibration target. This is particularly important for intensity-ratio-based methods, where a small misalignment can result in significant errors after ratio calculation. If the imaging system of both cameras is the same and the distance to the object of interest is similar, it can be sufficient to carefully align both cameras and the beam splitter, which is frequently done in literature [99]. If this is not possible, for example, due to space restrictions (e.g., in engine measurements) or if the cameras are inclined (e.g., heated jet measurements in this thesis), the images need to be mapped onto a common coordinate system in subsequent postprocessing. Depending on the measurement equipment used, this is either performed in imaging software (LaVision, Davis) or in a custom-developed MATLAB routine that transforms one image to the coordinate system of the other according to multiple control points selected on both images through translation, image rotation, and scaling. The spatial calibration is usually done at the beginning of each measurement day. However, some experimental arrangements, including the measurements in the heated jet (Section 6.2) and the burnt-gas flow reactor (Chapter **Error! Reference source not found.**), suffered from spatial displacement from thermal expansion-related hysteresis. Therefore, changes in the alignment of both imaging channels were found even between two subsequent measurement series. Therefore, a single-shot-based mapping procedure was developed for these measurements, where the displacement is calculated in every single-shot image based on a cross-correlation algorithm. This will be described in Section 3.3.2

Filtering

Different filtering methods are applied to the images in a post-processing step to decrease noise, and thus, statistical variation. An intensity cut-off filter is applied to exclude pixels of high uncertainty from further calculation, either because the intensity is too low (noise limit) or too high (saturation limit). Linden et al. found that non-linearities of intensified cameras are already observed below the saturation limit [100]. Unless otherwise mentioned, a cut-off filter from 5–95% of the dynamic intensity range of the camera is applied for all measurements. Spatial filtering (3 × 3 pixels, moving average) increases the signal-to-noise ratio at the expense of spatial resolution. The filtering operations are performed for both channels individually.

Flat-field correction and temperature calibration

Both images are divided to obtain intensity ratio maps. The resulting ratio image can still be subject to non-uniformities, e.g., due to variations in the collection efficiency of the optical system or angle-dependent transmission of interference filters such as dichroic beam splitters. Additionally, the absolute value of the ratio usually varies with the experimental setup (e.g., camera gain), thus, the temperature dependence of the intensity ratio needs to be translated into a temperature via calibration. There are different approaches to performing these operations, which will be discussed in Section 3.3.3., especially regarding its application in the burnt-gas flow reactor.

The signal ratio is calculated from the signal S at the pixel location i,j in the image k, where the signal from the background images (BG) is subtracted from the data images (Data) containing the luminescence signal, which is then corrected for the flatfield (FF). The background image is averaged over all images k. The subscript in the superscript indicates the imaging channel.

$$R(T) = \frac{S_{i,j,k}^{\mathrm{Data}_1} - S_{i,j,\bar{k}}^{\mathrm{BG}_1}}{S_{i,j,\bar{k}}^{\mathrm{FF}_1} - S_{i,j,\bar{k}}^{\mathrm{BG}_1}} \Big/ \frac{S_{i,j,k}^{\mathrm{Data}_2} - S_{i,j,\bar{k}}^{\mathrm{BG}_2}}{S_{i,j,\bar{k}}^{\mathrm{FF}_2} - S_{i,j,\bar{k}}^{\mathrm{BG}_2}} \tag{27}$$

3.3.1 Gain correction

Data can be taken at different intensifier gains of an ICCD to increase signal intensity while minimizing the relative noise contribution of noise produced in the imaging system downstream of the intensifier, e.g., read-out noise or thermally-induced charge on the sensor (dark image). This can become necessary as the intensity range varies significantly between measurements within a measurement series, and the lower intensities approach the noise limit. To compare measurements from different gains, the intensity response of the camera needs to be calibrated against the camera gain. In this case, a dark image needs to be subtracted, and the dark image of one camera is shown in Figure 17.

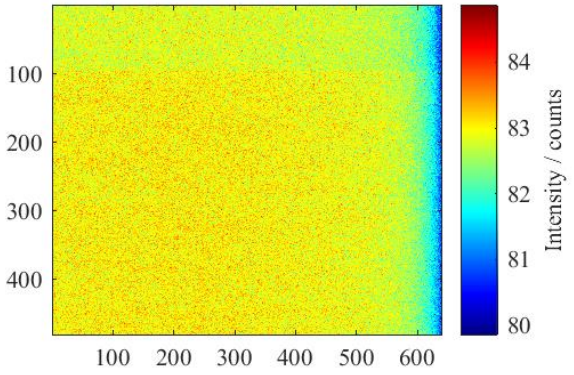

Figure 17: Dark image acquired from LaVision NanoStar camera.

For the calibration measurements, a spatially and temporally homogeneous light source is used (Ulbricht sphere), and the intensifier gain is varied. The exposure duration is chosen to avoid camera saturation. Due to the strong signal magnification of the intensifier, the range of gains used in the experiments (40–100) needs to be split into two exposure series (300 and 2000 ns).

Figure 18 shows the intensities from both exposure series (curves in red and blue). The second exposure (2000 ns) is scaled to the curve of short exposure at the gain of 70 (one-point calibration). This shows the correct functionality of the camera over different global signal intensities, and one calibration curve can be used for correcting measurements taken at different intensifier gains.

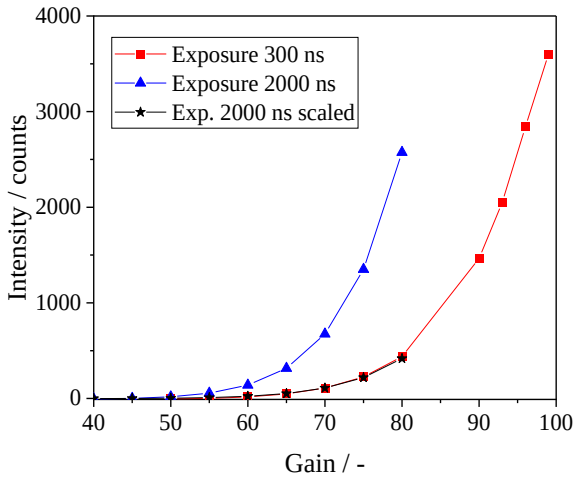

Figure 18: Camera intensities from two different exposure durations (red and blue lines). The intensities shown are corrected by the dark image of the camera. The black curve shows the measurements from 2000 ns calibrated to the short exposure (300 ns) at gain 70.

3.3.2 Development of a single-shot-based mapping algorithm

The images from the heated jet (Section 6.2) and the burnt-gas flow reactor (Chapter **Error! Reference s ource not found.**) showed systematic misalignment, despite accurate software mapping (Davis 8, LaVision), where the remaining error for both cameras is in the sub-pixel regime (0.038 and 0.082 pixels, respectively). Therefore, a single-shot-based cross-correlation mapping algorithm was developed and applied in this work to calculate the misalignment between both images in one set of measurements and correct for it. The procedure is developed with the single-shot image of a turbulent jet, as these images show a lot of structure. Finally, this procedure is adapted to the image data from the BGFR.

The algorithm generally follows the procedure for fast normalized cross-correlation by template matching [101,102]. The images to be correlated stem from both imaging channels from an open jet shown in the experimental setup in Figure 38. The 2D cross-correlation map between two associated images, A and B, is calculated based on the normalized cross-correlation coefficient[8] $\gamma(u,v)$

$$\gamma(u,v) = \frac{\sum_{i,j}\left[A(i,j) - \bar{A}_{u,v}\right]\left[B(i-u,j-v) - \bar{B}\right]}{\left\{\sum_{i,j}\left[A(i,j) - \bar{A}_{u,v}\right]^2 \sum_{x,y}\left[B(i-u,j-v) - \bar{B}\right]^2\right\}^{0.5}}, \tag{28}$$

where $A(i,j)$ is the image A, and $\bar{A}_{u,v}$ is the mean of image $A(i,j)$ in the region of a template image B positioned at (u,v), which is a normalized sum of all vector dot products. The cross-correlation coefficient is thus calculated for each position of $B(u,v)$ within $A(i,j)$, leading to a 2D cross-correlation matrix of the size $(i+u, j+v-1)$.

Figure 19a shows both raw images A and B in a false-color overlay to improve visibility and the 2D map of the cross-correlation coefficient before final translation (b) from an open jet at ambient conditions. The bright spots in (a) are due to phosphor agglomeration, which lead to pixel saturation in both channels. The narrow, vertical structure of the jet in the raw image can be found again in the 2D correlation map, where at the overlay of a given column (horizontal shift between both raw images), the correlation coefficient is high for various vertical overlay positions. The best match of the image overlay

[8] The normalized cross-correlation *coefficient* is more beneficial than the cross-correlation *term* for cross-correlation in strongly varying lighting conditions throughout the image, as found in the conditions of the heated jet, where the luminescence is significantly brighter than the background [101,102].

is clearly characterized by a global maximum within the vertical displacement between both images. Figure 19c shows the correlation coefficient over the index of the image, showing the distinct global maximum. The vector dot product (Equation 28) becomes 1 if the angle between both unity-normalized vectors is zero and –1 if it faces the opposite direction. Therefore, the cross-correlation coefficient can become negative. The translation coordinates (d*x*, d*y*) of the index position, where the coefficient is largest, are extracted and used to translate image B into B1. The overlay of both images (A+B1) is shown in Figure 19d. An additional study was performed to improve image mapping by rotation, but the result showed that this was not necessary because the images were already rotated by previous software mapping in DaVis.

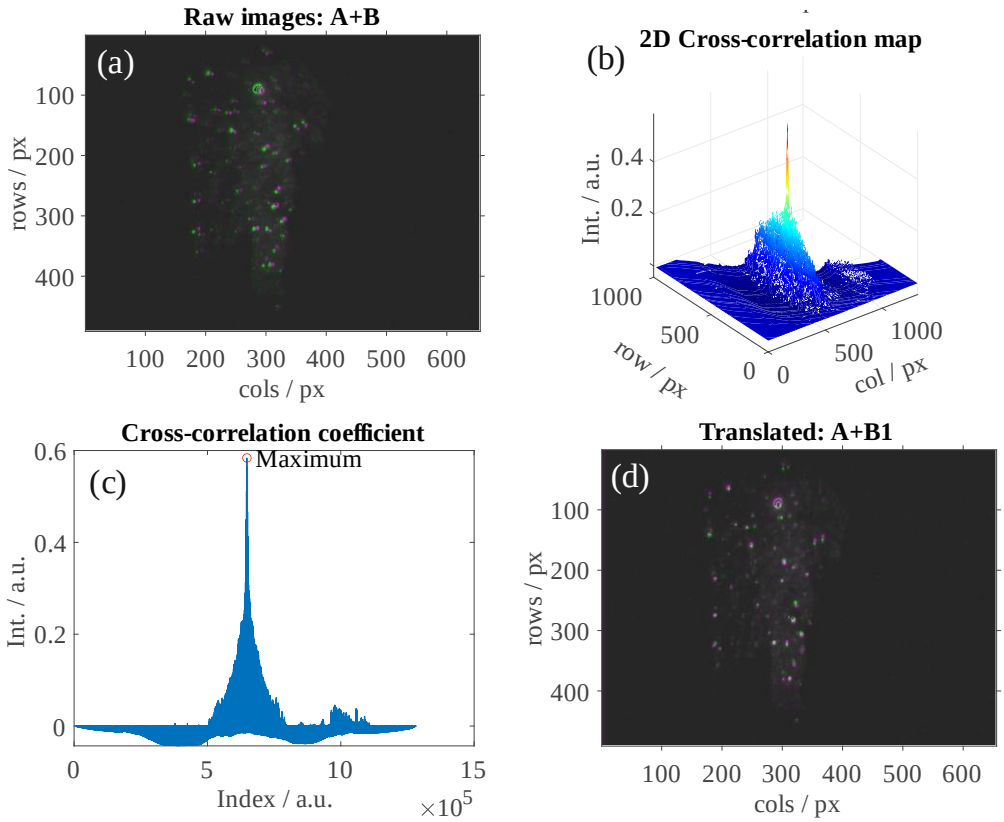

Figure 19: Top: Raw images from both imaging channels A+B of an open jet at ambient conditions in false-color overlay (a). The 2D cross-correlation map is shown on the right (b). Bottom: The cross-correlation coefficient of each possible pixel displacement is shown in (c), and the finally translated images A+B1 in (d) to the position where the cross-correlation coefficient is highest.

Figure 20 shows the outcome of the single-shot-based mapping algorithm applied to the ratio map from measurements in the BGFR. In the BGFR, a central gas flow is heated by a surrounding flame, thus, a radially symmetric temperature distribution is expected. However, due to the misalignment of the cameras relative to the thermally displaced jet, the profile is not symmetric in the raw data (Figure 20, left). The mapping algorithm is applied, and the horizontal and vertical displacement is –4 and 1 pixels, respectively, averaged from 200 single-shot images of this measurement series. The ratio distribution after translating one image is shown on the right in Figure 20.

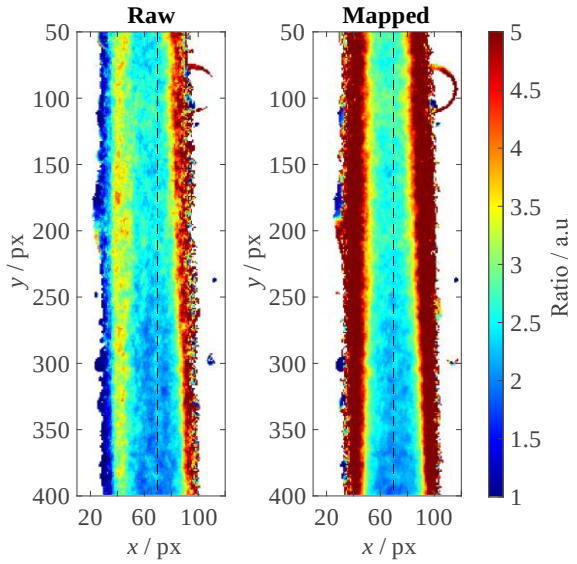

Figure 20: Ratio map from the BGFR from raw data (left) and single-shot-based average mapping correction (right). The resulting displacement is (d*x*, d*y*) = (–4,1) pixels.

3.3.3 Flat-field correction and temperature calibration

After calculating the intensity ratio, further corrections are required prior to calculating the temperature. White-field correction is necessary to correct for non-uniformities in the path of light collection, for example, from intensity inhomogeneities such as vignetting effects from camera lenses, or spectral inhomogeneities that are governed mainly by optics (dichroic beam splitter or interference filters) where the transmitted wavelength has an angular dependence[9]. In general, this should be performed with an identical optical setup (camera, filters) to reduce uncertainties. Subsequently, the measured ratio needs to be calibrated to the ratio–temperature calibration curve at a known temperature.

Both operations can be combined with an *in situ* calibration at seeded operation under known isothermal conditions, e.g., ambient temperature. In this case, the 2D image recorded as a flat field at known conditions is used to divide the ratio image of interest, and the resulting absolute ratio can be applied to the ratio-temperature calibration curve to obtain the respective temperature. It has to be ensured that the temperature of the phosphor particles is constant in the entire field of view. While this approach is straightforward and related to little experimental effort, any systematic error in the seeded flat field will be imposed onto the temperature fields. This is particularly relevant if the seeded areas are not entirely congruent between the flatfield and the measurement of interest, e.g., the locations of the particles in a heated jet at ambient temperature compared to their position at 800 K or in the BGFR, causing additional constraints.

The operations can also be separated by firstly correcting the spectral inhomogeneities with a homogeneous light source and secondly calibrating the ratio to temperature. The light source must cover the same spectral range as the phosphor luminescence, so a broadband emission source, such as a light source connected to an integrating sphere (Ulbricht sphere), can be used. In this case, the temperature known in one region is sufficient for temperature calibration (single-point calibration).

In the BGFR, imaging occurs at different imaging positions above the burner, and a flat-field correction is required for each imaging position as the collection efficiency varies at each position. Under normal

[9] The transmission profile provided by the manufacturer only applies to collimated light at the angle of incidence (AOI), usually 45° for a dichroic beam splitter. In real conditions, the angle of incidence of the signal originating varies with its position on the field of view.

operation, the flat-field correction is performed towards seeded operation at ambient temperature (without the surrounding flame). However, at increasing HABs, the jet is subject to turbulences from flow mixing with the surrounding air, which deteriorates the quality of the flat field in the outer regions. The decrease in particle density increases statistical uncertainty due to lower signal levels and the relative contribution of mapping errors from sub-pixel misalignment.

Figure 21 shows various approaches to applying the flatfield in the BGFR at two imaging position heights. Figure 21a and d present the flat field in the lower (P_0) and higher imaging position (P_1) from seeded operation at ambient temperature. While the flow profile of (a) has a well-defined form, the flatfield from the upper position (d) is subject to strong turbulent fluctuations. All seeded flat fields are background corrected, single-shot mapped, and averaged from 200 cycles. Figure 21c and d are both taken at the increased imaging position (P_1), but turbulences in (c) are reduced by adapting the flow rate of the shielding co-flow to similar flow velocities to the center one. While the impact of fluctuations is reduced, the flow field still diverges, and inhomogeneities are found at the outer positions of the gas flow that would strongly bias the temperature measurements. Figure 21b shows the intensity ratio from an integrated sphere with similar filters as used in the other images. The ratio gradient is due to the spectral inhomogeneities of several interference filters used within this filter set.

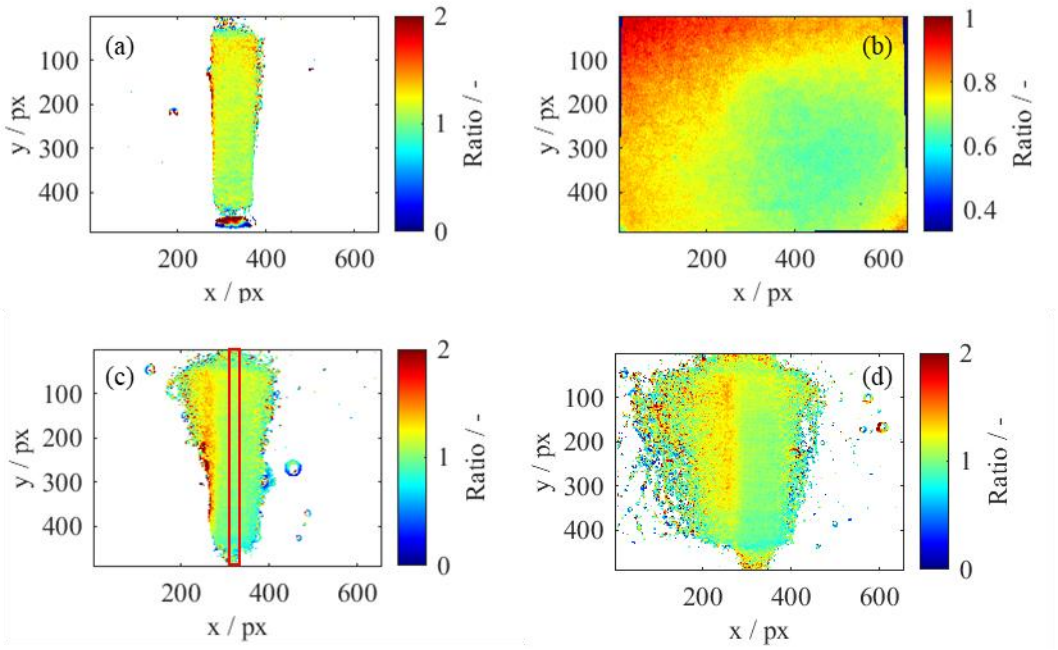

Figure 21: Different flat field approaches applied in the BGFR. (a) seeded operation at ambient temperature in the lowest imaging position (P_0). The burner exit nozzle is indicated at the bottom of the image. (b) white field taken from an integrated sphere with similar filters used for temperature measurements. (c-d) P_1 with (left) and without (right) shielding co-flow. The rectangle in (c) highlights the region used for ratio profile calculation in Figure 21.

Figure 22 shows the ratio profiles of different flat fields averaged from the region indicated in Figure 21c. While the profiles are qualitatively similar, the profile extracted from the homogeneous light source shows significantly fewer spatial fluctuations, despite averaging from the images in seeded operation. The fluctuations are due to the local nature of phosphor particles as a light source. Any artifact encountered in the flat field will deteriorate the spatial accuracy of the temperature images. Furthermore, a slight difference between the ratio profiles can be observed. The origin of the vertical offset between the ratio profile from P_0 and P_1 is unclear, where a higher ratio of P_0 indicates its increased temperature. Despite the lead time between measurements under fired and inert conditions, it is possible that hot surfaces from the burner increased the gas temperature directly above the burner, and the gas cools down

as it mixes with the surrounding ambient air. The deviation of the ratio based on an average between pixel 200–300, as indicated with the red rectangle in Figure 21c, is 5.5% between both imaging positions P_0 and P_1 and under similar conditions (ambient temperature), and the error that would arise from applying the flatfield at P_1 to the data instead of P_0 translates to a maximum of 16.7 K at ambient, and an error of 54.4 K at the highest temperature in the SMP:Sn calibration curve (811 K) that is applied to the BGFR measurements. Therefore, it is preferable to use the white-field correction if high temperature gradients are expected or spatially highly resolved measurements are desired. In the BGFR, the temperature of interest is the boundary region outside the center flow, where the center is heated by the surrounding hot gases, thus, the white field is used to correct for varying spectral collection efficiency.

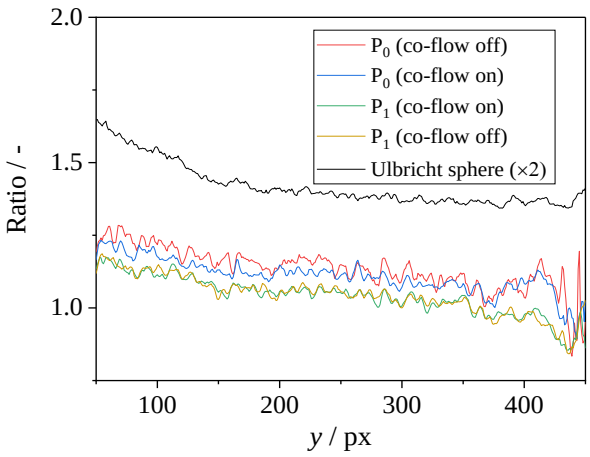

Figure 22: Signal-ratio profiles of different flat-field approaches: Ambient temperature (298 K) and the ratio from a homogeneous light source. Two repeated measurements are shown for each position with and without co-flow. The region used for ratio calculation is highlighted in Figure 21c.

If the white-field correction is performed with a homogeneous light source, the ratio at a known temperature from one position can be referenced to the ratio-temperature calibration curve (single-point calibration) at a known temperature. This is especially challenging at higher imaging positions, where the temperature is unknown, and a flat field under seeded operation cannot be applied. Therefore, for the temperature image processing in the BGFR, the following consecutive flat-field correction procedures are employed. The ratio images from the lowest imaging position (P_0), acquired under fired operation (with flame), are themselves divided by a flat field under seeded operation at ambient conditions (without flame) only to initially estimate the temperature from a small ROI in the center of the flow, where the temperature is approximately homogeneous. For further image postprocessing, the images are corrected by a white field (acquired with the integrated sphere), and the ratio from the congruent ROI of the white-field-corrected image is referenced to the temperature of the similar ROI from the flat-field-corrected image (single-point calibration). This operation combines ratio referencing from straightforward flat-field correction with white-field correction to correct for spectral inhomogeneities.

For temperature imaging in higher positions, a similar procedure is applied. An ROI is selected from an area where the images from both imaging positions overlap, and the temperature in this region of the upper imaging position is scaled towards the temperature from the bottom position after white-field correction.

The term “flat-field correction” is inconsistently used in literature and sometimes refers to both operations combined (white-field correction and single-point calibration), or one operation solely. In this work, flat-field correction always refers to both operations.

3.4 Calculation of in-cylinder gas temperatures from pressure traces

In this work, the temperature of in-cylinder gases is measured *in situ* by phosphor thermometry. A reference temperature is necessary to validate the temperature measurements from phosphor thermometry. The crank-angle resolved in-cylinder pressure p is measured from a pressure transducer, and the temperature can be calculated at each crank angle degree α from the ideal gas law

$$T(\alpha) = \frac{p(\alpha)V(\alpha)}{m\mathrm{R}}, \tag{29}$$

with the cylinder volume V, the mass m of the gases in the cylinder, and the universal gas constant R. The cylinder mass can usually be inferred with very good accuracy from the supersonic flow orifices upstream of the intake manifold, where the gas mix feeds into the engine (N_2 and O_2). This was done in previous work in the engine using ZnO:Zn. However, with the improvements in the seeding system, notably the seeder used (Topas, SAG 410), the phosphor powder is aspirated through the depression caused by the venturi nozzle, and thus, extra mass is introduced into the engine, which would cause a bias to the temperature calculation.

Therefore, an additional approach is employed within this work. At BDC, the cylinder mass m can be calculated from Equation 29 with the temperature measured by a thermocouple. The cylinder mass is then used to calculate the temperature from the cylinder pressure during the entire engine cycle, neglecting a change in the cylinder charge from valve overlap (between BDC and intake valve closing at 213 °CA). To measure the temperature at BDC, readings from two different thermocouples are used. The reading of the high-speed thermocouple (type K, 25 µm tip diameter) is used for motored operation, which was installed through an adapted exhaust valve. Under fired operation, the in-cylinder TC broke after some hundred fired cycles, so the reading of the thermocouple (type K, 1 mm tip diameter) located in the intake manifold is used to estimate in-cylinder mass.

3.5 Particle image velocimetry (PIV)

In this work, PIV imaging is only performed simultaneously with phosphor thermometry in the optical engine. The PIV camera is located on the opposite side of the optical engine, relative to the thermometry cameras. The PIV images are mapped to a global coordinate system with a custom-made calibration target that is printed onto a half-cylinder at a similar diameter as the engine bore. During the alignment process, it is ensured that the calibration target for thermometry and velocimetry is in plane with the 266 and 532 nm laser light sheet, respectively, by slightly rotating the half-cylinder with the calibration target.

The PIV images are post-processed using PIVlab version 2.56 in Matlab [103]. After background subtraction of an ensemble-averaged image, the PIV images are post-processed with a multi-pass cross-correlation algorithm with a decreasing interrogation area from 64 × 64 pixels to 32 × 32 pixels with 50% overlap. A Gaussian sub-pixel estimator validated in Ref. [104] was also used. It is sufficient to use a 2×3-point estimator that only takes into account the directly adjacent horizontal and vertical pixels (2 times 3-point fit) as the mapping towards the global coordinate system does not include shear distortion. The resolution of the final velocity vector is 1.65 mm^2.

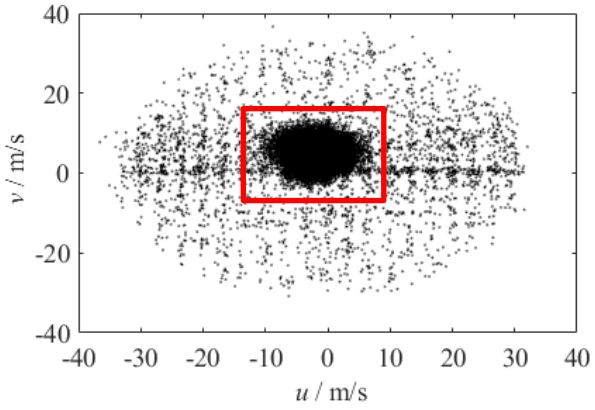

Figure 23: Scatter plot to select velocity limit for the velocity-based filter. The data from 430 °CA under motored conditions (standard intake temperature) are shown.

Finally, a velocity-based filter is applied to remove outliers and to reduce erroneous velocity calculation towards the outside of the engine cylinder. Figure 23 shows a scatter plot of both velocity components in the expansion stroke (430 °CA) at motored operation, where the flow motion is governed by the down-movement of the piston (positive *v*-direction) with a slightly negative *u*-component as a remainder of the clockwise tumble during the compression stroke. The red box shows the velocities considered for further evaluation after the velocity-based filter, and erroneous velocity vectors are linearly interpolated from the surrounding ones. The velocity limits are selected manually for each measurement. A variation in the selection of the velocity limits did not impact the final velocity calculation.

The scatter plot in Figure 23 shows the components of all velocity vectors calculated from pixel displacement. The region outside the dense area in the center shows systematic disturbances in the form of periodically reoccurring regions of higher vector density, commonly referred to as pixel-locking or peak-locking. This is an effect caused when the flow velocity analysis is constrained to integer values describing the displacement of a particle between pixels from the camera sensor. It is therefore an intrinsic error of this measurement technique related to the discrete nature of the sensor, but can drastically be mitigated through sub-pixel estimators [105]. Pixel-locking has the potential to bias the calculated flow characteristics, especially if the spatial scale of the turbulence that is aimed to be resolved is similar or smaller, compared to the spatial resolution of the detection system. Christensen reported that the mean velocity profile is the only turbulence statistic insensitive to pixel locking [106], which is the metric used throughout this work to quantify flow velocity. First-order data analysis was performed by illustrating the probability density function of particle image displacement, and the data did not show a relevant contribution of pixel-locking. Also, as the focus of this thesis lies on the challenges of temperature measurement, and the flow characteristics to be resolved are rather large-scale tumble motion in the engine than small-scale turbulence, a more detailed investigation is omitted here and the reader is referred to relevant literature [107,108].

3.6 Correction for combustion interference in engine post-combustion gases

One of the major challenges of thermographic measurements in the post-combustion regime in engines is the interference from combustion-related luminescence, such as chemiluminescence or blackbody radiation from particles (BBR). These signal contributions cannot be spectrally separated from the phosphorescence signal as the detection bands for YAG:Pr are 494±10 nm and 570–625 nm and thus overlay with the broad-band BBR and C_2* and CO_2* luminescence [109,110]. The pulsed laser-based signal can also only partially be separated from the continuous interference signal as exposure times required for

capturing ~95% (3τ) of the emitted signal at 800 K is approx. 9 and 175 µs for the blue and red imaging channels, respectively, providing ample opportunity for detecting background.

Interference from fast-decaying laser-induced signals, e.g., laser-induced incandescence (LII), can be efficiently suppressed by delaying detection by several tens of nanoseconds [111]. Chemiluminescence is negligible considering the short exposure duration for the blue imaging channel and the timing of the measurements very late in the cycle when the heat release is negligible (after 480 °CA). BBR is relatively strong compared to the thermally quenched phosphorescence signal, and the broadband emission interferes with the red imaging channel, given the long exposure duration. In this measurement setting, BBR must be distinguished between radiation emitted from soot particles as well as phosphor particles. The correction for the latter is particularly challenging because it cannot be accounted for by averaged background measurements from combustion under unseeded conditions as usually done because this signal only occurs when phosphor particles are added (see third category of systematic errors). In previous measurements, it was not possible to use average measurements as a background from seeded operations with the laser turned off because the signal from combustion interference was too strong and subject to strong fluctuations. However, the timescale of combustion interference is long in comparison to the timescales of phosphorescence or the conditions in the engine; thus, it can be assumed that the combustion-related background does not change during the time of two exposure durations that would be required to capture the phosphor luminescence signal (3τ). This fact is exploited in an *online* background correction approach, where an image acquired immediately prior to the phosphorescence image is used to correct for the combustion-related background. In the further course of this work, soot luminescence and blackbody radiation from phosphor particles is referred to as combustion-related interference.

3.6.1 Double-imaging for *online* background correction

The double-imaging mode is used for online correction to account for combustion-related signal interference. For this purpose, the first frame is recorded before the laser pulse at the same acquisition parameters (gain, exposure). The second image acquired 100 ns after the laser pulse, is a superposition of laser-induced phosphor luminescence and the combustion-related signal. This is possible due to the interline architecture of the CCD detector, which allows to take two images in rapid succession. This will be detailed in the further course of this section. The temporal delay between both frames is <50 µs, which is considered short relative to relevant timescales of combustion and transport. Therefore, we can assume that the combustion-related signal does not change significantly during the duration of the measurement[10]. In this case, the first frame, which only contains signal from combustion, can be used for background subtraction for the second image. The double-imaging mode for background correction is only applied to the red imaging channel (Ch 1) and not necessary for the other channel as the contribution of chemiluminescence is negligible at the related short exposure time in the blue channel. The timing diagram for post-combustion measurements is shown in Figure 24.

[10] The total measurement duration is 397.2 µs composed of the exposure from two frames (175 µs) and the delay between images (47.2 µs). This is less than the time required by the piston to move by 3 °CA, so the background from combustion is not considered to change significantly late in the expansion stroke of the engine. 1 °CA ≈ 134 µs at 1200 RPM.

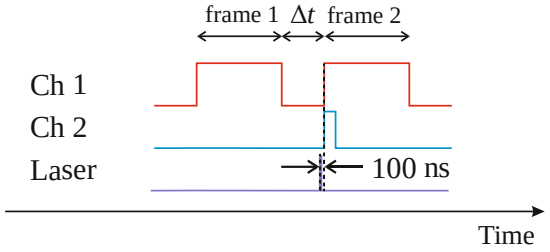

Figure 24: Timing diagram of the phosphorescence camera used in double-imaging mode. The exposure time of both frames is constant and separated by the delay Δt. Frame 2 from the double-imaging mode (Ch 1) and the image from Ch 2 are delayed relatively to the laser pulse by 100 ns.

Figure 25 shows single-shot double-frame images from the red imaging channel (Ch 1) acquired in the engine at 540 °CA under fired conditions using YAG:Pr with the timing strategy in Figure 24. The signal visible in the first frame stems from natural soot luminosity or blackbody radiation from the seeded phosphor particles. The second image is a superposition from laser-induced phosphorescence and the combustion-related signal from frame 1.

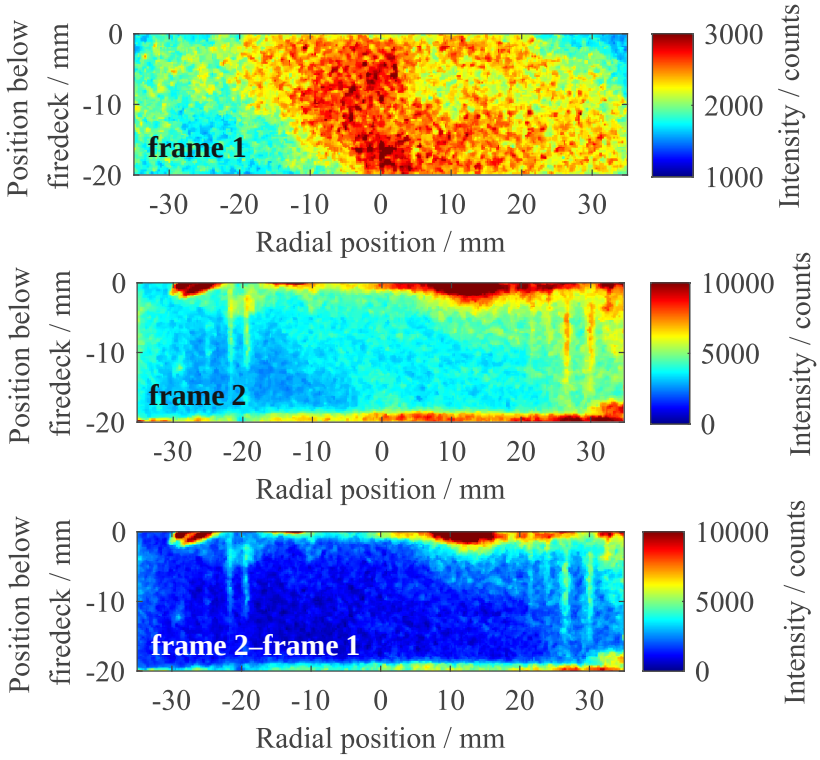

Figure 25: Top and center: Single-shot images of the first imaging channel (Ch 1) in double-imaging mode at 540 °CA under fired conditions using YAG:Pr. The intensity in both images is scaled for improved visibility. Bottom: Phosphor luminescence signal after background subtraction.

The capability of capturing two frames in rapid succession is state-of-the-art for cameras with interline CCD architecture used for double-pulse particle image velocimetry (PIV) applications. However, unlike PIV, where qualitative intensity information is sufficient to identify the position of a particle, for quantitative intensity analysis required for the intensity-ratio thermometry approach, it must be assured that both frames have the same intensity response. It is important to understand the architecture of these cameras and intensifiers to identify possible sources of systematic errors related to the double imaging mode.

A camera sensor consists of many pixels, where each pixel is treated as an individual detector that converts the incident radiation to an electric charge (photo-electric effect). Even if many different cameras (CMOS, CCD, EmCCD) use the same physical principle to detect light, there are significant differences in their layout and architecture. The detector used here is an intensified CCD (charge-coupled device) camera in interline architecture. Unlike a standard CCD camera, an interline camera consists of alternating columns of light-sensitive and adjacent masked pixels. The masked pixels can be used for storage, which allows to record a second image in rapid succession, even before the relatively slow readout process (usually in the order of 100 ms) for the first image is finished, which is referred to as the double imaging mode. The read-out noise increases with a faster camera readout due to the increasing bandwidth required. Therefore, the slowest readout mode is chosen for imaging. According to the camera's specifications, the readout noise is 12 e^- (root mean square) in the slowest mode [112]. The dark noise (thermal noise) is usually in the same order of magnitude and 10 electrons per pixel per second (e^-/pixel/s) in modern cameras, so readout noise is comparably low.

Dark noise is a thermally-induced charge that integrates on the CCD array, whether or not data acquisition occurs. Under regular operation, the dark noise is always discarded through the continuous clean operation of the camera before the first acquisition in a measurement series [112]. In repetitive imaging operations with more than one consecutive image, the dark noise is only wiped off the sensor for the first image. However, the dark noise of this camera (0.5 e^-/pixel/s) is significantly lower than, for example, the readout noise in operation, where the chip is cooled to –20 °C through thermoelectric cooling [112]. Nevertheless, the first image contains a spurious charge, which is always excluded from further analysis.

In double-imaging operation, continuous “cleaning” of the chip occurs only before the acquisition of the first frame of the first image pair. Likewise, to the post-processing from regular imaging operation, the first image pair is excluded from further analysis. For all further image pairs, dark current can be neglected because of the insignificant intensity (0.5 e^-/pixel/s) if the sensor is cooled. Additionally, it cancels out in background subtraction (see Section 5.3) since it contributes approximately similarly to all images, including the background image. Therefore, in repetitive imaging operations, the contribution of dark current is negligible except for the first image, which is always excluded from further analysis due to potentially spurious charge.

The intensifier in this ICCD camera (Princeton Instruments, PI-MAX2, gen II, sensor: Kodak KAI-1003) is coupled 1:1 via a fiber optics bundle to the CCD. The intensifier tube contains a multi-channel plate (MCP) that amplifies the signal by generating an electron avalanche from each incoming electron. For high repetition rates, intensifiers are susceptible to charge depletion [93]. This occurs if the device cannot build up sufficient charge in the amplifier between both images for signal intensification, either because the charge depletion is substantial from high signal levels or because the delay between both exposures is very short. Therefore, the intensity response of the intensifier is investigated as a function of gate delay and global signal intensity for double exposure. As there are no significant gradients in the signal stemming from combustion interference or blackbody radiation, it can be assumed that each pixel behaves independently and no charge leakage occurs between two neighboring pixels with significant intensity differences. For very high intensity gradients between neighboring pixels, the intensity response in the double-imaging mode could be investigated, for example, with the knife-edge method [113,114], but this is outside the scope of this work.

Figure 26 shows the experimental layout to characterize the intensity response from both frames in the double-imaging mode. As depletion effects can also vary with the illuminated region of the camera chip [40], the same camera position is employed for measurements in the engine environment, and camera

operation parameters (exposure duration and intensifier gain) are maintained similarly. A homogeneous light source behind a half-quartz ring illuminates the same region of interest (ROI) of the ICCD for the engine measurements. A combination of different neutral density (ND) filters enables the variation of the incident radiance, and the gate delay between both frames can be set in the camera software.

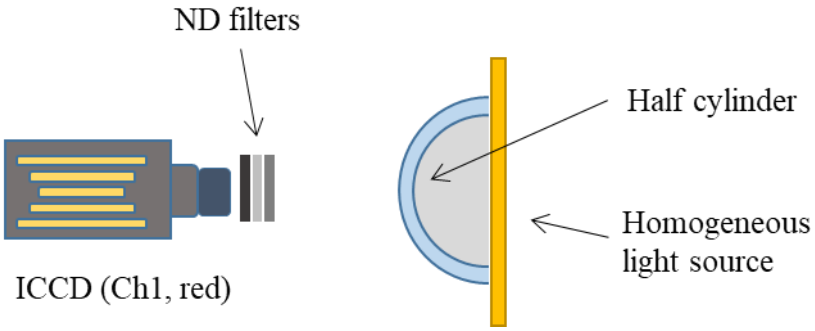

Figure 26: Experimental layout characterizing the double-imaging mode using a homogeneous light source with a half cylinder.

Figure 27 presents raw images from both consecutive frames from homogeneous illumination. The vertically averaged intensity profiles from the ROI, highlighted with a box, are shown in Figure 28. The region with nearly 4000 counts represents the backlighted half cylinder. The homogeneous light source is placed behind the half cylinder; thus, scattered and refracted light by the cylinder is visible in the rest of the image. The first frame is slightly brighter than the second one. The intensity peak at pixel column 360 stems from a misfunctioning pixel that does not have a statistically significant influence on the analysis. For further statistical evaluation, only pixel rows from 150–300 are considered, similar to the regions used for the analysis in the engine.

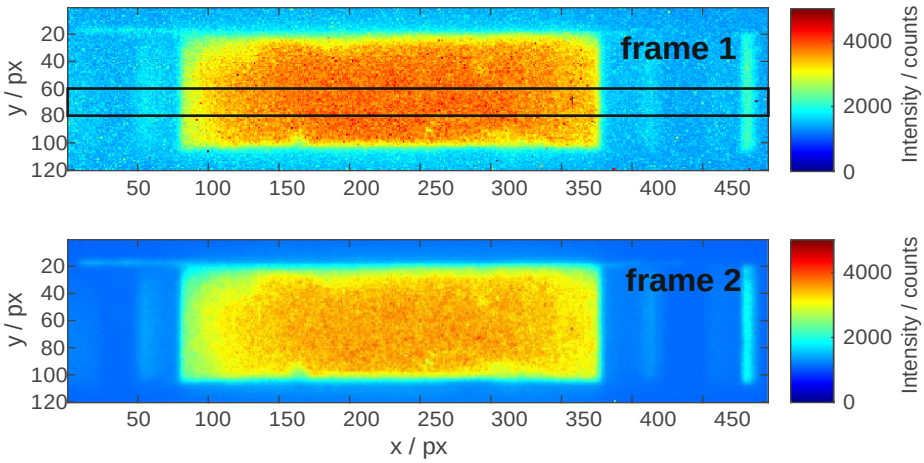

Figure 27: Images from two consecutive frames in the double imaging mode under constant illumination. The delay between both frames is 47.2 µs, similar to the measurements in the engine. The region highlighted with the box is used for intensity calculation throughout this section.

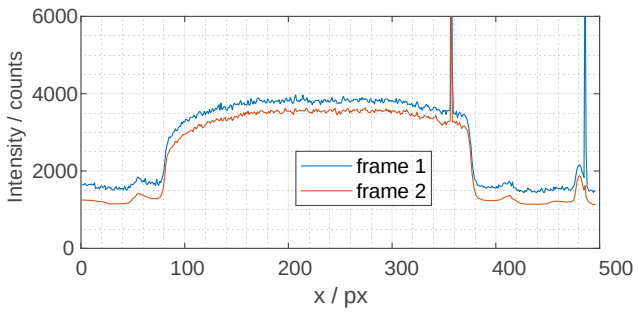

Figure 28: Intensity profile of the phosphorescence camera in double-imaging frame mode at low global intensities. The profile is vertically averaged over 20 pixels in the center of the image, as shown in Figure 27.

3.6.2 Intensity response for varying delays

The delay between both frames is varied in the imaging software at constant illumination. The camera specifications give a minimum delay of 3 µs. This limitation is primarily due to the camera architecture. The fluorescent phosphor screen built into the camera converts the electrons released by the multi-channel plate (MCP) to photons. This camera uses a fast-decaying phosphor (P46), which decays to 10% after 2 µs. Figure 29 shows the intensities from both frames, averaged from the ROI shown in the intensity maps in Figure 27. The difference between both frames is shown on the right *y*-axis in red. At delays between 5 µs and 1 ms, the calculated intensity difference ΔI is approximately constant, the first one being brighter, while at 10 ms, both frames have similar intensities (ΔI = –5.3 counts). No repetition measurement is carried out for this operation point, so erroneous operation cannot be excluded. No reasonable explanation is found for this behavior. However, the gate delay for the measurements in the engine is below 50 µs, and the intensity response in this regime is nearly linear.

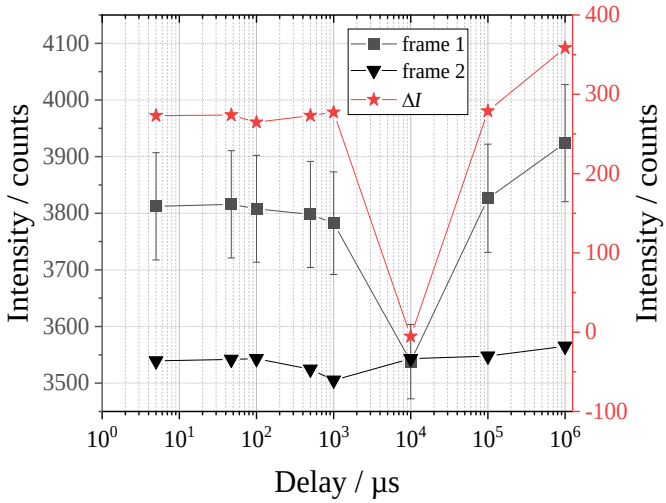

Figure 29: Signal intensity from both imaging frames at various delays between both images. The error bars show the standard deviation (±1σ) from the intensity in the first frame. The intensity difference (frame 1 – frame 2) is shown on the left axis.

3.6.3 Intensity response for varying radiance

To investigate the effect of the incident radiance on the intensity response of both frames, the illumination of the light source is held constant, and the incident radiance to the sensor is varied by combining various neutral density (ND) filters. The delay between both frames is set to 47.2 µs and the gain to 150, both parameters being similar to the engine measurements. In Figure 30, the intensity difference between both frames (frame 1 – frame 2) is plotted as a function of the intensity of the first frame. The relative deviation is shown on the right, where the difference is related to the average intensity of the first frame.

The intensity difference between both frames changes the algebraic sign over the entire range, implying that there are counteracting effects in different intensity regimes. While the findings of this study are not conclusive, a possible explanation is proposed based on the working principle of the camera. In the intensity regime between 3000 and 22.000 counts, the intensity of the first image is higher than the second one. This is qualitatively similar to the behavior shown above in the gate delay investigation.

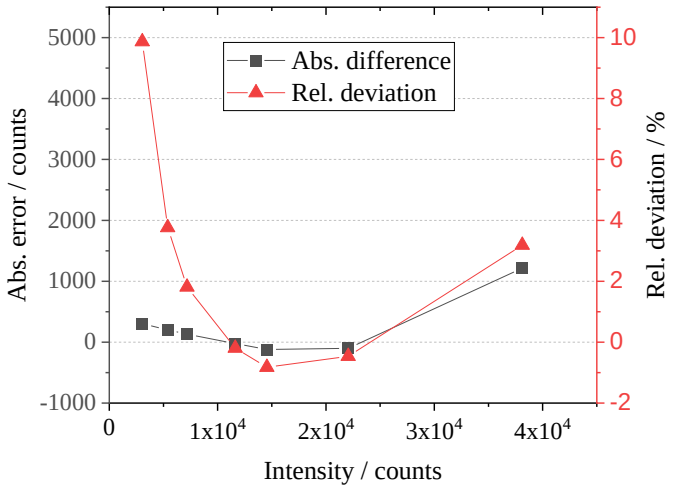

Figure 30: Intensity difference between both frames (frame 1 – frame 2) shown over the average intensity of the first frame. The relative deviation is calculated from the intensity difference and the intensity of frame 1.

In this range, the second image becomes constantly brighter with increasing intensity relative to the first one. The delay between both images is constant (47.2 µs) in this study, similar to the measurements in the engine. According to the manufacturer, it takes 2 µs for the phosphor emission from the fluorescence screen (P46) to decay to 10%. But the phosphor decay is not mono-exponential, so 1% of the phosphor emission can still be left after 100 µs [112], which accumulates on the CCD and thus contributes to the second image. While this percentage is constant for any incoming radiance (assuming the absence of saturation effects for the P46 phosphor), the residual signal from the first image in the second image may be too low to be detected for low radiances, e.g., because it is below the statistical read-out noise of the detector. However, if the incoming radiance is stronger, the absolute signal contribution on the CCD can become detectable, so the intensity of the second image increases at increasing radiance.

At increasing signal intensities (>20.000 counts), the intensity of the first frame is more significant than that of the second one, so the difference becomes positive again. In literature, the depletion effects of high-speed intensifiers are reported [93]. The higher the incoming radiance is, the more charge is required to ensure signal amplification. Therefore, the intensity of the second image may decrease due to charge depletion of the intensifier, compensating for the above-mentioned effect of residual signal intensity from the first image in the second image at increasing radiances.

In this scenario, the intensity difference increases because the intensity of the second image decreases relative to the first one. However, it is also possible that the intensity of the first image increases non-proportionally relative to the second one, leading to an increasing difference in intensity (frame 1 – frame 2). When the camera gate is closed, the voltage of the intensifier is inverted, and electrons from the photocathode are repelled. However, the rejection rate is not infinite. Therefore, at very long measurement durations in a bright environment, like in the current characterization measurements, electron leakage can cause the first image to be brighter. In this case, the first frame may be non-proportionally brighter than the second one.

Even if the characterization study is not conclusive and the manufacturer was not able to comment without functional testing all electronic components, it should be noted that in the intensity range between 5.000–20.000 counts, the intensity range relevant for post-combustion measurements, the absolute intensity difference is between 100 and 200 counts, which results in a relative deviation of less than 2%. This deviation adds to the measurement error that can be quantified and considered for the evaluation of post-combustion measurements.

3.6.4 Postprocessing procedure

The ratio calculation with images acquired in the double-imaging mode varies slightly from the procedure introduced in Section 3.3. The objective of employing the double-imaging mode is the online subtraction of combustion interference from the phosphorescence signal intensity in the red imaging channel (Ch1). Therefore, the first frame is considered the background (BG) in the red channel for the ratio calculation in Equation 27. The equation for ratio calculation using regular background subtraction is printed again as a reference in Equation 36 (left). The background subtraction of the camera in double-imaging mode is adapted, and the ratio calculation is shown on the right.:

$$R(T) = \frac{S_{\mathrm{i,j,k}}^{\mathrm{Data_1}} - S_{\mathrm{i,j,\bar{k}}}^{\mathrm{BG_1}}}{S_{\mathrm{i,j,k}}^{\mathrm{Data_2}} - S_{\mathrm{i,j,\bar{k}}}^{\mathrm{BG_2}}} \quad \rightarrow \; R(T) = \frac{\mathrm{Ch_1^{double\ frame}}}{\mathrm{Ch_2}} = \frac{A_{\mathrm{i,j,k}} \times S_{\mathrm{i,j,k}}^{\mathrm{Data_{1,frame2}}} - S_{\mathrm{i,j,k}}^{\mathrm{Data_{1,frame1}}}}{S_{\mathrm{i,j,k}}^{\mathrm{Data_2}} - S_{\mathrm{i,j,\bar{k}}}^{\mathrm{BG_2}}} \qquad (30)$$

The superscript to the signal *S* annotates the imaging channel and if it was acquired from a background measurement ("BG") or the measurement of interest ("Data"). Note that the second term in the numerator represents a single-shot image of the k^{th} cycle and is not an average image from all acquired cycles. An ensemble-averaged image is annotated as $\bar{k}$, for example, the averaged background subtraction in the denominator. As the intensity response of both frames is different, the intensity of each pixel in the second frame is corrected according to the intensity calibration curve in Figure 30. The correction matrix for the second frame is $A_{\mathrm{i,j,k}}$, where the intensity of every pixel is corrected according to the calibration curve in Figure 30. The second frame is intensity-corrected instead of the first one, as the noise level of the first frame is higher than in the second one (see Figure 27), to avoid that the intensity correction amplifies the noise level. All other postprocessing steps for temperature calculation, including the flat-field correction, are similar to the procedure in Section 3.3, and all images are hardware-binned (2 × 2). The ratio calculation for motored operation in the double-imaging mode follows the procedure with regular background subtraction, where the background image (BG) is acquired in a separate run, and the measurement of interest containing phosphorescence information (Data) is acquired in double-imaging mode as there is no combustion interference to correct for.

4 Experimental configurations for temperature and velocity measurements

This section introduces all experimental configurations used within this work, supplemented with some methods specific to these experiments. The order in which the measurement setups are presented follows the sequence of challenges identified within this work, (i) particle survivability, (ii) high-temperature characterization, and (iii) engine application: The survivability experiments in a premixed burner give rise to potential degradation of the phosphor particles in harsh environments as present in internal combustion engines. This includes the experimental setup and its implementation for CFD simulations of the premixed burner to quantify the temperature of the post-combustion gases (Section 4.1) as well as information about the techniques used for the analysis of the post-flame particles (Section 4.2), such as microscopic analysis (SEM/EDX) and x-ray diffraction (XRD). The setup used for the high-temperature characterization of phosphor aerosols in a heated jet is shown in Section 4.3. Finally, the experimental configurations and operating conditions are shown for the application environments, where two-color phosphor thermometry was shown in a burnt-gas flow reactor (BGFR) in Section 4.4 and in an optically accessible, reciprocal internal combustion piston engine (Section 4.5).

4.1 Particle survivability: Premixed burner

The objective is to study the particle survivability of the thermographic phosphors in a combustion environment. Phosphor particles are seeded into the oxidizer flow of a premixed propane/air flame. Temperature measurements based on the intensity-ratio method are attempted in the post-combustion regime, where the flow has cooled down to a temperature level that provides sufficient luminescence yields and, thus, a strong enough signal for measurements in the aerosol. Particles are recaptured from the exhaust for subsequent particle analysis. A CFD simulation of the reactive flow is carried out to determine the thermal history and derive the residence time of the particles in the high-temperature zone. This helps to interpret particle analysis results and draw conclusions about particle degradation. The experimental conditions and the simulation are detailed in the following subsections, and the outcome will be discussed together with the results from the particle analysis in Section 5.3.

4.1.1 Hardware and optical diagnostics

The experimental layout for two-color measurements and recovery of the phosphor particles above a premixed burner is shown in Figure 31. A custom-built premixed burner is used with a chimney extension featuring a passive co-flow to stabilize the flow downstream of the reaction zone. The shielding co-flow is controlled with inlet flaps at the bottom of the extension, which influences the shear between both flows and, thus, natural convection between them. The phosphor particles are seeded into the oxidizer flow (dry air) with a magnetically agitated stirrer. Both flowrates are controlled with Bronkhorst mass-flow controllers (propane: F201C-RAA-22V, air: F201C-RAA-33V) and varied to change the stoichiometric ratio and thus the adiabatic flame temperature (ϕ = 0.62–1.0, $T_{\mathrm{adiabatic}} \approx$ 1650–2350 K) [115].

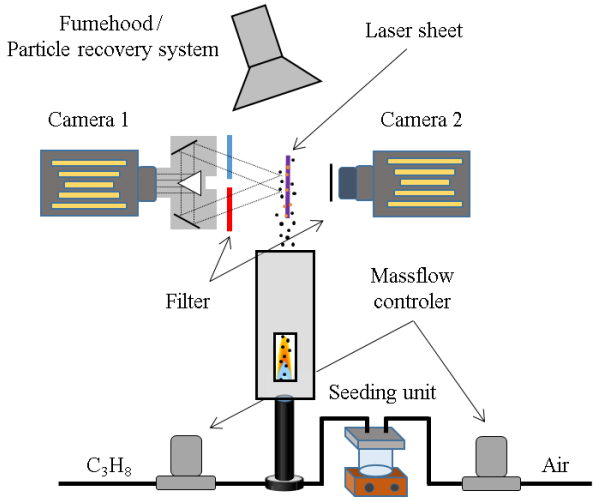

Figure 31: Arrangement for temperature measurements using thermographic phosphor in the post-combustion zone of a premixed burner (side view). Reproduced from Ref. [68] with permission from IOP Publishing.

For two-color luminescence temperature measurements above the burner, a quadrupled Nd:YAG laser (266 nm) is used with the combination of a plano-convex (f = –200 mm) and a spherical lens (f = 1000 mm) and formed to a laser light sheet (90 mJ/cm^2) with the thickness of 0.5 mm. Camera 1 (PIMax 4, EmCCD, 16 bit, intensifier gen2, 512 × 512 pixels) is equipped with a Nikkor lens (f = 28 mm, f/2.8) and an image doubler (LaVision) to project signal from the laser-illuminated area through two optical filters onto the same camera chip. Camera 2 is identical to camera 1 and used for Mie-imaging with two extensions (Nikon PK-11A), a Cerco lens (f = 45 mm, f/1.8), and multiple neutral density filters to prevent sensor saturation.

The equivalence ratios with the respective flow rates and the resulting adiabatic flame temperatures are shown in Table 2. The particles are recovered from the exhaust gases approx. 300 mm above the burner extension with a filter membrane for particle analysis at a fuel/air equivalence ratio of ϕ = 0.71.

Table 2: Equivalence ratios, propane flame flow rates, and adiabatic temperatures according to [115] for the premixed burner.

ϕ / -	$\dot{m}_{prop}$ / l$_n$/min	$\dot{m}_{air}$ / kg/h	$T_{adiabatic}$ / K
0.62	47	0.4	1650
0.71	53	0.4	1900
0.83	62	0.4	2050
1.0	75	0.4	2350

4.1.2 CFD simulation and determination of the particle residence time

The objective of the CFD simulation of the reactive flow conditions is to obtain information about the thermal history of the phosphor particles. A two-dimensional, axisymmetric, steady-state numerical simulation with a mesh side size of 0.5 mm was carried out in Ansys Fluent to calculate the residence time of the phosphor particles in the hot zone of the flame. Figure 32 shows the simulation environment of the burner with the respective boundary conditions. The species and inlet velocity from the burner central flow are calculated from the measured mass flows from propane and air (ϕ = 0.71). A mole fraction of 0.0004 of OH-radicals was added to the inlet flow to initiate the ignition of the mixture. The inlet velocity of the passive, shielding co-flow (pure air) was iteratively adapted to match the thermocouple temperatures in the flow above the reaction zone. Both outlets annotated in Figure 32 are defined as pressure outlets towards ambient air conditions.

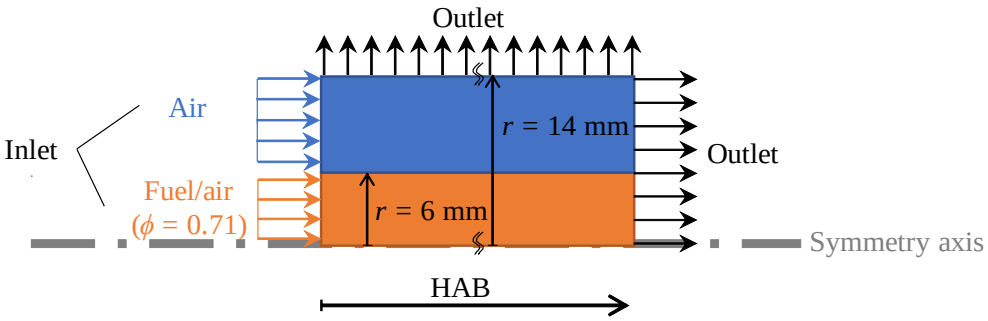

Figure 32: Schematics of the simulation environment with the related boundary conditions.

Radiation from the metal chimney, gravity, and the heat capacity of the phosphor particles are neglected. In the fluid, thermal diffusion and species transport are considered and the chemical kinetics were calculated with the CHEMKIN CFD solver using the complete San Diego mechanism [116].

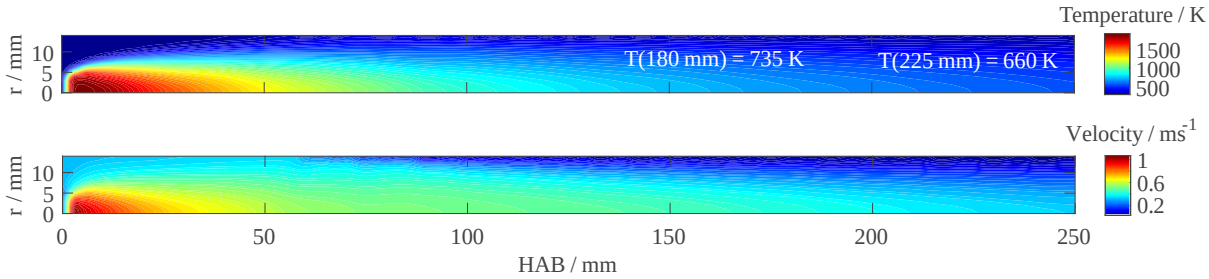

Figure 33: Simulated 2D temperature and velocity map of a premixed burner flame (ϕ = 0.71).

Figure 33 shows the steady-state 2D temperature and velocity fields from the premixed propane/air flame, which is needed to calculate the residence time at a certain temperature. At increasing heights above burner (HAB), the flow cools down due to convective mixing with the passive co-flow. The time-dependent variation of temperature and velocity along the center line is shown in Figure 34.

For simplified residence time calculations, it is assumed that the particles only travel in the vertical direction on the axis. Therefore the radial component of the velocity and variation across the flame cross-section is negligible. While this simplification is reasonable for the accuracy required for this survivability study, it should be noted that radial velocity contributions could increase the residence time at the related temperature. Therefore, the following residence time calculation should be interpreted as a simplified, lower estimation of the residence time.

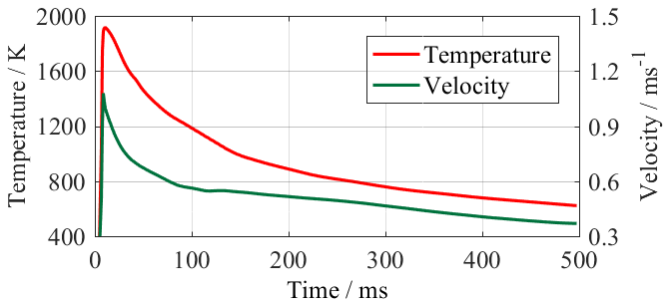

Figure 34: Simulated temperature and gas velocity over time of a particle in the flame and post-combustion gases. Reproduced from Ref. [68] with permission from IOP Publishing.

The discretized residence time of a phosphor particle in each cell can be calculated by dividing the mesh size (0.5 mm) by the absolute value of the local flow velocity. With the corresponding temperature in the respective cell, the cumulative residence time of a particle at a certain temperature can be determined. This can give rise to the thermal history of a particle propagating through a premixed flame and the post-

combustion gases at given conditions. Figure 35 shows the residence time, during which a particle remains at a certain temperature or above. The time, where the phosphor particles remain at temperatures higher than 1473 and 1920 K is 38 and 0.9 ms, respectively.

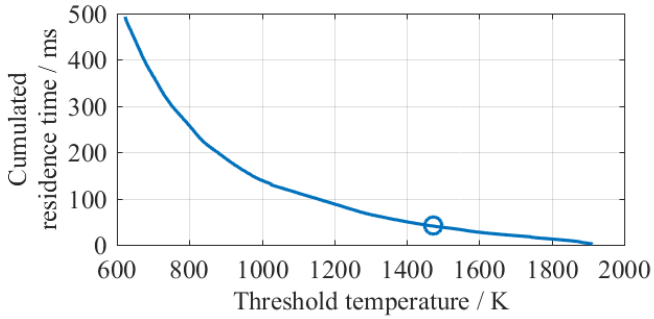

Figure 35: Cumulative residence time of a particle traveling along the burner axis at a given temperature or above in a premixed propane/air flame (ϕ = 0.71). The residence time for $T \geq 1473$ K is highlighted with a circle. Reproduced from Ref. [68] with permission from IOP Publishing.

Theoretical heat transfer considerations on the response time t_{95} until a particle reaches 95% of the steady-state temperature following a step change in temperature of the surrounding gas temperature is below 30 µs [4] for a 2 µm phosphor particle (YAG) for a step change from 300 to 2000 K. The melting temperature of SMP:Sn is above 1473 K according to the manufacturer's specification [78]. The residence time at temperatures above the melting temperature is three orders of magnitude longer (38 ms) than the heat-up time, thus, thermal equilibrium between the surrounding gas and the particle can be assumed, and therefore complete melting of the particle. The impact of exposure to a high-temperature environment on the particle luminescence properties will be discussed in Section 5.2, and phosphor degradation mechanisms will be proposed in Section 5.3.

4.2 Particle analysis

This section outlines different particle analysis techniques that have been used to identify morphological modifications or structural changes in the crystal lattice of a thermographic phosphor. These changes can deteriorate the luminescence properties of a phosphor and can lead to a total loss of its capabilities to sense temperature.

4.2.1 X-ray diffraction (XRD)

X-ray diffraction (XRD) is an experimental analysis method to investigate the lattice structure of a crystal. Figure 38 shows the schematic layout of an x-ray diffractometer. The incident x-ray beam interacts with the atoms of the material's crystalline structure and is partially diffracted. The periodic repetition of crystal planes characterizes a crystalline structure. The diffracted beams are subject to constructive and destructive interference from different planes, which results in a diffraction pattern as a function of the incident angle θ. A diffraction pattern is unique for each crystalline structure, and the resolution is in the range of θ = 0.01°. The radiation source used in the x-ray diffractometer (Bruker, D8 Discovery) is a copper anode (1.540562 Å), and the angle θ of incidence is varied between 10 and 80°.

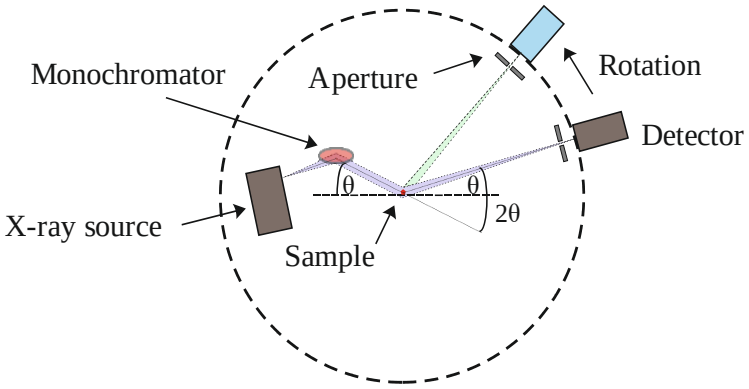

Figure 36: Schematics of x-ray diffraction measurements.

4.2.2 Microscopic analysis (SEM/EDX)

A scanning electron microscope (SEM) can be used to analyze organic or inorganic materials on a microscopic scale. A fine electron beam (primary electrons) is focused onto a specimen, and its interaction with the material's atoms is used to image the material's topography or chemical composition. The emission of secondary electrons (SE) is confined to the first nanometers of the surface and is captured by an SE detector (or Everhart-Thornley, ET detector, cf. Figure 37) and enables high-resolution topographic images at the resolution of the focused electron beam. Backscattered electrons (BSE) are elastically scattered electrons emitted from a larger penetration volume due to their higher energy. The extent of backscattering depends on the atomic number of the element. It therefore enables to image areas of varying chemical composition, however, at a lower resolution due to its increased penetration depths. Quantitative analysis of the chemical composition can be obtained from element-specific x-ray emission in what is called energy-dispersive x-ray spectroscopy (EDX). The related x-ray radiation is generated if incident high-energy electrons release an electron from an inner shell and an electron from an outer shell fills the gap and releases the difference in energy by emitting x-ray radiation, which is characteristic for each chemical element. Most SEM are equipped with an EDX detector. For more detail, the reader is referred to the respective literature [117].

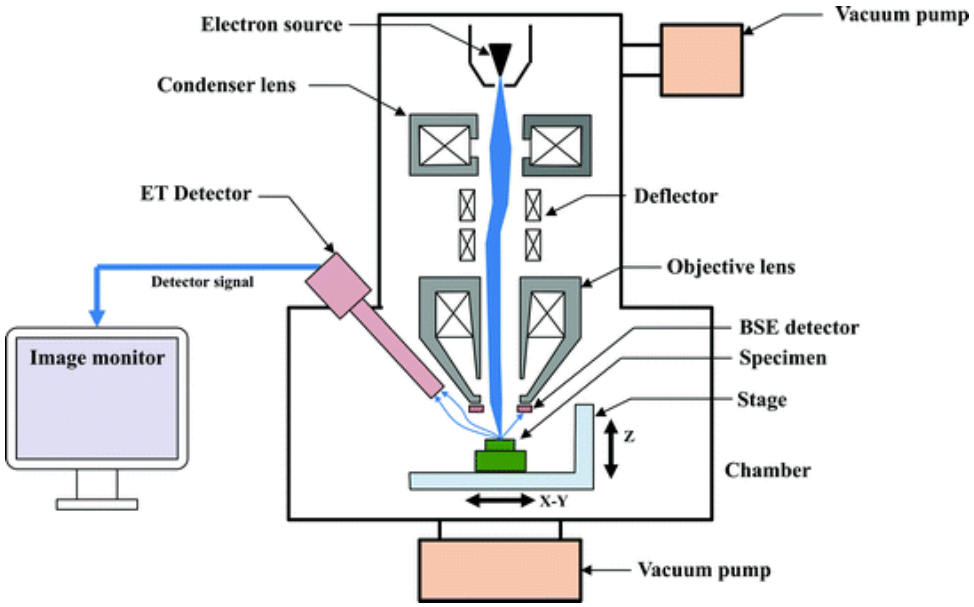

Figure 37: Simplified schematics for combined SEM/EDX microscopy. ET: Everhart-Thornley detector; BSE: backscattered electrons; Reproduced from Ref. [118].

In this work, the phosphor material is captured from the exhaust gases of the premixed burner and compared to the unburned samples of the phosphor material. Initial SEM/EDX measurements from bulk powder material are carried out with an acceleration voltage of 15 kV and an anode current of 750 pA (Zeiss, EVO MA10). However, the unknown penetration depths in the bulk material and possible shading effects only allow a semi-quantitative analysis of the chemical composition.

For further analysis of the chemical composition, the post-flame phosphor material is embedded in epoxy resin and cut into thin slices using an ultra-microtome (Leica EM UC). The thickness of the slices is between 100 and 200 nm, so the electron penetration depth is expected to be constant for any point in the cross-section of a particle. The chemical composition of the particle cross-sections is analyzed using an EDX detector (Bruker, XFlash 6I10 SDD) built in an Auger microscope (Ulvac-Phi, Phi 710 Nanoprobe).

4.3 Aerosol characterization: Heated jet

The optical characteristics of phosphor aerosols at elevated temperatures are analyzed in a heated jet. The objective is to measure the temperature-dependent luminescence properties of both phosphors studied in this work (SMP:Sn and YAG:Pr). These will form the basis to provide the ratio-temperature calibration curve for measurements in the BGFR (Chapter 7) and the engine (Chapter 8), as well as the luminescence lifetime characteristics of YAG:Pr, which will be used as an input for the reduction of combustion interference reduction in post-combustion measurements (Section 8.2). The phosphor luminescence is probed in direct proximity and using the same optical equipment as for measurements in the BGFR to ensure the reproducibility of the aerosol calibration to the measurements. Figure 38 shows the experimental layout, including the excitation system, aerosol heating, and particle dispersion system, as well as the optical diagnostics. The latter can be differentiated into two individual detection systems: (i) two-color detection system comprising two ICCDs and a high-resolution CMOS camera for particle counting, and (ii) the spectral detection system including a spectroscope and a PMT for luminescence lifetime measurement.

Excitation system: A double-cavity Nd:YAG laser (Thomson-SCF, PLV400, 10 Hz) is frequency-quadrupled to 266 nm and used to excite the phosphor particles. The laser crystal (second harmonic generator, SHG) is slightly detuned from pure emission of 266 nm to increase the 532 nm residual for Mie imaging. The UV laser fluence is continuously measured with a 5% reflection beam splitter and an energy monitor (LaVision: VZ09-0283) equipped with a 266 nm band-pass filter. Two lenses (f_1 = 1000 mm and f_2 = −200 mm) form the beam into a 400 µm-laser sheet (65 mm high), and the average fluence resulting is 50 mJ/cm^2 if not mentioned otherwise.

Aerosol dispersion: The phosphor particles are dispersed in a nitrogen gas flow with a seeding unit (Topas, SAG 410). In this device, the flow is directed through a venturi nozzle that creates a depression slightly below atmospheric pressure to release particles from a rotating ring. The phosphor material is deposited on the ring by a transportation belt. The belt feed rate can be adjusted independently from the rotation speed of the ring and thus controls the particle loading in the released aerosol. Such a concept is more flexible in controlling the feed rate compared to cyclones or magnetically agitated seeders.

A metal tube (d = 8 mm) transports the aerosol through a furnace (Carbolite, MTF 12/38/400) and redirects the flow with a 90° bend into the field of view of the diagnostics systems as a vertical open jet. The aerosol is further heated with a heating sleeve (Host GmbH, #21002) placed around the metal tube between the output of the furnace and the measurement volume. The aerosol temperature is measured with a thermocouple (0.5 mm, type K).

Measurement procedure: The aerosol is heated to a target temperature verified with a thermocouple placed in the jet. The thermocouple is mounted on a two-axis motorized translation stage (Thorlabs DDS100) to identify the hottest region in the flow and account for slight displacement of the metal tube due to the thermal expansion of the metal[11]. For positioning the optical elements relative to the desired measurement location, a red diode laser (633 nm) is coupled into the fiber optics at the spectrometer side to target the focal point of the PMT detection system to the tip of the thermocouple (TC), where the hottest temperature is measured. For two-color measurements, the position of the TC is imaged. Finally, the excitation laser (266 nm) is realigned to the position of the TC before each measurement.

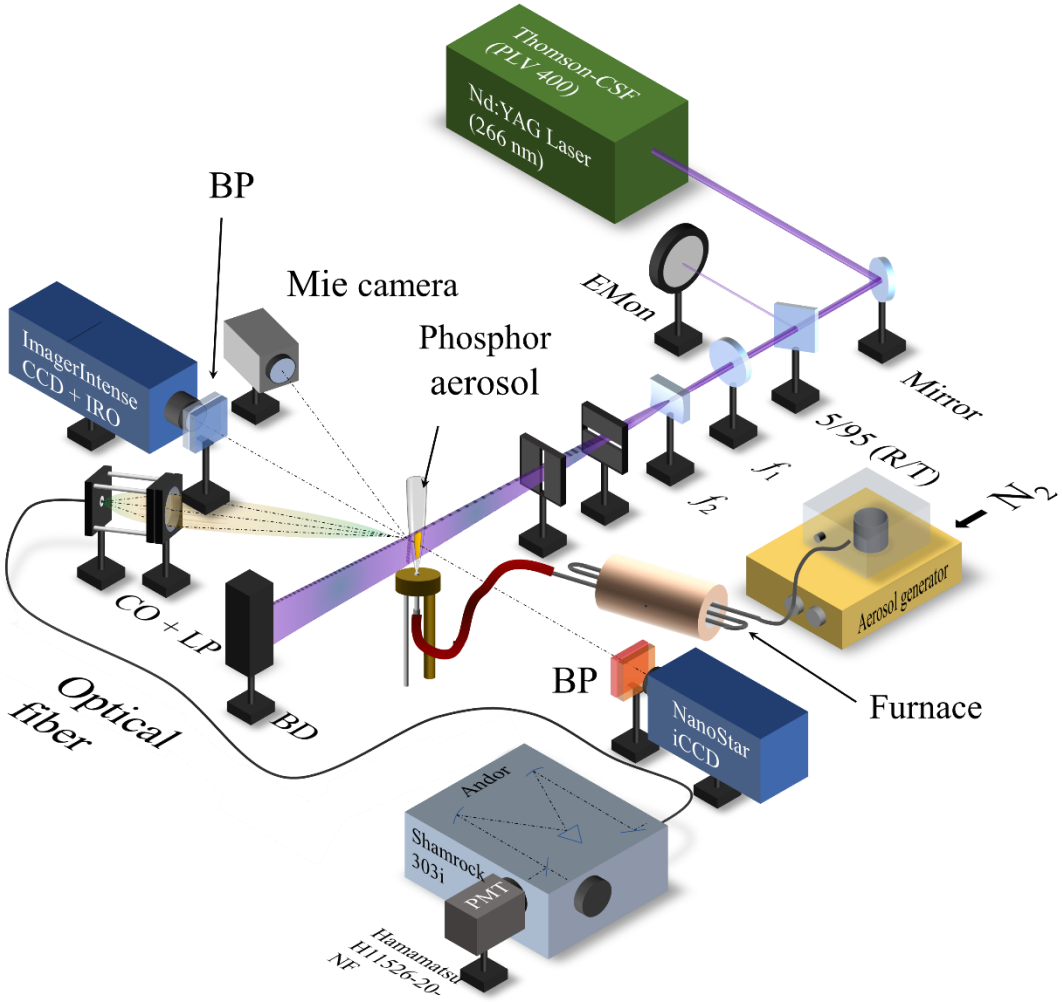

Figure 38: Experimental layout for dual-purpose aerosol characterization: (i) Two ICCDs for two-color detection of phosphor luminescence and a CMOS camera for particle imaging (elastic scattering) and counting, and (ii) spectral characterization including an optical fiber with collection optics and lowpass filter (CO + LP) and a PMT coupled to spectrometer. BD: Beam dump, BP: Bandpass, EMon: Energy monitor. Adapted from Ref. [94].

4.3.1 Two-color characterization

Two intensified CCD cameras are applied for ratiometric measurements. The first camera (LaVision, ImagerIntense, #VC08-0085) is coupled with intensified relay optics (IRO) and used with a Nikon Nikkor lens (f = 50 mm, f/1.8). The second camera (LaVision, NanoStar), equipped with an f = 50 mm, f/1.2 lens (Nikon, Nikkor), is mounted on a 12-mm distance ring. Both cameras are tilted by 15° relatively to the axis normal to the laser sheet to avoid the detection of reflections off the opposite cameras. A

[11] At increasing temperatures, this hottest spot is not in the center of the flow. This is due to non-symmetric mixing as the installation space of the metal outlet tube is very limited and thus the 90° bend is only approx. 15 mm below the tube outlet, preventing full development of the flow.

combination of Schott colored glass (BG39) and Edmund Optics 550 nm short-pass filter (EO550, #69-664) are used for the blue imaging channel, and a Schott colored glass (OG570) and 625 nm short-pass filter (EO625, #69-604) for the red channel for SMP:Sn. The optical density of both short-pass filters is OD ≥ 2 for the spectral regions outside the specified range. The filter combinations are similar for characterization measurements in the heated jet and the systems of interest. All filter combinations for both phosphors are shown in Table 4. Elastic scattering is collected with a high-resolution CMOS camera (Basler acA4600–10uc, 1.4 × 1.4 µm² pixel size, 4608 × 3288 pixels) with an f = 25 mm, f/1.4 lens (Basler, Computar). No transmission or bandpass filters are necessary as the contribution of elastic scattering is significantly stronger than the phosphor luminescence, and a CMOS camera is not susceptible to sensor damage from high exposure.

4.3.2 Phosphor luminescence lifetime and spectral characterization

For luminescence lifetime and spectral analysis, the phosphor luminescence is collected with fiber-coupled collection optics using two large achromatic doublets (f_1 = 100 mm and f_2 = 150 mm) to increase the signal yield and avoid chromatic aberration[12]. The collection optics were developed by Mansmann [119], combined with a 400 nm long-pass filter (Thorlabs, FELH0400), and coupled into a 200 µm-diameter fiber. The fiber directs the luminescence into a spectrometer (Andor Shamrock, SR-303i-B-SIL, 1 µm slit width), where it is spectrally dispersed using a 300 l/mm grating with a 4.3° blaze angle (Newport Spectra-Physics, #1294). The spectrometer features two outputs for a point-, as well as a line detector, which can be selected by flipping the output mirror in the spectrometer. The output of the point detector is equipped with an exit slit (set to 0.1 µm) to change the spectral resolution range to the nm-range and a gated photomultiplier (Hamamatsu H11526-20-NF) for the detection of the phosphor intensity decay curve. Gated operation is advantageous to decouple the emission decay curve from the scattered laser light, and the PMT exposure gate is delayed by 100 ns relative to the laser pulse.

Luminescence decay characterization: The luminescence decay measurements can be used to determine both the lifetimes at transitions selected by the monochromator. The photomultiplier delivers a signal to an oscilloscope (LeCroy Wavesurfer 104MXs-B) for signal conversion and acquisition via a 50 Ω coaxial cable. For measurements where fast time response is critical, as is the case for decay time measurements, the output pulse in the measurement can suffer from waveform distortion if impedance matching is not provided in the measurement equipment. This is due to the measurement principle and signal conversion and can induce a systematic error (see Section 2.5) if not handled correctly.

The PMT outputs a current in the lower nA regime, which is proportional to the incident photons during gated exposure, while signal processing circuits such as an oscilloscope are designed to handle voltage signals. In an ideal system, the internal resistance of the oscilloscope is purely resistive, enabling voltage detection over the simple correlation $U = I_{\mathrm{PMT}} \times R_{\mathrm{L}}$ with the known load resistance R_{L} and the PMT current I_{PMT}. However, in practice, stray capacitance and stray inductance are added, thus, especially at high-frequency operation, the system needs to be considered as compound impedance [120]. Therefore, the oscilloscope's input resistance is an important parameter, which can bias fast-response the lifetime measurements. A higher impedance increases sensitivity but imposes temporal lowpass characteristics. The input resistance is set to 100 Ω for lifetime measurements and 1 MΩ for spectral measurements. It is verified that the calculated lifetime does not change for 50 Ω and 100 Ω. Since the output voltage

[12] Achromatic doublets reduce the chromatic aberration, however they are only optimized for a given range of wavelength. The collection efficiency ϕ_{i} from the achromatic lenses from [119] are 1.0 and 0.98 in the ranges of 500 nm and 684 nm, respectively, showing only slight variation between to both ends of the wavelength ranges used.

becomes very low for resistances as low as 100 Ω and thus the relative noise contribution increases, 200 decay curves are hardware-accumulated in the oscilloscope before readout.

Spectral characterization: Phosphor emission spectra can be determined with the same arrangement when changing the spectrometer position in subsequent measurements. The emission intensity is then determined at each wavelength position from the temporally integrated signal. The position of the grating selects the wavelength, and the spectrometer is tuned through the wavelength range of interest (400–800 nm). A LabView routine was developed to automatize spectrometer control, data acquisition, and read-out from the oscilloscope. The spectral calibration is done with a Hg-Ar lamp, and the intensity calibration is done with an Ulbricht sphere. This approach will be presented and discussed in Section 3.1.

In a master thesis supervised within this work [94], it was attempted to use a CMOS line camera (Coptronix, 8M–S11637, 12.5 × 500 μm^2, 1024 pixels) on the line detector output of the spectrometer to simplify spectral measurements. However, signal intensities at high temperatures were too low to be detected with non-intensified detection equipment.

4.4 Burnt-gas flow reactor

The burnt-gas flow reactor is designed as a co-flow burner consisting of a central, inert nitrogen flow (d = 6 mm) that can be seeded with precursor species leading to soot formation and a surrounding rich premixed ethylene/air flame (d_{ext} = 63 mm). The flame and the surrounding hot post-combustion gases heat the seeded central nitrogen flow. A cooled bronze sinter matrix ensures the mixing of the combustion educts (Figure 39). The flame is stabilized with a metal cone (d_{upper} = 50 mm, h = 45 mm, not shown in the figure). The burner is described in work by Peukert et al. [121]. The flow rate of the center flow is varied between 1.96 and 4.96 slm (standard liters per minute), resulting in exit velocities of 115–292 cm/s (Reynolds number between Re = 453 and 1147). The outer flow consists of 56 slm air and 7 slm ethylene, which results in a rich flame with the fuel/air equivalence ratio of ϕ = 1.41.

The optical diagnostics setup is similar to that used for aerosol characterization (Figure 38), only that the heated jet is replaced with the BGFR. This ensures excellent applicability of the calibration measurements to the measurements in this environment. The two-color and particle counting detection system are detailed in Section 4.3.1. The camera detecting elastic scattering is equipped with an IR absorption filter (Schott color glass KG2) to protect the camera from excess heat due to the proximity to the hot flow. The burner can be vertically displaced with a motorized stage relative to the diagnostic systems to enable measurements over different heights above the burner (HAB).

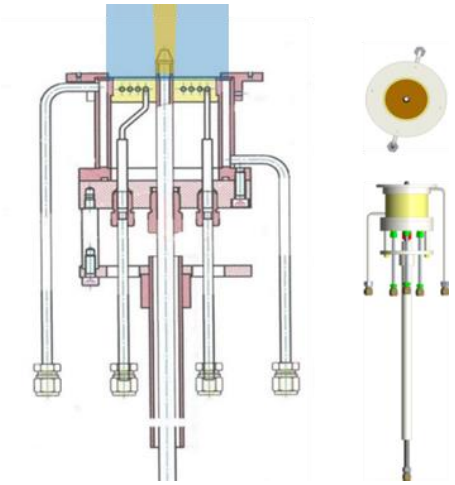

Figure 39: Cross-section (left) with a top and front view (right) of the burnt-gas flow reactor. The flame is indicated in blue, which surrounds an inert nitrogen flow (yellow).

4.4.1 Application of the fluorescence tracer

The tube system of the burner is adapted to support the delivery of soot precursors, thermographic phosphor (SMP:Sn) as well as molecular fluorescence tracers (here: toluene). Measuring temperature in this zone of the BGFR is of interest for analyzing soot formation from the precursor. The alternative use of thermographic phosphors and toluene-LIF provides an additional option to compare both approaches for temperature measurements. The particle seeding system is similar to the system used for aerosol characterization (Section 4.3). For toluene-LIF temperature measurements, the particle disperser is removed, and a bubbler is installed to vaporize toluene. The bubbler is supplied with a constant flow of nitrogen (1.96 slm), and the flow is mixed downstream with additional nitrogen if necessary for operation points of higher flow rates to ensure a constant amount of fluorescence tracer for all measurements.

4.4.2 Pneumatic particle recovery system

In Section 4.1, the particle survivability study in the lean premixed burner was presented to evaluate to effect of exposure to high temperatures. Now, the particle survivability is to be investigated in the environment of a rich flame in this burner. For this purpose, phosphor particles are extracted by thermophoresis from the central, inert flow using a pneumatically operated soot sampling device [122]. The sampling height is designed such that the central flow is approximately at the same temperature as the maximum temperature in the premix flame from Section 4.1. A TEM grid (transmission electron microscope) is fixed on the device and exposed to the flame for less than 1 ms to deposit particles by thermophoresis such that no modification in the flow condition is expected. The short exposure time is achieved by double-acting pneumatic actuation with the TEM grid attached to a spring-loaded mass that is pneumatically accelerated and retracted. The mass can be changed to adjust the spring deflection and thus the sampling grid's travel. The positioning is done with the help of high-speed cameras, such that the turning point of the travel is precisely in the middle of the inert flow. The sampling device is explained in Ref. [122] with more details.

4.4.3 Thermocouple measurements

For temperature reference measurements in the heated aerosol, thermocouple (TC) measurements are performed. This is particularly challenging since in the BGFR, the central gas stream to be measured is surrounded by a ~2000 K hot flame, imposing additional restrictions. The material should not only have high melting temperatures but also not exhibit catalytic interaction in reacting flow conditions. Furthermore, the diameter of the junction and that of the suspension, should be particularly thin to prevent temperature bias from conductive heat losses. In addition, the measurement must be carried out very slowly to ensure that the thermocouple is always in thermal equilibrium with its environment (see systematic errors, see Section 2.5).

For this purpose, an in-house built type R thermocouple with an inert SiO_2 protective layer applied through a CVD process is used. The junction diameter is 270 µm, and the arm length of the suspension is 10 mm. The thermocouple is mounted on two motorized linear translation stages (Thorlabs MTS50-Z) to enable controlled displacement in *xy*-direction. The translation stages are driven by a K-Cube servo motor controller (Thorlabs KDC101) and actuated by a customized LabView routine with a maximum translation speed of 0.025 mm/s. Despite the hardware specifications being beneficial to minimize heat conduction, a correction procedure for radiative heat losses is necessary for such measurements. The procedure is similar to that one in Ref. [123] with emissivity values for fused quartz (coated SiO_2).

4.5 Optically accessible internal combustion engine

One of the main objectives of this thesis is the application of simultaneous temperature and velocity measurements in the post-combustion gases of an optically accessible engine using thermographic

phosphor particles as tracers. This section presents the engine hardware, optical diagnostics, and engine timing, along with the operating conditions and improvements from previous work [25].

4.5.1 Hardware and engine characteristics

A single-cylinder, four-valve double overhead camshaft (DOHC) optically accessible research engine is used with a fused silica (corning 7980) fully transparent cylinder for motored operation and a ring (20 mm height) for fired operation. The displacement volume of the engine is 399.5 cm^3 with a bore and stroke of 82.7 and 86 mm, respectively, and a geometric compression ratio $\varepsilon = 10.3$. The engine is equipped with a flat piston crown in a Bowditch layout [124] and a pent-roof cylinder head. The direct injection spark-ignition (DISI) engine is designed and manufactured by IFPEN [125] and features a five-hole centrally mounted injector (Bosch HDEV 5.2). The engine layout and operation are similar to the work in Ref. [25], and further engine parameters are shown in Table 3. The pressure in the cylinder, as well as in the intake and exhaust manifold, is measured through piezoelectric pressure sensors (AVL QC34D), resolving the measured value respectively every 1/10 °CA (72 kHz at 1200 RPM). The temperature of the intake manifold is monitored with a thermocouple (type K, 1 mm tip diameter).

Table 3: Engine parameters.

Description	Value
Displacement	399.5 cm^3
Speed	1200 RPM
Geometric CR	10.3
Bore	82.7 mm
Stroke	86 mm
Connecting rod lengths	155
Intake valve open (IVO)	9 °CA aTDC (10% of full travel)
Intake valve close (IVC)	213 °CA aTDC (10% of full travel)
Exhaust valve open (EVO)	508 °CA aTDC (10% of full travel)
Exhaust valve close (EVC)	712 °CA aTDC (10% of full travel)
Intake temperature (at BDC)	304–379 K
Intake pressure (at BDC)	1 bar (SMP:Sn); 0.65 bar (YAG:Pr)
Tumble ratio[13]	1.25
Injection pressure	200 bar
Start of injection	160 °CA
Injection duration	1540 µs (≈11.5 °CA)
Ignition	335 °CA
Fuel	iso-octane
IMEP	3.9 ± 0.57 bar

4.5.2 Optical setup for simultaneous temperature and velocity imaging (T-PIV)

A quadrupled Nd:YAG laser (266 nm, SpectraPhysics, Quanta-Ray GCR170, 50 mJ/cm^2) excites the phosphors particles. The laser beam passes through a Pellin-Broca prism to remove other harmonics by refracting the residuals at slightly different angles. A fully automatized $\lambda/2$ plate was used with a polarizing beam splitter to adapt the laser fluence, measured through a 5-% reflecting wedged beam splitter (Thorlabs BSG2550) and an energy monitor (LaVision). The beam is formed into a laser sheet (95×0.2 mm^2 for measurements (with SMP:Sn) with the full cylinder and 18×0.9 mm^2 with the ring) using a combination of a cylindrical lens ($f_{1,\,UV} = -500$ mm) and a spherical lens ($f_{2,\,UV} = 1000$ mm). The thickness of the laser sheet is measured with a microscope from one individual laser shot on photo-

[13] The flow characterization of the cylinder head and calculation of the tumble ratio is similar to the methodology explained in Ref [25] and in appendix A. 1:

sensitive paper. This sheet geometry is used for measurements with SMP:Sn only and shows the feasibility of high spatial resolution measurements, possible due to the phosphor's high luminescence emission.

A second laser (SpectraPhysics, PIV400, 10 mJ/pulse) illuminates the particles at 532 nm with a double-pulse laser sheet of the same dimensions as the other sheet ($f_{1,\,vis} = -100$ mm, $f_{1,\,vis} = 1000$ mm) in motored operation. Both beams are overlayed with a beam combiner to penetrate vertically into the center of the optical cylinder. Both lasers are operated at 10 Hz and synchronized with the engine through a crank-angle encoder.

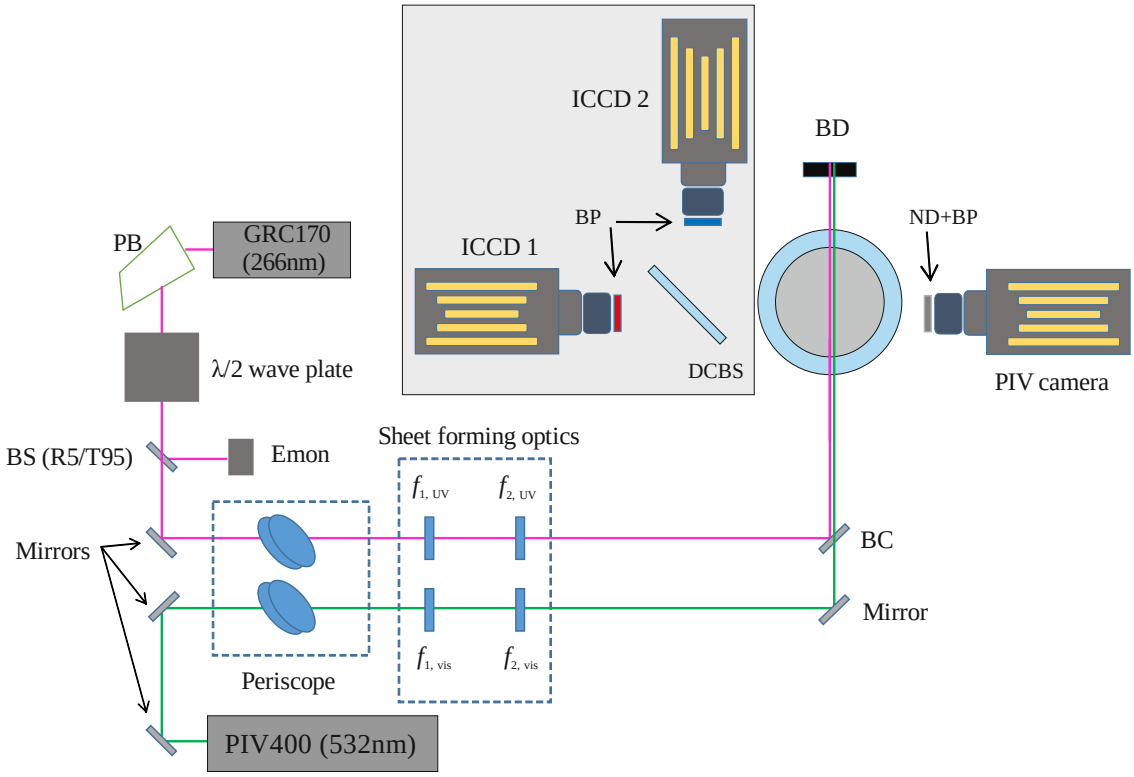

Figure 40: Optical layout for combined temperature and velocity measurements. PB: Pellin-Broca prism; BS: Beam splitter; Emon: Energy monitor; BC: Beam combiner; BD: Beam dump; ND: Neutral density filter; BP: Bandpass filter; DCBS: Dichroic beamsplitter.

The signals were detected at right angles through the transparent cylinder wall (Figure 40). Elastic scattering for PIV is detected through neutral density (ND) filters and a 532-nm bandpass filter (Andover Corp, FWHM 2 nm centered at 532 nm) with a Photron SA1 high-repetition-rate camera with a f = 50 mm, f/1.2 lens (Nikon). The ND filter was slightly tilted to minimize reflections on the cameras on the opposite side of the engine. Two intensified CDD cameras from the opposite side collected the phosphor luminescence signal, separated by a dichroic beam splitter (DCBS). The cameras are PIMax2 and PIMax3 for the red and blue imaging channel, respectively, of the same design (Princeton instruments, 16 bit, 1024 × 1024 pixels, 12.8 ×12.8 µm^2 pixel size, gen2 intensifier). Both cameras have a f = 50 mm, f/1.2 lens (Nikon). All dichroic mirrors and filters used for the different phosphors are similar to those from the aerosol characterization measurements and are summarized in Table 4.

Table 4: Mirrors and filters used for T-PIV measurements in the engine. LP longpass, SP shortpass.

	Red channel	**Blue channel**	**Dichroic beam splitter**
SMP:Sn	OG570 LP + EO625 SP	BG39 LP + EO550 SP	Thorlabs DMLP567
YAG:Pr	OG570 LP + EO625 SP	Semrock FF01-494/20	Semrock FF580-FDi01

The entire detection system for phosphor thermometry mounted on a separate optical table was height-adjustable to optimize the field of view and minimize vignetting effects at higher crank angles when the piston partially blocked the field of view. The measurements were carried out with the cameras set to two heights: An elevated camera position is optimized for 300–420 CAD, and a low position for all other measurements. In the course of this work, both positions will be referred to as the lower position ("P0") and the upper position ("P1"), as shown in Figure 41.

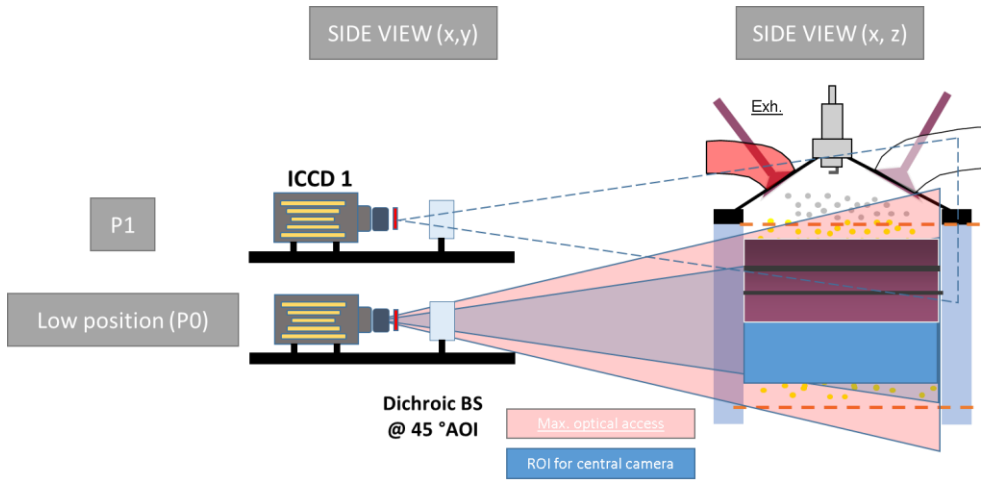

Figure 41: The cross-section of the optically accessible engine is shown on the right. The orange dashed line indicates the heights of the laser sheet. The left shows the qualitative arrangement of the height-adjustable plate with the cameras and the beam splitter (at 45 °AOI). The field of view from the camera in a standard position ("P0") is used to maximize the field of view for normal operation. The increased camera position ("P1") is used when the piston at elevated piston positions blocks the field of view. The optical axis is approximately aligned with the fire deck to enable optical access as much as possible. The drawing is not to scale. BS: beam splitter; AOI: angle of incidence.

4.5.3 Engine operation

The timing diagram is shown in Figure 42, which is adapted from the timing diagram used in previous work [25]. The master TTL signal (transistor-transistor logic) is sent from the in-house built engine control software SynAll, which is synchronized with the engine crank angle encoder at the desired °CA. The first delay generator triggers the lamp and Q-switch of the PIV laser with a delay time of 30 µs between both pulses. The PIV camera receives an initial TTL signal, and the double exposure of 100 µs each is given by the repetition rate of the high-speed camera (10 kHz). The long exposure is chosen to be robust against the jitter of the laser pulse.

The second delay generator controls the phosphor luminescence excitation and detection system. The interline camera used for the red detection channel is operated in double-imaging mode for measurements in the post-combustion gases. Both subsequently measured frames always have the same exposure duration. The exposure of the second frame starts with the exposure of the blue imaging channel and is delayed by 200 ns relative to the laser pulse. The exposure duration for both channels for measurements with YAG:Pr is adapted to the threefold of the lifetime at the expected temperature (3τ).

In motored operation, measurements were carried out at two different intake temperature conditions ($T_{\text{in, reference}}$ = 323 K and T_{in} = 379 K). The intake temperature can be varied by conditioning the engine coolant temperature and is additionally increased by heating the intake manifold with a heating tape at 165 °C. The tumble ratio is similar for both test cases (TR = 1.25) and is similar to the increased tumble test case in [25]. The intake pressure is p_{in} = 1 bar for measurements with SMP:Sn, leading to a peak temperature of 750 K at TDC as inferred from the cylinder pressure (see Section 3.4) for the increased intake temperature condition.

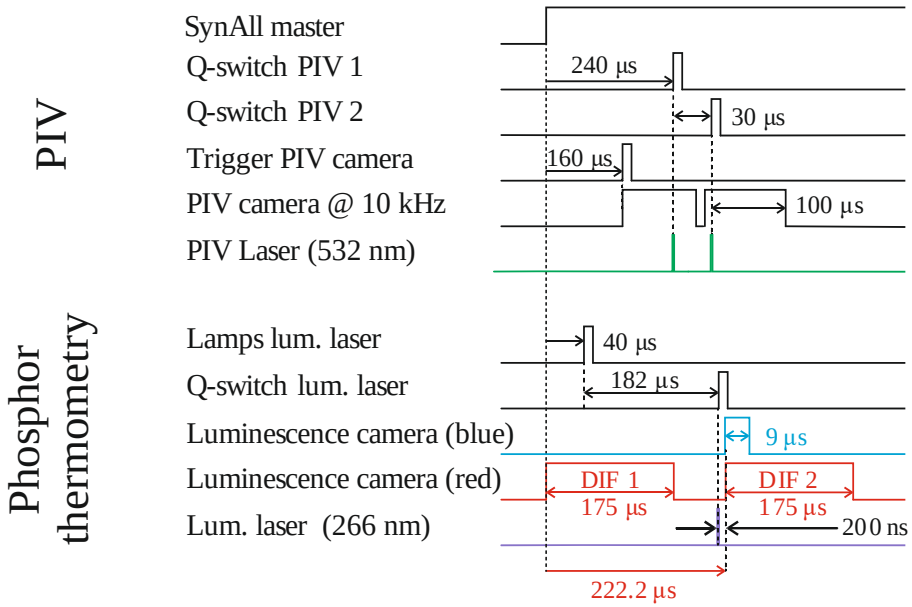

Figure 42: Timing diagram for simultaneous temperature and velocity measurements, where the red camera of the two-color phosphor luminescence is operated in double-imaging mode. The SynAll master signal from the engine acquisition software is given by the crank angle encoder at the desired imaging crank angle degree. The drawing is not to scale.

For post-combustion measurements with YAG:Pr, the intake temperature is 303 K, and the intake pressure is lowered to p_{in} = 0.65 bar to reduce the peak pressure and the temperatures of the exhaust gases. The lower intake pressure is maintained for motored operation with YAG:Pr, leading to peak temperatures of ~550 K at TDC.

4.5.4 Engine adaptations and setup improvements

The general experimental layout and measurement procedure are similar to those presented in similar work [25,126]. For the measurements in this work, the following improvements are implemented:

Implementation of a low-inertia thermocouple: A fast-response thermocouple (type K) is inserted into the engine via the exhaust valve. The junction diameter is 25 µm, and the sampling frequency is 25 kHz. The thermocouple signal is recorded and translated to a temperature value with the calibration on a heated plate (300–650 K). The correlation is linear and extrapolated to the temperature range in the motored operation of the engine (up to 800 K).

Seeding system: In the previous experiments, the plastic tube redirecting the phosphor aerosol from the seeder was introduced upstream of the engine intake manifold, which resulted in phosphor deposits in the entire intake manifold. As a consequence, residual phosphor particles from the intake manifold always leaked into the engine, even seeding was deactivated. To avoid this problem, the tubing system was adapted and rerouted directly above the intake valves. Due to the operation mode of the seeder (venturi nozzle), the seeding system always operates at ambient pressure, e.g., at 0.65 bar for measurements with YAG:Pr. If operated below ambient pressure, this can lead to phosphor particles being sucked into the engine. To prevent this, the seeding system was upgraded with a spring-loaded one-way valve and a 3/2 normally-closed (NC) solenoid valve for remotely controlled seeding activation.

Timing: Due to the design of the SynAll control software, the delays in the trigger chain between the initial master signal at the desired °CA and the laser emission (and start of the phosphorescence camera exposure) add up to 423 µs, which is equivalent to 3.06 °CA. Due to this artifact, the actual measurement occurs ~3 °CA later than desired, irrespective of the piston position. Consequently, the difference in the piston position is >6 °CA between the mirrored position in the compression and expansion stroke, e.g.,

300 and 420 °CA. This was not accounted for in previous experiments [126] and is controlled by introducing a negative delay of the crank angle encoder and the master TTL signal for the measurements presented in this work.

5 Phosphor particle survivability in flames

Temperature measurements using thermographic phosphors in reacting flows suffer from low signal intensities at high temperatures due to thermal quenching. This makes temperature measurements very challenging or impossible if the phosphor luminescence is strongly quenched such that the remaining signal approaches the noise level of the detector. Additional signal loss can occur when the phosphor material deteriorates, e.g., by passing through a flame zone. As there is interest in measuring temperature in post-combustion gases, where the flow has cooled down again to a measurable temperature range (e.g., in the expansion stroke of the engine or downstream of a premix burner upon mixing with surrounding air), the survivability of the phosphor in the flame becomes an important issue. If the phosphor does not disintegrate in the reaction zone (e.g., from oxidation or change of the crystal structure upon particle melting), the phosphor luminescence should be recovered as the temperature decreases again. In a previous study, post-combustion temperature measurements in the expansion stroke of an optical IC engine were attempted using ZnO:Zn, where temperatures around 700 K were expected from simulations. In that particular experiment, the signal-to-noise ratio (SNR) approached unity at around 600 K during compression because of the strong temperature-induced signal decrease [25]. Therefore, it was inconclusive if temperature measurements above this temperature were not possible in the post-combustion gases due to thermal quenching or particle disintegration during combustion.

So far, no systematic investigation is available if thermographic phosphors of practical interest can withstand combustion and if they maintain their temperature-dependent luminescence properties (referred to as particle survivability) in the cooler post-combustion regime. In this section, the two phosphors YAG:Pr and SMP:Sn are evaluated for temperature measurements in the post-combustion gases of a premix burner with a two-color detection system and a particle recovery system introduced in Section 4.1. The premix burner is operated in lean conditions to reproduce conditions found in internal combustion engines.

The content of this chapter follows mainly results that were presented in a conference talk at the 2nd International Conference on Phosphor Thermometry (July 27–29th, 2020) and were subsequently published in Ref. [68] in a Special Edition of Measurement Science and Technology [127] with me as a first author. Figures in this chapter are altered and reproduced from this publication with permission from IOP Publishing, and some text is analogously adapted from the publication. This publication would not have been possible without the support of the co-authors. Eric Kohler performed the microscopic particle analysis (SEM/EDX) and XRD measurements and interpretation. Michele Bardi strongly contributed to conceptualizing the experiments and data post-processing, most notably during the revision process. The publication was initiated and conceptualized by me, and I was responsible for data acquisition, data analysis, and investigation, as well as writing and visualization. All authors read, commented, and approved the final manuscript.

5.1 Premixed burner

5.1.1 Validation as a temperature-varying environment

To investigate particle survivability, the thermal load on the particles in a burner can be emulated by varying the equivalence ratio of the flame. The adiabatic flame temperature of the propane/air premix flame is between 1650 and 2350 K for equivalence ratios ϕ = 0.62–1.0 [115]. At increasing height above the reaction zone of the premix burner, the flow cools down due to turbulent flow mixing with the surrounding cold air. The height above burner (HAB) of the two-color detection system is increased until the flow temperature decreases to a measurable range. The temperatures are monitored with six thermocouples (type K, tip diameter 1.0 mm) in the flow. A chimney stabilizes the flow, nevertheless, the exhaust gases are subject to strong turbulent fluctuations at the measurement location (HAB > 14 *d*). The fluctuations of the flow also resulted in the fluctuations of the thermocouple reading, so it was necessary to validate if a change in the fuel/air equivalence ratio also results in a measurable temperature change at increased HABs. The thermocouple measurements are averaged from approx. 5 s.

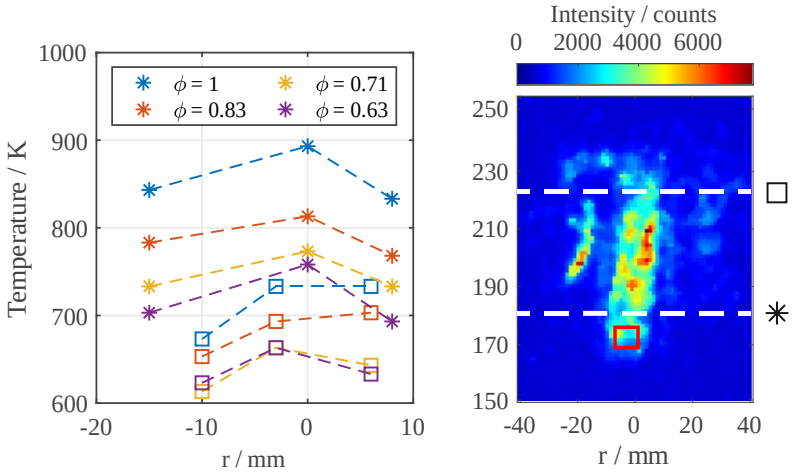

Figure 43: Left: Thermocouple measurements for various equivalence ratios at two HABs 180 (∗) and 225 mm (□) shown with different symbols. Right: The position of the thermocouples on a 2D single-shot luminescence image as a reference.

Figure 43 shows thermocouple measurements at two different HABs for various equivalence ratios. These measurements are not corrected for radiative losses, thus, they likely underestimate the gas temperature at lower HABs and higher equivalence ratios. Despite these uncertainties, the measurements qualitatively follow the trends expected, decreasing temperatures at (i) increasing HABs and (ii) decreasing equivalence ratios. Therefore, this environment can be used for survivability tests and post-flame temperature measurements using thermographic phosphors.

5.1.2 Thermographic post-flame measurements

Temperature measurements employ the two-color approach with YAG:Pr as the thermographic phosphor. With increasing temperature, the phosphor emission is thermally quenched; thus, the SNR must be evaluated in the hottest region for reliable temperature measurements. Figure 44 shows single-shot images from both imaging channels in the exhaust gas of the premix burner at ϕ = 1.0, and the SNR of both imaging channels is calculated from the two regions highlighted in Figure 44.

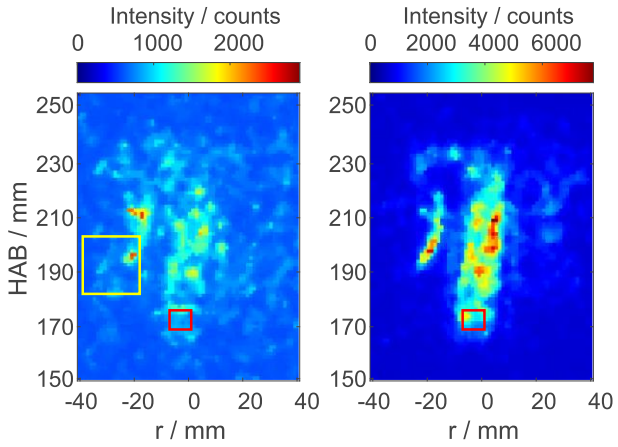

Figure 44: YAG:Pr single-shot phosphor luminescence images of the blue (left) and red (right) channels in the exhaust gas at ϕ = 1.0. The red and yellow boxes highlight the regions used for SNR calculation. The intensity scale in each image was adjusted for improved visibility. Reproduced from Ref. [68] with permission from IOP Publishing.

The SNR is evaluated based on the 90th and the 10th percentile of the signal intensities from the respective regions of interest. The signal was calculated in the hottest region in the center of the gas flow (red box), and the noise was estimated from a region outside the flow (yellow box). The lower threshold for SNR calculation was chosen to avoid a bias from turbulent fluctuations outside of the center flow. The SNR of YAG:Pr for various fuel/air ratios is shown in Figure 45. Even if the blue imaging channel (Ch1) suffers from thermal quenching at increasing temperatures, the SNR is still acceptable for temperature measurements at stoichiometric conditions.

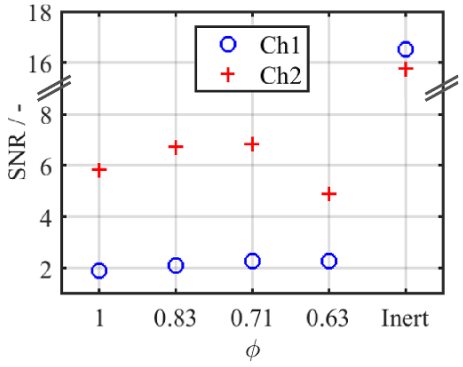

Figure 45: Signal-to-noise ratio for both imaging channels for inert conditions and various fuel/air equivalence ratios. Reproduced from Ref. [68] with permission from IOP Publishing.

The image correction and post-processing procedure for temperature calculation are detailed in Section 3.3. A large dataset of 1000 images is evaluated to reach homogeneous signal distributions despite variations in particle seeding and flame fluctuations. A reference measurement at ambient temperature (T = 299 K) is used to link the signal ratio measurements from the reacting flow conditions to the calibration curve [24,71]. Figure 46 shows the average temperature fields from two different equivalence ratios ϕ = 0.83 (left) and 0.63 (right). The measured temperatures decrease at increasing distances from the center of the flow, where mixing is less pronounced. The temperature profile is not symmetric due to the ventilation of the exhaust system.

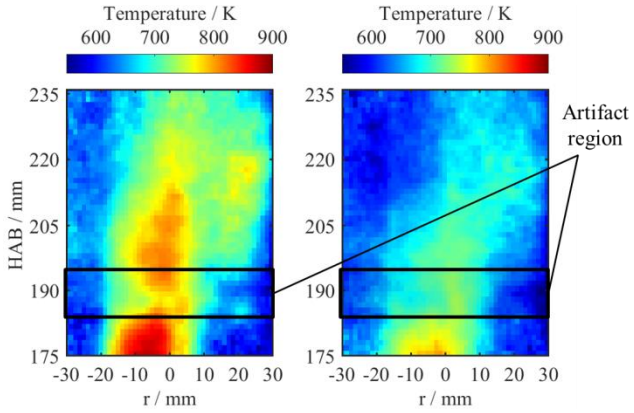

Figure 46: Average temperature field of the exhaust gas for ϕ = 0.83 (left) and ϕ = 0.63 (right) from two-color luminescence measurements using YAG:Pr. Temperature is measured with thermocouples at 180 and 230 mm HAB. Reproduced from Ref. [68] with permission from IOP Publishing.

Figure 47 shows the vertical temperature profiles extracted from the two-color luminescence images at various fuel/air equivalence ratios. Measurements from the center thermocouple from Figure 44 at 180 and 225 mm HAB are also shown as references. The region affected by reflections from a metal surface of the burner chimney (marked as an artifact region in Figure 46) was neglected in the evaluation.

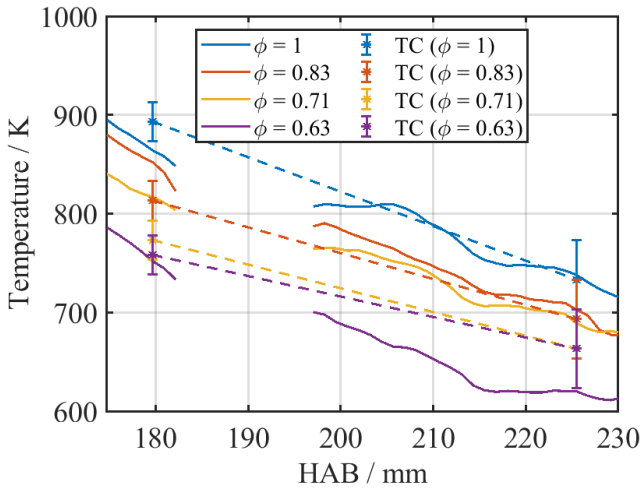

Figure 47: Temperature profiles from thermographic phosphor measurements above the burner along the vertical direction (solid lines) for various fuel/air equivalence ratios for YAG:Pr derived from the two-color luminescence measurements. TC: thermocouple measurements with error bars. Reproduced from Ref. [68] with permission from IOP Publishing.

The gas temperature decreases with increasing distance from the burner and with decreasing fuel/air equivalence ratio as the adiabatic flame temperature decreases, both trends which are expected and confirmed from thermocouple measurements. Despite the uncertainties of these measurements, the seeding system, and variations from flame fluctuations, these measurements clearly show that YAG:Pr maintains its temperature-dependent luminescence properties upon passing through the flame of a premix burner.

Temperature measurements were also attempted with SMP:Sn. While the phosphor has strong luminescence emissions under inert conditions, no laser-induced luminescence was detectable in the post-combustion gases within the stability limits of the flame (ϕ = 0.58–1.25). Measurements were also not possible at increased HAB, where the temperature is lower, even if temperature measurements were successful on a coated surface at temperatures up to 873 K [128], indicating that the phosphor loses its temperature-dependent luminescence properties on the path through the flame.

5.2 Particle analysis

The luminescence properties of thermographic phosphors strongly depend on the crystal structure of the host lattice, as introduced in Section 2.1.5. Changes in the chemical composition of the material, e.g., from oxidation, can also lead to the loss of its luminescence [129]. In order to investigate structural or chemical changes from post-flame material, the phosphor particles are recaptured from the exhaust gases (ϕ = 0.71), as shown in the schematics in Figure 31. The particles from both phosphors are analyzed using microscopic imaging techniques (SEM/EDX) and x-ray diffraction (XRD) measurements and compared to the initial material. The results for both phosphors are presented in the next subsections and then discussed together in Section 7.2.3.

5.2.1 YAG:Pr

Figure 48 shows the SEM image from initial and post-flame YAG:Pr phosphor particles. The initial phosphor material shows agglomerates of mostly sharp-edged particles. Apart from a few isolated spherical particles (highlighted with a red circle), YAG:Pr post-flame material does not show any morphological alteration relative to the initial material. Results from EDX measurements do not show a statistically significant modification of the post-flame YAG:Pr from the initial material in the chemical composition of the yttrium garnet host material ($Y_3Al_5O_{12}$). The praseodymium concentration is too low to be measured.

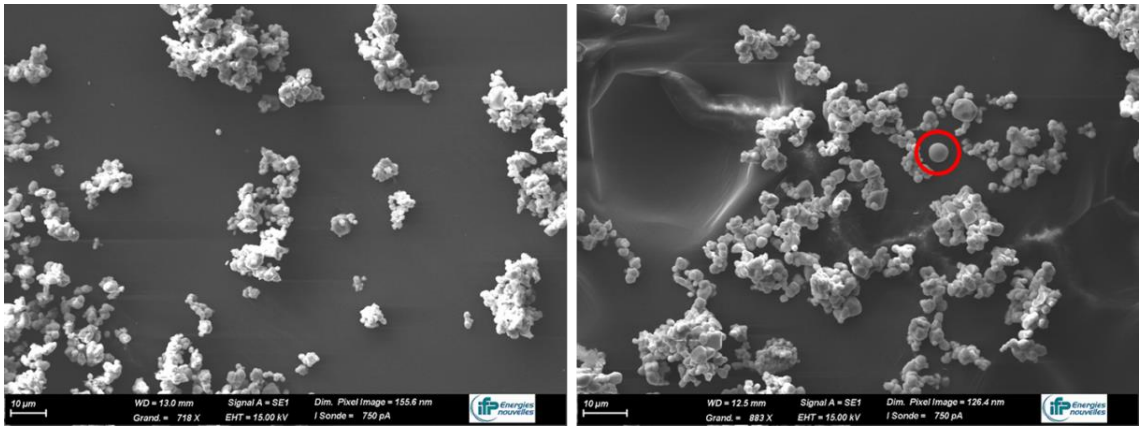

Figure 48: SEM image of initial (left) and post-flame (right) YAG:Pr phosphor particles. A spherical particle is highlighted with a circle in the post-flame material. Reproduced from Ref. [80] with permission from IOP Publishing.

Figure 49 shows the diffraction pattern of the YAG:Pr phosphor. The post-flame material does not vary from the initial material and is in excellent agreement with the YAG:Pr diffraction pattern (COD #1529037 [130]) from the crystallographic open database [131]. The pattern was calculated with crystallographic information using the emission characteristics of the copper anode (Cu, 1.5406 Å), similar to the one used for the XRD measurements.

These measurements confirm that both the morphology and crystal structure of the YAG:Pr phosphor material remains unaffected by passing through the reaction zone of a lean premixed propane/air flame (ϕ = 0.71), where the adiabatic flame temperature is approximately 1900 K.

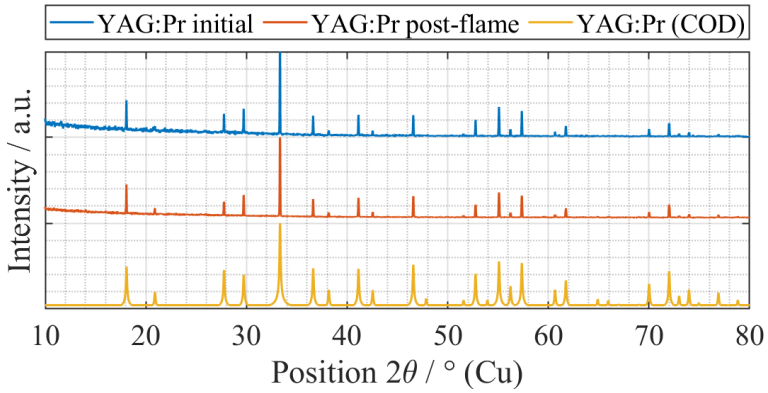

Figure 49: Diffraction pattern from initial and post-flame YAG:Pr phosphor material with its COD reference pattern from [130]. Intensities are normalized towards the intensity of the highest peak. Reproduced from Ref. [68] with permission from IOP Publishing.

5.2.2 SMP:Sn

Figure 50 shows the SEM images from the SMP:Sn phosphor material. The initial powder also forms small agglomerates similar to YAG:Pr, whereas the morphology of the post-flame material is altered towards spheres. This morphological modification indicates transformation to the liquid state during the residence time at high temperatures.

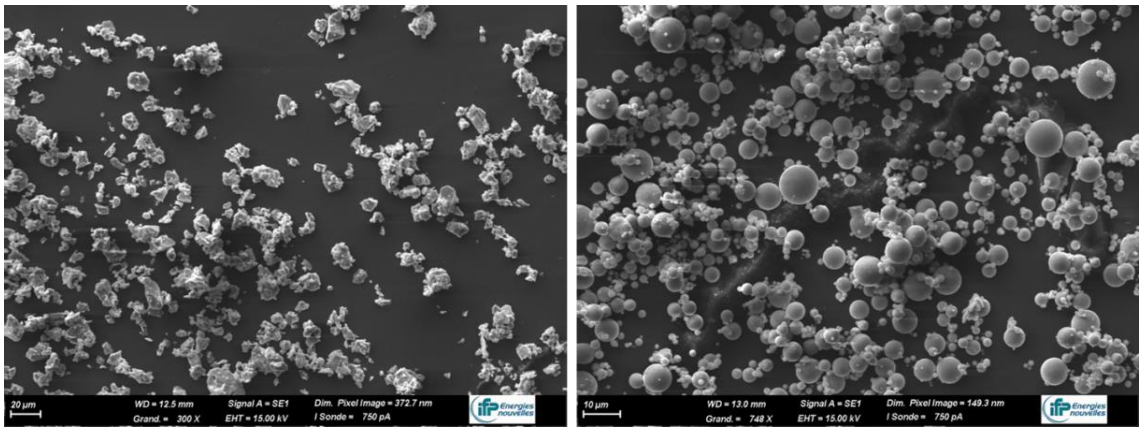

Figure 50: SEM image of initial (left) and post-flame (right) SMP:Sn particles. Reproduced from Ref. [68] with permission from IOP Publishing.

The chemical composition from EDX measurements in the initial material is $Sr_{2.62}Mg_{0.38}(PO_4)_2:Sn^{2+}$, which is equivalent to 12.5 mol% $Mg_3(PO_4)_2$ of the mixed (Sr,Mg)-phosphate. The post-flame material is slightly enriched in the relative strontium content $Sr_{2.66}Mg_{0.34}(PO_4)_2:Sn^{2+}$ (11.3 mol% $Mg_3(PO_4)_2$). EDX measurements provide semi-quantitative results only, and thus small changes should be interpreted with care. However, the phase diagram of this phosphor (cf. Figure 7) shows that a small change in the chemical composition can be accompanied by a change in the crystal structure that can lead to a total loss of the materials' luminescence properties. Therefore, it is likely that the loss of the luminescence properties is related to phase change following particle melting and solidification. The return to the solid state after melting does not seem to be accompanied by a general phase demixing since the change in chemical composition is low compared to the initial state.

EDX measurements from bulk material only give an average chemical composition from near-surface regions, where the sample volume is penetrated by the incident electron beam. As the penetration depth of the measurement is not known, EDX measurements from bulk powder material only give quantitative results. To confirm the local change of the materials' composition, the EDX analysis is extended to the

particle cross-section, where the phosphor particles are embedded into a resin, cut into thin slices using an ultra-microtome (Leica EM UC), and polished for EDX analysis. The thickness of the slices is between 100 and 200 nm.

Figure 51 shows the cross-section from a polished sample containing three phosphor particles (1–3). The first subfigure (a) shows the secondary electron (SE) image of the cross-section, representing the topographic map of the particles. A perfectly flat surface would theoretically result in a homogeneous gray image, so any structure visible in the SE image is attributed to a locally varying surface topography that is either preparation artifacts or indicate different material properties. For example, the parallel marks in the resin at ~30° clockwise relative to the vertical image axis are preparation artifacts in the cutting direction of the microtome blade. It is also possible that the surface irregularities cause EDX analysis artifacts specific to each chemical species. The gradient inside the particle (3) is due to shading effects, as confirmed by a series of rotated images.

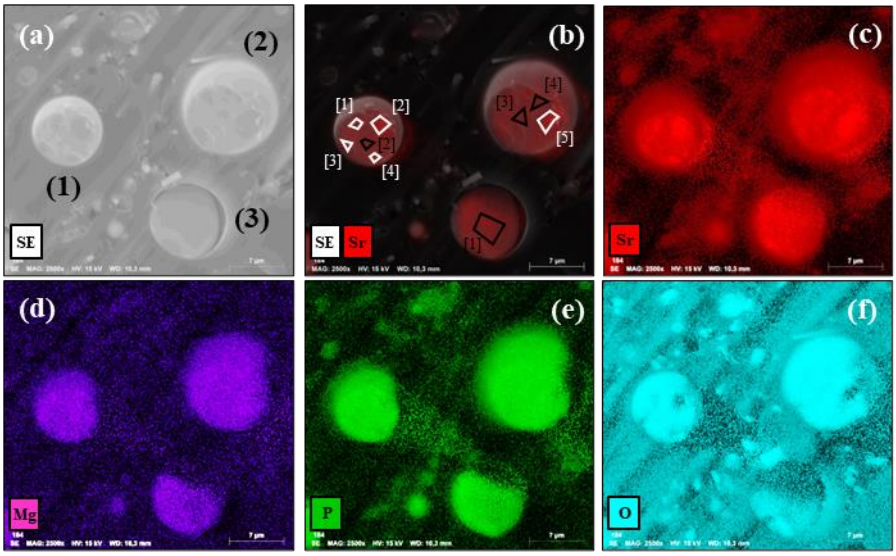

Figure 51: SE (a), SE + EDX for Sr (b) and EDX (c)–(f) images from a polished surface as a function of the respective chemical species (Sr, Mg, P, O). The highlighted regions in (b) are regions of high Sr content (white) and regular Sr content (black). Note that the EDX images (c)–(f) are not overlaid with SE images. The normalized Sr wt% are shown in Table 2. Adapted from Ref. [68] with permission from IOP Publishing.

The surface inhomogeneities on the particles, annotated as (1) and (2), likely stem from locally varying materials properties, indicating changed crystal phase properties. Figure 51c–f show the relative distribution of the chemical species of SMP:Sn. Particles (1) and (2) show a mostly homogeneous distribution of both the phosphate (P, O) as well as Mg, whereas there are spots with relatively increased Sr concentration. Figure 51b shows an overlaid SE/EDX image, where regions of varying material properties are highlighted. These regions with increased Sr concentration, numbered in white in Figure 51b, show a mean Sr content of 52.8 wt%. Regions of reference, where the Sr content is not visibly increased, numbered in black, have an average Sr content of 43.5 wt%. The averaged content of Sr of the entire particle (annotated as (1)−(3) in Figure 51a) are 46, 44, and 43.4 wt%, respectively. This confirms a local change in the chemical composition of these particles towards higher Sr content.

Table 5: Normalized Sr content in various areas in the particle cross-section shown in Figure 51.

	1	2	3	4	5	$\bar{x}$
Sr high (wt%)	48	60	46	50	60	52.8
Sr low (wt%)	46	41	45	42	-	43.5

In the phase diagram in Figure 7 from Sarver et al. [45], where different crystal phases of SMP:Sn are shown as a function of the chemical composition of the mixed (Sr,Mg) phosphate, there is a phase transition at ~8–12% $Mg_3(PO_4)_2$. The average chemical composition from bulk EDX showed 12.5 and 11.3 mol% $Mg_3(PO_4)_2$ for the initial and post-flame material, also indicating a relative enrichment of Sr located at the concentration of a critical phase change in the phase diagram. To complement the analysis, XRD measurements are carried out to confirm the impact of flame exposure on the crystal structure of the phosphor.

The results from the XRD measurements from SMP:Sn are shown in Figure 52. The diffraction pattern of the initial material matches well with the diffraction peaks of the β-$Sr_3(PO_4)_2$ shown in yellow from Ref. [45]. The diffraction peaks from the post-flame material are less pronounced than in the initial material, indicating at least partial changes in crystal structure. Moreover, two crystal phases, α-$Sr_3(PO_4)_2$ and $SrMg_2(PO_4)_2$, are detected in the post-flame material, which does not exist in the initial material (see an enlarged section of the pattern in Figure 52). Both phases also appear in the phase diagram of the mixed $(Sr,Mg)_3(PO_4)_2$ at different mol% higher than 35% $Mg_3(PO_4)_2$ shown in Figure 7.

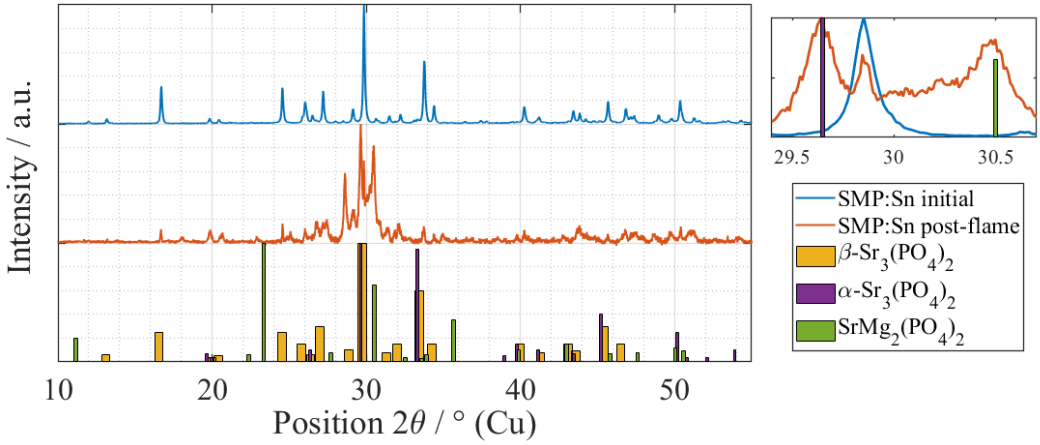

Figure 52: Diffraction pattern from initial and post-flame SMP: Sn phosphor material (top and center). The diffraction peaks (bottom) are visualized in different widths to improve the visibility of closely adjacent peaks. Inset plot (right): enlargement from 2θ = 29.4–30.6°. Adapted from Ref. [68] and published with permission from IOP Publishing.

Even if it is difficult to quantify the distribution of all phases, it is clear that crystal properties of SMP:Sn post-flame material are modified relatively to the initial material. Moreover, local and average changes in chemical composition are indicated from EDX measurements from a polished surface and bulk material, respectively. Two of the phases detected in the XRD measurements, β-$Sr_3(PO_4)_2$ and α-$Sr_3(PO_4)_2$, are similar to the phases of the "brightest" and non-luminescent phase, and both phases are adjacent to the chemical compositions measured in the EDX experiments (12.5 mol% and 11.3 mol% $Mg_3(PO_4)_2$, respectively in the phase diagram in Figure 7 from Sarver et al. [45]. It can be concluded that the particle melting and phase transformation following the exposition of a lean propane/air flame (ϕ = 0.71, $T_{adiabatic} \approx$ 1900 K) is responsible for the loss in luminescence properties of SMP:Sn.

5.3 Particle degradation and luminescence deterioration

The previous sections presented the attempts of temperature measurements in post-combustion gases and microscopical particle analysis of the two thermographic phosphors, YAG:Pr and SMP:Sn. It was shown that thermographic measurements were successful with YAG:Pr, whereas the SMP:Sn phosphor particles deteriorated in the flame, resulting in the loss of their luminescence properties. However, these are before/after measurements and do not give rise to particle degradation paths. In this section, a conclusion will be drawn, and some possible degradation mechanisms for SMP:Sn are proposed based on

the results from particle analysis in Section 5.2 and the simulated particle residence time in the burner flame from Section 4.1.1.

The thermographic phosphor YAG:Pr enables temperature measurements in the post-combustion gases of a premixed propane/air flame at various equivalence ratios up to $\phi = 1.0$. No structural or chemical changes were identified from particles that have passed the flame front ($\phi = 0.71$), where the adiabatic flame temperature is approx. 1900 K. The melting temperature for YAG particles is 2213 ± 7 K [132]. For a stoichiometric flame, the adiabatic flame temperature is approx. 2350 K, thus melting could have occurred. Isolated spherical particles are visible in the SEM images, which indicate melting. However, this study is not conclusive if they recover their luminescence properties after melting or if the melting temperature is not reached due to a deviation from the adiabatic flame temperature.

The second phosphor SMP:Sn does not show any luminescence after passing the high-temperature reaction zone in the flame. The melting temperature of the mixed $Sr_3(PO_4)_2$–$Mg_3(PO_4)_2$ orthophosphate at the given lattice mole fraction is not exactly known but given with $T \geq 1473$ K by the manufacturer [78]. The melting temperature of pure $Mg_3(PO_4)_2$ is 1630 K [133]. The melting point of pure $Sr_3(PO_4)_2$ is also not exactly known but can be assumed to be lower due to the decreased crystal field strength of the Sr–O bond (2.641 Å) relative to the Mg–O bond (2.046 Å) [134]. The simulation of the burner environment shows that the residence time in the high-temperature zone is significantly higher than the time needed for thermal equilibrium (Section 4.1.1). Therefore, in the current experimental conditions, where the particles were recaptured and analyzed ($\phi = 0.71$, $T_{\text{adiabatic}} \approx 1900$ K), melting is expected for SMP:Sn, which is accompanied by the loss of its luminescence properties.

According to the EDX measurements, the lattice composition of the initial SMP:Sn material is 12.5 mol% $Mg_3(PO_4)_2$, which is located in the area of the highest luminescence region (“B”) in the phase diagram (Figure 7) and can be associated with the β-$Sr_3(PO_4)_2$ according to the XRD analysis. In the reaction zone, the particles liquify and change their crystal phases in the subsequent solidification. During flow cool-down, the crystalline material can follow the phase boundary between different crystal phases and can solidify in the adjacent two-phase regions. In the diffraction pattern of the post-flame material, additional crystalline phases are detected (α-$Sr_3(PO_4)_2$ and $SrMg_2(PO_4)_2$), where the α-phase of the Sr-phosphate is non-luminescent. Pure $Mg_3(PO_4)_2$ can be amorphous and would not be visible in the XRD pattern [45]. The measurement of the lattice composition from the post-flame material is 11.3 mol% $Mg_3(PO_4)_2$, which is slightly enriched in relative Sr content compared to the initial sample. This finding aligns with the phase diagram, where this composition is in the direct vicinity of the region containing the non-luminescent α-$Sr_3(PO_4)_2$ (cf. Figure 7).

An additional mechanism for the loss of the material’s luminescence can be related to the oxidation of the dopant. The Sn^{2+} ion can oxidize towards the more stable Sn^{4+} ion ($E^0(Sn^{4+}/Sn^{2+}) \approx 0.28$ V) [135]. The luminescence properties of SMP:Sn did not change when the phosphor was heated three times up to 900 K in air [136]. However, at increasing temperatures, a reduction of the luminescence of 8% was observed for exposure to air at 973 K for 15 min, and further storage under similar conditions leads to a total loss of luminescence after 100 h [137].

The simulation of the residence time of the particles in the flame shows that the time at temperatures above melting temperature is three orders of magnitude higher than the time required for thermalizing the particles with their environment in these conditions. However, if the particle survivability is limited by the residence time above a certain temperature and only temperature measurements in the post-combustion regime are relevant, it can be of particular interest to choose a large particle diameter to increase the thermal inertia of the particle. This will limit the accuracy at high temperatures but may prevent

melting if the time scales in the high-temperature zone are short enough. In a previous study, it was shown that the response time to reach steady-state temperature increases significantly with the particle size (t_{95} increases from 27 µs for a 2 µm YAG particle to 577 µs for a particle size of 8 µm) [84].

6 Phosphor aerosol characterization in a furnace: Heated jet

Temperature measurements using thermographic phosphors require establishing the relationship between signal luminescence and temperature prior to measurements in the system of interest. The two-color thermometry approach requires characterizing the luminescence intensity-ratio detected with a given combination of optical filters as a function of temperature. Recent literature indicates that a bias can be introduced when calibration data from phosphor bulk or coated surface measurements are applied to aerosol measurements. Therefore, calibration data are acquired from phosphor aerosols.

Thermometric measurements using thermographic phosphors at high temperatures usually suffer from low signal intensities due to thermal quenching, which makes temperature measurements very challenging or impossible if the phosphor luminescence approaches the noise level of the detector, or if the phosphor luminescence cannot be distinguished anymore from interfering signal. This is true for well-controlled laboratory environments and even more so for reactive flows in technical systems of practical interest, such as burners or combustion engines, where competing signals make signal quantification from phosphor luminescence challenging. The relative signal from phosphor luminescence increases if the contribution of the interfering signal is reduced to a minimum, e.g., if exposure from thermometry cameras is limited to 3τ of the intensity decay, which allows capturing 95% of the total luminescence. For the measurements in the post-combustion regime, this is particularly important for long lifetimes and if the spectrum overlaps with, e.g., soot luminescence and thermal emission of the particles. This is referred to as the lifetime-based camera gating approach and requires the knowledge of the decay characteristics of each emission band (or emission line) used for thermometry purposes. In this chapter, the intensity ratio and the emission lifetime response of all phosphors are characterized against temperature in the aerosol state.

6.1 Phosphor luminescence lifetime characterization

Characterizing the intensity decay characteristics of all transitions used for temperature measurements in reacting flows for the relevant temperature range is an important prerequisite for using thermographic phosphors for quantitative measurements. The intensity decay is analyzed to determine the temperature-dependent phosphor luminescence lifetime providing the input for a calibration curve to be used to analyze the practical measurements. The characterization of the phosphor lifetime is carried out with a gated photomultiplier tube (PMT) in a heated jet according to the experimental setup presented in Section 4.3.1. A monochromator is used to select specific transitions. The Brübach algorithm [58] is used to determine the lifetime assuming mono-exponential decay. The procedure is described in Section 3.1.

6.1.1 YAG:Pr

YAG:Pr has multiple emission bands, which each show different lifetimes. The Dieke diagram showing the energy levels and their relevant transitions is presented in Figure 53. For thermometry purposes, only the emission bands centered at 490 nm ($^3P_J \rightarrow {}^3H_4$) and 610 nm ($^1D_2 \rightarrow {}^3H_4$) are used in this work. A third transition ($^3P_J \rightarrow {}^3H_5$) centered at 566 nm that is frequently mentioned in the literature in the context of phosphor thermometry is also probed. The ^3P_J transitions correspond to emissions from the

$^3P_0$, $^3P_1$, $^3P_2$, and $^1I_6$ energy levels, with a large proportion stemming from the $^3P_0$ state [138]. However, the nomenclature of the transitions is inconsistent in literature, therefore, they will be referred to as the ^3P_J transitions according to [24]. In this section, the temperature-dependent emission characteristics for all three transitions will be presented separately and then discussed together.

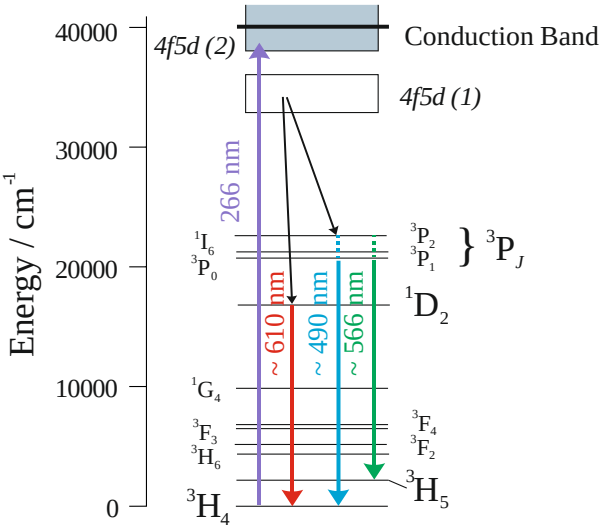

Figure 53: The Dieke diagram for YAG:Pr^{3+} according to Ref. [139]. The energy levels are taken from [138]. The relevant energy levels are printed in bold, and the relevant transitions are shown in color. The figure is adapted from Ref. [24].

The intensity decay of the blue emission at 490 nm follows a mono-exponential function and is therefore fitted using the Brübach algorithm (Section 3.1.1). Figure 54 shows the intensity decay at several temperatures in linear (top) and logarithmic scale (middle) with its residuals from the fit (bottom). The slope of the straight line in the logarithmic plot corresponds to the value of the lifetime and decreases with temperature, as expected. An exponential function is fitted to the data only in the region obtained from the fitting algorithm (t_1 to t_2) and shown with a bold line. The luminescence lifetime is extracted from the fit in this respective region and decreases from 8.04 µs at 298 K to 2.73 µs at 825 K. The lifetime found for this emission band at ambient temperature is in excellent agreement with the value of 8 µs from Ganem et al. [140] and close to the value of 5 µs from Özen et al. [98] and ~9 µs in Ref. [141]. The phosphor in the latter work is excited directly into the $^3P_0$ state with a 460 nm dye laser, and the state of the phosphor particles (either bulk material or particles coated on a surface) is not exactly known, which could be responsible for the slight deviation. There is no data available in the literature for temperatures above 300 K.

The luminescence decay of the green emission, centered at 566 nm, is presented in Figure 55, together with the exponential fit as well as the residuals. The residual from the data to the fit is mostly below 5%, showing good agreement of the mono-exponential function to the data. The decay characteristics are very similar to that of the 490 nm emission and decrease from 9 µs at ambient temperature to 2.8 µs at 825 K. Both emission bands de-excite from the ^3P_J manifold to neighboring energy levels ($^3H_4$ and $^3H_5$), so it is expected that the decay characteristics are similar even if the wavelengths are different. This is consistent with Ref. [142], where mono-exponential decay curves with a lifetime of 8 µs were found for both neighboring emissions $^3P_0$ and $^3P_1$ at 300 K. No data is available in literature at elevated temperatures.

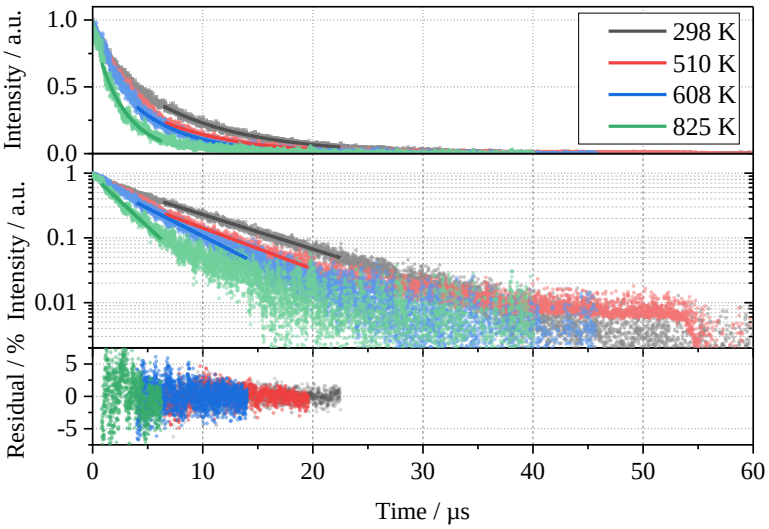

Figure 54: Luminescence decay of the blue YAG:Pr transition ($^3P_J \rightarrow {}^3H_4$) centered at 490 nm at various temperatures between 298 and 825 K shown on a linear and a logarithmic scale with the data fit obtained according to the Brübach algorithm. Residuals are shown on the bottom of the figure and for the region used for data fitting.

Both transitions (490 and 566 nm) show very similar behavior. The rate constant of the non-radiative transition connecting both lower energy levels ($^3H_5 \rightarrow {}^3H_4$) is in the same order of magnitude as the radiative transition from both ^3P_J emission [140], making both emissions $^3P_J \rightarrow {}^3H_4$ and $^3P_J \rightarrow {}^3H_5$ equally probable at ambient temperature. Spectral measurements at ambient temperatures showed approximately similar intensities of both emission bands. This finding is particularly interesting for thermometry purposes, as the depopulation from the ^3P_J level can be collected in either wavelength bands (490 and 566 nm). However, if excitation towards the 4f5d conduction band occurs using a quadrupled Nd:YAG laser (266 nm), the emission at 566 nm can interfere with the green residual harmonics at 532 nm. As simultaneous T-PIV measurements also include the use of a dual-pulse 532 nm laser, only the $^3P_J \rightarrow {}^3H_4$ emission will be used for thermographic measurements using YAG:Pr. For future thermometry approaches, both emission bands can be used with an appropriate filter combination to improve signal yield.

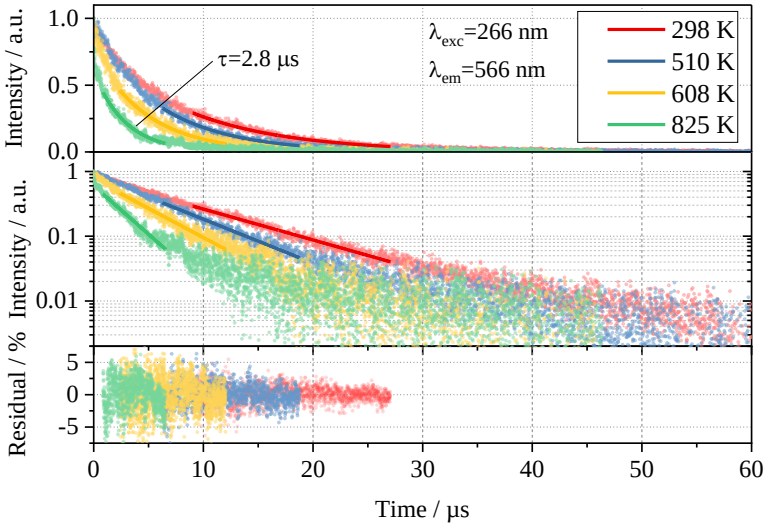

Figure 55: Luminescence decay characteristics for the 566 nm emission ($^3P_J \rightarrow {}^3H_5$) band for various temperatures shown on a linear (top) and a logarithmic scale (center) with the fit obtained according to the Brübach algorithm. Only every second data point is shown to improve visibility. The residuals from the fitted regions are shown at the bottom of the figure and for the regions used for data fitting.

The third emission probed is centered at 610 nm and corresponds to the transition of $^1D_2 \rightarrow {}^3H_4$. Unlike the previous transitions from the ^3P_J levels, this decay deviates from mono-exponential, indicating additional energy transfer [98]. A bi-exponential function showed the best fit to the experimental data, consisting of a short (τ_1) and a longer-lived lifetime component (τ_2). Figure 56 shows the intensity decay in linear and logarithmic scale with the residual to the bi-exponential fit (bottom). The lifetimes are extracted from the fitting parameters as mentioned in Section 3.1.1, and each straight line from the bi-exponential fit in the logarithmic plot corresponds to one lifetime constant. Note that the measurement range for the two temperatures, 700 and 825 K, has been reduced to 180 and 90 µs, respectively, in order to increase the resolution and resolve the strong intensity drop at the beginning of the decay.

The short lifetime component (τ_1) constantly decreases from 41 µs at ambient temperature to 12.5 µs at 825 K. This can be observed in the linear representation of the decay curve. The lifetime of the second lifetime component (τ_2) initially increases from 108 µs at 298 K to 135 µs at 510 K and then decreases to 59 µs at 825 K. The slope of the straight lines for 298 K and 608 K, as well as 396 K and 510 K, are parallel in the logarithmic plot, showing that these lifetimes are approximately similar. Literature provides various information on both lifetime components. Özen et al. only reported a lifetime of 110 µs at ambient temperature [98], which is in excellent agreement with the measurements of the long lifetime component (108 µs). The authors remarked an additional faster decay at the beginning of the decay but were unable to quantify the short lifetime. The only work where two lifetimes are explicitly quantified is in Ref. [142], with the lifetimes of 25 and 55 µs for the short and long component. However, excitation was directly into the $^1D_2$ level (approx. 610 nm) using a tuneable laser and not into the conduction band. When the authors excited into the $^3P_0$ level (approx. 490 nm), only the long component (55 µs) of the 610 nm emission was detected. The short component can not be detected because a signal increase during ~10 µs is observed at the beginning of the emission. In both cases, only a duration of 80 µs was analyzed, which hampers the detection of longer-lasting lifetime components under real conditions. Thus it is possible that the long lifetime of 55 µs found in Ref. [142] corresponds to the short lifetime component (τ_1) of the current measurements. No data is available for temperatures above 300 K.

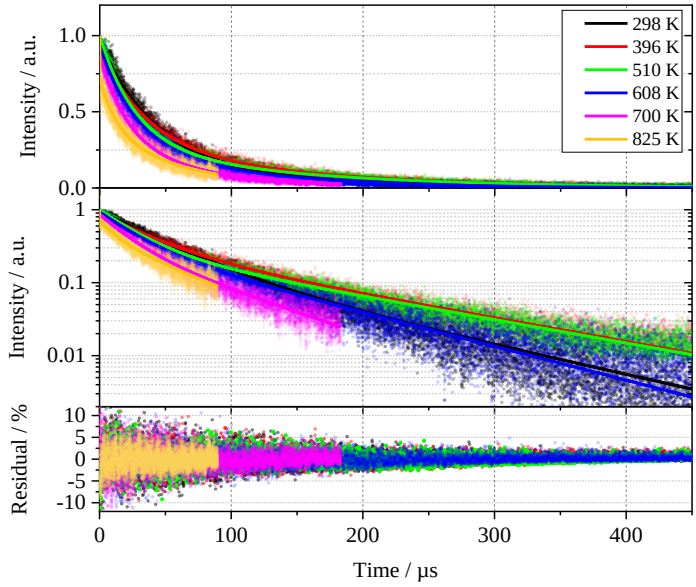

Figure 56: Luminescence characteristics of the 610 nm transition ($^1D_2 \rightarrow {}^3H_4$) from aerosolized YAG:Pr phosphor at various temperatures between 298 and 825 K shown on a linear (top) and a logarithmic scale (middle). The data is fitted using a bi-exponential function, and residuals are shown in the bottom figure.

Figure 57 represents the lifetime of the three different transitions of aerosolized YAG:Pr after 266 nm laser excitation. The error bars show the single-shot standard deviation ($\pm 1\sigma$) from all measurements. For the 490 and 560 nm transition, the deviation is below 3% (±0.19 µs at 510 K) and is mostly too small to be visualized. The highest variation for the 610 nm transition is 6.5% for τ_2 (0.81 µs at 825 K). The confidence interval (95%) of the fit is highlighted with the transparent area.

The lifetimes for the 490 and 566 nm transition (both decaying from ^3P_J) constantly decrease with increasing temperature. Özen et al. observed a decrease in the lifetime of the $^3P_0 \rightarrow {}^3H_4$ transition with increasing lifetimes over a temperature range from 20 to 300 K [98] and attributed the decrease to an enhancement of the non-radiative $^3P_0 \rightarrow {}^1D_2$ relaxation rate, probably via multiphonon emission. The energy of the most energetic phonon in YAG:Pr is 865 cm^{-1}, so the emission of 5 phonons would be required to bridge the $^3P_0 \rightarrow {}^1D_2$ energy gap via multiphonon relaxation [141]. The dopant concentration (Pr^{3+}) in the previously mentioned reference is similar to that one used in this work (0.5%).

The short lifetime component (τ_1) of the 610 nm emission also decreases constantly at increasing temperature, however, the long lifetime (τ_2) component (decaying from $^1D_2$) initially increases from 110 µs (298 K) to 135 µs at 510 K and then decreases to 59 µs at 825 K. A precise explanation for this behavior cannot be derived from these available measurements, but the following explanation is provided. As mentioned above, it is reported that the $^1D_2$ level is populated by multi-phonon relaxation from the $^3P_0$ level at increasing temperatures. This is supported by Malta et al. [142], who reported that the emission intensity from $^1D_2$ initially increases after excitation when excited to the $^3P_0$ level, whereas intensity decreases immediately when pumped into the $^1D_2$ level. This suggests that the population of the $^1D_2$ level can also occur via the $^3P_0$ level, and that this transition is enhanced at increasing temperatures [141]. Thus, it is possible that this level ($^1D_2$) relaxes then into the $^3H_4$ ground level at increasing rates with temperature by radiating 610 nm emission only up to a threshold temperature. It is known that multi-phonon emission becomes significant above a threshold temperature [40,143].

The luminescence lifetime decreases again above ~500 K. A possible explanation could be that the energy levels change at increasing temperatures, and thus multi-phonon emission populating the $^1D_2$ level is not possible anymore, or other deactivation pathways become dominant.

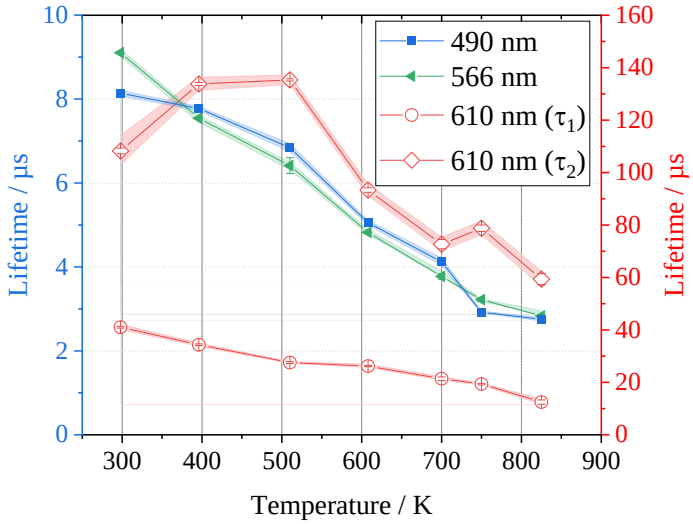

Figure 57: Luminescence lifetime of three different emission bands of YAG:Pr after the excitation with 266 nm over a range of different temperatures. The lifetimes of the 610 nm transition are shown on the right axis. The error bars show the shot-to-shot variation ($\pm 1\sigma$) from all consecutive measurements and are too small to be visualized for most points. The shaded area shows the confidence interval (95%) of the fit.

In this section, the decay time constant of the relevant transitions in a YAG:Pr phosphor aerosol was investigated over a wide range of temperatures (298–825 K). The knowledge of the exact lifetime is important to reduce the signal contribution from other sources than laser-induced phosphorescence in reacting flow conditions, for example, via the adaptation of the camera gating. These measurements provide the basis for the lifetime-based gating approach used for engine post-combustion measurements.

6.1.2 SMP:Sn

The phosphor SMP:Sn has a broad band emission over the entire temperature range centered between 630 and 570 nm. The FWHM is approx. 160 nm at 300 K and 185 nm at 1000 K. Thus, the phosphor decay curve is probed in 50 nm increments between 450 and 750 nm. Figure 58 shows the intensity decay for various temperatures illustratively at the detection wavelength of 550 nm with an exponential fit using the Brübach algorithm. The residuals are shown in the bottom figure. The lifetime decreases constantly from 28 µs at 298 K to 11.3 µs at 1000 K.

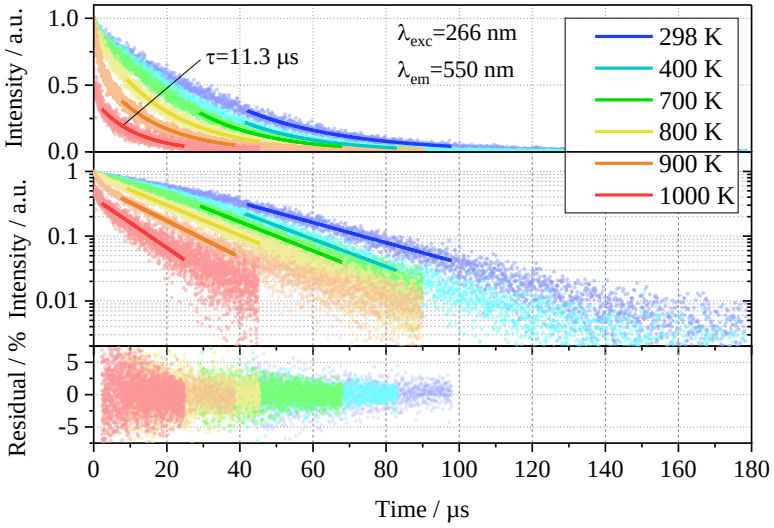

Figure 58: Phosphor luminescence decay detected at 550 nm in linear and logarithmic representation for SMP:Sn aerosol for various temperatures between 298 and 1000 K. The data is fitted using the Brübach algorithm. Only every third point is displayed in the scatter plot to improve visibility. The residuals to the fit are shown below.

For lower temperatures (298–700 K), the decay curves are not purely exponential but show a linear dependence at the beginning and become mono-exponential after 1τ, which is atypical for thermographic phosphors. Assuming the absence of measurement artifacts[14], this means that there is a net increase in the population relative to a pure exponential decay, indicating additional energy transfer towards the upper state at the beginning of the decay. This does, however, not impact the calculation of the lifetime as the fitting window evaluated in the Brübach algorithm only starts at 1.5τ for the relatively low temperatures. The width of the fitting window is 2τ for all measurements. The parameters defining the fitting window are evaluated by the algorithm to be delayed for those measurements which are not purely exponential (298–700 K) relative to those showing pure mono-exponential decay characteristics. The reason for this is that the residual error between two iterations in the linear regime is too high, and therefore the fitting window is delayed until the begin of the exponential regime. This shows the robustness of the Brübach algorithm against interfering short-lived signals. Further investigation of the non-exponential regime is not possible within the scope of this work, but it is also not necessary given the objective of this study and the consistency of the current results.

[14] Detection of scattered laser light is prevented as the PMT gate is delayed 100 ns relatively to the laser pulse and the PMT is operated within its specifications.

Figure 59 shows the emission lifetime of aerosolized SMP:Sn for various wavelengths over temperature. The lifetime decreases from ~30 µs at ambient temperature and decreases to ~10 µs at 1000 K, where all probed wavelengths follow a similar trend. The lifetimes measured at 500, 600, and 700 nm follow the same trend [94] but are not shown in the figure for visibility.

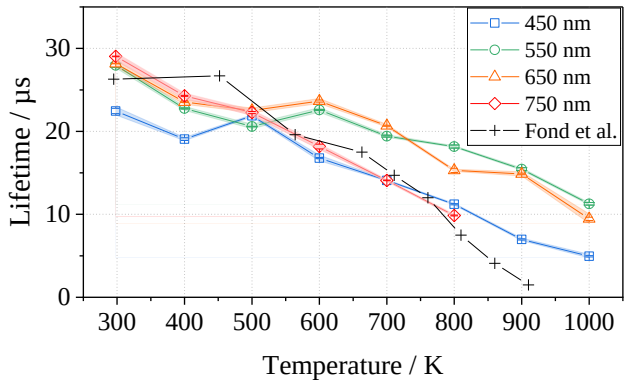

Figure 59: Luminescence lifetimes for the phosphor aerosol with SMP:Sn from 300–1000 K for various wavelengths. Error bars show the single-shot deviation over 50 consecutive measurements, and the shaded region represents the confidence interval (95%) of the fit. The lifetimes of SMP: Sn (bulk material) from Fond et al. [136] are shown in black as a reference.

The lifetimes measured in the SMP:Sn aerosol are in good agreement with data from the literature. Fond et al. found a lifetime of 24–27 µs at 300 K for measurements in bulk material and in liquid suspension (water) [136] and a phosphor lifetime (bulk material) at 900 K of ~1.5 µs. The authors did not mention the detection wavelengths of the PMT, so it can be assumed that their results represent an average over the entire spectral range. Furthermore, the authors used a fitting window of 5–50 µs. Thus it is possible that the lifetimes are biased at high temperatures from applying a constant fitting window over the entire temperature range [58].

6.2 Two-color characterization in a heated jet

This chapter shows the results from the characterization of a phosphor aerosol in a heated jet using the luminescence-based intensity-ratio approach to determine the temperature from the setup introduced in Section 4.2.2. The objective is to obtain a ratio–temperature calibration curve for the detection filter sets that are used in further experiments. The post-processing procedure is described in Section 3.4 with a flat-field correction towards seeded operation (Section 3.3.3) at ambient conditions (298 K) with a cut-off filter from 2–90% of the dynamic range.

6.2.1 SMP:Sn

Figure 60 shows the average ratio maps of a heated jet with dispersed SMP:Sn phosphor particles at various temperatures up to 811 K according to the post-processing procedure explained in section 5.3.1. The temperatures are measured with a thermocouple (type K, 1 mm tip diameter) at the position indicated by the red cross. The thermocouple is mounted on a motorized *xy*-stage to localize the hottest spot in the jet prior to every measurement. This is necessary because the hottest region is not centered above the nozzle of the heated jet, as the metal tube from the furnace is bent by ~90° only 3 cm below the outlet of the nozzle due to space restrictions in the experimental arrangement, leading in non-symmetric temperature maps.

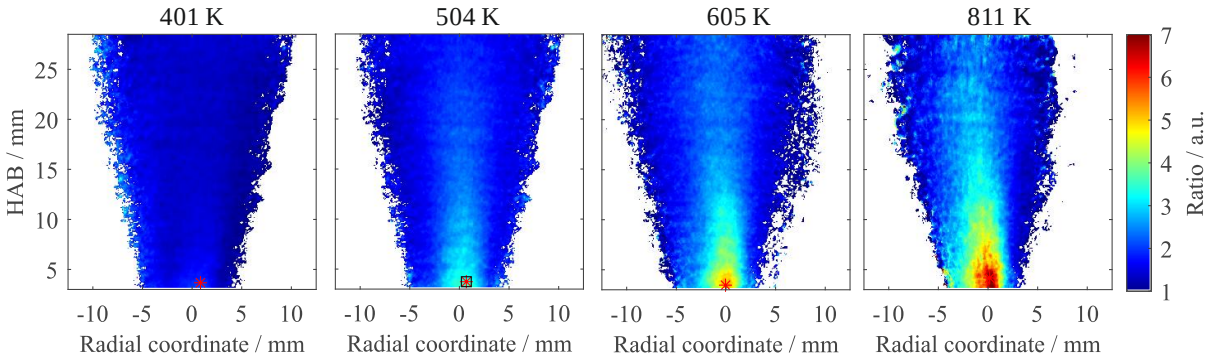

Figure 60: Average signal-ratio images at various temperatures from aerosolized SMP:Sn (set #1) in a heated gas jet. The images are mapped based on the single-shot mapping algorithm. The location of the thermocouple is highlighted with a red cross, and the surrounding region used to calculate the signal ratio at the respective temperature is shown with a black rectangle in the 504 K frame (approx. 1 × 1 mm^2).

The signal ratio in the center of the jet increases with increasing temperatures, as expected, and the ratio decreases at increasing height above the nozzle. The ratio calculation is performed such that the ratio increases with temperature. It can be seen that the hot air from the jet mixes with the surrounding cold air.

The horizontal structure in the center of the image that is visible at HAB ≈ 20 mm can be due to the laser sheet that remained after the ratio calculation of both imaging channels. This should not occur for ideal ratio-based methods and indicates a cross-dependency of the laser fluence to the signal ratio. SMP:Sn is reported to have a very low cross-dependency of the laser fluence to the signal ratio that results in a temperature error in the order of 0.6 K/10% change in the laser fluence at 20 mJ/cm^2 for the filter combination used Ref. [136]. In this work, the laser fluence is held constant between characterization measurements and measurements in the system of interest, and the periphery of the laser sheet, where laser sheet inhomogeneities are particularly high due to the Gaussian beam profile, is blocked with beam dumps. If the region of the laser sheet that is equivalent to ±2σ, based on the intensity distribution of the beam profile, is used for measurements, the maximum uncertainty would be <5 K (~75% variation)[15]. Nevertheless, in future work, cross-dependency investigations may be required over a wider range of laser fluences.

Figure 61 shows the ratio distribution of 225 independent signal ratio measurements after flat-field correction in a histogram. The values are calculated from the ROI (15 × 15 pixels) around the thermocouple highlighted with a black rectangle in the signal ratio map in the 504 K frame. The size of the ROI is equivalent to the size of the thermocouple in the image as determined from image acquisition. The data is fitted with a normal distribution to visualize the mean value and its standard deviation. The histogram is analyzed as a normal distribution to determine the uncertainty that is induced as the thermocouple reading averages the temperature from the region identical to its projected size in the flow. The first histogram represents the measurements from a signal-ratio image at ambient temperature (298 K) that was itself used as a flat field, so it is equal to unity after flat-field correction. The standard deviation increases with increasing temperature as the global signal level decreases, and thus the relative noise contribution increases.

The accuracy of the thermocouple used in the measurements is ±0.75% of the temperature value in Celsius or ±2.2 °C, which ever is greater, according to the manufacturer. It should be noted that this does not include radiation correction. At the highest temperature, that would only translate into an uncertainty of 6.1 K. However, the thermocouple accuracy here is not the governing error, as the flow is

[15] For a normal distribution with $\sigma^2 = 1$ the intensity drops to approx. 25% within of ±2σ , thus, the highest variation is 75%.

subject to fluctuations, and the thermocouple reading represents an average from the region covered by the thermocouple junction. The ratios (and thus temperatures) in this area are widely scattered, as can be seen in Figure 61, especially at high temperatures, so the accuracy of the calibration is limited by the size of the thermocouple junction (here, 1 mm tip diameter).

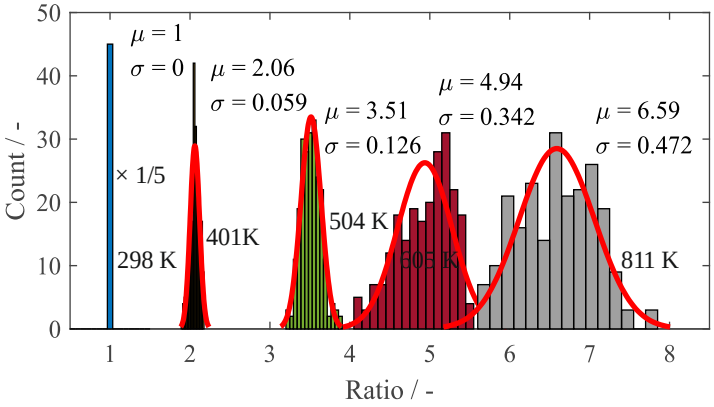

Figure 61: Histogram of all 225 independent measurements of the signal ratio in the ROI around the thermocouple from SMP:Sn (set #1) shown in Figure 60 as a rectangle in the 504 K map. The data is fitted with a normal distribution, and its mean and standard deviation are also shown. Note that the height of the first histogram (298 K) is reduced by a factor of five to improve visibility.

From the fitted normal distribution, a ratio-temperature calibration curve can be established (Figure 62). Figure 62 shows the ratio-temperature calibration curve for two different filter sets that are used with the phosphor SMP:Sn (see Table 4). The signal ratios on the *y*-axis represent the mean of the normal distribution, and thermocouple readings are shown on the *x*-axis. To take into account the uncertainty of the thermocouple size, the standard deviation of the normal distribution of the signal ratios from the area covered by the thermocouple is shown as vertical error bars, and the temperature error bars result from applying the ratiometric error to the calibration curve. Multiple datapoints at one temperature represent repetition measurements, which proof excellent reproducibility.

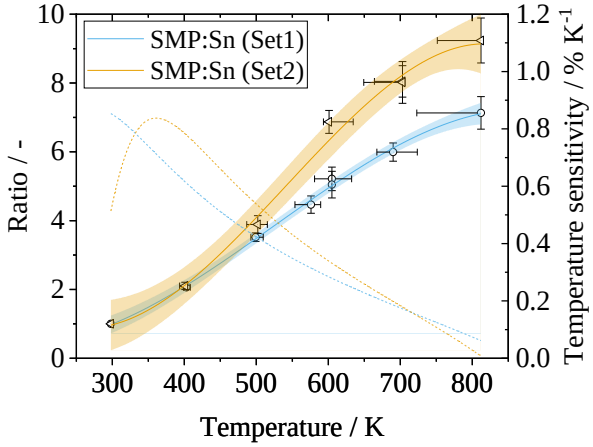

Figure 62: Calibration curve for signal-ratio-based thermometry using aerosolized SMP:Sn for two different filter sets. The vertical error bars represent the standard deviation (1σ) calculated from the normal distribution in Figure 61. The horizontal error bars result from the ratio error applied to the calibration curve. The 95% confidence interval of the polynomial fit (3rd order) is shown as a transparent overlay. The temperature sensitivity ψ is shown as a dashed line on the right axis ($\psi(T) = \frac{1}{I_R}\frac{dI_R}{dT}$, with the intensity ratio I_R).

The signal-ratio curve can be applied to the same measurements from the heated jet to obtain 2D temperature images. Figure 63 represents several single-shot images of the heated jet at different exit temperatures. The left image pair (401 K) shows a single-shot ratiometric image (top) with the associated map translated into temperature (bottom). The temperature image lacks multiple pixels which have a

ratio below unity and can, therefore, not be mapped in the calibration curve because the temperature is below ambient temperature. The issue problem occurs at the upper end of the calibration curve if the ratios measured are outside the calibration curve, either due to statistical uncertainties or if the temperature is higher. This is particularly visible in the white regions in the center of the jet at 811 K. There are some spherical blank spots in the maps of 504 K, which is due to the agglomeration of the phosphor material. This led to excessive signal intensities and is therefore excluded from analysis through the upper cut-off filter (see the procedure for temperature image processing in Section 3.3).

The temperature maps averaged from 200 subsequent measurements are shown in the bottom row of Figure 63. The temperature was first inferred from the calibration curve and averaged afterwards. This leads to underestimating the measurement at high temperatures as only temperatures below 811 K are considered, even though the temperature is normally distributed around 811 K. Note that this is also the case if the ratio measurements are averaged first and then converted to temperature using the calibration curve. However, the bias towards lower temperatures is so high, but there are invalid data points in the center of the jet where the ratio from the average is outside the calibration curve. This is more clearly demonstrated in Figure 64, where both postprocessing ways are shown and compared.

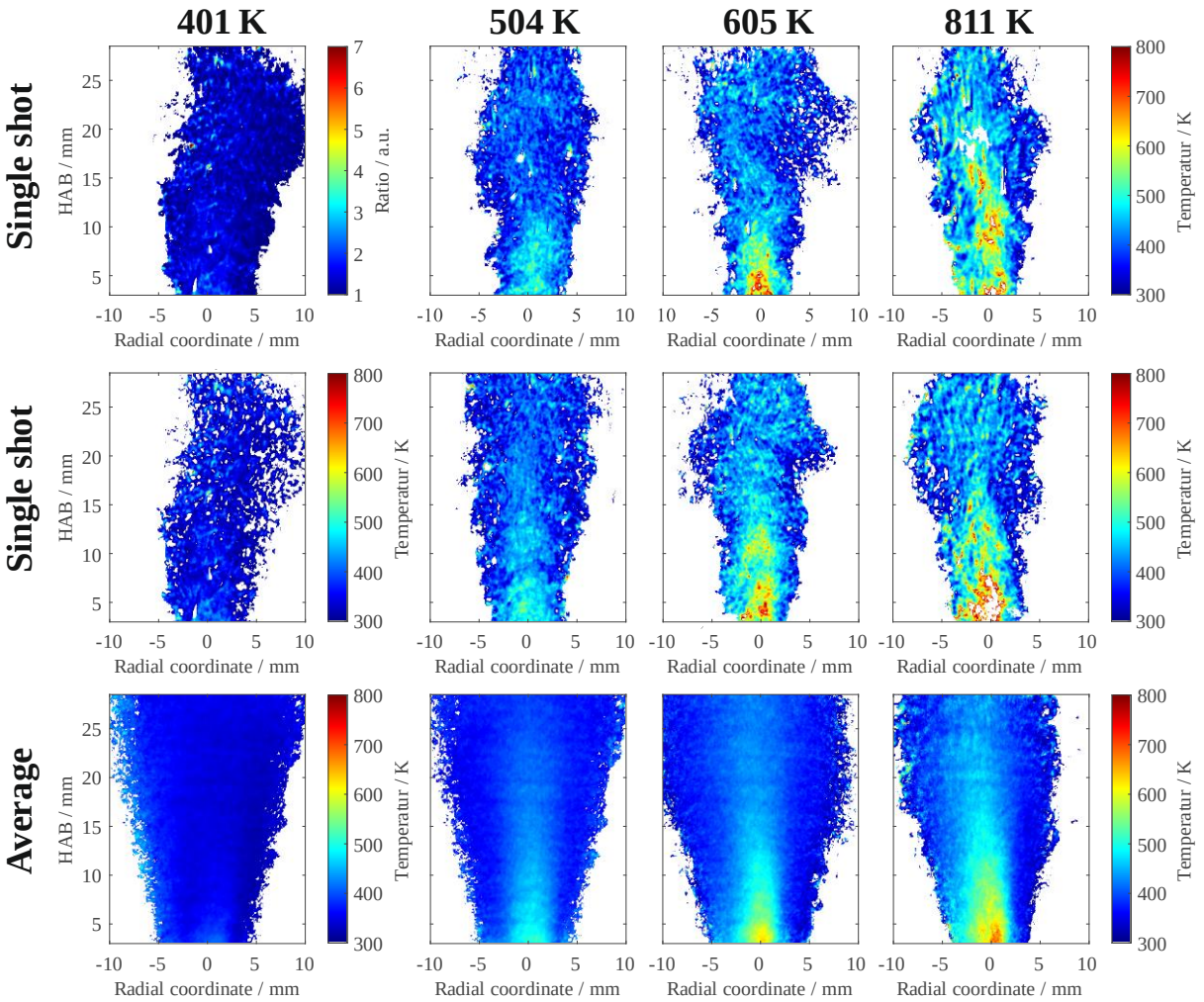

Figure 63: Several single-shot temperature images at various temperatures from aerosolized SMP:Sn (filter set #1) in a heated jet. A ratio map is shown on the top left (401 K) for direct comparison. The associated ensemble-averaged temperature images, compiled from single-shot temperature images, are shown in the bottom row.

Figure 64 shows two averaged temperature maps obtained from two different post-processing methods. In (a), the signal-ratio images are first averaged and then translated to temperature, whereas the order is

inversed in (b), where the temperature is determined in every single-shot image and then averaged. Neglecting statistical uncertainties, both approaches should give similar results in ideal steady-state conditions (no shot-to-shot fluctuations) as long as the calibration curve is linear and covers a wide enough temperature range (no clipping effects of the calibration curve). Linearity of the calibration curve can be assumed with good accuracy at intermediate temperatures for both filter sets used for SMP:Sn. The temperature profiles at various heights are shown for both cases on the right. The profiles above 10 mm above the jet exit are below ~550 K and do not vary significantly for both methods. This is firstly because this temperature range is well covered in the calibration curve, and the calibration curve is mostly linear in this regime, and secondly because the temperature amplitude of shot-to-shot fluctuations is also smaller at increased HABs due to flow mixing with cold air.

The maximum temperature at 4 mm is ~715 and 670 K, respectively, for both methods, even if the jet exit temperature was measured to be 811 K. The calibration curve in this temperature regime is non-linear, so a slight difference between both methods is expected. The average temperature for the first postprocessing method (a) is higher than (b), as ratios above the maximum value from individual images are considered through averaging before its conversion to temperature. However, a large region in the center is then above this value and cannot be displayed in temperature. Temperature is generally biased towards lower temperatures at the upper end of the calibration curve (clipping effect), but this is more pronounced for method (b). The difference to the measured target temperature is as large as approx. 100 K as the phosphor luminescence sensitivity at this temperature is not very high, thus, a little change in ratio leads to a large temperature difference. Furthermore, the ROI representing the region of TC sensing, which is used to establish the calibration curve, is relatively large for the high gradient present in these conditions. Thus, the average ratio from the ROI is also biased towards lower temperatures.

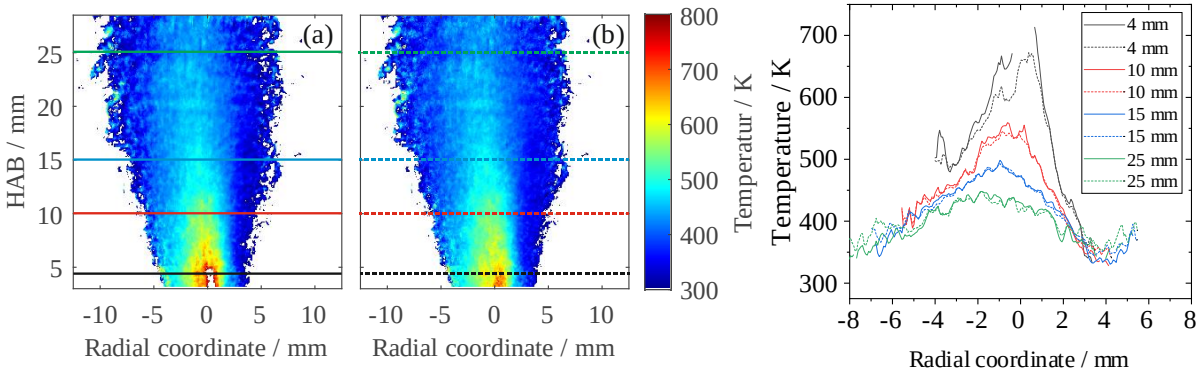

Figure 64: Comparison between two different averaging methods with the temperature profiles at different heights from SMP:Sn (filter set #1): (a) average signal-ratios + calculate temperature and (b) calculate single-shot temperature + average temperature. The temperature profiles are averaged from 10 pixel rows.

For calibration curves that cover a wide enough temperature range, the temperature is always biased away from the periphery of the calibration curve. At the upper end, the temperature is biased towards lower temperatures, and at the lower end, the temperature is inversely biased towards higher temperatures. Therefore, the calibration curve should always cover more than the equivalent temperature in the observed system, e.g., $\pm 1\sigma$ of the ratio. However, in practice, this is difficult to obtain as statistical uncertainty increases with increasing temperature due to thermal quenching, which as a consequence, would strongly limit the observable temperature range.

Depending on whether the observed system is subject to strong fluctuations, the post-processing approach (b) should be chosen to minimize the effects from a non-linear calibration curve, whereas in

temperature-stable systems the approach (a) is beneficial to minimize statistical uncertainties by increasing the signal-to-noise ratio.

6.2.2 YAG:Pr:

In this section, the characterization of the temperature-dependent properties of YAG:Pr is presented in heated jet measurements. The validation of this setup for 2D laser-sheet-based imaging is given in the previous section, and different problems are addressed within the results of SMP:Sn, so the scope of this section is limited to presenting the results and highlighting the differences and difficulties encountered with this phosphor.

The height of the laser sheet is reduced, and the thickness is increased to 1 mm to increase signal yield and reduce experimental complexity. The laser pulse energy is adapted to maintain the laser fluence of 50 mJ/cm^2. Unlike the measurements for SMP:Sn, the focal point of the laser was positioned a few centimeters behind the heated jet because focusing the laser into the center of the jet led to a clattering sound once the phosphor particles were seeded, likely to stem from laser-induced breakdown. This ensures the signal captured by the cameras is not biased with interfering signals from plasma breakdown. This behavior is also reported in literature for YAG:Pr imaging in a heated jet for a fluence of 40 mJ/cm^2 [24,71]. Additional measurements to investigate the origin of this clattering sound were not feasible within the scope of this thesis and were not necessary for the objective of obtaining the temperature calibration of a YAG:Pr phosphor aerosol.

Figure 65 shows the average temperature maps for various jet exit temperatures. The procedure to calculate temperature is detailed in Section 3.3., where the flat-field correction is performed towards seeded operation at near-ambient temperatures (306 K). Some sub-mm structures that form small areas are visible, for example, in the center of the jet at HAB ≈ 5 mm at 490 K, which results in random inhomogeneities of the temperature map. Some of them are highlighted by arrows as examples. This is a postprocessing artifact stemming from the dysfunction of one camera. Whenever a larger region of the camera is saturated (4095 counts) from excessive light, the pixels in the center of this region have the nonphysical constant value of ~800 counts. This region itself is not considered for temperature calculation because the second imaging channel is also saturated, and the cut-off filter applied before ratio calculation prevents further consideration of this pixel. However, the neighboring pixels of this region, which fall just below the cut-off filter, are considered for temperature calculation and cause the appearance of a contiguous area or an edge in the case of slight misalignment between the cameras. The camera concerned is the second imaging channel (Ch2), which is in the denominator of the intensity ratio. Therefore, the regions are slightly biased towards higher ratios and, thus, temperatures.

This problem was reduced to a minimum by adapting camera gain and lowering the particle density of the phosphor aerosol to avoid excessive signal and by descending the cut-off filter to 90%, but it could not be entirely removed. Despite the use of aerosil, the phosphor YAG:Pr tends to form more agglomerates than SMP:Sn. As phosphor agglomerates are likely to lead to pixel saturation, this problem is more severe for YAG:Pr than for the previously used phosphor SMP:Sn. This problem could be further mitigated in image postprocessing by automated detection and neglect of the saturated region and the surrounding pixels, but this was also not possible within this work.

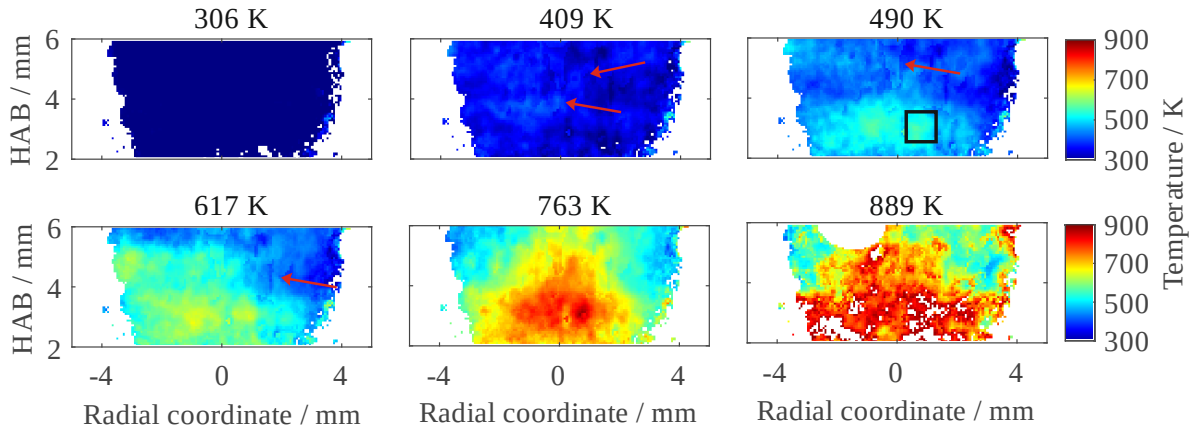

Figure 65: Ensemble-average of 200 single shot temperature images at various temperatures up to 889 K. The black rectangle (approx. 1 × 1 mm^2) in the 2D temperature map of 490 K represents the region covered by the tip of the thermocouple and is also used for statistical evaluations. The red arrows highlight regions where camera malfunction leads to the inhomogeneous appearance of the temperature maps. The ratio-temperature calibration curve used to determine temperature is shown in Figure 67.

Additional systematic errors are visible at HAB ≈ 3 mm close to the centerline for all temperatures. This is an artifact in the ambient temperature field (306 K), which is used as a flatfield and thus imposes an error on all temperature fields. This artifact could be removed by neglecting these pixels and interpolating them in the flatfield. The temperature field at 889 K appears to be noisier. This temperature was recorded with an increased camera gain due to low global signal intensities and gain-corrected, as introduced in Section 3.3.1. However, the exponential character of the camera gain increases the events, where excessive signal from seeding fluctuations led to saturation effects and depletion effects, as introduced in the previous paragraph. This temperature field also shows multiple white regions at low HABs. These are pixels that are excluded from temperature inference from the calibration curve because they fall above the mean intensity ratio (I_R = 10.31) for 889 K.

The area covered by the black rectangle (15 × 15 pixels, 1.06 × 1.06 mm^2), shown in the 490 K image, is similar to the resulting size of the thermocouple (1 mm tip diameter). The arithmetic mean of the intensity ratio from this region is used to establish the ratio calibration curve against the reference temperature measured from the thermocouple, similar to the approach in the last section. All pixels of the average temperature map that fall into this region are considered for statistical evaluation to determine the precision of the calibration curve.

Figure 66 shows the histogram of 225 independent signal-ratio measurements from the ROI shown in Figure 65 for several temperatures before the ratio was converted to temperature. A normal distribution is fitted to the data to calculate the standard deviation ($\pm 1\sigma$) as a measure to quantify precision. The deviation constantly increases from ambient temperature to a maximum of σ = 2.47 at 889 K due to decreasing phosphorescence emission at increasing temperatures and, thus, relatively increased noise contribution. The positive and negative temperature error resulting from this deviation can be calculated by evaluating the temperature at $T(R \pm \sigma)$, which is annotated as a horizontal error bar in the calibration curve in Figure 71. The data points are fitted with a power function of the form $a + b\,(I_R)^c$ with the intensity ratio I_R and the coefficients a, b, and c. The vertical ratiometric error bar (±0.11) at 409 K is too low to be visualized; this, however, results in temperature uncertainty of ± 31 K due to the low incline of the fitted calibration curve at this temperature. Even if the absolute ratio deviation increases until 617 K, the resulting temperature error decreases due to the increasing slope of the curve. The ratio distribution of σ = ±2.47 at 889 K results in a temperature variation of 78 K (11.4%).

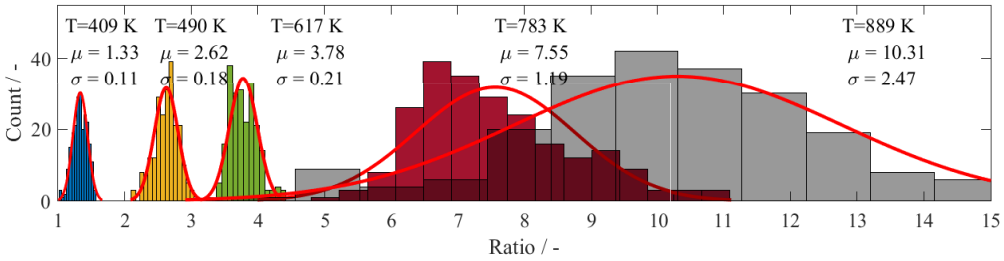

Figure 66: Histogram for 225 independent signal-ratio measurements with a fitted normal distribution above the nozzle exit for three different temperatures in the ROI determined from the size of the thermocouple.

Note that the temperature errors are symmetric, as the ratio baseline for the temperature error calculation is the ratio extracted from the fit and not from the measurement data at the reference temperature. Otherwise, the positive temperature error, for example, at 717 K, would be near zero (or even negative), and the negative temperature error would be twice the error that is now displayed. This calculation method is chosen because this error is a measure of the scatter of the data and not the accuracy of the calibration. This latter will be discussed in Section 6.3, where the accuracy of the calibrations from both phosphors, SMP:Sn and YAG:Pr are compared.

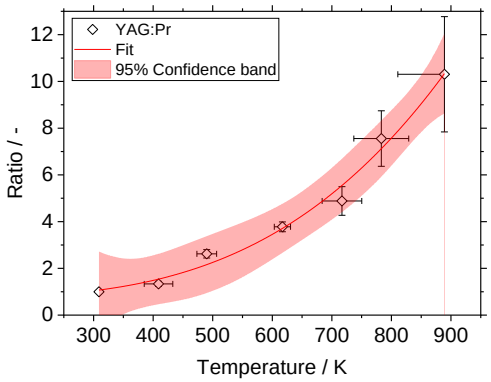

Figure 67: Signal-ratio-based temperature calibration curve for YAG:Pr from heated jet measurements. The vertical error bars denote one standard deviation ($\pm 1\sigma$) from a normal distribution fitted to the data (see Figure 66). The temperature sensitivity is shown in Figure 68.

6.3 Comparison between both thermographic phosphors

In the previous sections, the signal-ratio-based temperature calibration curves of both phosphors (SMP:Sn and YAG:Pr) measured in a heated aerosol jet were presented. Systematic characterization and comparison between both phosphors, such as thermal quenching, is not the scope of this work, and a ranking between both phosphors does not appear to be meaningful, as not all phosphors cannot be used in all measurement conditions (see Chapter 5). However, an attempt will be made here to compare the two phosphors based on their calibration curves in terms of temperature sensitivity or measurement uncertainty.

Figure 68 (left) shows the calibration curves from both characterized phosphors, where the standard deviation from the calibration is expressed in error bars. Firstly, the measurement uncertainty for both phosphors can be compared. The relative standard deviation Figure 68 (right) relates the signal-ratio-based single-shot temperature precision to the ratio and is expressed in percent. The relative standard deviation of YAG:Pr increases up to ~25% at 889 K, whereas the relative standard deviation of SMP:Sn is always below 7.5%. This is a measure for the statistical uncertainty in the calibration measurements

which increases with the relative noise as the signal decreases. Note that this does not represent the single-shot temperature precision.

The temperature sensitivity, calculated from the fit to the calibration, is shown on the right axis in the left figure. The temperature sensitivity expresses the change in the intensity ratio per change in temperature. For SMP:Sn, the temperature sensitivity decreases from 0.85%/K at ambient temperature to near-zero at 800 K, and for YAG:Pr, the sensitivity is between 0.31 and 0.45%/K over the entire temperature range. The second filter set for SMP:Sn, has a similar maximum temperature sensitivity but is approx. 0.1%/K higher than the first filter set in the temperature range between 350 and 550 K.

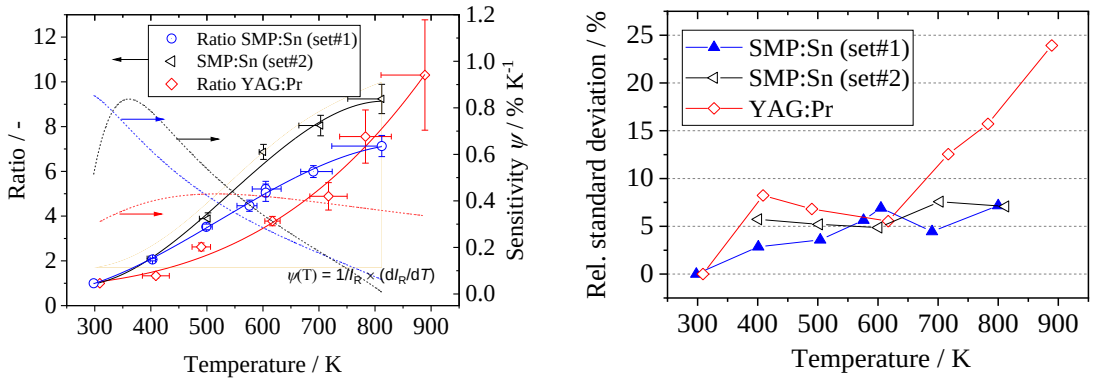

Figure 68: Left: Signal-ratio-based temperature calibration curve and the temperature sensitivity (dashed lines). The relative standard deviation of the ratios, which are shown as the error bars in the left plot, are shown on the right.

Even though the thermal quenching behavior was not analyzed quantitatively on a particle basis, the high uncertainty for YAG:Pr confirms the very low global signal levels encountered during measurements at high temperatures. While this fact clearly favors the use of SMP:Sn, offering the possibility for very high-precision measurements, the accuracy of SMP:Sn is relatively low at high temperatures, given the low temperature sensitivity. This can be increased by using different filter sets, which favor the light collection of the flanks of the emission spectrum. This can be achieved at the expense of signal intensity either by decreasing the collection bandwidth or shifting the collection band towards the flanks.

7 Thermometry in a burnt-gas flow reactor

In this chapter, *in situ* temperature measurements in a burnt-gas flow reactor (BGFR) are presented. This measurement environment can be used to study pyrolytic soot formation from hydrocarbons under well-controlled conditions [121]. Interpreting measurements in the BGFR requires knowledge of the thermal history of the gases. The simulation of this process is complex and quite cumbersome due to the thermochemistry in the central flow in case of pyrolysis and particle formation and the interaction of radiative processes of the growing soot particles. Therefore, non-intrusive measurement techniques are necessary to investigate the temperature field of the flows. Measuring temperature with conventional laser-based diagnostics, such as LIF using the hydrocarbons seeded as a precursor, would seem evident. However, this can be challenging as the tracer pyrolyzes above a given temperature and forms fluorescing species, which are not anymore suitable for temperature measurements. Thermographic phosphors offer great potential for temperature measurement under these challenging conditions. The BGFR was used to compare three temperature measurement techniques: LIF measurements using gaseous toluene as a fluorescence tracer, phosphor thermometry, and lastly, temperature measurements obtained from thermal gas expansion through Mie-scattering from the phosphor particles.

A central, oxygen-free flow is seeded with thermographic phosphors and heated by the surrounding fuel-rich premixed flame. Unlike in the previous experiments using a premixed burner (Chapter 5), the central flow does not undergo combustion but is constantly heated. Therefore, the thermographic phosphor SMP:Sn is chosen due to its beneficial luminescence properties. The signal-ratio–temperature calibration curve used to infer temperature in the BGFR was obtained in a phosphor aerosol, heated with an electric furnace (Section 6.2.1), and imaged with the same optical equipment. Particle number densities are determined simultaneously from Mie-scattering images to provide a proof-of-concept for simultaneous temperature and velocity measurements. The temperature results are compared to LIF measurements using gaseous toluene as a fluorescence tracer and to temperature measurements obtained from thermal gas expansion through Mie-scattering.

7.1 Temperature measurements using phosphor thermometry

In the BGFR, it is of interest to measure gas-phase temperatures at various heights above the burner to obtain information about the temperature history of the gases. This results in elongated areas of interest that cover this width of the central flow but considerable height. Due to the high aspect ratio of the flow of interest, it is preferable to vertically move the cameras relatively to the burner and image various heights above the burner (HAB) instead of increasing the measurement distance to maintain a reasonable spatial resolution for the high temperature gradients. However, the compilation of multiple imaging positions at various heights above the burner (HAB) into one image bears challenges for further data post-processing, like the flat-field correction. The procedure of white-field and flat-field corrections is explained in Section 3.3.3. The signal-ratio–temperature calibration curve from aerosol measurements is used to convert the signal ratio to temperature.

Figure 69 shows the temperature field from two imaging positions. The region highlighted by the rectangle in red is the region that is used to calibrate the temperature of P_1 to P_0. The white pixels in the center of the flow (P_0) are neglected from temperature calibration because their intensity is outside the intensity range defined by the cut-off filter (Section 5.3.) or the value of the ratio falls below the lowest value of the ratio-temperature calibration (298 K) and the calibration curve is not extrapolated. After averaging 200 individual images, pixels are masked out that do not show temperature values from at least five instantaneous measurements. Note that this is not the same operation as excluding signal-ratio values that are not covered by the calibration curve and that it is designed to decrease uncertainty of pixels in the periphery of the flow.

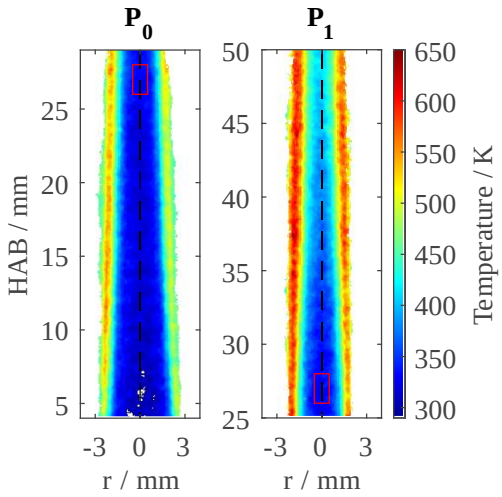

Figure 69: Temperature map from two imaging positions above the burner. The rectangle shown in red is the ROI considered for the single-point calibration to connect both imaging positions. The centerline is indicated with a black dashed line and used to extract a vertical temperature profile. P_0: lower imaging position; P_1: elevated imaging position.

Figure 70 (left) shows results from both imaging positions (P_0 and P_1) compiled into one image. The central flow is heated by the surrounding flame, and a steady increase in temperature is expected at increasing radial position, however, a local temperature maximum appears in the regime between the flame and the center flow. The relatively lower temperatures outside the maximum only stem from a few measurements and were removed by adjusting the masking condition that does exclude pixels where less than five independent measurements have contributed to the averaged signal (see above).

The transition region between both imaging positions at HAB ≈ 30 mm, where the imaging positions are stitched together, can still be identified, mostly in the boundary region between both flows where the gradients are steep (black ellipse). This can either be a post-processing artifact from the single-point calibration but could also be due to a minor hardware misalignment between both measurement positions. For example, this can occur if the laser sheet is tilted relatively to the central axis of the burner or if the burner is not perfectly vertically displaced. If this technique is used to image multiple vertical positions, this should be further investigated. However, the differences are small and negligible for this purpose. Figure 70 (right) shows various horizontal temperature profiles above the burner. The temperature increases at increasing HABs as well as at increasing radial position. In regions outside the local maximum (e.g., at 20 mm above the burner) where the temperature decreases, the uncertainty is higher because the average only consists of a few data points that could be removed by adjusting the masking condition.

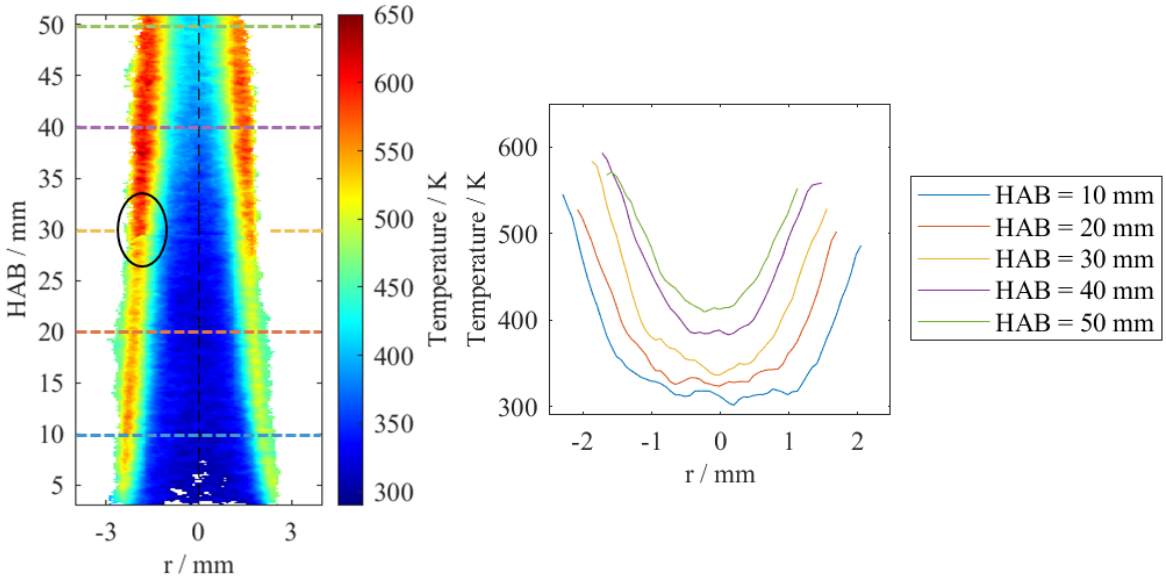

Figure 70: Left: Averaged temperature map combined from two imaging positions (P_0 and P_1) at standard flow conditions (1.96 slm) using dispersed SMP:Sn particles as thermographic phosphor tracers. The aspect ratio is not the scale to improve visibility. The horizontal line at HAB = 30 mm is intermitted to not cover artifacts from image superposition. Right: Horizontal temperature profile at various HABs as indicated on the left image. The profiles are averaged from five horizontal pixel rows.

In this section, a proof-of-concept is provided for temperature measurements in the central inert flow of the BGFR, which are particularly challenging for conventional intrusive measurement techniques due to the surrounding pilot flame (> 2000 K) and the high temperature gradients in this environment. Due to geometric boundary conditions, optical measurements here are a tradeoff between high (horizontal) resolution and the combination of multiple vertical measurement positions. A procedure to combine different vertical measurement positions by one-point calibration is proposed and implemented. In this current optical layout of 0.07 mm projected pixel size, horizontal gradients of >200 K/mm are resolved.

7.2 Temperature from particle number density measurements

The gas temperature can also be derived from variations in particle density as the particle-bearing gas expands with increasing temperature. Figure 71 (left) shows the average volumetric particle number density (PND) from elastically scattered laser light. The post-processing procedure for particle counting is detailed in Appendix A. 3: and includes noise reduction through Gaussian smoothing, which is necessary because of the globally low signal intensities. The gas temperature is calculated from the variation in PND-based ideal gas law, calibrated to the luminescence-based temperature to generate absolute temperatures, however, with some limitations. In the center of the flow, the particle number density is significantly higher than at the peripheral regions of the inner flow ($r \gtrless \pm 2$ mm), which results from two phenomena. Firstly, the central flow is heated by the burnt gases, and thus, the gas density decreases. Secondly, the surrounding burnt gas can dilute the central flow and thus reduce the PND. While neglecting gas entrainment is a reasonable assumption for analyzing the gas temperature along the centerline, this assumption is not applicable for an off-axis position close to the surrounding particle-free flow. If the co-flow, which is particle-free in this experiment, was seeded at comparable PND, the determination of temperature from the PND would be applicable throughout the entire width, including regions that are subject to flow mixing.

In regions of high temperature gradients, thermophoretic effects could still influence the PND measurements, biasing high PND towards the central (cold) part of the flow. Under constant gas temperature, aerosol particles are subject to arbitrary impulses from surrounding gas molecules. If particles are

exposed to a temperature gradient, the impulse from the side of higher temperatures is superior to that from the cold side, resulting in a net impulse towards the cold side.

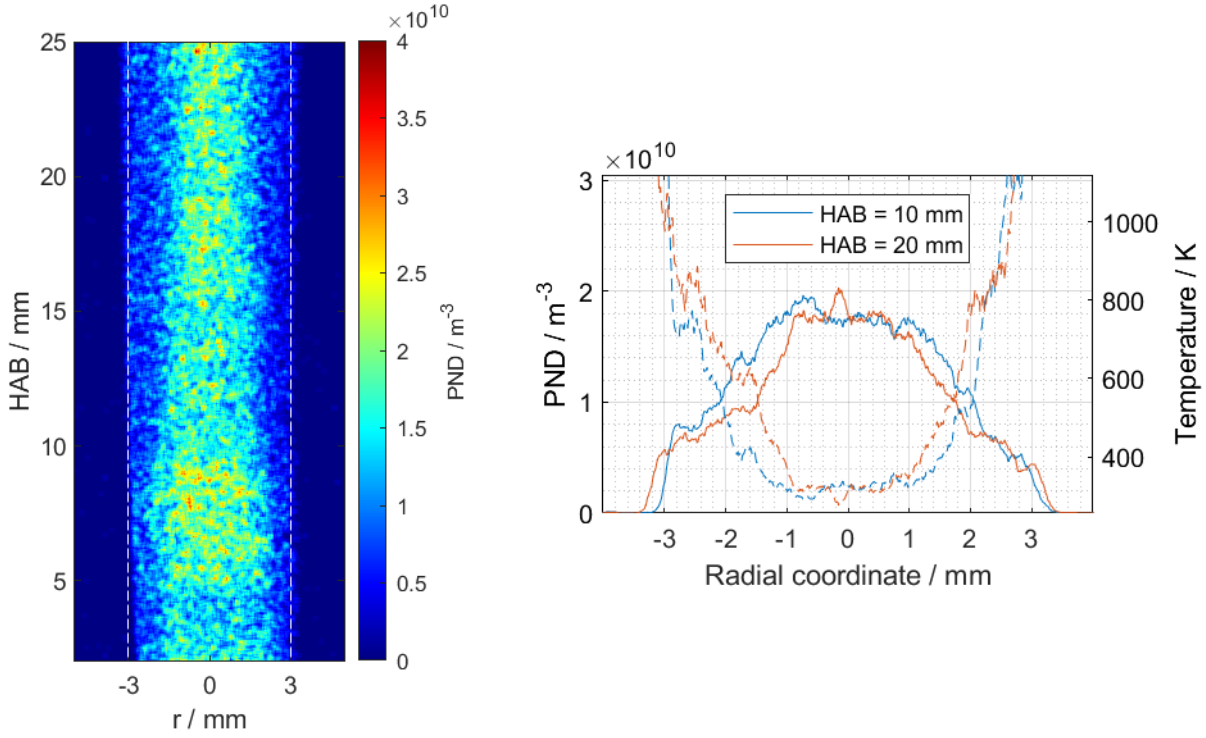

Figure 71: Left: Average 2D map of the volumetric particle number density (PND) at standard operating conditions (1.96 slm) from simultaneous measurements. Right: Horizontal profiles of PND at two different HABs. The temperature, calculated from a change in gas density, is shown on the right axis (dashed profiles).

7.3 Temperature measurements from two-color toluene-LIF thermometry

This section presents results from two-color toluene-LIF temperature measurements, which had been acquired previously within the thesis of Atheer Sallom [144]. For LIF measurements, the aerosol generator is bypassed, and toluene is vaporized in a bubbler and used as a molecular tracer for temperature measurements (Section 4.4). Both measurements employ a similar flow-stabilizing cone (h = 45 mm) and have similar measurement conditions, both in the central flow (1.96 slm) and the surrounding flame.

Figure 72 shows both signal-ratio–temperature calibration curves that are used to convert the measured intensity ratios to temperature. Toluene LIF emission spectra measured by Faust et al. [145] in a high-temperature flow cell are convoluted with the transfer function of the optical filters to calculate the calibration curve, and the ratio-dependence to temperature of SMP:Sn is measured in a heated jet (see Section 6.2.1). The post-processing procedure for toluene-LIF measurements is similar to that of phosphorescence temperature measurements. The flat-field correction is performed towards ambient temperature at seeded operation. For LIF measurements, images are only taken in one imaging position.

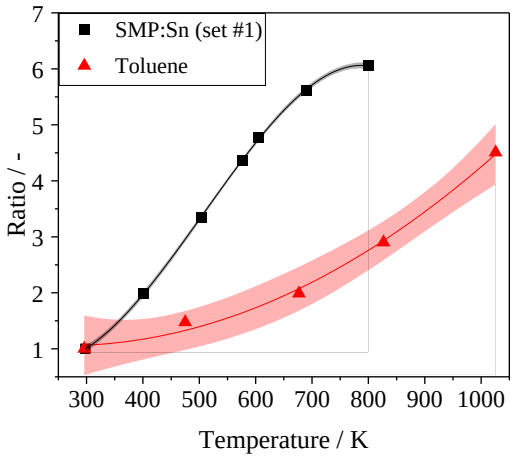

Figure 72: Signal-ratio–temperature calibration curve for SMP:Sn (filter set #1) and toluene-LIF.

Figure 73 shows two single-shot temperature measurements and the average temperature map (right) from standard measurement conditions (1.96 slm). The temperature increases towards the periphery of the central flow and, with increasing HAB, qualitatively as expected. While the vertical temperature profiles from toluene-LIF and SMP:Sn phosphor luminescence measurements are qualitatively similar, the profile from toluene-LIF is significantly higher than that of SMP:Sn. In the next section, the three previously introduced temperature measurement techniques will be discussed, and uncertainties related to the experimental setup or the measurement conditions will be identified.

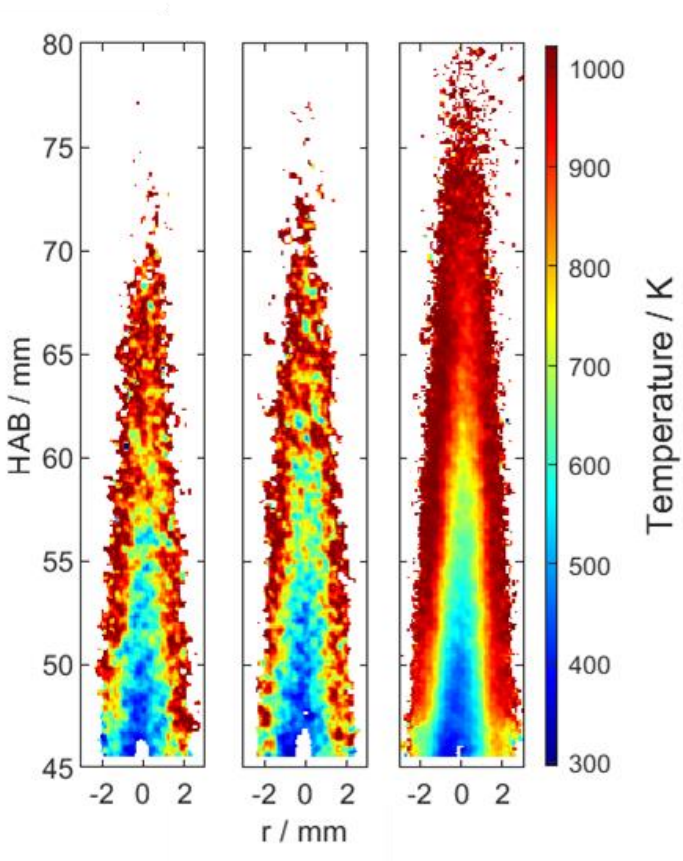

Figure 73: Two single-shot and averaged (right) temperature maps from toluene-LIF temperature measurements.

7.4 Discussion

This section aims to discuss potential errors or uncertainties related to the three temperature measurement techniques. Potential uncertainties in the LIF temperature measurements can be related to the experimental layout or data acquisition and post-processing. Toluene-LIF can potentially be affected by the presence of molecular oxygen [146]. In this experimental layout (co-flow burner with a central, inert nitrogen flow), it is possible that oxygen diffuses from the ambient air through the rich flame towards the center flow while traveling vertically with the burnt gases. The setup and experimental conditions for the measurements are similar to those in Ref. [121]. Within the work of this publication by Peukert et al., the lowest position (HAB), where O_2 can be expected in the central inert flow, is estimated to be above HAB = 180 mm. As conditions are similar, it is very unlikely that toluene-LIF temperature measurements in this present work are affected by oxygen quenching.

Toluene-LIF signal intensities are dependent on tracer concentrations, which can introduce an error if both parameters don't scale linearly. Even if the toluene concentration was not monitored in the measurements of Ref. [144], they can be expected to be close to vapor pressure (room temperature) and constant due to the architecture of the bubbler used to seed the fluorescence tracer into the central flow (see Section 4.4). Nevertheless, the non-linear signal response was reported for toluene concentrations already ten times below vapor pressure at room temperature [146]. Therefore, it is possible that temperature measurements are affected by self-quenching.

In the measurements, the laser fluences are also not exactly known, and subject to variations from the Gaussian laser sheet profile and saturation effects are reported for fluences below ~15 mJ/cm^2 [146], bearing the potential for a bias. Additionally, signal intensities from flat-field images (room temperature) are close to the saturation limit of the detector. Those pixels are excluded from the condition of the upper cut-off filter within the temperature post-processing procedure; however, the average flat field image, as a consequence, consists of fewer independent measurements that inherently increase statistical uncertainty. Non-linearities have been observed for signal intensities below the saturation limit [100], which could deteriorate the quality of the images used for the flat-field correction.

Temperature measurements in the transition area between the outer flame and the inert central flow are particularly challenging. In the outer regions of the center flow, incipient pyrolysis might have altered the tracer resulting in additional fluorescence species [147] that are likely to generate a distinct (but strong) temperature-dependent signal ratio and therefore affect temperature evaluation. Also, the thermographic phosphor tracer particles are subject to particle deterioration once a certain threshold temperature is reached for a certain duration (cf. Section 5.3)

However, in the measurements using thermographic phosphors, it is possible that the resulting flow rates of the center flow slightly differ from the measured flow rates of 1.96 slm and that the gas composition is slightly enriched with ambient air. While the presence of molecular oxygen is not a problem for measurements with the thermographic phosphor SMP:Sn [136], a higher flow rate changes the thermal history of the center flow. The operating principle of the particle seeder is to evacuate particles from the rotating ring by creating a depression from the nitrogen flowing through a venturi nozzle. The additional air added to the flow, which is induced by the depression, increases the flow rate in the central flow. This net increase can be compensated by enclosing the seeder with a semi-hermetic container and flushing the container with the same amount of nitrogen gas. As the venturi nozzle might be clogged during operation, it is possible that the compensation is not precise, and thus excess air leads to flow cooling of the measurements with the thermographic phosphors relative to the LIF measurements.

Unlike the phosphor thermometry measurements, where the central flow is inert (nitrogen), the molecular fluorescence tracer (toluene) in LIF measurements undergoes a chemical reaction that can be easily recognized by the formation of soot when toluene is added. That yields a potential source of error from the resulting thermochemistry of toluene pyrolysis and soot formation.

For future investigation, it can be of interest to use the experimental data from inert measurements with thermographic phosphors (TP) to validate CFD simulations. In a next step, the molecular tracer can be added to the simulation, and temperature can be calculated in the simulation, including the heat release from soot formation. This would allow to compare the temperature maps from both measurement approaches. Theoretically, the spectral separation of the signal from LIF and TP would allow simultaneous temperature measurements from both approaches. While the TP detection bands would be susceptible to broad-band signal interference from natural soot luminescence, this could be accounted for with background measurements.

8 T-PIV in an optical engine using thermographic phosphors

This chapter presents the results from gas temperature and velocity measurements in an optical engine under motored and fired operation using two different thermographic phosphors (SMP:Sn and YAG:Pr). Both phosphors are used with two different objectives. While the first phosphor, SMP:Sn, is beneficial for thermometry purposes due to high signal yields and a high temperature sensitivity in the desired temperature range, it cannot be used for post-combustion measurements due to particle deterioration during combustion (see Chapter 5). Therefore, this phosphor is utilized under motored operation in the first part of this chapter to validate the experimental setup and improve the temperature measurement results relative to previous measurements. Consequently, the objective of YAG:Pr is to enable temperature measurements in the post-combustion regime, which will be presented in the second part of this chapter. Despite multiple approaches in literature using various phosphors, this was hitherto not possible due to combustion or stray signal interference [71,148]. In this chapter, a novel lifetime-based camera gating approach is also presented and validated to limit contribution from combustion interference and to enable temperature measurements in post-combustion conditions.

8.1 Measurements under motored operation (SMP:Sn and YAG:Pr)

The feasibility of these simultaneous measurements in an optical engine under motored conditions was already shown in previous work using the thermographic phosphor ZnO:Zn [25,126]. Therefore, the scope of the first part (Section 8.1.2) will be limited to show the applicability of different phosphors. SMP:Sn will be applied under two measurement conditions to improve the thermographic results in terms of statistical uncertainties under motored conditions relative to previous measurements with ZnO:Zn. The optical engine and the setup improvements are detailed in Section 4.4.2. Velocity measurements are carried out simultaneously in both measurement conditions but presented separately. Subsequently, the second phosphor (YAG:Pr) will be employed for thermometry under similar, well-controlled motored engine operation to validate the novel measurement approach, which is then used in post-combustion measurements.

8.1.1 Validation against engine bulk-gas temperature: Cycle-to-cycle variation

The objective here is to measure the gas temperature via phosphor thermometry over a wide range of crank angle degrees in an optical engine under two measurement conditions (standard and increased intake temperature condition) and validate these measurements with bulk-gas temperature from the cylinder pressure. The measurement duration for a sequence[16] of multiple crank angles of one measurement condition (compression and expansion stroke, lower and upper camera position) can take up to a few hours, including the acquisition of the flat fields and the background images, depending on the required amount of engine cleaning. Even if all parameters are held constant, this can lead to variations in the cylinder pressure during a measurement sequence, mostly from progressive engine wear (e.g.,

[16] A measurement sequence consists of multiple measurements (290, 300, 310, 400, 410, 420, and 430 °CA) from one diagnostics layout (elevated camera position). The measurement at one crank angle degree consists of 200 consecutive engine cycles.

compression rings) or varying the time required for cleaning, which affects the engine temperature and, thus, the pressure trace. If phosphorescence-based temperatures from discrete measurements are compared with bulk-gas temperature traces derived from the pressure traces, the highest achievable precision is governed by the variation of the bulk-gas temperature from all measurements used within this sequence. For example, the luminescence-based temperature measured at 280 °CA is an average value from 200 single shots, resulting in 200 pressure traces. So 20 imaged crank angle degrees, thus, result in 4000 pressure traces and cycles, which are all subject to inherent cyclic variations between subsequent measurement series. So the best accuracy for the luminescence-based images cannot be better than the variations from all pressure traces where the results are compared to.

In order to determine cycle-to-cycle variations of the in-cylinder gas temperature derived from the pressure traces, the variation of the bulk-gas temperature is investigated on a cycle and a measurement-sequence basis. Figure 74 shows the variation of the calculated bulk-gas temperature from several engine cycles. The bulk-gas temperature is calculated from the cylinder pressure according to the procedure explained in Section 3.4. The left figure shows the average temperature trace from 100 consecutive engine cycles in one measurement (standard conditions) where the phosphorescence images were taken at 200 °CA. The minimum and maximum curves are shown in a transparent overlay, and the difference is shown in the bottom figure. The right figure shows the average temperature trace from 18 measurements, where the minimum and maximum temperature is displayed in a similar manner as the left figure. The temperature traces from engine runs that were used to acquire background images are not considered here because the intake pressure is different for those measurements, which would lead to a bias in the bulk-gas temperature calculation if taken into account. The standard deviation ($\pm 1\sigma$) between the averages of one measurement sequence is 19.4 K is shown with a dashed line. For all further analysis, where luminescence-based temperatures are compared with pressure-based temperatures, the standard deviation from all pressure traces will be used as uncertainty visualization ($\pm 1\sigma$) around the average pressure trace to compare against phosphorescence images. The bottom plot shows the difference between the minimum and maximum bulk-gas temperature of one measurement sequence. At 320 °CA, the maximum difference is 28 K in bulk-gas temperature. This shows that despite very good repeatability within one measurement of 100 consecutive engine cycles, there can be a larger deviation for consecutive measurements within a sequence. The effect of these variations on the pressure trace increases at increasing °CA due to the polytropic nature of the compression process up to 52 K at 400 °CA, which is the highest deviation close to the engine top dead center.

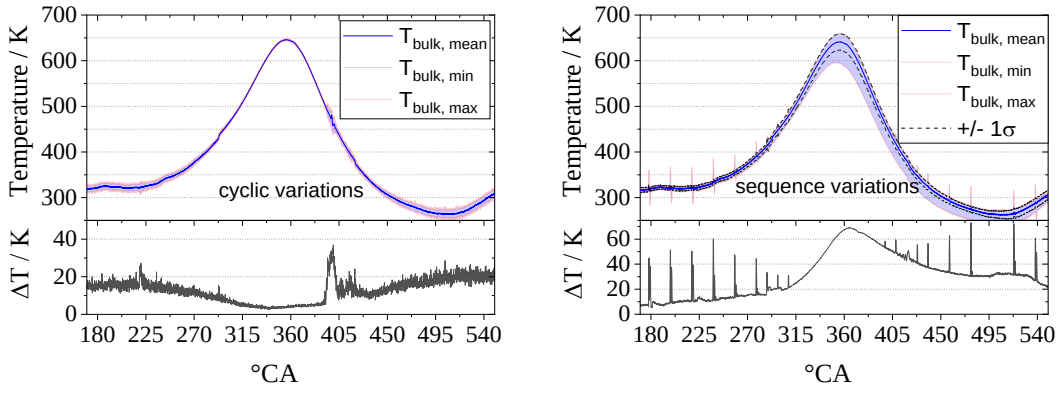

Figure 74: Left: Cyclic variation in cylinder bulk-gas temperature over 100 consecutive engine cycles for motored conditions. Right: Variations in cylinder bulk-gas temperature over one measurement sequence, consisting of eight measurements, each interrupted by the cleaning procedure. The spikes in the temperature traces are due to parasitic electronic signals in the engine signal acquisition system.

A possible explanation for these variations is not only the cyclic pressure variations in the intake manifold that determine the starting point of the polytropic compression but also the varying temperature of the engine itself. The temperature of the cylinder head is held constant by controlling the coolant temperature, however, the temperature of the quartz cylinder can change, for example, from non-constant cleaning durations between two runs. A solution to this problem would be multiple motored, unseeded runs prior to one measurement. This is, however, a tradeoff with increasing cylinder wear even under unseeded conditions due to residual phosphor particles in the crevices or the intake manifold. To minimize the insidious temperature variation, the phosphorescence images are acquired alternatingly in the compression and expansion stroke alternatingly to decrease the systematic errors over time.

8.1.2 SMP:Sn thermometry under standard & increased intake temperature conditions

Temperature measurements of the in-cylinder gas by means of phosphor thermometry are carried out in an optical engine under motored conditions at two different intake temperatures. Figure 75 shows time-averaged temperature maps from various crank angle degrees in the compression (top) and the expansion stroke (bottom rows) with SMP:Sn as a thermographic tracer at increased intake temperature conditions (T_{in} = 379 K). The images of the standard intake temperature condition are shown in Appendix A. 1: The temperature was calculated according to the procedure in Section 3.3. As the global signal intensities are high with SMP:Sn, each single shot ratio map is converted to temperature and averaged afterwards. The temperature-ratio calibration from aerosol measurements in the heated jet is applied to infer temperature. Flat-field correction is performed towards BDC (180 °CA) at seeded operation, where the temperature is expected to be homogeneous throughout the cylinder. This significantly reduces the experimental complexity. The camera position is adapted for different imaging timings to improve the field of view when the piston approaches TDC. The camera position is elevated for the measurements 290–320 °CA and 400–430 °CA in the compression and expansion stroke, respectively, when the piston would block a major portion of the field of view in the lower camera position. One flat field is acquired for each camera position as the relative position on the camera chip changes and thus the collection efficiency.

The temperature increases in the compression stroke and decreases in the expansion stroke, as expected. The piston is indicated with a sectional cut at the bottom of the field of view. Some systematic optical artifacts can be seen in Figure 75, which are mostly related to the application of the flatfield and are therefore visible only in one camera position, e.g., the lower position (180–280 °CA in the compression and 440–540 °CA. Reflections of the laser sheet are visible in (i), which are not removed by background subtraction. Excessive signal close to the optical cylinder and the cylinder head in (ii) is also due to reflections when the laser sheet crosses the cylinder. The backside of the upper end of the optical cylinder is visible in the lower camera position, as indicated by a red curved line in the temperature map at 280 °CA. This effect prevents a reliable determination of temperature in the upper part of the field of view at the lower camera position. The red rectangle indicates a region in the center of the cylinder that is used for temperature determination, which is then compared to the bulk-gas temperature derived from

the measured pressure trace. The region used to calculate temperature is maintained constant throughout several CAD, if possible, to reduce the impact from systematic interferences introduced above.

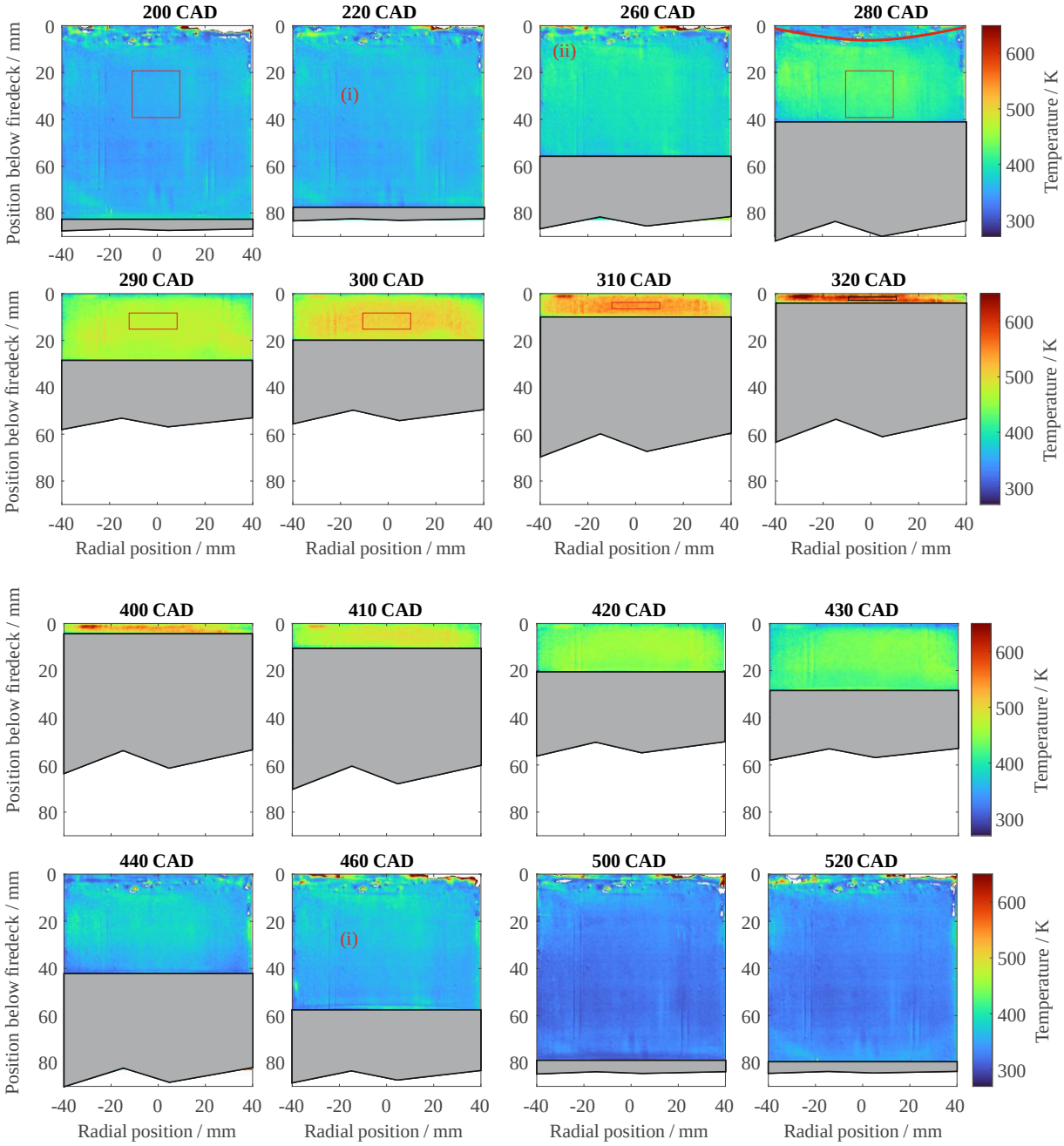

Figure 75: Averaged temperature maps from SMP:Sn phosphor thermometry at various °CA at increased intake temperature. The region used for temperature calculation is marked with a box.

Figure 76 compares the averaged temperature from the ROI from the two-color phosphor luminescence measurements to the bulk-gas temperature calculated from the cylinder pressure at standard (T_{in} = 322 K) and increased intake temperature condition (T_{in} = 379 K). The temperature from the thermocouple (25 µm tip diameter) located at the position of an exhaust valve (see Section 4.5.4) in the engine is used as a reference at BDC to calibrate the average bulk-gas temperature derived from the pressure trace. The temperature derived from SMP:Sn phosphor thermometry is in excellent agreement with the expected bulk-gas temperature at the beginning of the compression stroke at both conditions. At 300 and 320 °CA, the temperature from phosphor thermometry underestimates the bulk-gas temperature up to ~50 K at 320 °CA at standard intake condition. Even though the single-shot precision that

represents the variation between different cycles is very low (2.1%, 9.5 K at 320 CAD), the small ROI close to the cylinder head is susceptible to systematic interference. The temperature at 400 °CA at the standard condition is subject to a bias from the strong scattered signal from the cylinder head and can be considered an experimental outlier (see images in Appendix A. 1:). A repetition measurement was not carried out for this crank angle degree.

In the expansion stroke, the luminescence-based temperature information is in excellent agreement with the bulk-gas temperature for elevated temperatures. However, as the gas temperature approaches ambient temperature and falls below in the expansion stroke, an increasing number of pixels in the single-shot images are also below the ratio for ambient temperature (lowest temperature in the ratio-temperature calibration) and are thus not considered for temperature calculation, because the ratio-temperature calibration curve is not extrapolated below ambient temperature. Therefore, the temperature is overestimated towards the end of the expansion stroke. This effect is very pronounced for the standard intake temperature condition, where the bulk-gas temperature is below ambient temperature, but also for the increased intake temperature, where the bulk-gas temperature is slightly higher but is also overestimated by the limited calibration curve. This effect of clipping the calibration curve is reasoned in Section 6.2.1. In future measurements, and if the analysis focuses on the expansion stroke at temperatures close to or below ambient temperature, the calibration curve should be extended to sub-ambient temperatures. To sufficiently account for statistical uncertainty in the temperature measurements, the lowest ratio of the ratio-temperature calibration curve should be at least 1σ ratio-equivalent below the lowest temperature. In other words, the lowest reliable temperature is 1σ above the minimum temperature covered in the calibration curve.

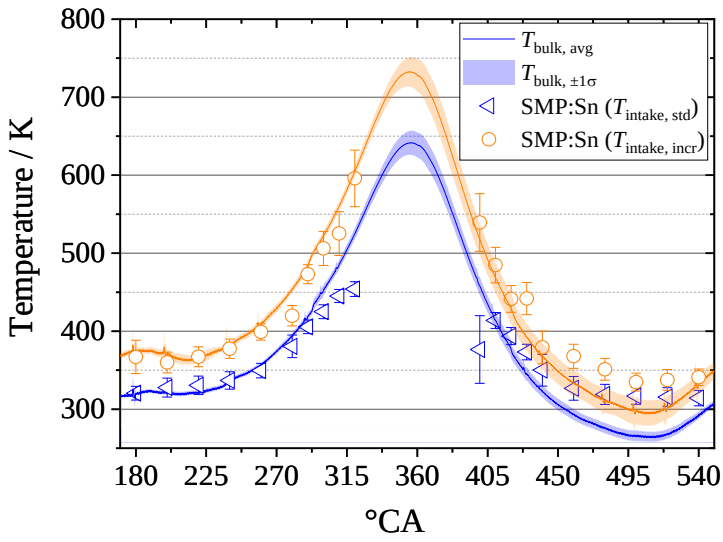

Figure 76: Temperature derived from two-color luminescence measurements using SMP:Sn (shown with symbols) and bulk-gas temperature derived from the in-cylinder pressure (solid line) for standard (blue) and increased intake temperature conditions (orange). The transparent overlay to the bulk-gas temperature represents the $\pm1\sigma$ deviation from the bulk-gas temperature averaged over all measurements concerned. The flatfield (at BDC) for both test cases is recorded at standard condition. The error bars denote the pixel-based shot-to-shot deviation (single-shot precision) and is calculated according to Equation 23 in Section 2.5.1.

Figure 77 shows single-shot images from various crank angle degrees from increased intake temperature condition. Some of the artifacts can still be observed in these images, e.g., the vertical reflections of the laser sheet (i). In 260 and 420 °CA, some highly inhomogeneous spots are visible and pointed with an arrow (ii). These spots stem from phosphor agglomerations, and the high gradient around it indicates a mapping error. The image post-processing procedure for the engine measurements does not include the

single-shot-based mapping algorithm (Section 3.3.2), as the expected temperature field in the engine is homogeneous. Reflections from the cylinder head are also observed (iii) in the single-shot images at all crank angle degrees where the camera is in the low imaging position. The temperature map at 520 °CA has some white spots in the center of the cylinder. These pixels are not considered for temperature calculation as they fall below the lowest value in the calibration curve.

In comparison to previously obtained single-shot images under similar measurement conditions using ZnO:Zn [25], where the temperature cannot be imaged in large areas in the cylinder due to low signal intensities, the strong phosphor luminescence of SMP:Sn allows calculating temperature in >95% of all images of a cycle. In the following section, the single-shot images will be used to estimate the single-shot precision and compare it to the phosphor ZnO:Zn, as well as the signal-to-noise ratio of both phosphors.

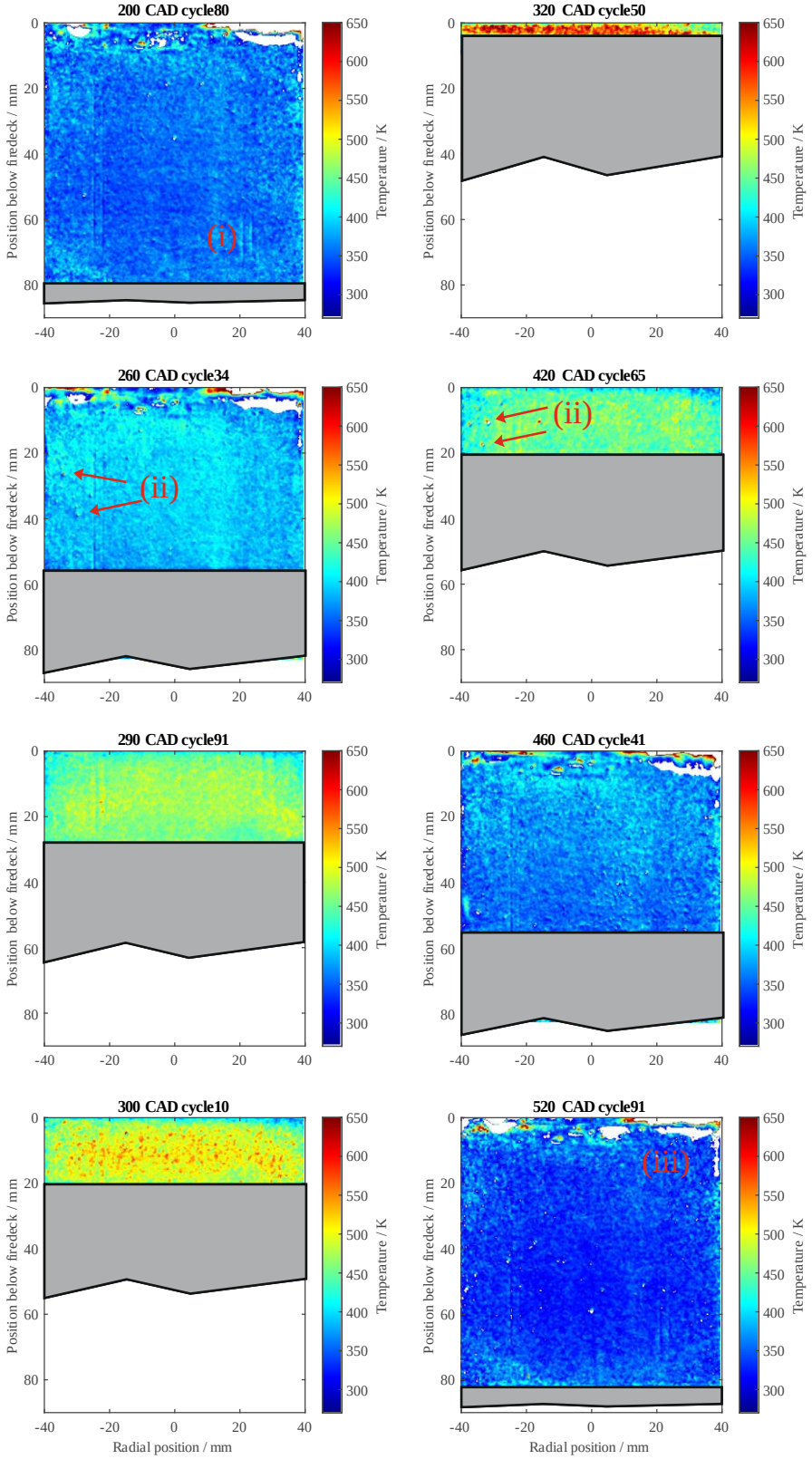

Figure 77: Single-shot temperature maps at various CAD from the increased intake temperature condition.

8.1.3 Uncertainty estimation from SMP:Sn thermometry and comparison to previous work

In this section, the error of the temperature measurements in the engine will be evaluated and compared with previous engine measurements using ZnO:Zn [25] in terms of single-shot precision and signal-to-noise ratio. The comparison is based on the data sets of the increased intake temperature condition from both measurements (ZnO:Zn and SMP:Sn) since this is the more challenging operation point.

Figure 78 (left) shows the signal-to-noise ratio (SNR) for two different phosphors used in the engine for temperature measurements. The SNR from both imaging channels of the phosphor SMP:Sn that are used for thermometry in this work are shown in color and compared to the SNR of the thermally quenched imaging channel from previous measurements using ZnO:Zn [25]. The signal is averaged from the ROI used for temperature calculations (rectangle in Figure 75), and the noise is inferred from a representative region outside the cylinder after subtraction of the background. Even if the global particle number density (PND) might vary from both measurements, the signal loss relative to ambient temperature can be used to compare both phosphors.

In Figure 78 (left), two contrasting phenomena can be observed. At increasing temperatures, the signal decreases due to thermal quenching, but the PND increases as the volume decreases[17], which again increases the global signal intensity. It is also known from measurements with SMP:Sn that the phosphor luminescence initially increases with temperature [149]. While the SNR for ZnO:Zn measurements in previous work approaches unity at increasing temperatures, the SNR for SMP:Sn measurements is always above ~4.5 at high temperatures. This shows that the decrease in volume in the cylinder at increasing piston position, which comes along with an increase in signal, overcompensates the signal loss from thermal quenching for SMP:Sn. This fact is beneficial for high-precision measurements in the engine and makes SMP:Sn superior to the previously used ZnO:Zn. This significant margin in the excessive signal would even allow the choice of more temperature-sensitive filters to the detriment of signal intensity.

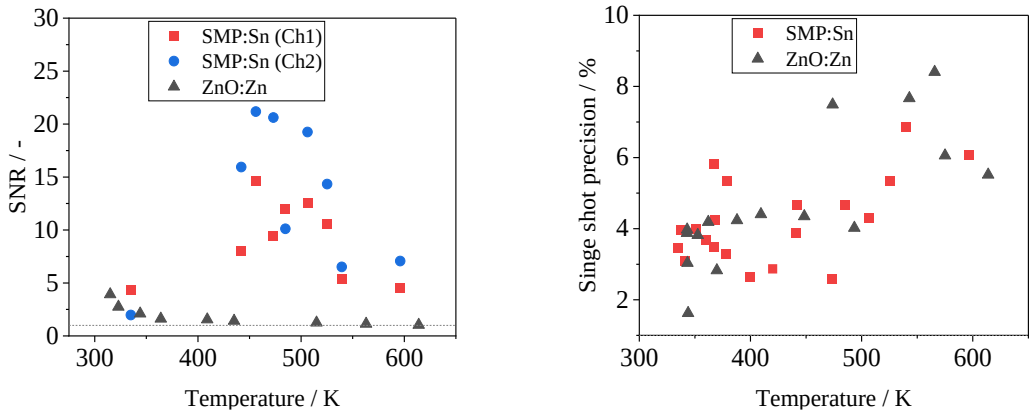

Figure 78: Comparison of two phosphors SMP:Sn and ZnO:Zn, for temperature imaging in the optical engine. The data for ZnO:Zn is taken from Ref. [25]. Left: Signal-to-noise ratio (SNR) of both imaging channels (SMP:Sn) and the thermally quenched imaging channel (ZnO:Zn) for two phosphors in an optical engine under motored condition. A reference line for SNR = 1 is shown to guide the eye. Right: Relative temperature single-shot precision for both phosphors (pixel-to-pixel variation calculated according to Equation 23 in Section 2.5.1).

Figure 78 (right) compares shows the relative temperature single shot precision for both phosphors. Both phosphors have approximately the same single-shot precision, with SMP:Sn being a little bit lower at elevated temperatures. The highest precision (and thus the lowest accuracy) is 8.4% for ZnO:Zn (47.5 K at 565.7 K) and 6.8% (36.9 K at 539.5 K) for SMP:Sn, providing improvements of nearly 20% relative

[17] The geometric compression ratios are very similar (ε = 10.3 in this work and 10.5 in the Ref. [25]).

to previous measurements using ZnO:Zn. Note that the single-shot precision data for ZnO:Zn varies slightly from the values given in Ref. [25], as the spatial single-shot deviation was calculated in this work instead of the temporal single-shot deviation, which is usually considered the single-shot precision (see Section 2.5) in respective literature. In Figure 78 (right), the temporal single-shot deviation is calculated for both phosphors to make the accuracy of both phosphor-based measurements comparable.

8.1.4 SMP:Sn velocity measurements under motored operation

The temperature measurements in the optical engine were presented in the previous chapter. Temperature and velocity measurements are acquired simultaneously, but the associated velocity results are presented separately for the ease of reading. Velocity data are acquired for both intake temperature conditions, but the present results show the increased intake conditions. The objective of this section is to show the feasibility of simultaneous temperature and velocity measurements using SMP:Sn following the T-PIV approach. A fidelity check, showing that these particles can be used for flow tracing of large-scale flow structures such as the tumble movement in the cylinder, is provided in Section 2.4.2 for in-cylinder conditions encountered in the engine. The PIV setup and engine layout is shown in Figure 40, and the PIV data are post-processed, as detailed in Section 3.5.

Figure 79 shows the velocity fields at various °CA in the optical engine using SMP:Sn as an optical tracer. Only every 6^{th} velocity vector is shown to improve visibility, and mirrored °CA around TDC are shown on the left and right column, respectively, to facilitate the comparison between the flow field in the compression and expansion stroke. The intake valve is located on the left side. At BDC, the intake valve is still open (42% of the total valve travel), and the air flows into the cylinder on both sides of the intake valve. The intake valve closes at 215 °CA (10% of total travel). A tumble forms on the bottom of the cylinder already at BDC and does not collapse until the highest crank angle imaged (320 °CA). The flow motion in the expansion stroke is governed by the down movement of the piston between 400 °CA and 500 °CA. The exhaust valve opens at 510 °CA (10% of total travel), and high gas velocities are encountered at 520 °CA (not shown) and 540 °CA on the right side of the cylinder, where the exhaust valve is located. The results for the in-cylinder flow under motored operation are as expected, and the data is in excellent agreement with similar engine conditions from previous work [25]. Note that the engine conditions “increased tumble” in the reference is similar to the condition presented in this work, as the intake flaps to improve tumble motion are used as a baseline for these measurements.

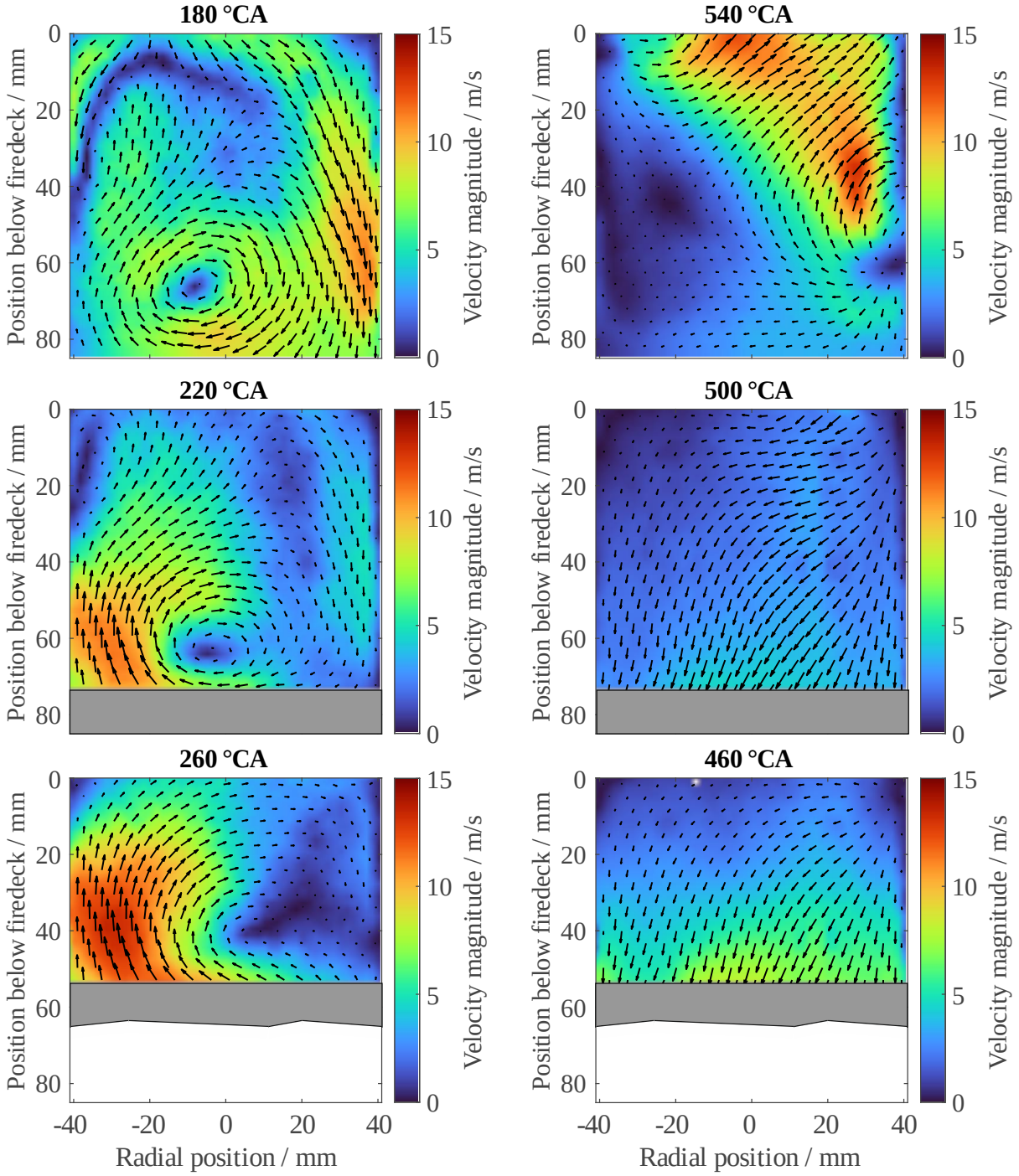
180 °CA
540 °CA
220 °CA
500 °CA
260 °CA
460 °CA
Position below firedeck / mm
Velocity magnitude / m/s
Radial position / mm
0
20
40
60
80
-40
-20
0
20
40
5
10
15

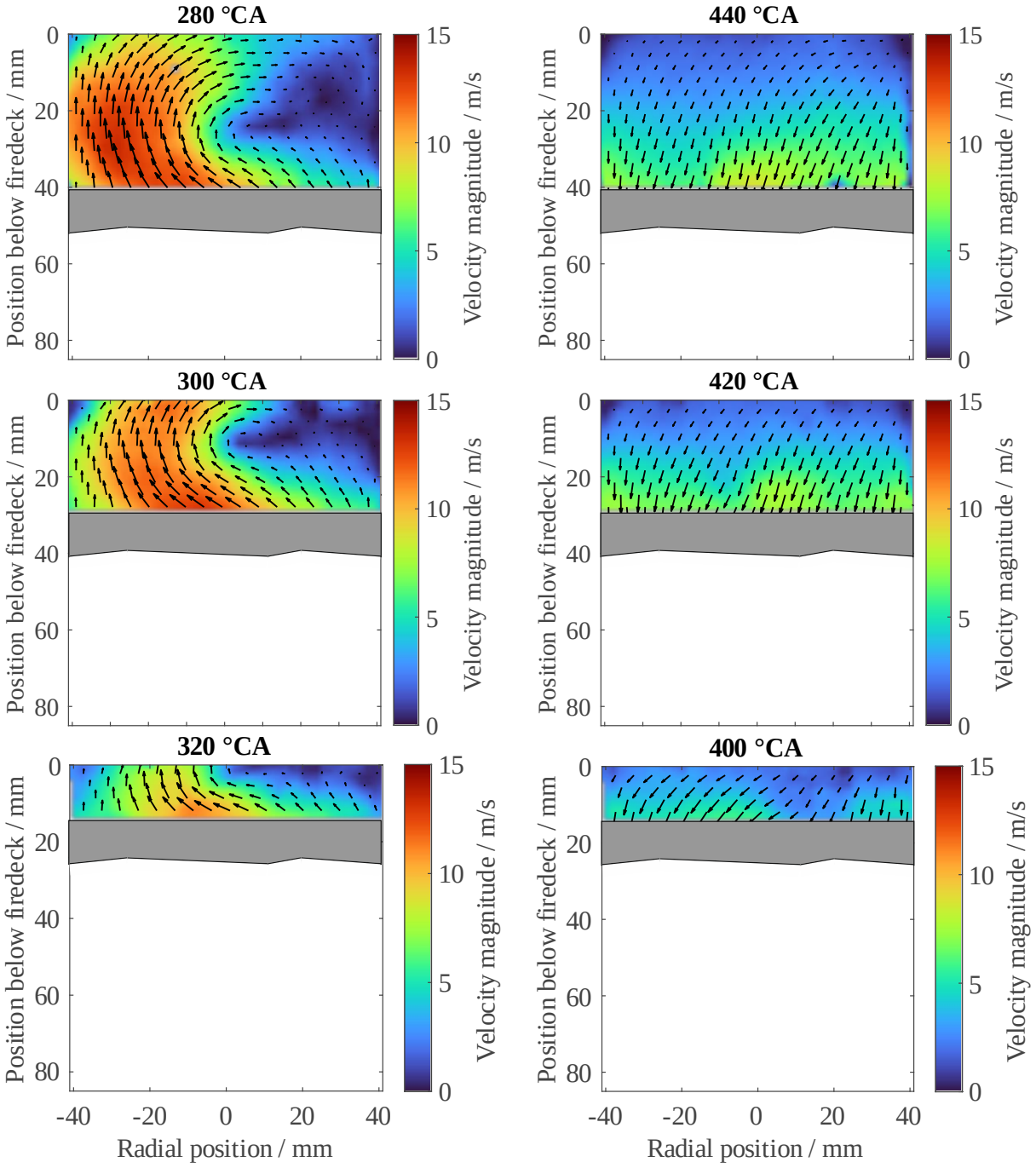

Figure 79: Time-averaged velocity fields in the engine under motored conditions at standard intake temperature using SMP:Sn as PIV tracer. Only every 6th velocity vector is shown for improved visibility. The compression stroke is shown on the left column, and the expansion stroke on the right column on both pages. The mirrored crank angle degree around TCD is shown in the same row, respectively. The piston is indicated as a gray rectangle.

8.1.5 Validation of the novel YAG:Pr thermometry approach under motored operation

The previous sections presented T-PIV results with SMP:Sn as a thermographic phosphor in motored engine operation and compared it with previous results from ZnO:Zn from Ref. [25]. YAG:Pr is less suitable for temperature measurements under inert conditions than SMP:Sn due to its lower global luminescence yield, which determines its best achievable temperature precision, and not at least its lower temperature sensitivity. However, measurements in post-combustion gases require the use of YAG:Pr (cf. Section 5). These measurements also require the use of a novel measurement approach that reduces interfering signals. This approach combines a lifetime-based gated camera approach that uses the lifetime of the phosphor at the estimated target temperature to adjust the exposure duration of the camera and the double frame imaging mode (Section 3.6) for *online* background subtraction. The objective of this section is the validation of this measurement approach, later used in post-combustion measurement, in a relatively well-controlled environment as it is found under motored operation.

Additionally, intensity-modulated illumination is applied to estimate the contribution of multiple scattering in the engine from YAG:Pr and to evaluate its impact on temperature calculation. This assessment is important for the interpretation of the post-combustion measurements, where the fraction of particulate matter varies with each measurement and can be subject to large spatial gradients at varying crank angle degrees. The laser sheet is entirely blocked every 5 mm by a height of 1 mm, where the laser sheet penetrates the optical ring, so the spatial illumination frequency is $f = 0.2\ \mathrm{mm}^{-1}$. The laser sheet is blocked at 7.5 and 12.5 mm below the fire deck, which is referred to as the laser "off" regions, and undisturbed at 10 mm (laser "on" region).

There are three objectives of this section: Firstly, the thermographic images are presented, and the temperature is calculated according to the novel measurement approach in a similar manner as later used for post-combustion temperature measurements. The temperature is compared against the cylinder gas temperature derived from the cylinder pressure. Secondly, the impact of structured illumination is evaluated on the calculated temperature, and lastly, the accuracy of the lifetime-based gated approach is determined with some additional error calculations.

Figure 80 shows the average ratio and temperature fields at various crank angle degrees under motored conditions using YAG:Pr. The red camera is operated in the double-imaging mode (cf. Section 3.6.1), and the camera exposure timing is set to 3τ of the lifetime of the temperature expected at the respective crank angle degree, based on previous measurements. All images are hardware binned (2 × 2 pixels) and post-processed according to the double-imaging procedure introduced in Section 3.6.4 for motored operation. The ratio-temperature calibration from aerosol measurements is used to translate the ratio to temperature (Figure 67). The top image in Figure 80 shows a ratio image at BDC that is used for flat-field correction. The vertical structure following the structured illumination, both in the ratio and temperature map, is congruent with the structure from intensity-modulated illumination, which was applied to evaluate the impact of potential multiple scattering and will be discussed in the next paragraph of this section. The vertical marks at the right and left side of the cylinder (between ±20 and ±30 mm) are reflections from the laser and are considered an artifact. The following images show the temperature at various crank angle degrees, and the gas temperature increases during the compression stroke and decrease during the expansion stroke as expected.

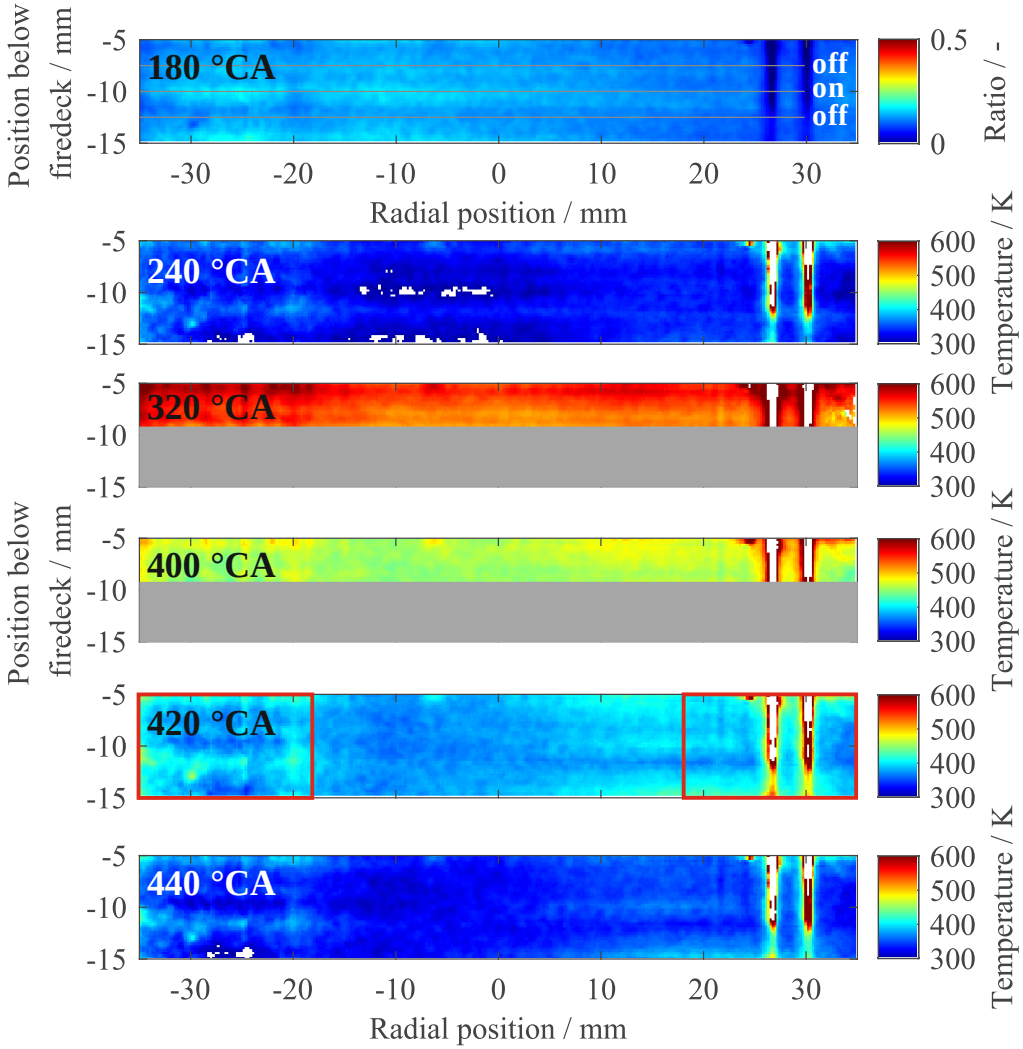

Figure 80: Average ratio image (top) and average temperature maps for various crank angle degrees in the compression and expansion stroke with YAG:Pr under motored conditions. The exposure duration of both cameras is set according to the expected lifetime (3τ) at this crank angle degree. The camera of the red imaging channel is operated in the double imaging frame mode and is also used for *online* background subtraction. The piston partially blocks the field of view at 320 and 400 °CA. The horizontal lines in 180 °CA indicate the regions of structured laser illumination, where the laser is entirely blocked (at 7.5 and 12.5 mm) and unmodulated at 10 mm. The red rectangles in the image of 420 °CA indicate the region that is neglected from the analysis due to reflections of the incident laser sheet.

As a first analysis, the temperature from laser "on" regions (10 mm below the fire deck) is probed and compared to the bulk-gas temperature of the cylinder gases in Figure 81. The intake pressure of the engine is reduced to 0.65 bar, similar to the intake pressure for post-combustion measurements, which globally results in lower gas temperature relative to previous measurements with SMP:Sn. To calculate the temperature from luminescence images, the average temperature is derived from 5 pixel rows (~1.15 mm width) from the images at 10 mm below the fire deck[18]. Due to the vertical reflections of the laser sheet, only the region in the center of the cylinder (–18…18 mm) is considered for temperature calculation. The error bars in the YAG:Pr measurements represent the single-shot precision ($\pm 1\sigma$) following Equation 23 in Section 2.5. The temperatures inferred from YAG:Pr phosphor thermometry is in very good agreement with the bulk-gas temperature. This shows that YAG:Pr, as a thermographic phosphor, enables measuring temperature using the lifetime-based exposure time approach in the engine.

[18] For the 320 and 400 °CA, the average is calculated at approx. –9 mm to avoid interference due to the elevated piston position.

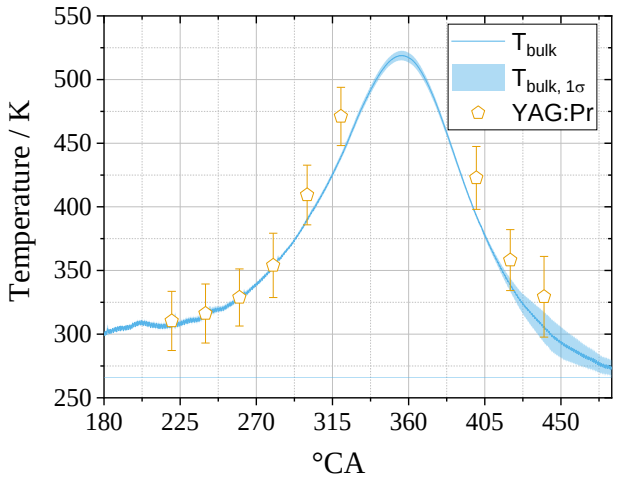

Figure 81: Engine bulk-gas temperature and temperatures derived from YAG:Pr two-color luminescence at various crank angle degrees under motored operation. The temperature is calculated for a location 10 mm below the cylinder deck and averaged from five pixel rows. The error bars represent the single-shot precision (±1σ) calculated according to Equation 23.

In the second analysis, the impact of intensity-modulated laser illumination on gas temperature calculation from two-color phosphor thermometry is evaluated. Figure 82 shows the temperatures calculated from different regions of the laser sheet. The three different heights are shown with horizontal lines in Figure 80, and five pixel rows (~1.15 mm) are considered for temperature calculation in the center of the cylinder (–18…18 mm).

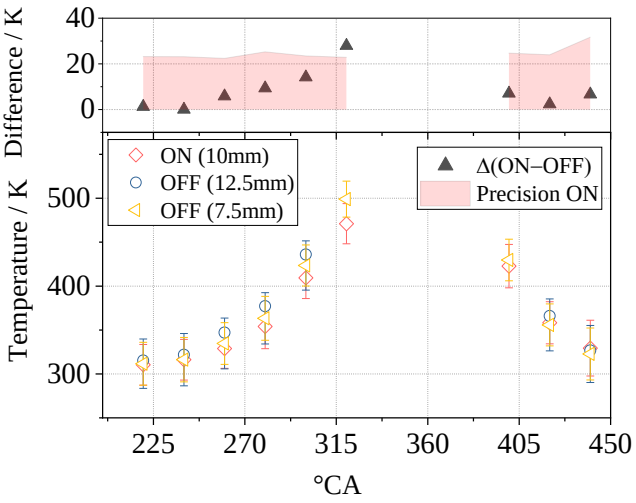

Figure 82: Temperature measurements from YAG:Pr phosphor thermometry for modified intensities of the laser sheet profile. “OFF” represents regions where the laser sheet is blocked. The error bars represent the single-shot precision (±1σ) and are shown as a transparent overlay on the upper plot (from 10 mm). The upper plot shows the temperature difference between the “on” and “off” regions of the laser sheet.

The temperatures from all three heights from two differently illuminated areas follow qualitatively the same trend and increase towards the top dead center. Both temperatures from “off” regions are almost similar. The error bars show the temporal single-shot precision (±1σ). The absolute temperature difference between “off” and “on” is shown on the upper plot and increases with increasing piston position to a maximum of 14 and 28 K at 300 and 320 °CA, respectively. The single-shot precision (+1σ) from the “on” regions is around 25 K and shown as a red transparent overlay. The temperature difference is always, with the exception of the measurement at 320 °CA, inferior to the single-shot precision. Therefore, the temperature difference between regions where the laser is blocked (“off”) and unmodulated (“on”)

is statistically not relevant and can be neglected. It should be noted that the temperature from the "on" position at 320 °CA is calculated in a region in very close proximity to the piston surface (9 mm instead of 10 mm for this crank angle where the piston is located), so it is possible that reflections from the piston induce an additional bias to this measurement.

The analysis shows that temperature-dependent luminescence can also be detected in regions that are not directly illuminated by the laser sheet but only indirectly by elastically scattered light. At increasing crank angle degrees, the particle number density increases by a factor of ~4 between 220 and 320 °CA due to compression of the cylinder charge[19] , and the contribution of multiply scattered light increases constantly. This can be both elastically scattered laser light that excites the phosphor particles in an off-region or phosphorescence emitted in the on-region and elastically scattered by a particle in the off-region towards the camera. Reabsorption for this phosphor is not very likely as the blue emission peak (489 nm) is separated by ~180 nm from the region, where the absorption intensity has dropped to 10% of that one of the closest absorption peaks (310 nm) [150].

This approach does not allow us to quantify the temperature bias from multiple scattering, also because the image postprocessing does not include low-pass filtering in the frequency domain as required within the SLIPI approach [151,152], which would be beyond the objective of this study. However, this measurement shows that there is strong out-of-plane illumination and that the temperature information stems from particles in the laser plane (even if they are not directly illuminated) rather than signal interference from cold particles sticking to the cylinder wall, which were shown to be a significant source of error in previous measurements using ZnO:Zn [25,126]. The temperature from off-regions in the laser sheet slightly underestimates the temperature from on-regions, even if it is within the single-shot precision. It is possible that cold particles from the cold cylinder wall also contribute and bias these measurements towards lower temperatures. However, the temperature difference is only 14 K at 300 °CA and can be considered negligible given the single-shot precision of 23.4 K from the "on" measurement at this crank angle (4.9% at 471 K).

The systematic error of this measurement approach is evaluated and introduced by estimating the exposure time duration from an estimated temperature. In this approach, an initial guess of the phosphor lifetime at the estimated cylinder temperature is used to set the exposure duration of the respective imaging camera (3τ). In both channels, the same proportion of the signal (~95% from 3τ) has to be captured to avoid an additional systematic error from applying the calibration curve. If the real gas temperature in the engine varies, the decay characteristics also vary, so different proportions of the signal are captured due to an erroneous camera exposure duration. This can be particularly severe for YAG:Pr as the luminescence lifetime for both emission channels inversely scales with temperature (Figure 57). For example, for the first measurements during the compression stroke (180–220 °CA), the temperature is estimated to be near-ambient, so the lifetime of the red emission channel is 110 µs, and thus, the camera gating is set to 330 µs. However, the temperature in the engine at 220 °CA is 322 K as of the images from phosphor thermometry, which results in a lifetime of 115 µs.

[19] The residual volume in the cylinder is 116 and 470 cm^3 at both crank angles, respectively.

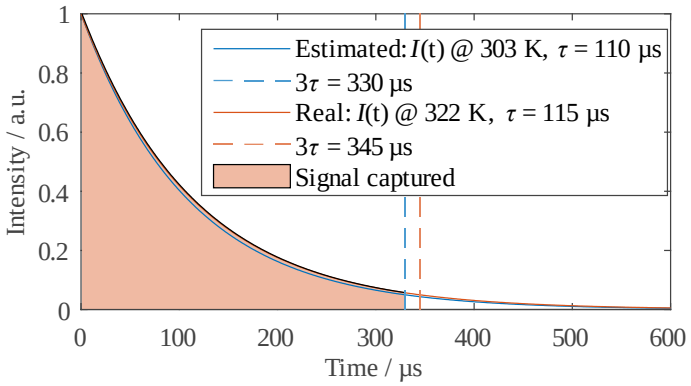

Figure 83: Modeled intensity decay curves of the luminescence emission, based on mono-exponential emission characteristics, captured in the red imaging channel (~610 nm) at the estimated and real temperature at 220 °CA. The variation of the lifetime constant induces an error from applying an erroneous lifetime constant as exposure duration from an initially guessed temperature to a measurement of dissimilar temperature.

Figure 83 shows modeled decay curves for both temperatures with the respective 3τ annotated as a vertical dashed line. The modeled decay characteristics are based on the mono-exponential intensity decay function. For the red emission band of YAG:Pr, the lifetime initially increases, so the phosphor decay curve at the real temperature in the engine is slightly higher but less than the signal from 3τ is captured. In this case, 99.3% of the signal obtainable from 3τ is captured in the red, and 100.1% of the 3τ signal in the blue channel, respectively. For the blue emission band, the lifetime continuously decreases, so more than 3τ is captured if the temperature is underestimated. The ratio of both signals gives 0.9916 of the ratio which would be obtained from exact 3τ exposure of both channels, which translates into a temperature error of approx. 2 K. Figure 84 shows the measured temperature from the estimated lifetime together with the residual to the corrected temperature from the real phosphor lifetime over crank angle degree. The measurement error based on an incorrectly assumed lifetime of the phosphor emission is within ±5 K relative to a measurement with the correct camera exposure. This shows that the measurement approach using lifetime-based camera acquisition parameters is valid despite inherent uncertainty due to varying phosphor emission lifetime at varying temperatures. This estimation can also be applied when large spatial temperature gradients are present, and the global camera exposure is not equal to 3τ of the phosphor luminescence emission at different temperatures.

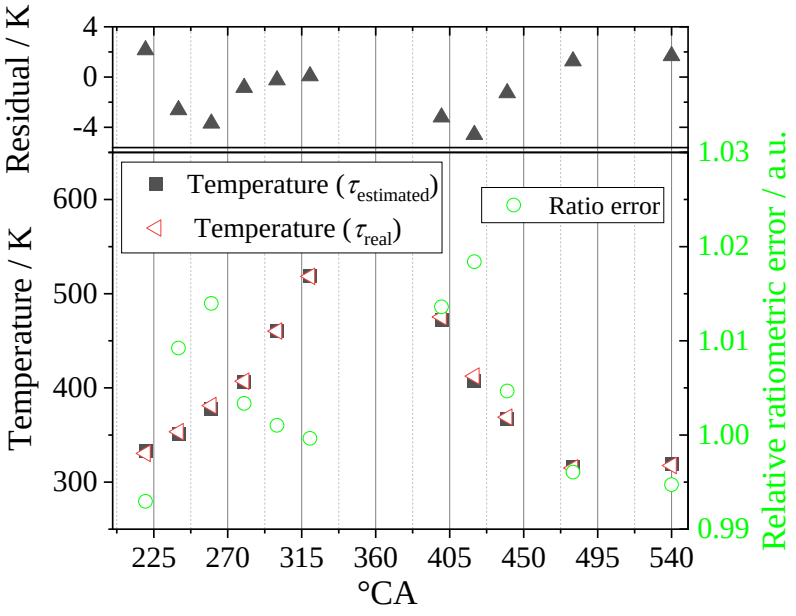

Figure 84: Accuracy calculation of temperatures acquired from measurements with camera exposure from estimated lifetime compared to temperatures theoretically calculated with the real lifetime.

Under these conditions, the error is well below the single-shot precision, also because the temperature is rather homogeneous throughout the engine, and it can be assumed accurately. This error is expected to be significantly larger when this measurement approach is applied to post-combustion measurements.

In this simplified error evaluation, it is assumed that the change in the absolute emission intensity is small in comparison to the change due to shortened lifetime for small temperature deviations. Furthermore, the emission decay of the red emission band is modeled with a mono-exponential decay curve using the long luminescence lifetime component, as this is the relevant one for the camera gating.

8.2 Post-combustion temperature measurements (YAG:Pr)

In the last chapter, a novel temperature imaging approach was presented and validated in an optical engine under motored conditions with YAG:Pr based on adaptive camera exposure times. It was shown that a systematic error stemming from incorrectly assumed exposure is well below the pixel-based single-shot precision of this approach. In this section, the same approach is applied to the post-combustion regime on the optical engine. All engine and post-processing parameters remain similar as before. The injection and ignition parameters are detailed in Section 4.5.1.

8.2.1 Thermographic measurements

Figure 85 shows the average temperature distribution of the post-combustion gases in the optical engine at 580 °CA using the thermographic phosphor YAG:Pr. The postprocessing procedure of the double-imaging settings of the camera is detailed in Section 3.6.4., most notably with the different images used for background correction. Due to increased engine load and resulting peak pressure, the optical cylinder was replaced with a 20 mm quartz ring but is similarly positioned relatively in the engine below the fire deck (cf. engine layout in Figure 41). The exhaust valve is shown on the top left (not to scale). The data close to the quartz ring at radial positions $r \gtrless \pm 35$ mm is excluded due to systematic interference from scattered laser light from the quartz ring.

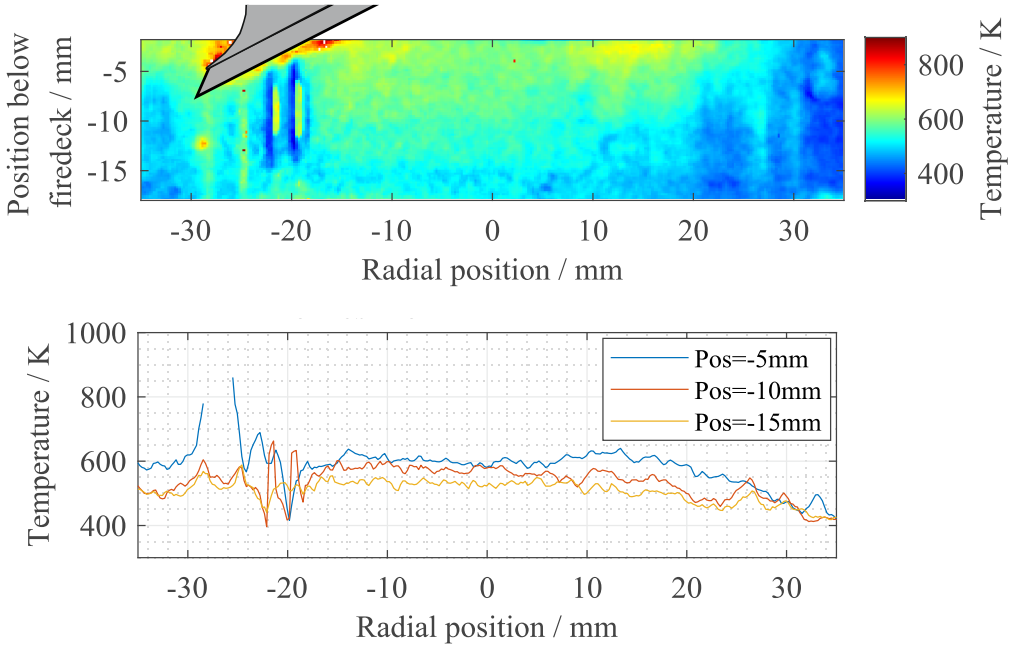

Figure 85: Average 2D temperature field (top) and temperature profiles at various heights (bottom) at 580 °CA in the post-combustion gases with YAG:Pr extracted from one pixel row. The exhaust valve is qualitatively shown on the top left at valve travel position $h(\alpha$=580 °CA) = 8.01 mm.

The temperature distribution is mostly homogeneous throughout the cylinder. Towards the cylinder walls, the temperature slightly decreases relative to the center. The temperature on the exhaust side (left)

is generally higher than on the side of the intake port (right), and the temperature difference becomes more significant at increasing distances below the fire deck.

The bottom figure (Figure 85) shows three temperature profiles at different heights below the fire deck, which are extracted from one pixel row. All profiles are quantitatively similar, but two trends are observed: the gas temperature increases slightly at increasing vicinity towards the fire deck, and the temperatures on the exhaust side are higher relative to the intake side. Both trends are expected as the intake side of the engine is cooled from fresh gases, and the fire deck is the hottest region in the engine. Some systematic interference from scattered laser light that could not be removed in background subtraction can be seen in both figures as vertical lines between $r = -20 \ldots -30$ mm.

Figure 86 shows the same temperature information for earlier crank angle degrees (560 and 540 °CA). The exhaust valve is only qualitatively shown and not to scale. The gas temperature at 560 °CA is qualitatively similar and approximately 50 K higher relative to the temperature at 580 °CA. This is expected from the temperature calculation from the cylinder pressure trace and will be compared to luminescence-based temperature information in the next section.

The temperature distribution of the in-cylinder gases at 540 °CA is less homogeneous. Neglecting the reflections from systematic interferences, it shows two zones of slightly increased temperatures in the vertical center and horizontally at ±15 mm. The temperature information at these horizontal positions indicates that the hottest center of this region is towards the lower end of the field of view (–20 mm below the fire deck) or even below. It is not entirely clear if this effect is physical or an artifact from data post-processing, so two hypotheses are proposed. It is possible that the correction for combustion-related interference based on the dual-imaging approach is not sufficient at early crank angles. If the combustion interference (measured in frame 1) is too strong to be corrected, the signal-ratio decreases (see Equation 36) and thus the derived temperature. The combustion interference is strongest in the center of the cylinder (see Figure 25). Therefore, it is possible that this contribution leads to a too-low temperature. However, this can also be physical, for example, an effect from the exhaust flow dynamics. At 540 °CA, the exhaust valve just opened (10% travel at 520 °CA), thus, the recently opened valve induces a tangential flow motion relative to the exhaust valve that could induce a tumble backflow from the center of the cylinder.

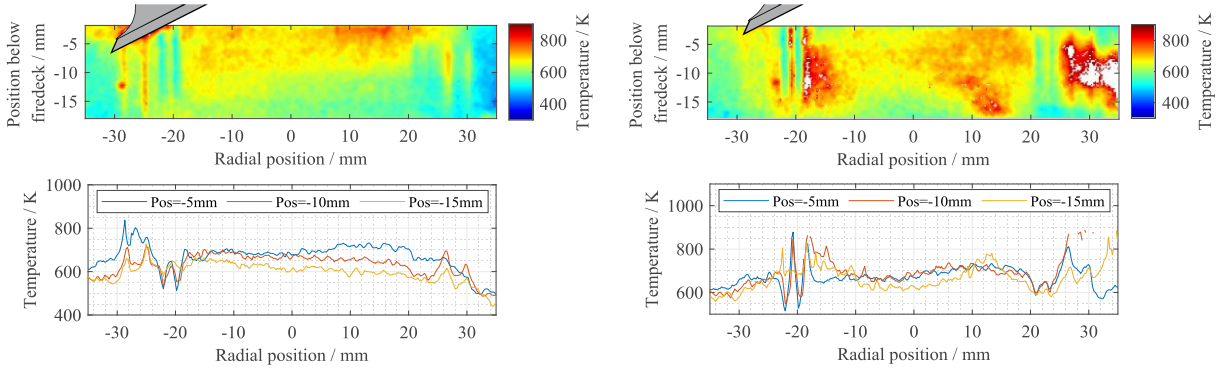

Figure 86: 2D temperature information for 560 (left) and 540 °CA (right). The exhaust valve is qualitatively shown at an approximate position at this respective crank angle and is not to scale.

8.2.2 Comparison between luminescence- and pressure-based gas temperature

In the previous section, temperature measurements derived from two-color phosphor thermometry were presented. The results are globally consistent for a variation in the imaged crank angle degrees, as the in-cylinder gas temperature decreases at belated crank angles. In this section, the temperature results are compared to the bulk-gas temperature, which is calculated from the cylinder pressure.

The bulk-gas temperature is inferred from cylinder pressure (Section 3.4) and can be interpreted as a global average of the gas temperature in the cylinder, following a 0D assumption. To minimize systematic interference from, e.g., the hot fire deck or laser reflection off the cylinder on the temperature calculation from phosphor thermometry, the furthest position (–15 mm below the fire deck) is chosen, and regions of reflections are excluded from the analysis. The temperature average at 580 °CA from phosphor luminescence measurements is 496.5 K, with a single-shot precision of 65.4 K (±1σ).

The average bulk-gas temperature from the cylinder pressure and the associated standard deviation (±1σ) from cyclic fluctuations at 580 °CA is 498 ± 8.3 K. The standard deviation is calculated from all averaged bulk-gas temperatures at this respective CA. The bulk-gas temperatures from the measurements of previous crank angle degrees are shown in Table 6. The temperature variation due to cycle-to-cycle variations increases at increasing temperatures from 8.3 K up to threefold at 540 °CA (25.3 K).

Table 6: Comparison between average temperatures derived from the cylinder pressure (bulk-gas) and from YAG:Pr phosphor luminescence with the standard deviation (±1σ) at various crank angles in engine post-combustion gases.

Crank angle degree / °CA	YAG:Pr luminescence-based temperature / K	Bulk gas (pressure-based) temperature / K
580 °CA	496.5 ± 65.4 K	498 ± 8.3 K
560 °CA	591.3 ± 54.2 K	541.1 ± 10.3 K
540 °CA	657.3 ± 73.9 K	730.8 ± 25.3 K
520 °CA	N.A.	910.8 ± 41.8 K
500 °CA	N.A.	951.5 ± 37.3 K

Figure 87 shows the comparison between bulk-gas temperature and the temperatures calculated from YAG:Pr phosphor thermometry. The cyclic temperature variations of the bulk-gas are shown with the transparent overlay for the measurement set at 580 CA, and the temperature precision from the YAG:Pr luminescence temperature is indicated with the error bars (both ±1σ). Both temperatures show very good agreement in the measurement points between 540–580 °CA, where the temperature decreases below 700 K. For earlier crank angle degrees (520 and 500 °CA), the pressure-based bulk-gas temperature is >910 K and already above the highest temperature of the calibration curve.

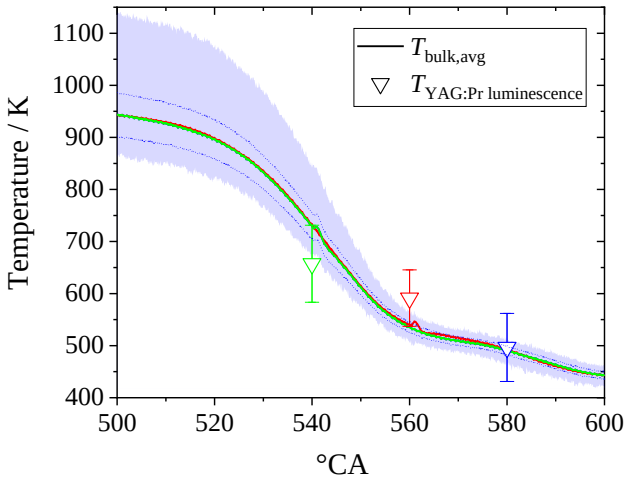

Figure 87: Bulk-gas temperature information calculated from the cylinder pressure (solid line) and YAG:Pr phosphor thermometry (symbols). Temperatures data of similar colors (line and symbol) originate from the same measurement (e.g., green for the measurement at BDC). The transparent overlay indicates the fluctuation of the measurement set at 580 °CA, and the dashed line indicates the 1σ standard deviation from the same measurement. The temperature from YAG:Pr is calculated from one pixel row in the ensemble-averaged image from valid pixels, as shown in Figure 86.

8.2.3 Uncertainty determination

In this section, different sources of uncertainty related to the temperature measurements in engine post-combustion gases will be discussed. The statistical uncertainty can be quantified from the single-shot deviation within one measurement set. The precision of the post-combustion measurements is given single-shot deviation ($\pm 1\sigma$) in Table 6, which is also denoted as the error bar in Figure 87. The single-shot precision decreases from 54.2 K at 591.3 K (9.2% at 580 °CA) to 73.9 K at 657.3 K (11.2% at 540 °CA). The uncertainty increases at earlier measurement timings as the phosphor luminescence signal decreases with increasing temperature. Furthermore, the combustion interference also increases at earlier measurement timings.

The correction of the combustion interference is unlikely to be a significant source of errors, as the signal contribution of combustion in the luminescence image used for the correction has similar spectral and temporal characteristics. The intensity variation between two subsequent images in the dual-imaging mode was quantified using a homogeneous light source and corrected for in the engine measurements. The intensity range of the measurements is similar to that of the calibration measurements (between 3.000–10.000 counts). Each pixel is considered an independent detector of light, so charge leakage between two neighboring pixels with large intensity differences is neglected. This is a reasonable simplification given the fact that combustion interference is not subject to high spatial gradients. However, if higher spatial resolution is required in future measurements, e.g., for near-wall temperature measurements investigating cooling effects from wall heat transfer, the contrast of both images of dual-imaging mode should be compared. The intensifier resolution in both frames can be quantified with the modulation transfer function (MTF) determined by the slanted-edge method in ISO 12233 [113], as demonstrated in Ref. [114].

A potential source of errors is the precise setting of the camera exposure, and an error estimation will be exemplarily done. According to the procedure introduced in Section 8.1.5, the temperature error resulting from erroneously assumed camera exposition that is based on 3τ of the phosphor emission lifetime is evaluated. It was assumed that the temperature is around 800 K, so all measurements in the post-combustion regime were performed with the same camera gating parameters according to the highest temperature from the lifetime characterization (812 K), where the relevant decay time constants are 63 µs for the red, and 2.7 µs for the blue emission channel, respectively. Figure 88 shows the modeled decay time of the red emission band at the estimated and real temperature. The signal captured by the camera is the surface below the decay curve at real temperature during the estimated exposure duration ($3\tau_{est}$).

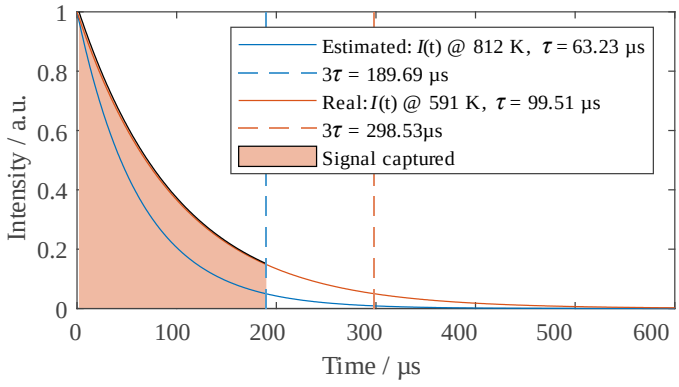

Figure 88: Modeled phosphor intensity decay for the assumed and real temperatures of the thermographic phosphors based on mono-exponential emission decay behavior with the signal captured from the real emission from camera gating from erroneously estimated lifetime.

If the gas temperature had been correctly assumed and the camera gating set accordingly to 3τ of the lifetime expected at this temperature, both imaging channels would see 95% of the total signal so that the ratio-temperature calibration curve could be applied. However, due to wrong temperature assumptions, the temperature is either higher or lower, resulting in shorter or longer emission lifetimes respectively. As a result, a different fraction than 95% of the signal is collected in each channel, and this deviation is referred to as the fractional intensity.

The fractional intensity, that is, the captured fraction of the signal relative to 95% that would be captured during an exposure duration of 3τ at the correctly assumed temperature, is presented for both imaging channels in Figure 89. The resulting ratiometric error is also shown on the right axis and translated into the actual residual temperature error plotted on the upper graph.

Since the temperature in the engine is not exactly known, a guess was proposed to calculate the luminescence lifetime initially and thus define the exposure time. If the temperature differs from the assumed one, the lifetime is incorrectly estimated. Despite the significant difference of ~200 K between the assumed and real temperature in the engine, the estimated temperature error is only 16.5 K at 560 °CA (2.7% at 607 K). This is because the relative change in the lifetime of both emission bands is approximately similar. From Figure 57, the relative decrease in lifetime in the range between 500 and 600 K is 23 and 29% per 100 K for the red and the blue emission, respectively, so the false estimation in lifetime cancels out in the ratio calculation.

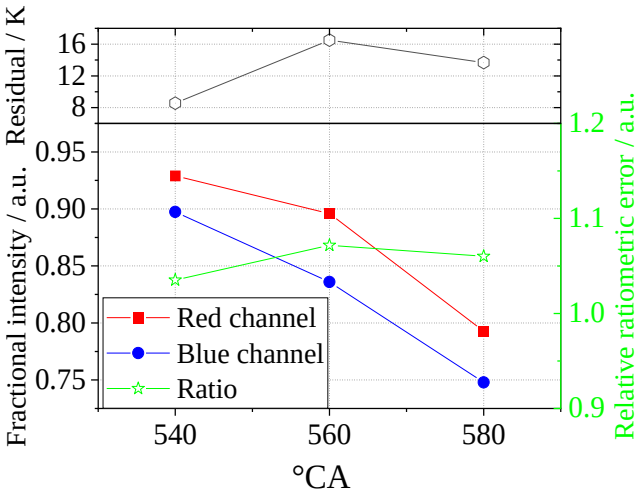

Figure 89: Fractional intensities (left axis) and the respective ratiometric error (right) resulting from erroneously assumed lifetime for post-combustion measurements. The resulting temperature error is shown on the top diagram.

The uncertainty estimation demonstrated here could also be applied to iteratively correct spatial temperature gradients, as the camera exposition can only be set for the entire detector and not individual pixels. For example, if the exposure time of the camera is correctly set according to the high temperature in one part of the image, the fractional intensity from the colder regions will be underestimated because the lifetime constant is usually longer at colder temperatures. This approach could then be iteratively applied. However, it should be noted that the estimated residual temperature error (16.5 K) from erroneous camera gating is three times lower than the statistical uncertainty induced by shot noise (54.2 K) at 560 °CA.

9 Conclusion and outlook

The objective of this dissertation was to develop an optical measurement technique based on thermographic PIV (T-PIV) for simultaneous measurements of gas temperature and velocity for application in the post-combustion regime of optically accessible internal combustion engines. The focus of the work was on the optimization of luminescence-based thermometry, which is far less mature than flow visualization via particle image velocimetry (PIV). Thereby, three challenges were identified, which were explored in this work.

Phosphor survivability: It was investigated to which extent thermographic phosphors change their luminescence (and thus temperature-dependent) properties after they have been exposed to reactive combustion conditions. For this purpose, the luminescent properties of thermographic phosphors were studied in the post-combustion regime of a lean premixed propane/air flame. While the laser-induced luminescence of YAG:Pr can be exploited for *in situ* temperature measurements in the exhaust gas above the flame, there is no *in situ* luminescence detectable for SMP:Sn. The particles were collected and *ex situ* analyzed for changes in macroscopic or chemical properties by microscopic analysis (SEM/EDX) and x-ray diffraction (XRD). For the measurements with SMP:Sn, it was found – contrary to the common understanding that thermographic phosphors are "mostly inert" – that the chemical composition and the morphology of SMP:Sn have been modified upon passing through the reaction zone, which is considered responsible for the loss of its luminescence properties. YAG:Pr, conversely, allows temperature measurement under post-combustion conditions of the lean premixed flame that are similar to the conditions found in the expansion stroke of a gasoline internal combustion engine. Theoretically, this would enable temperature measurements in the engine under the condition that the luminescent signal is stronger than the one from combustion interference (i.a., chemiluminescence) and blackbody radiation.

Characterization of the spectral and temporal luminescence properties of aerosolized phosphors: For the temperature measurements using the two-color approach, the luminescence properties of both thermographic phosphors used (SMP:Sn and YAG:Pr) were characterized in an aerosol at temperatures up to 825 K with the optical filters that are later used for temperature measurements in the optical engine. Additionally, the luminescence emission lifetime constants of the transitions used for two-color-based phosphor thermometry were characterized over the same temperature range, which provided the input for the lifetime-based camera gating approach employed for temperature measurements in post-combustion gases.

Suppression of signal interference from combustion luminescence: To increase the luminescence yield while minimizing the influence of interfering signals for temperature measurements in engine post-combustion gases, a novel online correction approach was developed. To this end, the exposure duration of the two-color detection channels was set to a threefold of the luminescence emission lifetime at the expected temperature. That enables the collection of 95% of the total luminescence while minimizing combustion interference. This method was combined with an *online* background correction approach, where the combustion background was corrected by taking two consecutive images before and after the

laser pulse. For this purpose, the first image, which contains only signals of the combustion, is subtracted from the second one containing signals from temperature-dependent phosphor luminescence. Possible saturation effects of the image intensifiers due to the fast sequence of both images are identified and corrected. Using this correction method, two-dimensional temperature fields were measured for the first time in the post-combustion gases of an optically accessible internal combustion engine between 540 and 580 °CA under fired operation.

Outlook: For future experiments, the image quality for post-combustion temperature measurements in the optical engine can be improved with simple measures. The information from the outer regions of the optical cylinder is useless due to strong laser reflections. In preliminary measurements, it was found that increasing the surface roughness can significantly reduce these reflections, e.g., by sandblasting the inner and outer surface of the cylinder on the side opposite to the side where the detection cameras are located. As a result, velocity measurements that were previously made through this opposite side of the optical quartz ring would no longer be possible without adaptations. However, the arrangement of the cameras can be adapted such that the camera for PIV imaging would be located on the same side of the cylinder as the cameras for the detection of temperature-dependent luminescence. This could either be a spectrally-independent beam splitter, or more specifically, for low-light conditions, an additional narrow-band notch dichroic beam splitter (e.g., Semrock NFD01–532) would need to be inserted in the light detection path upstream of the phosphorescence beam splitter. This beamsplitter would only reflect the elastically scattered light of the double-pulse PIV laser (532 nm) and transmit light of longer and shorter wavelengths towards the cameras that detect the phosphor luminescence.

More generally, for measurements with a similar objective of post-combustion temperature measurements under reacting flow conditions, the uncertainties can be reduced: The uncertainties of the online correction method can be further reduced by additional calibration measurements. More specifically, the influence of the double-imaging mode on the intensity of the dark image at varying gate delays and exposure durations of this double-imaging mode should be investigated.

In a wider sense in regards to phosphor thermometry: While there is a rapidly increasing interest in thermographic phosphors for remote thermometry and an increasing number of different thermographic phosphors being characterized for this purpose, there is no established (or standardized) characterization procedure that defines their operating conditions for reliable use as luminescence thermometers. This is equally true for the thermochemical stability in reacting multiphase flows as for the agglomeration state of the phosphors (phosphor aerosol, bulk, coated surface, dispersion in liquids). Such a procedure and the resulting information could significantly simplify the selection of the most-suitable thermographic phosphors for any operating conditions and broaden access, also for non-scientific applications.

.

References

[1] R.K. Pachauri, L.A. Meyer, Climate Change 2014: Synthesis Report: Contribution of Working Groups I, II and III to the Fifth Assessment Report of the Intergovernmental Panel on Climate Change, Geneva, Switzerland, 2014.

[2] United Nations, Framework Convention on Climate Change: Convention of the Parties, 2015, https://unfccc.int/resource/docs/2015/cop21/eng/l09.pdf, accessed 12 February 2019.

[3] H.C. Frey, Trends in onroad transportation energy and emissions, Journal of the Air & Waste Management Association 68 (2018) 514–563.

[4] International Energy Agency, CO_2 emissions from fuel combustion: Highlights, Paris, 2017.

[5] S. Solaymani, CO_2 emissions patterns in 7 top carbon emitter economies: The case of transport sector, Energy 168 (2019) 989–1001.

[6] B.C.G. Karlsson, R. Friedman, Dilution of whisky – the molecular perspective, Scientific Reports 7 (2017) 6489.

[7] S. Kook, C. Bae, P.C. Miles, D. Choi, M. Bergin, R.D. Reitz, The Effect of Swirl Ratio and Fuel Injection Parameters on CO Emission and Fuel Conversion Efficiency for High-Dilution, Low-Temperature Combustion in an Automotive Diesel Engine, SAE Technical Paper (2006) 2006-01-0197.

[8] H. Liu, J. Ma, L. Tong, G. Ma, Z. Zheng, M. Yao, Investigation on the Potential of High Efficiency for Internal Combustion Engines, Energies 11 (2018), doi:10.3390/en11030513.

[9] P.C. Ma, M. Greene, V. Sick, M. Ihme, Non-equilibrium wall-modeling for internal combustion engine simulations with wall heat transfer, International Journal of Engine Research 18 (2017) 15–25.

[10] T. Arment, J. Cowart, P. Caton, L. Hamilton, The Effect of Ceramic Thermal Barrier Combustion Chamber Coatings on the Performance and Efficiency of a Small Diesel Engine, SAE International (2010) 2010-32-0090.

[11] B. Peterson, E. Baum, B. Böhm, V. Sick, A. Dreizler, High-speed PIV and LIF imaging of temperature stratification in an internal combustion engine, Proceedings of the Combustion Institute 34 (2013) 3653–3660.

[12] S.H.R. Müller, B. Böhm, M. Gleißner, R. Grzeszik, S. Arndt, A. Dreizler, Flow field measurements in an optically accessible, direct-injection spray-guided internal combustion engine using high-speed PIV, Experiments in Fluids 48 (2010) 281–290.

[13] V. Sick, M.C. Drake, T.D. Fansler, High-speed imaging for direct-injection gasoline engine research and development, Experiments in Fluids 49 (2010) 937–947.

[14] V. Sick, High speed imaging in fundamental and applied combustion research, Proceedings of the Combustion Institute 34 (2013) 3509–3530.

[15] C.D. Meinhart, S.T. Wereley, J.G. Santiago, PIV measurements of a microchannel flow, Experiments in Fluids 27 (1999) 414–419.

[16] T.A. McManus, J.A. Sutton, Simultaneous 2D filtered Rayleigh scattering thermometry and stereoscopic particle image velocimetry measurements in turbulent non-premixed flames, Experiments in Fluids 61 (2020) 2–19.

[17] M. Braun, W. Schröder, M. Klaas, High-speed tomographic PIV measurements in a DISI engine, Experiments in Fluids 60 (2019) 1–26.

[18] E. Baum, B. Peterson, C. Surmann, D. Michaelis, B. Böhm, A. Dreizler, Investigation of the 3D flow field in an IC engine using tomographic PIV, Proceedings of the Combustion Institute 34 (2013) 2903–2910.
[19] C. Schulz, V. Sick, Tracer-LIF diagnostics, Progress in Energy and Combustion Science 31 (2005) 75–121.
[20] T. Lee, W.G. Bessler, H. Kronemayer, C. Schulz, J.B. Jeffries, Quantitative temperature measurements in high-pressure flames with multiline NO-LIF thermometry, Appl. Opt. 44 (2005) 6718–6728.
[21] J.L. Caslavsky, D.J. Viechnicki, Melting behaviour and metastability of yttrium aluminium garnet (YAG) and $YAlO_3$ determined by optical differential thermal analysis, Journal of Materials Science 15 (1980) 1709–1718.
[22] B. Fond, C. Abram, F. Beyrau, Characterisation of the luminescence properties of BAM:Eu^{2+} particles as a tracer for thermographic particle image velocimetry, Applied Physics B 121 (2015) 495–509.
[23] C. Abram, B. Fond, F. Beyrau, Temperature measurement techniques for gas and liquid flows using thermographic phosphor tracer particles, Progress in Energy and Combustion Science 64 (2018) 93–156.
[24] J. Jordan, D.A. Rothamer, Pr:YAG temperature imaging in gas-phase flows, Applied Physics B 110 (2013) 285–291.
[25] A. Kopf, V. Frattina, M. Bardi, T. Endres, G. Bruneaux, C. Schulz, In-cylinder thermographic PIV combined with phosphor thermometry using ZnO:Zn, International Journal of Engine Research 0 (2021) 1-19.
[26] N. Bohr, I. On the constitution of atoms and molecules, The London, Edinburgh, and Dublin Philosophical Magazine and Journal of Science 26 (1913) 1–25.
[27] P.W. Atkins, J. de Paula, Atkins' physical chemistry, 8th ed., Oxford University Press, Oxford, New York, 2006.
[28] A. Khalid, K. Kontis, Thermographic Phosphors for High Temperature Measurements, Sensors 8 (2008) 56735744.
[29] J.H. Bell, E.T. Schairer, L.A. Hand, R.D. Mehta, Surface pressure measurements using luminescent coatings, Annual Review of Fluid Mechanics 33 (2001) 155–206.
[30] A.C. Eckbreth, Laser diagnostics for combustion temperature and species, 2nd ed., Gordon & Breach, Amsterdam, United Kingdom, 1996.
[31] K. Kohse-Höinghaus, Applied Combustion Diagnostics, 0th ed., CRC Press, 2002.
[32] T. Kissel, Spektroskopische Methoden zur Charakterisierung wandnaher Verbrennungsprozesse, Dissertation, Darmstadt, 2011.
[33] D.A. Rothamer, J. Jordan, Planar imaging thermometry in gaseous flows using upconversion excitation of thermographic phosphors, Applied Physics B 106 (2012) 435–444.
[34] N.J. Turro, Modern molecular photochemistry, Benjamin Cummings Publication & Co, Menlo Park, California, 1978.
[35] G. Blasse, B.C. Grabmaier, Luminescent Materials, Springer, Berlin, Heidelberg, 1994.
[36] P. Dorenbos, Thermal quenching of Eu^{2+} 5d–4f luminescence in inorganic compounds, Journal of Physics: Condensed Matter 17 (2005) 8103–8111.
[37] P. Dorenbos, Mechanism of Persistent Luminescence in Eu^{2+} and Dy^{3+} Codoped Aluminate and Silicate Compounds, Journal of the Electrochemical Society 152 (2005) H107-H110.
[38] C. Knappe, Phosphor Thermometry on Surfaces - A Study of its Methodology and its Practical Applications, Dissertation, 2016.
[39] L.A. Riseberg, H.W. Moos, Multiphonon Orbit-Lattice Relaxation of Excited States of Rare-Earth Ions in Crystals, Physical Review 174 (1968) 429–438.

[40] M.J. Weber, Radiative and Multiphonon Relaxation of Rare-Earth Ions in Y_2O_3, Physical Review 171 (1968) 283–291.
[41] W.H. Fonger, C.W. Struck, Eu^{3+} ^5D Resonance Quenching to the Charge-Transfer States in Y_2O_2S, La_2O_2S, and LaOCl, The Journal of Chemical Physics 52 (1970) 6364–6372.
[42] C.W. Struck, W.H. Fonger, Role of the charge-transfer states in feeding and thermally emptying the ^5D states of Eu^{3+} in yttrium and lanthanum oxysulfides, Journal of Luminescence 1-2 (1970) 456–469.
[43] D. Witkowski, D.A. Rothamer, Scattering referenced aerosol phosphor thermometry, Measurement Science and Technology 30 (2019) 44003.
[44] L.P. Goss, A.A. Smith, M.E. Post, Surface thermometry by laser-induced fluorescence, Review of Scientific Instruments 60 (1989) 3702–3706.
[45] J.F. Sarver, M.V. Hoffman, F.A. Hummel, Phase Equilibria and Tin-Activated Luminescence in Strontium Orthophosphate Systems, Journal of the Electrochemical Society 108 (1961) 1103.
[46] D. Witkowski, D.A. Rothamer, Emission properties and temperature quenching mechanisms of rare-earth elements doped in garnet hosts, Journal of Luminescence 192 (2017) 1250–1263.
[47] D. Witkowski, Investigation of Thermographic Phosphors for Gas-Phase Temperature Measurements in Combustion Applications: Dissertation, 1st ed., ProQuest LLC, Ann Arbor.
[48] R.E. Palmer, SAND-89-8206, The CARSFT computer code calculating coherent anti-Stokes Raman spectra: User and programmer information, SAND-89-8206, 1989.
[49] P. Strehlow, J. Seidel, PTB-Mitteilungen: Themenschwerpunk Temperatur, 2007.
[50] K. Stierstadt, Thermodynamik: Von der Mikrophysik zur Makrophysik, Springer, Berlin, Heidelberg, 2010.
[51] P.R.N. Childs, J.R. Greenwood, C.A. Long, Review of temperature measurement, Review of Scientific Instruments 71 (2000) 2959–2978.
[52] M.D. Chambers, D.R. Clarke, Doped Oxides for High-Temperature Luminescence and Lifetime Thermometry, Annual Review of Materials Research 39 (2009) 325–359.
[53] F. Anghel, C. Iliescu, K. T. V. Grattan, A. W. Palmer, Z. Y. Zhang, Fluorescent-based lifetime measurement thermometer for use at subroom temperatures (200–300 K), Review of Scientific Instruments 66 (1995) 2611–2614.
[54] E. Hertle, L. Chepyga, M. Batentschuk, L. Zigan, Influence of codoping on the luminescence properties of YAG:Dy for high temperature phosphor thermometry, Journal of Luminescence 182 (2017) 200–207.
[55] N. Fuhrmann, E. Baum, J. Brübach, A. Dreizler, High-speed phosphor thermometry, Review of Scientific Instruments 82 (2011) 104903.
[56] J.S. Armfield, R.L. Graves, D.L. Beshears, M.R. Cates, T.V. Smith, S.W. Allison, Phosphor Thermometry for Internal Combustion Engines SAE Technical Paper (1997) 971642.
[57] S. Someya, Y. Okura, M. Uchida, Y. Sato, K. Okamoto, Combined velocity and temperature imaging of gas flow in an engine cylinder, Optics letters 37 (2012) 4964–4966.
[58] J. Brübach, J. Janicka, A. Dreizler, An algorithm for the characterisation of multi-exponential decay curves, Optics and Lasers in Engineering 47 (2009) 75–79.
[59] J.I. Eldridge, T.J. Bencic, S.W. Allison, D.L. Beshears, Depth-penetrating temperature measurements of thermal barrier coatings incorporating thermographic phosphors, Journal of Thermal Spray Technology 13 (2004) 44–50.
[60] R.M. Ranson, E. Evangelou, C.B. Thomas, Modeling the fluorescent lifetime of Y_2O_3:Eu, Applied Physics Letters 72 (1998) 2663–2664.
[61] M. Aldén, A. Omrane, M. Richter, G. Särner, Thermographic phosphors for thermometry: A survey of combustion applications, Progress in Energy and Combustion Science 37 (2011) 422–461.

[62] S.W. Allison, D.L. Beshears, M.R. Cates, M. Paranthaman, G.T. Gilles, LED-induced fluorescence diagnostics for turbine and combustion engine thermometry, Optical Diagnostics for Fluids, Solids, and Combustion 4448 (2001), doi:10.1117/12.449386.

[63] A. Augousti, K. Grattan, A. Palmer, A laser-pumped temperature sensor using the fluorescent decay time of alexandrite, Journal of Lightwave Technology 5 (1987) 759–762.

[64] P. Dragomirov, A. Mendieta, C. Abram, B. Fond, F. Beyrau, Planar measurements of spray-induced wall cooling using phosphor thermometry, Experiments in Fluids 59 (2018) 42.

[65] J. Brübach, J. Zetterberg, A. Omrane, Z.S. Li, M. Aldén, A. Dreizler, Determination of surface normal temperature gradients using thermographic phosphors and filtered Rayleigh scattering, Applied Physics B 84 (2006) 537–541.

[66] G. Särner, M. Richter, M. Aldén, Two-dimensional thermometry using temperature-induced line shifts of ZnO:Zn and ZnO:Ga fluorescence, Optics letters 33 (2008) 1327–1329.

[67] C. Abram, M. Pougin, F. Beyrau, Temperature field measurements in liquids using ZnO thermographic phosphor tracer particles, Experiments in Fluids 57 (2016) 115.

[68] A. Kopf, M. Bardi, E. Kohler, T. Endres, G. Bruneaux, C. Schulz, Survivability of the thermographic phosphors YAG:Pr^{3+} and SMP:Sn^{2+} in a premixed flame, Measurement Science and Technology 22 (2021) 74001.

[69] C. Abram, B. Fond, A.L. Heyes, F. Beyrau, High-speed planar thermometry and velocimetry using thermographic phosphor particles, Applied Physics B 111 (2013) 155–160.

[70] A. Omrane, P. Petersson, M. Aldén, M.A. Linne, Simultaneous 2D flow velocity and gas temperature measurements using thermographic phosphors, Applied Physics B 92 (2008) 99–102.

[71] N.J. Neal, J. Jordan, D. Rothamer, Simultaneous measurements of in-cylinder temperature and velocity distribution in a small-bore diesel engine using thermographic phosphors, SAE International Journal of Engines 6 (2013) 300–318.

[72] M. Raffel, C.E. Willert, F. Scarano, C.J. Kähler, S.T. Wereley, J. Kompenhans, Particle Image Velocimetry, Springer International Publishing, Cham, 2018.

[73] G.S. Elliott, M. Samimy, Compressibility effects in free shear layers, Physics of Fluids A: Fluid Dynamics 2 (1990) 1231–1240.

[74] M. Samimy, S.K. Lele, Motion of particles with inertia in a compressible free shear layer, Physics of Fluids A: Fluid Dynamics 3 (1991) 1915–1923.

[75] R.D. Keane, R.J. Adrian, Optimization of particle image velocimeters. I. Double pulsed systems, Measurement Science and Technology 1 (1990) 1202.

[76] B. Fond, Simultaneous temperature and velocity imaging in turbulent flows using thermographic phosphor tracer particles, Dissertation, London, 2014.

[77] B. Fond, C. Abram, F. Beyrau, On the characterisation of tracer particles for thermographic particle image velocimetry, Applied Physics B 118 (2015) 393–399.

[78] OSRAM GmbH, Material safety data sheet (SDS): Phosphor SV 253: Strontiummagnesiumorthophosphate: tin activated (#B4640219), Munich, 2011.

[79] E. Hertle, S. Will, L. Zigan, Characterization of YAG:Dy,Er for thermographic particle image velocimetry in a calibration cell, Measurement Science and Technology 28 (2017) 25013.

[80] I. Cosadia, J. Borée, G. Charnay, P. Dumont, Cyclic variations of the swirling flow in a Diesel transparent engine, Experiments in Fluids 41 (2006) 115–134.

[81] F.M. White, Viscous fluid flow, 3rd ed., McGraw-Hill, Boston, Massachusetts, 2006.

[82] Joint Committee for Guides on Metrology, Evaluation of measurement data — Guide to the expression of uncertainty in measurement, 2008, https://www.bipm.org/en/committees/jc/jcgm/publications.

[83] J. Brübach, Spektroskopische Methoden zur oberflächennahen Thermometrie in technischen Verbrennungsumgebungen, Dissertation, VDI-Verlag.

[84] B. Fond, C. Abram, A.L. Heyes, A.M. Kempf, F. Beyrau, Simultaneous temperature, mixture fraction and velocity imaging in turbulent flows using thermographic phosphor tracer particles, Optics Express 20 (2012) 22118–22133.
[85] J. Lindén, N. Takada, B. Johansson, M. Richter, M. Aldén, Investigation of potential laser-induced heating effects when using thermographic phosphors for gas-phase thermometry, Applied Physics B 96 (2009) 237–240.
[86] M. Luong, W. Koban, C. Schulz, Novel strategies for imaging temperature distribution using Toluene LIF, Journal of Physics: Conference Series 45 (2006) 133–139.
[87] J. Brübach, A. Dreizler, J. Janicka, Gas compositional and pressure effects on thermographic phosphor thermometry, Measurement Science and Technology 18 (2007) 764.
[88] L. Mannik, S.K. Brown, S.R. Campbell, Phosphor-based thermometry of rotating surfaces, Applied Optics 26 (1987) 4014–4017.
[89] G. Jovicic, L. Zigan, S. Will, A. Leipertz, Phosphor thermometry in turbulent hot gas flows applying Dy:YAG and Dy:Er:YAG particles, Measurement Science and Technology 26 (2014) 15204.
[90] B. Fond, C. Abram, M. Pougin, F. Beyrau, Characterisation of dispersed phosphor particles for quantitative photoluminescence measurements, Optical Materials 89 (2019) 615–622.
[91] D. Witkowski, D.A. Rothamer, Investigation of aerosol phosphor thermometry (APT) measurement biases for Eu:BAM, Applied Physics B 124 (2018) 202.
[92] E. Hertle, J. Bollmann, S. Aßmann, V. Kalancha, A. Osvet, M. Batentschuk, S. Will, L. Zigan, Characterization of the phosphor (Sr,Ca)$SiAlN_3$, Journal of Luminescence 226 (2020) 117487.
[93] V. Weber, J. Brübach, R.L. Gordon, A. Dreizler, Pixel-based characterisation of CMOS high-speed camera systems, Applied Physics B 103 (2011) 421–433.
[94] M. Ciapka, Charakterisierung lumineszenter Eigenschaften von Phosphor-Aerosolen bei verbrennungsrelevanten Temperaturen zur thermometrischen Anwendung, Masterarbeit, Duisburg, 2020.
[95] K. Levenberg, A method for the solution of certain non-linear problems in least squares, Quarterly of Applied Mathematics 2 (1944) 164–168.
[96] D.W. Marquardt, An Algorithm for Least-Squares Estimation of Nonlinear Parameters, Journal of the Society for Industrial and Applied Mathematics 11 (1963) 431–441.
[97] P. Halappa, H.M. Rajashekar, C. Shivakumara, Synthesis and structural characterization of orange red light emitting Sm^{3+} activated BiOCl phosphor for WLEDs applications, Journal of Alloys and Compounds 785 (2019) 169–177.
[98] G. Özen, O. Forte, B. Di Bartolo, Downconversion and upconversion dynamics in Pr-doped $Y_3Al_5O_{12}$ crystals, Journal of Applied Physics 97 (2005) 13510.
[99] C. Abram, B. Fond, F. Beyrau, High-precision flow temperature imaging using ZnO thermographic phosphor tracer particles, Optics Express 23 (2015) 19453–19468.
[100] J. Lindén, C. Knappe, M. Richter, M. Aldén, Limitations of ICCD detectors and optimized 2D phosphor thermometry, Measurement Science and Technology 23 (2012) 35201.
[101] J.P. Lewis, Fast Normalized Cross-Correlation/Fast Template Matching, Vision Interface, 1995.
[102] R.M. Haralick, L.G. Shapiro, Computer and robot vision, Addison-Wesley, Reading, Mass., 1992-93.
[103] W. Thielicke, R. Sonntag, Particle Image Velocimetry for MATLAB: Accuracy and enhanced algorithms in PIVlab, Journal of Open Research Software 9 (2021) 12.
[104] W. Thielicke, E.J. Stamhuis, PIVlab – Towards User-friendly, Affordable and Accurate Digital Particle Image Velocimetry in MATLAB, Journal of Open Research Software 2 (2014), doi:10.5334/jors.bl.
[105] F. Scarano, M.L. Riethmuller, Advances in iterative multigrid PIV image processing, Experiments in Fluids 29 (2000) S051-S060.

[106] K.T. Christensen, The influence of peak-locking errors on turbulence statistics computed from PIV ensembles, Exp Fluids 36 (2004) 484–497.
[107] D. Michaelis, D.R. Neal, B. Wieneke, Peak-locking reduction for particle image velocimetry, Meas. Sci. Technol. 27 (2016) 104005.
[108] R.J. Hearst, B. Ganapathisubramani, Quantification and adjustment of pixel-locking in particle image velocimetry, Exp Fluids 56 (2015) 1–5.
[109] J.E. Dec, C. Espey, Chemiluminescence Imaging of Autoignition in a DI Diesel Engine, SAE Technical Paper (1998) 982685.
[110] S.B. Gupta, B.P. Bihari, M.S. Biruduganti, R.R. Sekar, J. Zigan, On use of $CO2*$ chemiluminescence for combustion metrics in natural gas fired reciprocating engines, Proceedings of the Combustion Institute 33 (2011) 3131–3139.
[111] H.A. Michelsen, C. Schulz, G.J. Smallwood, S. Will, Laser-induced incandescence: Particulate diagnostics for combustion, atmospheric, and industrial applications, Progress in Energy and Combustion Science 51 (2015) 2–48.
[112] Princton Instruments, PI-MAX2: 1003 Specifications, 2nd ed.
[113] ISO 12233, Photography - Electronic still picture imaging - Resolution and spatial frequency responses, 2017.
[114] B. Peter D., M. Kenichiro, P. Kenneth, W. Dietmar, Updated Camera Spatial Frequency Response for ISO 12233, ei 34 (2022) 357-1-357-6.
[115] C. Kennel, J. Göttgens, N. Peters, The basic structure of lean propane flames, Symposium (International) on Combustion 23 (1991) 479–485.
[116] Mechanical and Aerospace Engineering (Combustion Research), University of California at San Diego, Chemical-Kinetic Mechanisms for Combustion Applications: San Diego Mechanism web page, 2016, https://web.eng.ucsd.edu/mae/groups/combustion/mechanism.html, accessed 2 December 2020.
[117] J.I. Goldstein, D.E. Newbury, P. Echlin, D.C. Joy, C.E. Lyman, E. Lifshin, L. Sawyer, J.R. Michael, Scanning Electron Microscopy and X-ray Microanalysis: Third Edition, Springer US, Boston, MA, 2003.
[118] The Surface Science Society of Japan, Compendium of Surface and Interface Analysis, Springer, Singapore, 2019.
[119] R.A. Mansmann, Multi-color time-resolved laser-induced incandescence for the measurement of soot and nanoparticle aerosols, Dissertation, Duisburg, 2019.
[120] Hamamatsu Photonics K. K., Photomultiplier tubes: Basics and Application, 3rd ed., 2007.
[121] S. Peukert, A. Sallom, A. Emelianov, T. Endres, M. Fikri, H. Böhm, H. Jander, A. Eremin, C. Schulz, The influence of hydrogen and methane on the growth of carbon particles during acetylene pyrolysis in a burnt-gas flow reactor, Proceedings of the Combustion Institute 37 (2019) 1125–1132.
[122] M. Leschowski, T. Dreier, C. Schulz, An automated thermophoretic soot sampling device for laboratory-scale high-pressure flames, The Review of scientific instruments 85 (2014) 45103.
[123] P.A. Skovorodko, A.G. Tereshchenko, D.A. Knyazkov, A.A. Paletsky, O.P. Korobeinichev, Experimental and numerical study of thermocouple-induced perturbations of the methane flame structure, Combustion and Flame 159 (2012) 1009–1015.
[124] F.W. Bowditch, A New Tool for Combustion Research A Quartz Piston Engine, SAE Technical Paper 610002 (1961), doi:10.4271/610002.
[125] D. Maligne, J. Kashdan, V. Ricordeau, Base de données ide: moteur optique: Projet ICAMDAC: Phase 4.1. IFPen.

[126] V. Frattina, Development and application of simultaneous 2D flow velocity and gas temperature measurements using thermographic phosphors under engine-relevant conditions, Dissertation, Paris, 2019.
[127] F. Beyrau, B. Fond, C. Abram, A summary of new developments in phosphor thermometry, Measurement Science and Technology 32 (2021) 120101.
[128] A. Kopf, M. Bardi, G. Bruneaux, B. Fond, T. Endres, C. Schulz, in: Poster presented at: 37th International Symposium on Combustion, 2018; Dublin, Ireland.
[129] H. Koelmans, A.P.M. Cox, Luminescence of Modified Tin-Activated Strontium Orthophosphate, Journal of the Electrochemical Society 104 (1957) 442.
[130] H.S. Yoder, M. Keith, Complete substitution of aluminum for silicon: The system $(MnO)_3Al_2O_3(SiO_2)_3$—$(Y_2O_3)_3(Al_2O_3)_5$, Geological Society of America, Bulletin (1950) 1516–1517.
[131] S. Gražulis, D. Chateigner, R.T. Downs, A.F.T. Yokochi, M. Quirós, L. Lutterotti, E. Manakova, J. Butkus, P. Moeck, A. Le Bail, Crystallography Open Database - an open-access collection of crystal structures, Journal of Applied Crystallography 42 (2009) 726–729.
[132] J.L. Caslavsky, Viechnicki Dennis J., Melting behaviour and metastability of yttrium aluminium garnet (YAG) and $YAlO_3$ determined by optical differential thermal analysis, Journal of Materials Science 15 (1980) 1709–1718.
[133] J. Berak, The System Magnesium Oxide - Phosphorus Pentoxide, Roczniki chemii 32 (1958) 17–22.
[134] K. Li, D. Chen, R. Zhang, Y. Yu, Y. Wang, Eu^{2+}:$SrMg_{1-x}Mn_xP_2O_7$ (x = 0–1) phosphors with tunable yellow–red emissions, Journal of Alloys and Compounds 555 (2013) 45–50.
[135] T. Gajda, P. Sipos, H. Gamsjager, The standard electrode potential of the Sn^{4+}/Sn^{2+} couple revisited, Monatshefte Für Chemie - Chemical Monthly 140 (2009) 1293–1303.
[136] B. Fond, C. Abram, M. Pougin, F. Beyrau, Investigation of the tin-doped phosphor $(Sr,Mg)_3(PO_4)_2$:Sn^{2+} for fluid temperature measurements, Opt. Mater. Express 9 (2019) 802–818.
[137] H. Koelmans, A.P.M. Cox, Luminescence of Modified Tin-Activated Strontium Orthophosphate, Journal of the Electrochemical Society 104 (1957) 442.
[138] J.B. Gruber, M.E. Hills, R.M. MacFarlane, C.A. Morrison, G.A. Turner, Symmetry, selection rules, and energy levels of Pr^{3+}:$Y_3Al_5O_{12}$, Chemical Physics 134 (1989) 241–257.
[139] G.H. Dieke, H.M. Crosswhite, The Spectra of the Doubly and Triply Ionized Rare Earths, Applied Optics 2 (1963) 675–686.
[140] J. Ganem, W.M. Dennis, W.M. Yen, One-color sequential pumping of the 4f5d bands in Pr-doped yttrium aluminum garnet, Journal of Luminescence 54 (1992) 79–87.
[141] G. Özen, O. Forte, B. Di Bartolo, Upconversion dynamics in Pr-doped $YAlO_3$ and $Y_3Al_5O_{12}$ laser crystals, Optical Materials 27 (2005) 1664–1671.
[142] O.L. Malta, E. Antic-Fidancev, M. Lemaitre-Blaise, J. Dexpert-Ghys, B. Piriou, Up-conversion in YAG:Pr^{3+}, Chemical Physics Letters 129 (1986) 557–561.
[143] M.J. Weber, Nonradiative decay from 5d states of rare earths in crystals, Solid State Communications 12 (1973) 741–744.
[144] A. Sallom, In situ measurements of soot formation in a burnt-gas flow reactor, Dissertation, Duisburg, 2021.
[145] S. Faust, G. Tea, T. Dreier, C. Schulz, Temperature, pressure, and bath gas composition dependence of fluorescence spectra and fluorescence lifetimes of toluene and naphthalene, Applied Physics B 110 (2013) 81–93.
[146] D. Fuhrmann, T. Benzler, S. Fernando, T. Endres, T. Dreier, S.A. Kaiser, C. Schulz, Self-quenching in toluene LIF, Proceedings of the Combustion Institute 36 (2017) 4505–4514.

[147] S. Zabeti, A. Drakon, S. Faust, T. Dreier, O. Welz, M. Fikri, C. Schulz, Temporally and spectrally resolved UV absorption and laser-induced fluorescence measurements during the pyrolysis of toluene behind reflected shock waves, Applied Physics B 118 (2015) 295–307.

[148] R. Hasegawa, I. Sakata, H. Yanagihara, G. Särner, M. Richter, M. Aldén, B. Johansson, in: SAE International, p. 20077078.

[149] W.M. Yen, S. Shionoya, H. Yamamoto, Phosphor Handbook, Second Edition, CRC Press, Boca Raton, FL, 2007.

[150] M. Wisniewska, D. Wisniewski, A.J. Wojtowicz, S. Tavernier, T. Lukasiewicz, Z. Frukacz, Z. Galazka, M. Malinowski, in: 2001 IEEE Nuclear Science Symposium Conference Record (Cat. No.01CH37310), 2001, 341-345 vol.1.

[151] F. Zentgraf, M. Stephan, E. Berrocal, B. Albert, B. Böhm, A. Dreizler, Application of structured illumination to gas phase thermometry using thermographic phosphor particles, Experiments in Fluids 58 (2017) 82.

[152] E. Kristensson, E. Berrocal, M. Richter, S.-G. Pettersson, M. Aldén, High-speed structured planar laser illumination for contrast improvement of two-phase flow images, Optics letters 33 (2008) 2752–2754.

A: Appendix

A. 1: Tumble calculation

The calculation of the tumble ratio was published in Ref. [25]. The dimensionless tumble ratio is defined as the quotient between the tangential (v_t) and the vertical gas velocity v_v along the axis perpendicular to the axis of the of the engine cylinder.

$$TR = \frac{v_t}{v_v} \tag{31}$$

The tumble ratio of a cylinder head is calibrated on a static aerodynamic flow bench. The vertical velocity is calculated from the pressure p_0 in the intake manifold and the pressure difference Δp from the intake manifold and the outlet tube representing the engine cylinder, measured by pressure transducers, where ρ is the density and κ the isentropic exponent of the gas.

$$v_v = \sqrt{2 \cdot \frac{\kappa}{\kappa - 1} \cdot \frac{p_0}{\rho_0} \cdot \left[1 - \left(\frac{p_0 - \Delta p}{p_0}\right)^{\frac{\kappa-1}{\kappa}}\right]} \tag{32}$$

The tangential velocity is calculated from angular momentum of a gas flow, where the righting torque M exerted by the flow is measured directly with a honeycomb torquemeter (Entran ELC-16), and the averaged mass flow rate from both ports of the intake manifold Q and the diameter d of the tube representing the engine bore.

$$v_t = \frac{4 \cdot M}{Q \cdot d} \tag{33}$$

A. 2: Temperature measurements from the standard intake temperature case

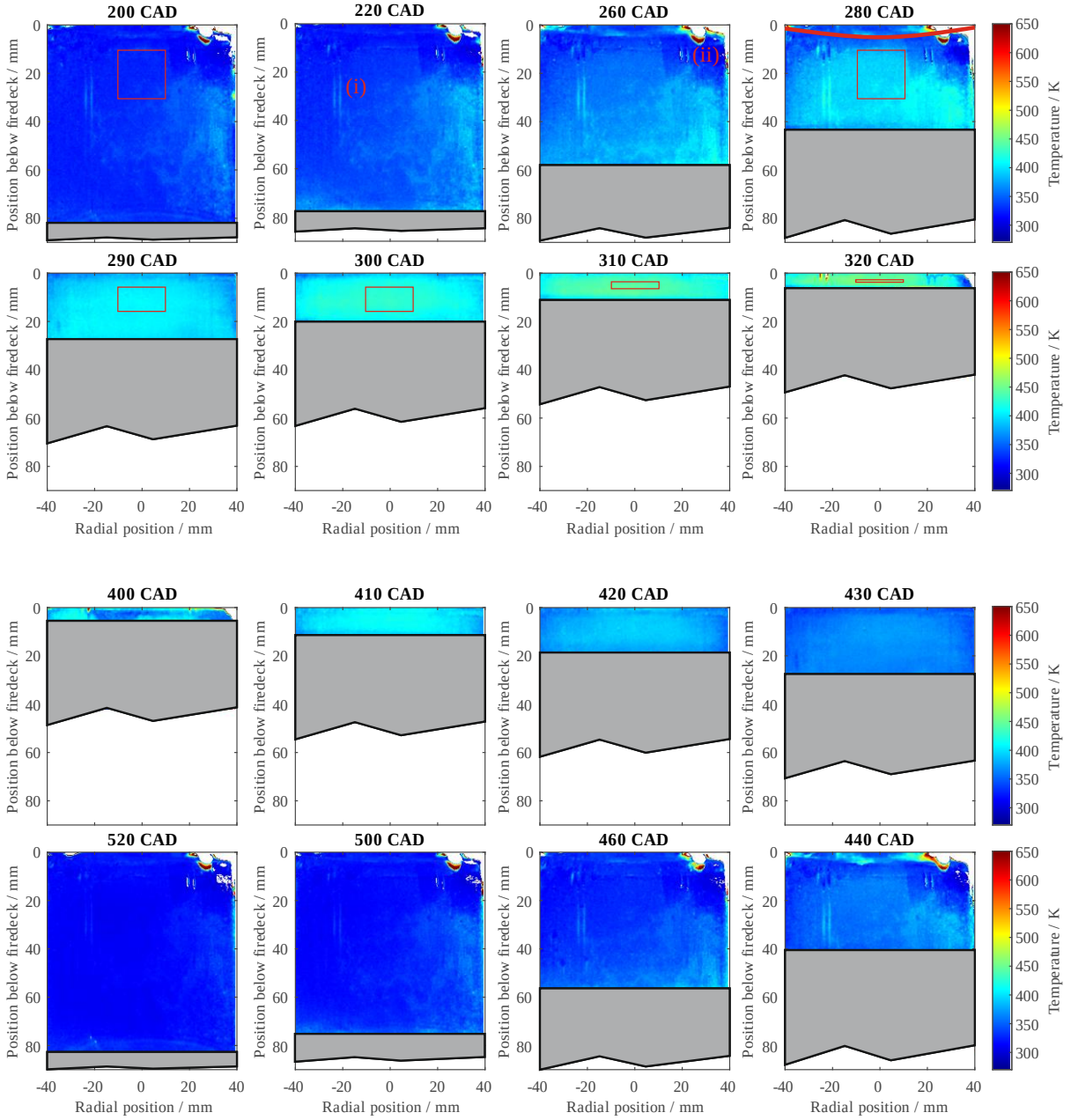

Figure 90: 2D averaged temperature maps from SMP:Sn phosphor thermometry at various CAD at standard intake temperature case. The images are the equivalent of Figure 75 (increased intake temperature).

A. 3: Particle counting

In image processing, particle counting relies on edge detecting is thus very sensitive to noise, therefore a smoothing filter needs be applied to reduce noise level if signal intensities are low. The filter most frequently used for this purpose is a spatial moving average filter (e.g., 3 × 3 pixels) that underestimates PND due to noise reduction. A moving average filter has a rectangular kernel that is beneficial for random noise reduction in spatial domain, however it has poor performance in the frequency domain as it cannot separate frequency bands (stopband attenuation). In this work, a Gaussian filter is used that has a gauss-shaped kernel and thus weights the intensity as a function of the distance from the center of the filter. Figure 91 shows a single-shot raw image from Mie-scattering in the spatial domain (left) measurements and its absolute FFT image in the spatial frequency domain (right). Figure 92 shows a single-shot image before (left) and after (right) noise reduction with an average noise level calculated in the red ROI. Figure 93 shows the PND that is determined from the raw (left) and noise-reduced (right) Mie-scattering image. A sensitivity analysis is performed for intensity threshold and the cut-off frequency (stopband attenuation) and they did not show significant variations in the determined PND within reasonable choice of the parameters.

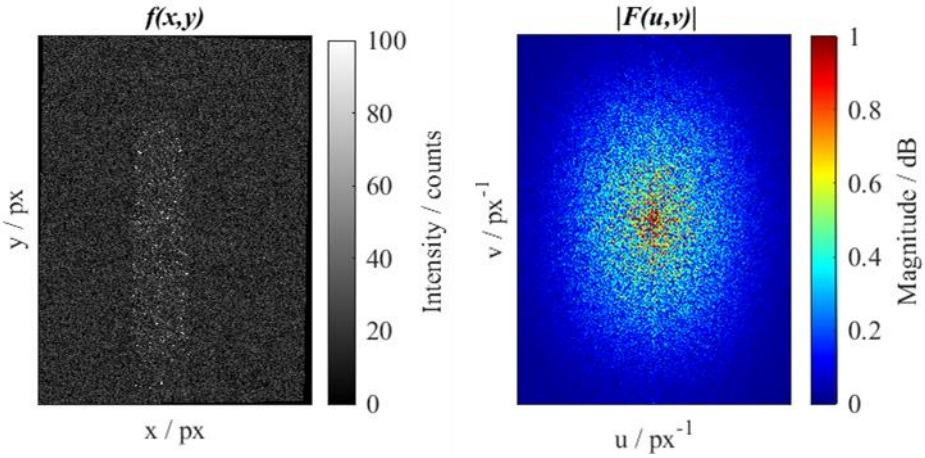

Figure 91: Left: raw Mie image. Right: FFT of the same image in the spatial frequency domain, where the zero-frequency is shifted to the center of the image.

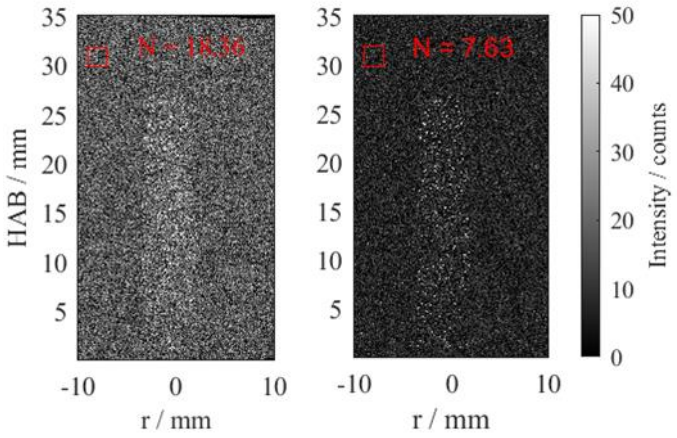

Figure 92: Mie image before (left) and after (right) noise reduction through gaussian smoothing. Images are displayed in global coordinates after mapping. The average signal intensity that is calculated from the region highlighted by red rectangle is printed in red.

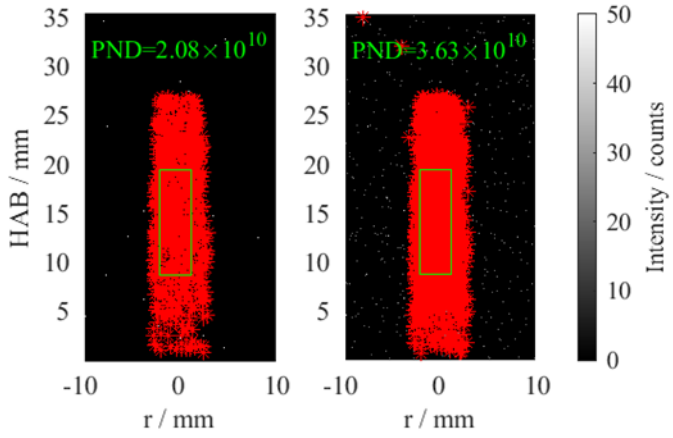

Figure 93: Determination of the volumetric particle number density after intensity thresholding and particle detection from original (left) and gaussian filtered image (right). Each detected particle is highlighted with a red cross and the PND from the region in the center of the flow are 2.08×10^{10} and 3.63×10^{10} m^{-3}, respectively for unfiltered and for the filtered image.

A. 4: Toluene-LIF images

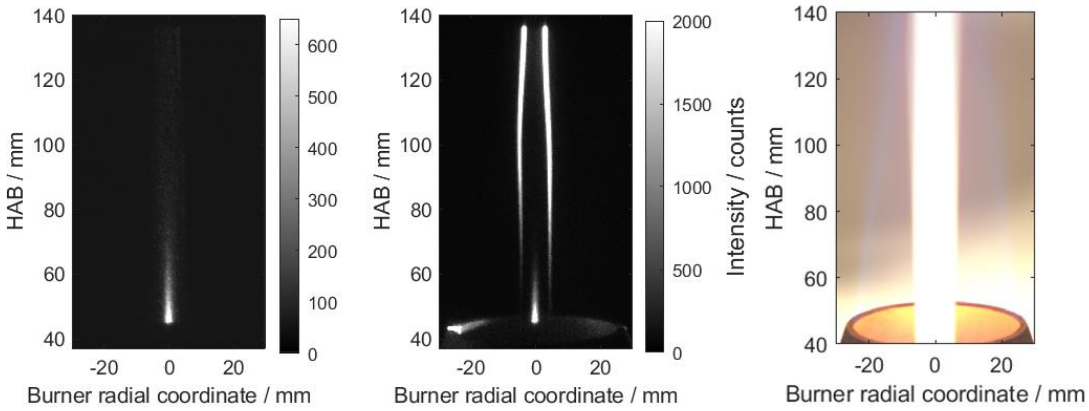

Figure 94: Raw images from toluene two-color-LIF measurements in the BGFR: blue (left) and red channel (center). Luminescence from intermediate species also contribute in the blue channel in the transition area to the flame. The flame and PAH-soot luminosity are shown in the right RGB image. The cone used for all measurements at HAB > 45 mm is also visible on the bottom.

Figure 94 shows the raw images from the two-color toluene-LIF measurements (left and center) with a natural luminosity image (right) showing soot formation after the pyrolysis of toluene.

B: List of Publications

B. 1: Publications in peer-reviewed journals

[1] **A. Kopf**, M. Bardi, E. Kohler, T. Endres, G. Bruneaux, C. Schulz, Survivability of the thermographic phosphors YAG:Pr^{3+} and SMP:Sn^{2+} in a premixed flame, Measurement Science and Technology 22 (2021) 74001.

[2] **A. Kopf**, V. Frattina, M. Bardi, T. Endres, G. Bruneaux, C. Schulz, In-cylinder thermographic PIV combined with phosphor thermometry using ZnO:Zn, International Journal of Engine Research 0 (2021) 1-19.

[3] **A. Kopf**, M. Bardi, T. Endres, G. Bruneaux, C. Schulz, Temperature measurements in engine post-combustion gases using YAG:Pr^{3+} **(in preparation).**

B. 2: Conference contributions

[1] **A. Kopf**, M. Bardi, G. Bruneaux, B. Fond, T. Endres, C. Schulz, **(Poster)**, *The potential of* $(Sr,Mg)_3(PO4)_2:Sn^{2+}$ *for gas-phase phosphor thermometry in post-combustion gases,* 37th International Symposium on Combustion, 2018; Dublin, Ireland.

[2] **A. Kopf**, M. Bardi, T. Endres, G. Bruneaux, C. Schulz, **(Talk)**, *Phosphor survivability study of YAG:*Pr^{3+} *and SMP:*Sn^{2+} *in a premixed flame,* 2nd International Conference on Phosphor Thermometry (July 27–29th 2020); Magdeburg (online conference), Germany.

DOI: 10.17185/duepublico/78790
URN: urn:nbn:de:hbz:465-20230907-085009-4